CRYSTALLINE METAL-ORGANIC FRAMEWORKS BASED ON CONFORMATIONALLY FLEXIBLE PHOSPHONIC ACIDS

A Dissertation

by

KEVIN JAMES GAGNON

Submitted to the Office of Graduate Studies of
Texas A&M University
in partial fulfillment of the requirements for the degree of

DOCTOR OF PHILOSOPHY

Chair of Committee,	Abraham Clearfield
Committee Members,	Timothy Hughbanks
	Hongcai Zhou
	Hae-Kwon Jeong
Head of Department,	David Russell

August 2013

Major Subject: Chemistry

ABSTRACT

The goal of the work described in this dissertation was to investigate the structure of metal phosphonate frameworks which were composed of conformationally flexible ligands. This goal was achieved through investigating new synthetic techniques, systematically changing structural aspects (i.e. chain length), and conducting *in situ* X-ray diffraction experiments under non-ambient conditions. First, the use of ionic liquids in the synthesis of metal phosphonates was investigated. Reaction systems which had previously been studied in purely aqueous synthetic media were reinvestigated with the addition of a hydrophobic ionic liquid to the reaction. Second, the structural diversity of zinc alkylbisphosphonates was investigated through systematically varying the chain length and reaction conditions. Last, the structural changes associated with externally applied stimuli (namely temperature and pressure) on conformationally flexible metal phosphonates were investigated. Elevated temperature was used to investigate the structural changes of a 1-D cobalt chain compound through three stages of dehydration and also applied pressures of up to 10 GPa were used to probe the structural resilience of two zinc alkylbisphosphonate materials under.

The iminobis(methylphosphonic acid) type ligands are a good example of a small, simple, conformationally flexible ligand. There are three distinct different structural types, utilizing this ligand with cobalt metal, described in the literature, all of which contain bound or solvated water molecules. The addition of a hydro-

phobic ionic liquid to an aqueous synthesis medium resulted in new anhydrous compounds with unique structural features.

Systematic investigations of zinc alkylbisphosphonate materials, constructed with three to six carbon linker ligands, resulted in four new families of compounds. Each of these families has unique structural features which may prove interesting in future applications developments. Importantly, it is shown that whether the chain length is odd or even plays a role in structural type although it is not necessarily a requirement for a given structural type; furthermore, chain length itself is not strictly determinative of structural type.

Dehydration in a cobalt phosphonate was followed via *in situ* single crystal X-ray diffraction. The compound goes through a two-stage dehydration mechanism in which the compound changes from a 1-D chain to a 2-D sheet. This process is reversible and shows unique switchable magnetic properties.

The high pressure studies of an alkyl chain built zinc metal phosphonate showed that the chains provide a spring-like cushion to stabilize the compression of the system allowing for large distortions in the metal coordination environment, without destruction of the material. This intriguing observation raises questions as to whether or not these types of materials may play a role as a new class of piezofunctional solid-state materials.

DEDICATION

I would like to dedicate this dissertation to my family and friends. I thank my parents, Roland and Sheron Gagnon for their continued love, support, and unending belief in my ability, even in my own faltering of that belief. I would also like to thank my brother, Roger, for always taking an interest in my work and always encouraging me to reach for more. I cannot stress enough that I would not have completed this work if not for their support; furthermore, I must thank Tracey Kniffin for her never ending love, encouragement, and all around support through this grand endeavor.

ACKNOWLEDGEMENTS

I would like to thank my committee chair, Dr. Abraham Clearfield, and my committee members, Dr. Timothy Hughbanks, Dr. Hongcai Zhou, and Dr Hae-Kwon Jeong for their guidance and support throughout the course of this research. I would also like to thank Mr. Zachary Beal, Ms. Alyssa Embry, and Ms. Megan Strayer who worked as undergraduate researchers with me and provided much support in the completion of this work. I would like to extend thanks to the many colleagues I have interacted with in the tenure of my graduate career: Dr. Russell Morris, Dr. Andrey Prosvirin, Dr. Nattamai Bhuvanesh, Dr. Joseph Reibenspies, Dr. Agustin Diaz, and Dr. Kim Dunbar. I would like to further thank Drs. Simon Teat and Christine Beavers, as their mentoring and support have molded me into the X-ray crystallographer I am today and without whom most of this work would not have seen the light of day. I cannot forget to thank those individuals that helped me on the way to graduate school: Dr. Cees L. H. Thieme, Dr. John Voccio, and Dr. Venkat Thalladi. Lastly I would like to thank my friends who have made Texas A&M a great experience as well as often providing helpful conversation and collaboration along the way: Dr. Houston Perry, Dr. Christopher Dorsey, Dr. Casey Wade, Dr. Trevor Makal, Mr. Kyle Kuskie, Mr. Scott Dempsey, and Mr. Jose Delgado.

In addition to the individuals named above I would like to thankfully acknowledge the National Science Foundation for providing funding through

grants DMR-0652166, HRD-0832993, and DGE-0750732. I would also like to acknowledge the Robert A. Welch Foundation for supplemental funding through grant A0673. The Advanced Light Source is supported by the Director, Office of Science, Office of Basic Energy Sciences, of the U.S. Department of Energy under Contract No. De-AC02-05CH11231.

NOMENCLATURE

AlMePO	Aluminum Methylphosphonate
ALS	Advanced Light Source
BBMP	2,2'-biphenylbis(phosphonic acid)
BTMP	1,3,5-benzenetris(methylphosphonic acid)
[BdMIM][BF_4]	1-Butyl-2,3-dimethylimidazolium Tetrafluoroborate
DAC	Diamond Anvil Cell
ddi	Deionized Distilled
FC	Field Cooled
H_4Ln	$H_2O_3P(CH_2)_nPO_3H_2$
IBMPA	Iminobis(methylphosphonic acid)
KPI	Kitaigorodskii Packing Index
LBNL	Lawrence Berkeley National Lab
MIBMPA	N-Methyliminobis(methylphosphonic acid)
MOFs	Metal-Organic Frameworks
MPMS	Magnetic Property Measurement System
PTFE	Polytetrafluoroethylene
PV	Psuedo-Voigt
PXRD	Powder X-ray Diffraction
SBUs	Secondary Building Units
SQUID	Superconducting Quantum Interference Device

TGA	Thermogravimetric Analysis
ZAC	Zinc Alkyl Cation
ZAG	Zinc Alkyl Gate
ZAL	Zinc Alkyl Layer
ZAS	Zinc Alkyl Sheet
ZAT	Zinc Alkyl Tunnel
ZBH	Zero Background Holder
ZFC	Zero Field Cooled

TABLE OF CONTENTS

Page

ABSTRACT ii

DEDICATION iv

ACKNOWLEDGEMENTS v

NOMENCLATURE vii

TABLE OF CONTENTS ix

LIST OF FIGURES xi

LIST OF TABLES xvi

CHAPTER I INTRODUCTION 1

Hydro-ionothermal Synthesis of Metal Phosphonates 3
Systematic Investigation of Zinc Alkylbisphosphonates 4
Effects of External Stimuli on Metal Phosphonates 6

CHAPTER II MATERIALS AND EXPERIMENTAL 9

Materials 9
Ligand Syntheses 10
Instrumentation 11

CHAPTER III HYDRO-IONOTHERMAL SYNTHESIS OF METAL PHOSPHONATES 15

Introduction 15
Experimental 18
Results 22
Discussion 55
Conclusion 57

CHAPTER IV SYSTEMATIC INVESTIGATION OF ZINC ALKYLBISPHOSPHONATES 58

Introduction 58

Page

Experimental 59
Results 65
Discussion 108
Conclusion 115

CHAPTER V STRUCTURAL CHANGES THROUGH THERMALLY INDUCED DEHYDRATION 116

Introduction 116
Experimental 118
Results 124
Discussion 146
Conclusion 146

CHAPTER VI STRUCTURAL CHANGES UNDER HIGH PRESSURE 148

Introduction 148
Experimental 151
Results 152
Discussion 170
Conclusion 171

CHAPTER VII SUMMARY 172

REFERENCES 173

APPENDIX A NEW EQUIPMENT DESIGNS 183

APPENDIX B CHAPTER IV SUPPLEMENTARY INFORMATION 201

LIST OF FIGURES

Page

Figure 1. Crystallization diagram for the system $CoCl_2 \cdot 6H_2O$/IBMPA/[BdMIM][BF_4]. 23

Figure 2. Thermal ellipsoid plot of compound 1. 26

Figure 3. Compound 1 viewed down the *a*-axis. 29

Figure 4. The interlayer hydrogen bonding in compound 1. 30

Figure 5. Thermal ellipsoid plot of compound 2. 32

Figure 6. Compound 2 viewed down the *b*-axis (top) showing the 1-D chains. 34

Figure 7. Thermal ellipsoid plot of compound 3. 36

Figure 8. Compound 3 viewed down the *a*-axis. 38

Figure 9. The interlayer hydrogen bonding in compound 3. 39

Figure 10. Thermal ellipsoid plot of compound 5. 41

Figure 11. Compound 5 viewed down the *c*-axis. 43

Figure 12. Compound 5 viewed down the *b*-axis. 44

Figure 13. IR spectra of compounds 1 through 5. 46

Figure 14. The temperature dependence of χT (♦) and of the inverse susceptibility $1/\chi$ (●) for compound 1. 50

Figure 15. FC, ZFC and remnant magnetization for compound 1. 51

Figure 16. The temperature dependence of χT (♦) and of the inverse susceptibility $1/\chi$ (●) for compound 2. 52

Figure 17. Temperature dependence of χT (●) and χ (♦) for compound 5. 54

Figure 18. Thermal ellipsoid plot of ZAG-6. 68

Figure 19. Corner shared 8-membered Zn-O-P-O rings which make up the 1-D inorganic chain unit of ZAG-6. 70

Page

Figure 20. ZAG-6 viewed along the *b*-axis showing the cross-linking of the 1-D chains to form the 3-D network.....71

Figure 21. Localized hydrogen bonding scheme of ZAG-6 showing the interconnection between 1-D chains via the interstitial water molecule.....72

Figure 22. ZAG-6 viewed down the *c*-axis showing the diamond shaped channels.....74

Figure 23. Side by side comparison of ZAG-4 (left) and ZAG-6 (right) viewed down the *b*-axis. 75

Figure 24. Side by side comparison of ZAG-4 (left) and ZAG-6 (right) viewed down the *c*-axis.....76

Figure 25. Thermal ellipsoid plot of ZAT-3. 78

Figure 26. Edge shared fused 8-membered Zn-O-P-O rings that make up the 1-D inorganic chain of ZAT-3.....80

Figure 27. Fused 8-member and 24-member rings which make up the 2-D sheets of ZAT-3. 81

Figure 28. ZAT-3 viewed down the *c*-axis showing the two different 1-D channels. 83

Figure 29. ZAT-3 (left) and ZAT-5 (right) viewed down the *b*-axis showing the alkyl pillars bridging together the 2-D sheets. 84

Figure 30. ZAT-3 (left) and ZAT-5 (right) as viewed down the *c*-axis showing the various 1-D tunnels. 85

Figure 31. Thermal ellipsoid plot of ZAS-3.....87

Figure 32. Fused 12-member rings which form the tube-like 1-D chain of ZAS-3.....89

Figure 33. The 1-D chains of ZAS-3 are bridged by pairs of H_4L3 linkers to form a 2-D slab. 90

Figure 34. Localized H-bonding in ZAS-3. 91

Figure 35. ZAS-3 (top) and ZAS-5 (bottom) slabs. 93

Figure 36. Thermal ellipsoid plot of ZAC-6. 95

Figure 37. The 1-D tube-like chain of ZAC-6. 97

Page

Figure 38. ZAC-6 viewed down parallel 1-D tubes showing how they are bridged via O-P-O pairs to form new 16-membered rings that bridge to form the 2-D sheet. 97

Figure 39. ZAC-6 viewed down the *a*-axis showing the 24-membered rings. 98

Figure 40. ZAC-6 viewed down the *a*-axis showing the encapsulated $Zn(H_2O)_6^{2+}$ in the 24-membered rings. 99

Figure 41. ZAC-6 viewed down the *c*-axis. 101

Figure 42. ZAC-4 (left) and ZAC-6 (right) viewed down the *c*-axis. 102

Figure 43. Thermal ellipsoid plot of ZAL-5. 104

Figure 44. ZAL-5 viewed down the *a*-axis showing the 2-D layer. 106

Figure 45. ZAL-5 viewed down the *b*-axis showing the ligand pillars linking together the 2-D sheets to form the 3-D network. 107

Figure 46. ZAL-6 viewed down the *b*-axis. 109

Figure 47. 1-D chain in ZAL-6 looking down the tube (left) and along the chain (right). 110

Figure 48. ZAL-6 viewed down the 1-D tubes showing the pairs of O-P-O bridges between neighboring chains. 110

Figure 49. The 2-D layer of ZAL-6 viewed down the *a*-axis. 111

Figure 50. Comparison of the 1-D chain building units in ZAG, ZAT, ZAC, ZAS, and ZAL-6. 114

Figure 51. Thermal ellipsoid plot of MnBBMP-4H_2O. 122

Figure 52. Thermal ellipsoid plot of CoBBMP-4H_2O. 123

Figure 53. Representation of CoBBMP-4H_2O chains running along the *b*-axis showing the ligand bridged 0-D cobalt octahedra. 126

Figure 54. The unit cell of CoBBMP-4H_2O as viewed down the *b*-axis 127

Figure 55. Thermogravimetric analysis curves for CoBBMP-4H_2O run at 10 °C/min (A) and at 1 °C/min (B). 129

Page

Figure 56. Thermal ellipsoid plot of CoBBMP-2H_2O. 132

Figure 57. CoBBMP-2H_2O showing the pendant ligand arrangement as well as the composition of the 1-D inorganic chain. 133

Figure 58. CoBBMP-2H_2O arrangement showing the neighboring 1-D chains as viewed down the *b*-axis (top) and top down showing a few of the hydrogen bonding interactions (bottom). 134

Figure 59. Photo of the crystal of CoBBMP after dehydration, which has begun to peel like a banana. 136

Figure 60. Thermal ellipsoid plot for CoBBMP. 137

Figure 61. CoBBMP viewed perpendicular to the 2-D inorganic layer showing the fused 8- and 24- memebered rings. 139

Figure 62. CoBBMP viewed down the *b*-axis showing the inorganic layer and how the biphenyl groups decorate the surface 140

Figure 63. The temperature dependence of χT (♦) and of the inverse susceptibility 1/χ (●) for CoBBMP-4H_2O. 143

Figure 64. Field dependence of the bulk magnetization of CoBBMP-4H_2O. 143

Figure 65. The temperature dependence of χT (♦) and of the inverse susceptibility 1/χ (●) for the 350 K data. 144

Figure 66. Field dependence of the bulk magnetization of the 350 K data. 144

Figure 67. The temperature dependence of χT (♦) and of the inverse susceptibility 1/χ (●) for CoBBMP. 145

Figure 68. Field dependence of the bulk magnetization of CoBBMP. 145

Figure 69. ZAG-4 as viewed down the *c*-axis for the ambient (left) and 7.32(7) GPa (right) structures. 150

Figure 70. Experimental relative lattice parameter variation observed with respect to increase in pressure. 154

Figure 71. Experimental unit cell volume variation observed with respect to increase in pressure. 154

Page

Figure 72. Representations for ZAG-4 of the 8-membered chain-link at ambient pressure (A, C) and 7.32(7) GPa (B, D) both showing the ring (top) and the chair-like conformation (bottom). 157

Figure 73. View down the *b*-axis of the ambient (left) and 7.32(7) GPa (right) ZAG-4 structures. 158

Figure 74. ZAG-6 as viewed down the *c*-axis for the ambient (left) and 6.9 GPa (right) structures. 163

Figure 75. Experimental relative lattice parameter variation observed with respect to increase in pressure for ZAG-6. 164

Figure 76. Experimental unit cell volume variation observed with respect to increase in pressure for ZAG-6. 164

Figure 77. Representations of the 8-membered chain-link in ZAG-6 at ambient pressure (A, C) and 6.9 GPa (B, D) both showing the ring (top) and the chair-like conformation (bottom). 166

Figure 78. View down the *b*-axis of ZAG-6 of the ambient (left) and 6.9 GPa (right) structures. 167

Figure 79. Side by side comparison of the alkyl chain conformations in ZAG-6 in the ambient pressure (left) and at 6.9 GPa (right). 168

LIST OF TABLES

Page

Table 1. Crystallographic data for $Co(HO_3PCH_2NH_2CH_2PO_3H)_2$ (1), $Co(H_2O)_2(HO_3PCH_2NH_2CH_2PO_3H)_2$ (2), $Co(HO_3PCH_2NH(CH_3)CH_2PO_3H)_2$ (3), and $CuClPO_3CH_2NH_2CH_3$ (5). 21

Table 2. Bond lengths [Å] and angles [°] for compound 1. 27

Table 3. Bond lengths [Å] and angles [°] for compound 2. 33

Table 4. Bond lengths [Å] and angles [°] for compound 3. 37

Table 5. Bond lengths [Å] and angles [°] for compound 5. 42

Table 6. Crystallographic data for ZAG-4, ZAG-6, ZAS-3, and ZAS-5. 62

Table 7. Crystallographic data for ZAT-3, ZAT-5, ZAL-5, ZAL-6. 63

Table 8. Crystallographic data for ZAC-4, ZAC-5, and ZAC-6. 64

Table 9. Selected bond lengths [Å] and angles [°] for ZAG-4 (left) and ZAG-6 (right). 69

Table 10. Selected bond lengths [Å] for ZAT-3. 79

Table 11. Selected bond lengths [Å] for ZAS-3 (left) and ZAS-5(right). 88

Table 12. Selected bond lengths [Å] for ZAC-6. 96

Table 13. Selected bond lengths [Å] and angles [°] for ZAL-5. 105

Table 14. Crystallographic data for MnBBMP-$4H_2O$, CoBBMP-$4H_2O$, CoBBMP-$2H_2O$, and CoBBMP. 120

Table 15. Some bond lengths [Å] for MnBBMP-$4H_2O$ (left) and CoBBMP-$4H_2O$ (right). 121

Table 16. Selected bond lengths [Å] for CoBBMP-$2H_2O$. 131

Table 17. Selected bond lengths [Å] for CoBBMP. 137

Table 18. Results of equation of state calculations from eosfit. 155

Table 19. K. P. I's for ZAG-4 at each pressure. 155

Page

Table 20. Cell parameters and crystallographic information for ZAG-4 at different pressures. 161

Table 21. Cell parameters and crystallographic information for ZAG-6 at different pressures. 169

CHAPTER I

INTRODUCTION*

Coordination polymers are a classification of compounds which consist of both inorganic and organic building units. These compounds have shown promise as ion-exchangers,[1] heterogeneous catalysts,[2] and for gas sorption/storage.[3] In coordination polymers, metal ions are covalently linked by organic moieties that may or may not possess chemical functionality. One of the largest subgroups of this classification is called metal-organic frameworks (MOFs).[3-8] This class of materials is primarily defined by crystalline porous 3-D frameworks and semi-amorphous porous pillared metal phosphonates.[3-9] The use of these materials for the aforementioned applications depends heavily upon their structural characteristics. Compounds designed for gas sorption or storage must have regular crystalline pores and high surface area,[3, 4, 7] while ion exchangers and catalyst materials must incorporate applicable accessible functional groups within the framework.[2, 10] To achieve the goals of high surface area, or a robust functional framework, the appropriate synthetic approach must be taken. Classically, this field is dominated by the use of rigid aryl organic carboxylic acid moieties which complex metal ions or small metal cluster secondary building units (SBUs). Carboxylate-based MOFs have been shown to have remarkably high surface area and uniform pore size distribution, but their lack of stability in air and water poses a significant problem if they are to be used in

---

*Sections of this chapter have been reproduced with permission from Gagnon, K. J.; Perry, H. P.; Clearfield, A., *Chemical Reviews* **2011**, *112* (2), 1034-1054 and Gagnon, K. J.; Beavers, C. M.; Clearfield, A., *J. Am. Chem. Soc.* **2013**, *135* (4), 1252-1255. Copyright 2011 and 2013 American Chemical Society. Gagnon, K. J.; Prosvirin, A. V.; Dunbar, K. R.; Teat, S. J.; Clearfiel, A., *Dalton Transactions* **2012** *41* (14), 3995-4006. – Reproduced by permission of The Royal Society of Chemistry. http://pubs.rsc.org/en/content/articlelanding/2012/dt/c2dt11907b.

industrial or commercial applications. MOFs prepared with divalent metals are subject to hydrolysis and are usually quite soluble in acid solution. It should be pointed out that other types of MOFs, such as those based on pyrazolate ligands, can be much more robust.[11]

Phosphonates form stronger bonds than carboxylates do with metal atoms, so it is natural that investigators should try to prepare phosphonate-based MOFs. Phosphonic acids possess three oxygen atoms capable of bonding to metals. They are oriented tetrahedrally around the phosphorus atom with the organic R-group occupying the fourth site of the tetrahedron. They can coordinate metals when they are in any state of protonation, which results in many possible modes of coordination and myriad different arrangements that the structures can take, many of which are not porous, and more often than not are involved in linking extended arrays of metal ions rather than discrete units (i.e. chains or planes).

The current field of metal phosphonates is encompassed by crystalline, semi-crystalline, and semi-amorphous porous and non-porous materials. Typically these can easily be defined by materials made with divalent, trivalent, and tetravalent cations, respectively. Experience has shown that monovalent metal phosphonates are highly soluble and often will form large single crystal supramolecular structures. Divalent phosphonates are less soluble and single crystal coordination networks can be obtained through hydro- or solvo-thermal methods. Trivalent phosphonates are rather insoluble and often produce microcrystalline powder materials, and tetravalent phosphonates are very insoluble, even in strong acid solution, and often form as semi-amorphous powders that are

likely to be nanoparticles. For this reason, those studies which focus on the structure of materials tend to focus on the use of divalent metals, as it is easier to form large single crystals for X-ray diffraction studies; however, applications may better benefit from the use of tri and tetravalent metals. The use of multifunctional phosphonic acids, new solvent systems, and high-throughput combinatorial synthetic methods has resulted in a plethora of materials of 0-D, 1-D, 2-D, and 3-D nature.

Hydro-ionothermal Synthesis of Metal Phosphonates

Hydrothermal techniques have been demonstrated to be the best method for synthesizing crystalline metal phosphonates.[12, 13] The area of carboxylate MOFs has shown that expanding this technique to include other solvents, such as dimethylacetamide, dimethylformamide, ethanol, and methanol, can result in a diversity of crystalline materials exhibiting a variety of interesting properties.[14, 15] In many instances, utilizing a different solvent with the same metal/ligand combination can have a dramatic impact on the final structure of the target material. Recently, the use of bulky organic templates has been explored to help control the regularity of the size and shape of the pores of a material.[16-18] The use of ionic liquids in the synthesis of metal phosphonates has not been explored to any great degree, despite the fact that its use in zeolite and framework-type materials is being extensively investigated.[19-23] Ionic liquids show interesting properties that make them excellent designer solvents, such as low melting points, viscosity, and solubility.[21] These solvent systems can also be mixed to provide accurate tuning of hydrophobicity/philicity, solubilizing properties, and working temperatures. In some cases, the

ionic liquid itself (or simple degradation products) is incorporated into the framework or trapped inside the pores.[24] The recent explosion of literature on the use of ionic liquids in the synthesis of porous materials leads one to believe that their use in metal phosphonate synthesis should be no different.

The work presented in Chapter III systematically investigates the varying of ionic liquid to water ratio in the synthesis of a variety of metal phosphonates utilizing imino-bis(methylphosphonic acid) type ligands. What is shown is that even in the presence of a large excess of water, the compounds resulting from the addition of a hydrophobic ionic liquid are anhydrous and a variety of new structures can be obtained through this new synthetic technique.[25]

Systematic Investigation of Zinc Alkylbisphosphonates

The first 3-D phosphonate framework containing open channels was reported in 1994 by Bujoli and coworkers, who had synthesized $Cu(O_3PCH_3)$ containing 24-membered rings lined by pendant methyl groups.[26] While the pore size of this compound was too small (~3 Å) to incorporate any typical molecule used to characterize them, this framework was the first of a kind. The first viable zeolitic type frameworks, α- and β-AlMePO were reported in the subsequent months by Maeda and coworkers.[27-29] After the developments made by Maeda, the field extended to use alkylbis(phosphonic acids) in the synthesis of new compounds. In 1997, Lohse and Sevov reported a 3-D open framework material with methylenediyl(phosphonic acid) and cobalt(II) which contained 1-D tunnels.[30] A plethora of work has been done on methylenediylphosphonate materi-

als, including the stable nickel materials, VSB-3 and VSB-4, reported by Férey and coworkers.[31] With the extension of the chain length of alkylbis(phosphonic acids) ($H_2O_3P(CH_2)_nPO_3H_2$) (H_4Ln) from n = 1 to n = 2, a change in structure occurs. The longer alkylbis(phosphonic acids) form frameworks possessing a dense layered motif or channeled open frameworks; and in some cases even form helical rods.[32] It has been shown, with a number of divalent metals and ligands of varying chain lengths, that pillared structures with elliptical tunnels running along either the *a*- or *b*-axis can be obtained.[33-35] This type of structure was first observed in a divalent metal framework utilizing H_4L3 and copper(II);[33] however, this was not uncommon in the vanadyl alkylphosphonates of the time.[36] It was speculated that the pore size may be controlled by varying the length of the alkyl spacer. Further investigations into the use of chains with n = 3 - 5 produced both zinc and copper frameworks all containing unidirectional tunnels filled with solvent water that could be removed with heat.[34, 35] Some of these structures contained coordinated water molecules which lined the pores and could be removed with heat as well, providing accessible metal coordination sites. Unfortunately, the channels are unable to be refilled after removal of the water due to the hydrophobic nature of the walls of the tunnel and likely structural collapse.

Chapter IV presents a systematic study on the synthesis of zinc alkylbisphosphonates from aqueous acetic acid solutions at both room temperature and under solvothermal conditions. This work results in the synthesis of four discrete families of frameworks and nine new compounds. Two members of these families had been previously

synthesized; however, this study shows how structural archetypes can be retained by careful control of synthetic conditions even while changing the linker length.

Effects of External Stimuli on Metal Phosphonates

MOFs and coordination polymers in general have revolutionized the field of crystal engineering, and stand to potentially revolutionize the field of solid-state chemistry.[37-41] Now that these compounds have presented themselves as being useful for engineering applications (such as ion-exchange or gas storage/separations), more information is needed as to what their mechanical properties and limitations may be. This information will lead to a variety of beneficial applications which might be based on unique piezo- or thermofunctional properties and characteristics.

Structural Changes through Thermally Induced Dehydration

Recently, coordination polymers possessing solid-state structural transformations have been researched due to their potential as interesting functional materials in applications such as switches, sensors, and storage materials.[42-45] The reversible nature of these structural changes makes applications centered on magnetic behavior favorable, as magnetic properties can often be controlled through external means. Drastic structural transformations, including changes in dimensionality and coordination environment are the most interesting to study as they result in the largest property changes; however, these transformations usually destroy crystallinity and cause much difficulty in the structural characterization of the transformation product. As a result, there are very few examples

of single-crystal-to-single-crystal transformations involving changes in dimensionality.[46-49]

Chapter V introduces compounds constructed using a 2,2'-biphenylbis-(methylphosphonic acid) (BBMP) linker. This compound is composed of a 1-D chain of octahedral cobalt ions which are bridged by the ligand. The coordination environment of the cobalt includes four water molecules and the structure contains an additional two waters of crystallization. Upon dehydration this compound undergoes structural condensation first to a new 1-D chain and ultimately to a new 2-D sheet of tetrahedrally coordinated cobalt ions. This dehydration process has been followed via *in situ* single crystal X-ray diffraction and the magnetic susceptibility has been studied at each stage of dehydration.

Structural Changes under High Pressure

A recent review paper presented a number of cases where mechanical properties of hybrid materials had been investigated; however, that number was relatively small compared with the number of MOFs published to date.[50] Many of these cases were computational. Of the few experimental studies that have been conducted, very interesting properties have been uncovered. The study of crystalline compounds under isostatic pressure loading has yielded remarkable results.[50, 51] Chapman and coworkers have shown that the compressibility of crystalline MOFs can be affected by guest inclusion and that the porosity of these materials can be modified by treating them first with small pressures.[52, 53] Moggach and coworkers have shown the effects of pressure on single

crystalline porous frameworks, and the structural changes associated with forcing solvent into the pores.[54, 55] The main application front for MOFs has been around gas storage and the understanding of how these structures change with applied pressure will be important if these materials are to have any industrial viability.

Chapter VI studies the effects of external isostatic applied pressure on one of the zinc alkylbisphosphonate families presented in chapter IV.[56] A full systematic investigation of the compound made with a four carbon linker shows that, up to 10 GPa, there exists no discernible amorphitization point nor is there any structural change. The resilience of the system is remarkable, as after application of 10 GPa of pressure, the pressure is removed and the single crystal reverts to its original state. An isostructural compound constructed with a six carbon linker was also investigated. The results of these experiments will be presented and conclusions will be drawn as to the effect of chain length on the compression mechanism.

CHAPTER II

MATERIALS AND EXPERIMENTAL

Materials

Cobalt(II) chloride hexahydrate, cobalt(II) perchlorate hexahydrate, copper(II) chloride dihydrate, manganese(II) perchlorate hexahydrate, zinc acetate dihydrate, zinc sulfate heptahydrate and anhydrous zinc chloride were obtained from Alfa-Aesar and used without further purification. 1,3-dibromopropane, 1,4-dibromobutane, 1,5-dibromopentane, 1,6-dibromohexane, 1-butyl-2,3-dimethylimidazolium tetrafluoroborate ([BdMIM][BF_4]), triethylphosphite and triisopropylphosphite were all obtained from Sigma-Aldrich and used without further purification. Methylamine (40% w/w in water) was purchased from Sigma-Aldrich and used without further purification. Paraformaldehyde and phosphorous acid were purchased from Fisher Scientific and used without further purification. All solvents were obtained through VWR International and used without further purification. Iminobis(methylphosphonic acid) (IBMPA) was obtained from Sigma-Aldrich and recrystallized from ethanol before use. The alkylbis(phosphonic acids) were synthesized similar to preparations previously described in the literature,[33] with modifications outlined below. *N*-methyliminobis(methylphosphonic acid) (MIBMPA) was synthesized according to the literature procedure and outlined below.[57] The 2,2′-biphenylbis(methylphosphonic acid) was kindly provided by Dr. Jerzy Zon of the University of Wroclaw, Poland. The deionized water used was purified with a Barnstead Nanopure II System to a resistivity of 17.6 MΩ·cm.

Ligand Syntheses

N-Methyliminobis(methylphosphonic Acid)

MIBMPA was prepared via a Mannich type reaction according to the previously published procedure.[57] In a 150 mL round bottom flask fitted with a reflux condenser was added methylamine (3.77 mL of 40% w/w in H_2O), H_2O (5 mL), phosphorous acid (16.1 g), and HCl (8.6 mL 12 M) and brought to reflux with stirring at 120 °C for 1h. After this, paraformaldehyde (4.49 g) was added and the resulting mixture was refluxed for an additional 1 h. Solvents were removed *in vacuo*, ethanol was added several times and removed *in vacuo* as well, affording a white powder of MIBMPA. This powder was recrystallized in ethanol and yielded 5.46 g of product (Yield: 43%). The powder was used in future reactions without further purification.

Alkylbisphosphonic Acids

In a typical reaction a 250 mL round bottom flask fitted with a reflux condenser was charged with a dibromoalkane and trialkylphosphite. The mixture was brought to reflux with stirring at 150 °C overnight. The resulting mixture was distilled at 160 °C until no further liquid is collected. The distillate was discarded and to the remaining liquid, 25 mL of 50% (v/v) HCl was added and brought to reflux at 120 °C overnight. Solvents were removed *in vacuo*, ethanol was added several times and removed *in vacuo* as well, affording an off-white gel. This gel was triturated with 150 mL of acetonitrile af-

fording a white crystalline powder of the alkylbis(phosphonic acid) (Yield: ~45%). The powder was dried at 100 °C for two hours and used without further purification.

Instrumentation

Thermogravimetric analyses (TGA) were carried out with a TGA Q500 from TA instruments at a heating rate of 10 °C min^{-1} under an air–N_2 mixture of 90 : 10 mL min^{-1}unless otherwise specified. Infrared spectra were measured on a Shimadzu IRAFFINITY-1 FTIR equipped with a Pike Technologies MIRacle™ ATR using a diamond plate. The polytetrafluoroethylene (PTFE) lined steel pressure vessels used in these experiments were designed and manufactured in-house. (See Appendix A) Both 25 mL single chamber and 25 mL × 16 chamber vessels were used. The microwave used in these experiments is a CEM® Discover S series microwave equipped with an Explorer12® auto-sampler. Elemental analyses were performed by Robertson Microlit Laboratories Inc. (Madison, NJ) and Atlantic Microlab Inc. (Norcross, GA). Magnetic susceptibility measurements were performed at 1000 Oe from 2 - 300 K on a Quantum Design Inc. Magnetic Property Measurement System (MPMS) Superconducting Quantum Interference Device (SQUID) magnetometer.

Single Crystal X-ray Diffraction

Single crystal X-ray diffraction data were collected on a Bruker APEX II diffractometer using Mo-Kα radiation (λ = 0.71073 Å). The samples were mounted on MiTeGen kapton pins. The cell constants were indexed from reflections obtained from

36 frames with exposure times of 10 – 20 seconds per frame. In most cases a full sphere (2400 frames at 6 cm detector distance) was collected with scan widths of 0.30° in ω and exposure times of 1 - 30 seconds per frame.

Several datasets were collected on Beamline 11.3.1 at the Advanced Light Source (ALS), Lawrence Berkeley National Lab (LBNL) using monochromatic radiation (λ = 0.77490 Å) at 100(2) K. The cell constants were indexed from reflections obtained from 36 frames with an exposure time of 1 second per frame. In most cases a full sphere (2400 frames at 5 cm detector distance) was collected with scan widths of 0.30° in ω and exposure times of 1 second per frame.

Data reduction and cell refinement for all compounds were performed with SAINT.[58] SADABS[59] was used to obtain absorption-corrected data. The structures were solved by direct methods and refined by full-matrix least squares on F^2 using the Bruker SHELXTL package.[60] All non-hydrogen atoms were refined anisotropically. Hydrogen atoms were placed geometrically on the carbon atoms and refined using a riding model. Any hydroxyl and amine hydrogen atoms were found in the difference map, their distance to their O or N atoms were restrained but the coordinates were allowed to refine, also the displacement parameters were ridden on their N or O atom.

The high pressure X-ray diffraction presented in Chapter VI was collected on Beamline 11.3.1 at the ALS, LBNL at room temperature. The Merrill-Bassett-type diamond anvil cell (DAC) used was designed and built in house. (See Appendix A) The DAC was equipped with Bohler-Almax cut diamonds, with culets of 600 μm in tungsten-carbide backing seats, and a tungsten gasket with a hole diameter of 350 μm. Full

details of the experimental for this work will be covered in Chapter VI. The pressure in the DAC was monitored via ruby fluorescence stimulated by a 100W 447 nm diode, measured via fiber-optic coupled to a Princeton Instruments Acton 300i spectrometer.

Data reduction and cell refinement were processed in a similar manner to the ambient datasets, utilizing SAINT;[58] however, the program ECLIPSE was used to generate masks to remove the gasket reflections and the DAC steel shadow from the frames before data reduction.

Powder X-ray Diffraction

Powder X-ray diffraction (PXRD) data were collected at 298 K on a Bruker D8 short arm diffractometer equipped with a multi-wire lynx eye detector using Cu-Kα (λ = 1.542 Å) and operated at a potential of 40 kV and a current of 40 mA. Most PXRD patterns were collected to determine phase purity through comparison to single crystal calculated powder patterns. Data for Rietveld refinement and structural analysis were collected over 4 to 60° in 2θ on a zero background holder (ZBH) at 298K. The small amount of sample and the need to use a ZBH has resulted in inaccurate intensities especially at higher angles. A combination of multiple samples was not done to avoid inhomogeneity in the sample. Accurate peak positions were obtained by fitting a few individual peaks using a pseudo-Voigt (PV) function included in the peak picking routine in TOPAS.[61] Indexing of the peaks was further carried out by TOPAS using the first 25 reflections. The range in 2θ of 8 to 57° was used for profile fitting and Rietveld refinement. The unit cell parameters were validated by profile matching using the '*hkl*-phase'

refinement in TOPAS using a Pawley fit.[62] For this fitting a 5th order Chebychev function was used to model the background and a parameter was included to account for the sample displacement caused by the ZBH. After a suitable refinement for the Pawley fit was found, the cell parameters were matched to that of a previously published isostructural compound.[13]

The atomic coordinates were obtained from the isostructural compound and were entered into TOPAS to perform Rietveld refinement. Initially, the profile parameters obtained from the '*hkl*-phase' were used without refinement. Further to restrict the number of adjustable parameters in TOPAS, a rigid-body refinement was performed with limited meaningful small variations in bond lengths, angles, and torsion angles. After reaching a stable refinement, the background and profile parameters were released for refinement. The final structural refinement was carried out with sufficient freedom on the bond lengths, angles, and torsion angles for the rigid body. No attempts were made to locate or refine the H atoms.

CHAPTER III

HYDRO-IONOTHERMAL SYNTHESIS OF METAL PHOSPHONATES*

Introduction

Metal phosphonates have historically been synthesized via hydrothermal techniques, in which the metal salt and phosphonic acid are sealed in PTFE lined steel high pressure vessels with water and heated to temperatures greater than 100 °C.[12, 13] In recent years, the interest in porous materials has led to the incorporation of template materials and designer solvents in the synthesis of metal phosphonates.[16, 17, 63] One such attractive solvent is the ionic liquid, which has had limited use in the synthesis of metal phosphonates, but has had increasing use in the synthesis of zeolites and a variety of other chemical processes.[22]

Ionic liquids are salts which are in the liquid state; while NaCl above 801 °C is technically an ionic liquid, the definition is generally considered to be limited to those salts which have melting points below ~100 °C. One of the largest families of compounds which fit this description are the salts of substituted imidazoles, the imidazolium family.[64] The simplest of these compounds are N,N-dialkylimidazolium halides, they are typically prepared through a neat quarternization reaction of an alkylimidazole with an alkylhalide. The alkyl groups may be the same or different to produce symmetrical or asymmetrical imidazolium compounds. To further derivatize this family the three carbon atoms in the imidazole ring may also be functionalized and the halide salts may be react-

---

*Gagnon, K. J.; Prosvirin, A. V.; Dunbar, K. R.; Teat, S. J.; Clearfiel, A., *Dalton Transactions* **2012** *41* (14), 3995-4006. – Reproduced by permission of The Royal Society of Chemistry. http://pubs.rsc.org/en/content/articlelanding/2012/dt/c2dt11907b.

ed with simple metal salts to produce ionic liquids with less coordinating or more complicated anions as necessary.

The purpose of the aforementioned derivatization is to allow for subtle adjustments to the properties of the potential solvent, such as viscosity, hydrophobicity/philicity, and melting point, to adjust the ability of the ionic liquid to solubilize a variety of species.[21] In the synthesis of porous materials, ionic liquids often act as templates and help to control the regularity of the size and shape of the pores of the material. In some cases the cation (and in less cases the anion) of the ionic liquid (or simple degradation products) incorporates into the framework of the porous material or is trapped inside the pores.[24]

The addition of amino, carboxyl, hydroxyl, halo, and sulfonyl groups to the phosphonic acid ligands has proven to aid in the synthesis of porous framework materials, and also to incorporate functionality to these materials through the added groups.[1, 12, 65-68] These groups also have been shown to play a role in directing the structure of a material. Recently, our lab demonstrated that by changing the position of the phosphonic acid group on a pyridyl ring results in drastic changes in the backbone structure of the resulting materials made with Sn(II).[65] Our research and that of others has shown that amino-phosphonic acids are capable of forming open framework materials with interesting properties and structural motifs.[13, 57, 69-83] The use of magnetically active metals in these syntheses has resulted in compounds with interesting magnetic properties.[13, 57, 76, 78, 79, 84] Many of these compounds, in hydro- and solvothermal systems, have been extensively explored and form 1-D, 2-D, and 3-D pillared-layered and open framework struc-

tures. Several divalent metal phosphonates, with ligands of the type $RN(CH_2PO_3H_2)_2$ (R= H, Me, Et, etc.), have been reported by our group and others. In 2006, Yang et al. reported the structure and magnetic properties of a cobalt iminobis(methylphosphonic acid) complex with formula $Co(H_2O)_2(HO_3PCH_2NH_2CH_2PO_3)_2 \cdot H_2O$ which exhibits antiferromagnetic interaction between neighboring cobalt centers within the layer.[71]

The ability to investigate the synthesis of new materials utilizing ionic liquids is further aided through combinatorial techniques. Stock and coworkers have shown in several examples how the use of a systematic modification of starting reagent ratios and solvents can result in a large diversity of structural types in metal phosphonates.[85] In this study I utilize combinatorial techniques to investigate the use of ionic liquids in the synthesis of iminobismethylphosphonates and utilized a PTFE lined pressure vessel that I designed containing a 4 x 4 array of chambers. The design of this vessel can be found in Appendix A.

Here we present the combination of combinatorial techniques with ionothermal synthesis to produce new highly stable hybrid materials from divalent metals and iminobis(methylphosphonic acids). Our aim is to utilize the structure directing abilities of a hydrophobic ionic liquid (1-butyl-2,3-dimethylimidazolium tetrafluoroborate) with the presence of added water to synthesize new metal phosphonates. The primary reason for the addition of the water is to generate pressure *in situ*; however, there are no doubts about water playing a role in the synthesis. The term "Hydro-Ionothermal"[63] has been used to describe the technique of combining a three component solvent which contains water and a deep eutectic mixture. Herein we have truly utilized a hydro-ionothermal

method by the addition of water to a room temperature ionic liquid. Our research efforts have led to five new divalent metal phosphonates with: 1-D structure, $Co(H_2O)_2(HO_3PCH_2NH_2CH_2PO_3H)_2$, (2), 2-D layered structures $Co(HO_3PCH_2NH_2CH_2PO_3H)_2$, (1), $Co(HO_3PCH_2NH(CH_3)CH_2PO_3H)$, (3), and $CuClO_3PCH_2NH_2CH_3$, (5), and 3-D network structure $Zn_3(O_3PCH_2NH_2CH_2PO_3)_2$, (4). Herein we report their syntheses, characterization, magnetic properties, and crystal structures. We also report the micro-wave assisted synthesis of the known compound $Co(H_2O)_2(HO_3PCH_2NH_2CH_2PO_3H)_2$, (6), resulting in high quality single crystals in a short period of time.[81]

Experimental

Synthesis of $Co(HO_3PCH_2NH_2CH_2PO_3H)_2$ (1)

In a typical experiment: a 25 mL PTFE lined steel pressure vessel is loaded with $CoCl_2 \cdot 6H_2O$ (0.984 mmol in 0.25 mL deionized distilled (ddi) H_2O), IBMPA (0.195 mmol in 0.5 mL ddi H_2O), and [BdMIM][BF_4] (2.07 mmol). To this mixture was added 0.25 mL ddi H_2O to give a total H_2O volume of 1.0 mL and to generate pressure autogenously *in situ*. The pressure vessel was sealed and heated for four days at 140 °C. The resulting large pink-purple crystals were filtered and washed with ddi H_2O and dried at room temperature. (Yield: 0.091 g, 93% based on IBMPA. Found: C, 10.49%; H, 3.15%; N, 5.93%. Calculated: C, 10.28%; H, 3.45%; N, 6.00%.)

Synthesis of $Co(H_2O)_2(HO_3PCH_2NH_2CH_2PO_3H)_2$ (2)

In a typical experiment: a 25 mL PTFE lined steel pressure vessel is loaded with $CoCl_2 \cdot 6H_2O$ (0.171 mmol in 0.125 mL ddi H_2O) and IBMPA (0.195 mmol in 0.5 mL ddi H_2O). To this mixture was added 0.375 mL ddi H_2O to give a total H_2O volume of 1.0 mL and to generate pressure autogenously *in situ*. The pressure vessel was sealed and heated for 4 days at 140 °C. The resulting pink needles were filtered and washed with ddi H_2O and dried at room temperature. (Yield: 0.034 g, 97% based on IBMPA. Found: C, 9.50%; H, 3.90%; N, 5.35%. Calculated: C, 9.55%; H, 4.01%; N, 5.57%.)

Synthesis of $Co(HO_3PCH_2NH(CH_3)CH_2PO_3H)_2$ (3)

In a typical experiment a 25 mL PTFE lined steel pressure vessel is loaded with $CoCl_2 \cdot 6H_2O$ (0.15 mmol in 0.25 mL ddi H_2O), MIBMPA (0.15 mmol in 0.5 mL ddi H_2O), and [BdMIM][BF_4] (3.12 mmol). To this mixture was added 0.25 mL ddi H_2O to give a total H_2O volume of 1.0 mL and to generate pressure autogenously *in situ*. The pressure vessel was sealed and heated for 4 days at 140 °C. The resulting pink blades were filtered and washed with ddi H_2O and dried at room temperature. (Yield: 0.015 g, 40% based on ligand.)

Synthesis of $Zn_3(O_3PCH_2NH_2PO_3)_2$ (4)

In a typical experiment a 25 mL PTFE lined steel pressure vessel is loaded with $ZnCl_2$ (0.9 mmol in 0.25 mL ddi H_2O), IBMPA (0.15 mmol in 0.5 mL ddi H_2O), and [BdMIM][BF_4] (2.07 mmol). To this mixture was added 0.25 mL ddi H_2O to give a total

H_2O volume of 1.0 mL and to generate pressure autogenously *in situ*. The pressure vessel was sealed and heated for 4 days at 140 °C. The resulting white powder was filtered and washed with ddi H_2O and dried at room temperature. (Yield: 0.043 g, 95% based on IBMPA Found: C, 8.28%; H, 1.94%; N, 4.62%. Calculated: C, 8.00%; H, 2.02%; N, 4.67%)

Synthesis of $CuClPO_3CH_2NH_2CH_3$ (5)

In a typical experiment, a 25 mL PTFE lined steel pressure vessel is loaded with $CuCl_2{\cdot}2H_2O$ (0.25 mmol), IBMPA (0.25 mmol), and [BdMIM][BF_4] (3.1 mmol). The pressure vessel was sealed and heated for 3 days at 140 °C. After allowing to cool to room temperature, excess [BdMIM][BF_4] was dissolved in absolute ethanol, and the resulting turquoise crystals were collected by filtration and washed with absolute ethanol. (Yield: 0.044 g, 79% based on Cu. Found: C, 10.86%; H, 2.89%; N, 6.16%. Calculated: C, 10.77%; H, 3.16%; N, 6.28%)

Synthesis of $Co(H_2O)_2(HO_3PCH_2NH_2CH_2PO_3H)_2$ (6)[81] In a typical experiment a 10 mL microwave glass pressure vessel is loaded with $CoCl_2{\cdot}6H_2O$ (0.3 mmol in 0.125 mL ddi H_2O), IBMPA (0.15 mmol in 0.5 mL ddi H_2O), and [BdMIM][BF_4] (2.07 mmol). To this was added 0.375 mL ddi H_2O to give a total H2O volume of 1.0 mL. The reaction was sealed and subjected to microwave irradiation for 2 hours in steps: 30 min at 80 °C, 60 min at 140 °C, 10 min at 120 °C, 10 min at 80 °C, and 10 min at 60 °C before being cooled to room temperature. The resulting pink

Table 1. Crystallographic data for $Co(HO_3PCH_2NH_2CH_2PO_3H)_2$ (1), $Co(H_2O)_2(HO_3PCH_2NH_2CH_2PO_3H)_2$ (2), $Co(HO_3PCH_2NH(CH_3)CH_2PO_3H)_2$ (3), and $CuClPO_3CH_2NH_2CH_3$ (5).

Sample	**1**	**2**	**3**	**5**
Chemical formula	$CoP_4O_{12}N_2C_4H_{16}$	$CoP_4O_{14}N_2C_4H_{20}$	$CoP_4O_{12}N_2C_6H_{20}$	$CuClPO_3NC_2H_7$
Formula mass	467.00	503.03	495.05	223.05
Crystal system	monoclinic	triclinic	monoclinic	monoclinic
Space group	$P2_1/c$	$P\bar{1}$	$P2_1/c$	$C2/m$
λ (Å)	0.71073	0.71073	0.7749	0.71073
a (Å)	9.3609(3)	4.618(3)	9.411(4)	14.354(7)
b (Å)	8.5315(3)	6.049(2)	8.711(4)	6.278(2)
c (Å)	9.3542(3)	13.927(5)	9.859(4)	7.706(3)
α (deg.)	90.00	87.525(4)	90.00	90.00
β (deg.)	96.530(2)	85.217(4)	93.209(7)	112.927(7)
γ (deg.)	90.00	84.475(4)	90.00	90.00
Z	2	1	2	4
V ($Å^3$)	742.2(2)	385.7(2)	807.0(6)	639.6(4)
Temperature (K)	110(2)	110(2)	100(2)	110(2)
Density (g/cm^3)	2.090	2.166	2.037	2.316
Measured reflections	8184	3668	7649	3741
Unique reflections	1386	1363	1430	800
Parameters	130	115	124	58
Restraints	2	1	3	0
R_{int}	0.0229	0.0284	0.0684	0.0202
θ range (deg.)	3.24 - 25.49	1.47 - 25.00	3.41 - 27.50	2.87 – 27.48
R_1, wR_2 all data	0.0226, 0.0616	0.0345, 0.0862	0.0342, 0.0840	0.0177, 0.0477
S (GooF) all data	1.118	1.071	1.067	1.088
Max/min res. Dens. ($e/Å^3$)	0.329/-0.508	0.666/-0.796	0.460/-0.488	0.462/-0.482

needles were filtered and washed with distilled deionized H_2O and dried at room temperature. (Yield: 0.028 g, 75% based on IBMPA.)

Single Crystal X-ray Diffraction

X-ray diffraction data for 1, 2, and 5 were collected at 110(2) K on a Bruker APEX II diffractometer as outlined in Chapter II. Data for 3 were collected at 100(2) K on Beamline 11.3.1 at the ALS, LBNL. The space groups were uniquely determined to be $P2_1/c$ (No. 14), $P\bar{1}$ (No. 2), $P2_1/c$ (No. 14), and $C2/m$ (No. 12) for 1, 2, 3 and 5 respectively. Crystal parameters and information pertaining to data collection and refinement for all structures are summarized in Table 1. Important bonding distances and angles are listed in further tables in this chapter.

Results

Syntheses

The synthesis field for cobalt chloride with IBMPA was investigated in two combinatorial experiments, from which we obtained two new products. The reaction system used to obtain these products as well as the result is shown in Figure 1. This system was investigated through the manipulation of two variables in a 4 X 4 reaction vessel; the variables were the amount of $CoCl_2 \cdot 6H_2O$ and the amount of [BdMIM][BF_4] utilized in the reaction. The ranges explored were Co^{2+} amounts of 0.171, 0.246, 0.315, 0.39, 0.612, 0.984, 1.272, and 1.56 mmol resulting in Co:P ratios of 1:2.3, 1:1.6, 1:1.2, 1:1,

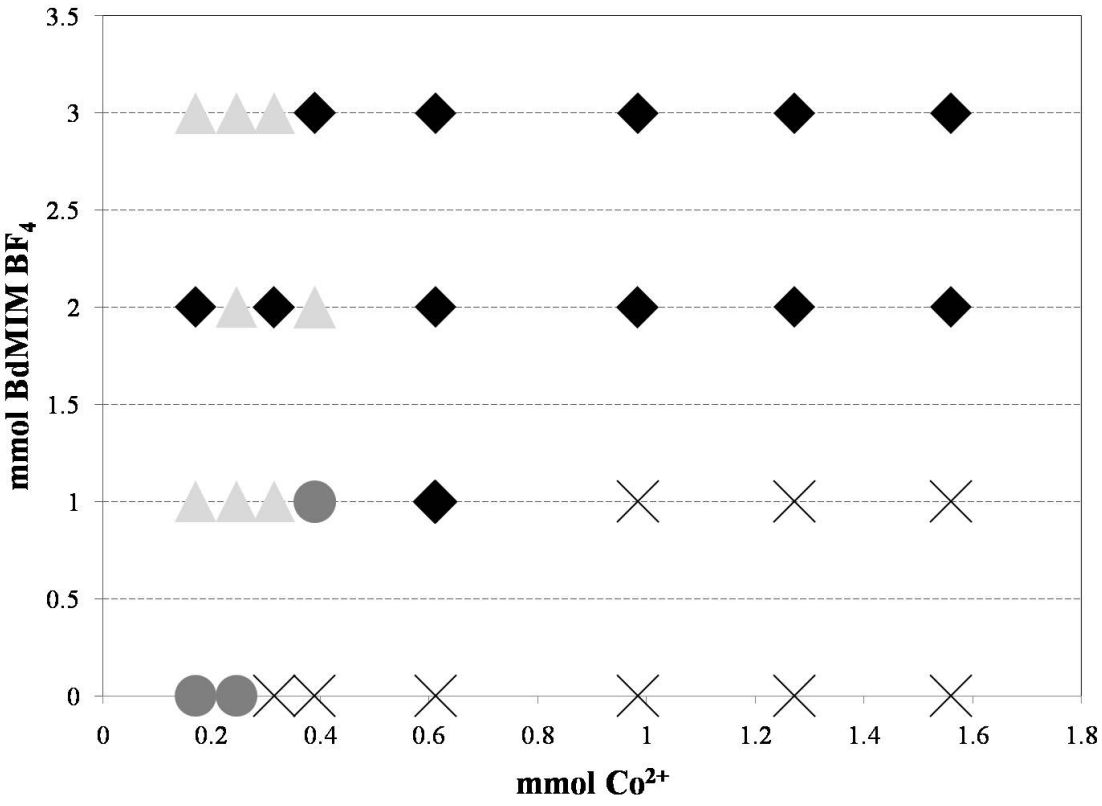

Figure 1. Crystallization diagram for the system $CoCl_2 \cdot 6H_2O$/IBMPA/[BdMIM] [BF_4]. IBMPA = 0.15 mmol and H_2O = 1.0 mL in all reactions. × = no reaction, ♦ = 1, •: 2, ▲: mixture of 1 and 6.

1.6:1, 2.5:1, 3.3:1 and 4:1, respectively. The amount of [BdMIM][BF_4] was varied from 0.0 to 3.0 mmol at even intervals. At higher concentrations of cobalt and ionic liquid, compound 1 is formed exclusively; but as the concentration of cobalt is reduced, a mixture of compound 1 and 6 is formed. At low concentrations of cobalt and little to no [BdMIM][BF_4], compound 2 is formed.

The same synthesis field as mentioned previously has been applied to the reaction of zinc chloride with IBMPA. The result of this set of reactions was less diverse as every reaction produced only one product, 4. A diagram depicting this synthesis field can be found in Appendix B.

The reaction of cobalt chloride under these same conditions with MIBMPA was less successful, as it resulted in only one product in poor yield, 3. The majority of the reaction conditions produced no solid product, as the result was simply a solution.

Lastly, reaction of copper chloride dihydrate with IBMPA under the identical conditions produced a product which had previously been reported. We also attempted this reaction system with the MIBMPA but were unable to characterize any of the products, due to poor crystal quality and an apparent mixture of phases; however, reaction of these reagents in [BdMIM][BF_4] in the absence of water did produce a new anhydrous 2-D network material, 5.

Crystal Structures

In compounds 1–3 there are several similar characteristics. In all three compounds there is an octahedrally coordinated cobalt center that is slightly distorted. Co-O

bond lengths range from 2.045(2) – 2.158(2) Å which is in good agreement with previously reported compounds of this nature. The distortion most likely arises due to a Jahn-Teller effect which is common for high-spin Co^{2+} complexes. Furthermore, the PO_3C tetrahedra in these structures all contain P-O bond distances of 1.494(2) – 1.585(2) Å. The large range in the P-O bonds can be attributed to the presence of protons on some of the oxygen atoms which results in an elongation of the P-O bond compared to a chelated or double-bonded oxygen atom.

In all five compounds the amino functional group contains a proton. This is necessary for charge balance in each of the respective structures, which was confirmed through bond valence calculations, based on the method of Brown and Altermatt.[86] The results of these calculations were 2.047 (1), 1.973 (2), and 1.953 (3) for the three Co^{2+} centers, and 1.981 (5) for the Cu^{2+} center. These values also confirm the reported local coordination environments around the respective metal centers. Calculations for 4 were not necessary as the compound is isostructural to a previously reported compound.

$Co(HO_3PCH_2NH_2CH_2PO_3H)_2$ (1)

Compound 1 consists of 2-D sheets which are hydrogen bonded together to form a 3-D supramolecular structure. Figure 2 shows the asymmetric unit. 1 crystallizes in the space group $P2_1/c$ (no. 14) with the cell parameters given in Table 1. Bond lengths and angles are given in Table 2.

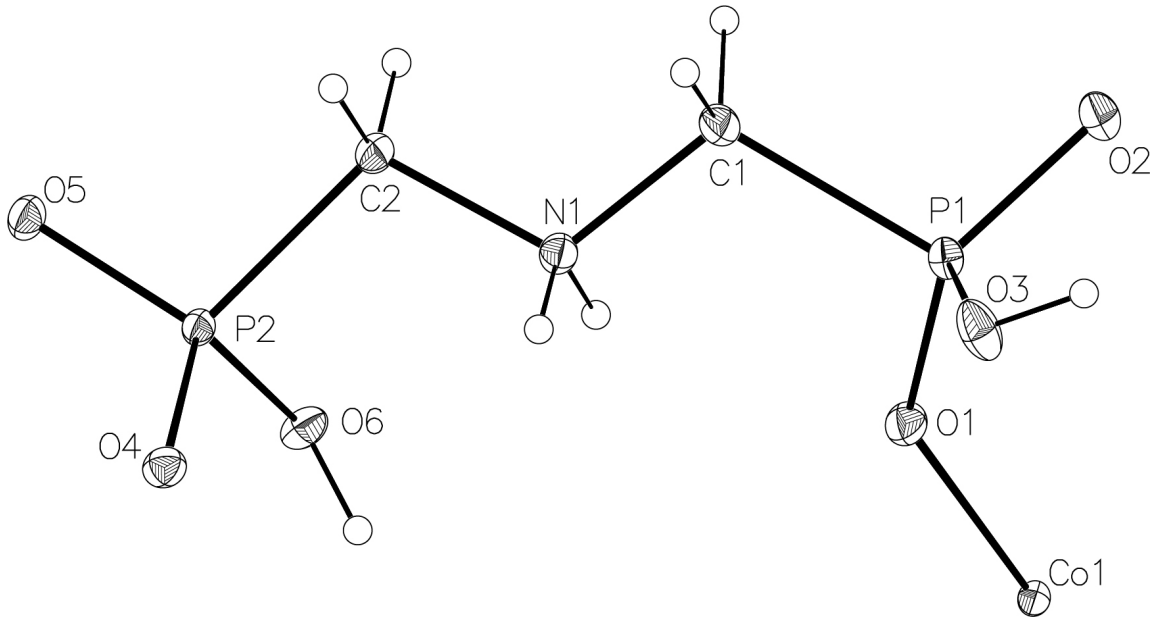

Figure 2. Thermal ellipsoid plot of compound 1.The thermal ellipsoids are at 50% probability.

Table 2. Bond lengths [Å] and angles [°] for compound 1.

Co1-O1	2.045(2)	P2-O4	1.497(2)
Co1-O1[a]	2.045(2)	P2-O5[b]	1.506(2)
Co1-O4[a]	2.095(2)	P2-O6	1.585(2)
Co1-O4	2.095(2)	P2-C2	1.820(2)
Co1-O5[a]	2.138(2)	N1-C1[c]	1.492(3)
Co1-O5	2.138(2)	N1-C2	1.495(3)
P1-O1	1.494(2)		
P1-O2	1.510(2)		
P1-O3	1.571(2)		
P1-C1	1.833(2)		
O1-Co1-O1[a]	180	O1-P1-O2	118.96(8)
O1-Co1-O4[a]	92.16(6)	O1-P1-O3	110.62(9)
O1[a]-Co1-O4[a]	87.84(6)	O2-P1-O3	109.90(8)
O1-Co1-O4	87.84(6)	O1-P1-C1	103.56(9)
O1[a]-Co1-O4	92.16(6)	O2-P1-C1	106.49(9)
O4[a]-Co1-O4	180	O3-P1-C1	106.32(9)
O1-Co1-O5[a]	87.56(6)	O4-P2-O5[b]	116.43(8)
O1[a]-Co1-O5[a]	92.44(6)	O4-P2-O6	110.85(8)
O4[a]-Co1-O5[a]	91.53(5)	O5[b]-P2-O6	110.06(8)
O4-Co1-O5[a]	88.47(5)	O4-P2-C2	108.29(9)
O1-Co1-O5	92.44(6)	O5[b]-P2-C2	107.49(9)
O1[a]-Co1-O5	87.56(6)	O6-P2-C2	102.76(9)
O4[a]-Co1-O5	88.47(5)	P1-O1-Co1	141.93(9)
O4-Co1-O5	91.53(5)	P2-O4-Co1	130.71(8)
O5[a]-Co1-O5	180	P2[d]-O5-Co1	136.32(9)
		C1[c]-N1-C2	115.1(2)
		N1-C2-P2	109.5(2)
		N1[e]-C1-P1	110.2(2)

Symmetry transformations used to generate equivalent atoms:
a: -x+1,-y,-z+2; b: x,-y+1/2,z+1/2; c: -x+1,y-1/2,-z+5/2;
d: x,-y+1/2,z-1/2; e: -x+1,y+1/2,-z+5/2

The Co(1) center is bridged to four symmetry-related cobalt ions through O-P-O bridges and to two others through full ligand O-P-C-N-C-P-O bridges. This connectivity results in 2-D sheets of edge-shared 16-membered rings as shown in Figure 3. The ligand loses only one proton per phosphonic acid group, whereas the amine is protonated. The ligand coordinates to the cobalt through only three of its six available oxygen atoms. The protonated amine forms hydrogen bonds with phosphonate oxygens within a given layer, {N(1)-H(3A)···O(2) 2.691(2) Å, 156(2)°} and {N(1)-H(3B)···O(1) 2.750(2) Å, 114(2)°}. Also internally H(6) hydrogen bonds to a coordinated O(5), {P(2)-(O6)-H(6)···O(5), 2.590(3) Å, 168(3)°}. The layers are held together by a network of free O-P-O-H interconnected hydrogen bonded dimers, {P(2)-O(5)-H(5)···O(2)-P(1), 2.562(2) Å, 175(2)°} as shown in Figure 4. The layers of this compound lie in the *bc*-plane. When viewed down the *b*-axis (Figure 4) one can see the hydrogen bonds that hold the layers together; furthermore, the hydrogen bonding network actually forms channels between the layers lined mostly by hydrophobic methylene units, visible when viewed down the *c*-axis (Figure 4). The arrangement of the layers and the channels formed by the hydrogen bonds may allow for intercalation of amines between the layers. Although the coordination sphere of the cobalt is filled, it may be possible for the amine to replace one or more of the coordinated oxygen atoms, which would result in a major structural change rather than the anticipated intercalation or exfoliation.

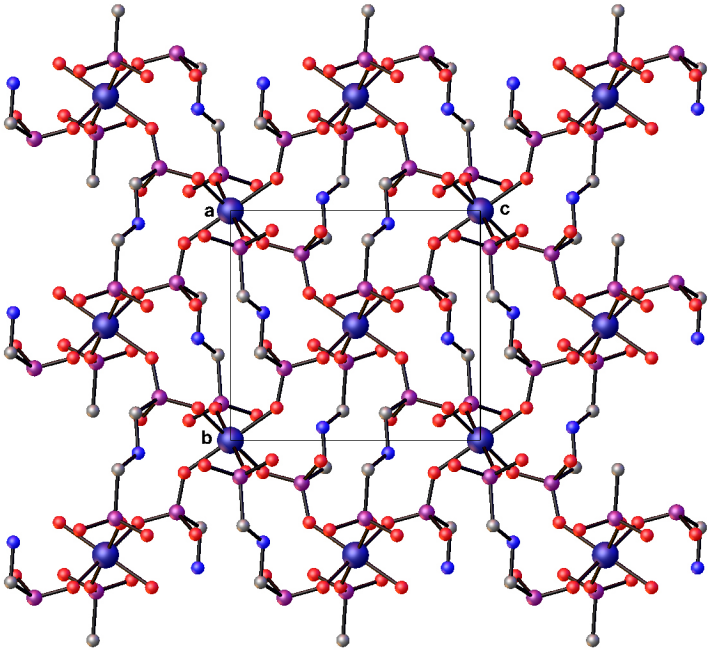

Figure 3. Compound 1 viewed down the *a*-axis.Notice the edge shared 16-membered rings made of four cobalt atoms and four phosphorus atoms.

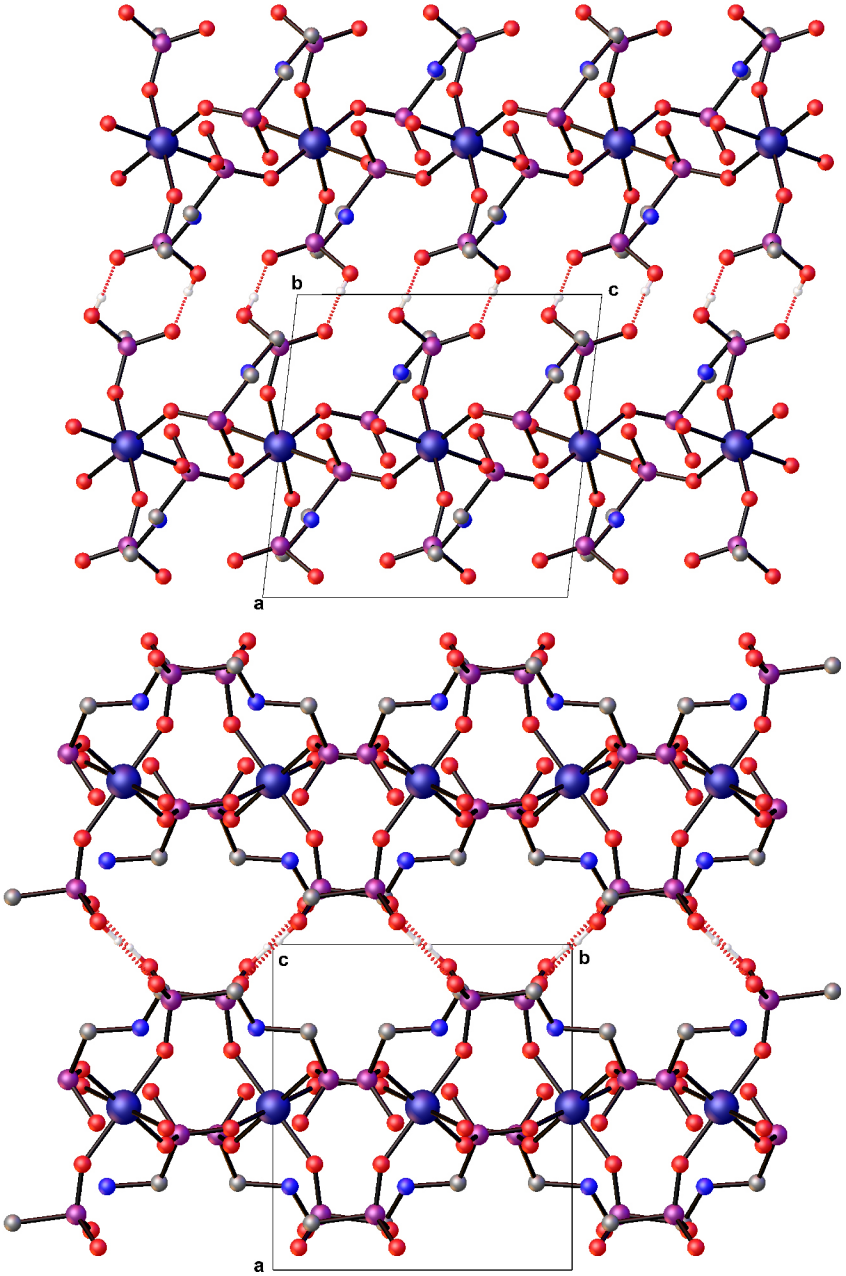

Figure 4. The interlayer hydrogen bonding in compound 1.Viewed down the *b*-axis (top) and the *c*-axis (bottom). Notice in the bottom the hydrophobic pockets that are formed by the hydrogen bonded dimers.

$Co(H_2O)_2(HO_3PCH_2NH_2CH_2PO_3H)_2$ (2)

Unlike its 2-D polymorph, compound 6, compound 2 consists of 1-D chains which hydrogen bond together to form a 3-D supramolecular structure. Figure 5 shows the thermal ellipsoid plot of the asymmetric unit. Compound 2 crystallizes in the space group $P\bar{1}$ (no. 2) with the cell parameters given in Table 1. Bond lengths and angles are given in Table 3.

The chains that make up compound 2 are formed by pairing O-P-O bridges connecting Co(1) to form 8-membered rings. These chains are interconnected to form a hydrogen bonded 2-D sheet through a network involving the coordinated water molecules and the free P-OH in the bound phosphonate. This 2-D network is further bridged to neighboring sheets through paired P-O-H···O bonding between the uncoordinated phosphonic acid. A table containing the important hydrogen bond distances, shown in Figure 6, can be found in Appendix B. The differences between this compound and its related polymorph arise from the coordination mode of the ligand. Coordination occurs through only one of the ligands available phosphonate groups. Two of the phosphonate oxygen atoms bridge between the symmetry related cobalt centers. Although only one of the phosphonate groups coordinates the cobalt atom, the ligand still loses one proton per phosphonic acid group. The unbonded phosphonic acid was initially considered to be doubly protonated to satisfy charge balance in the structure; however, the zwiterionic nature of the ligand is prevalent and the P-O bond distances do not satisfy having two protonated oxygen atoms as there is only one long P-O bond of 1.550(2) Å. Therefore the amine must be protonated to maintain charge balance.

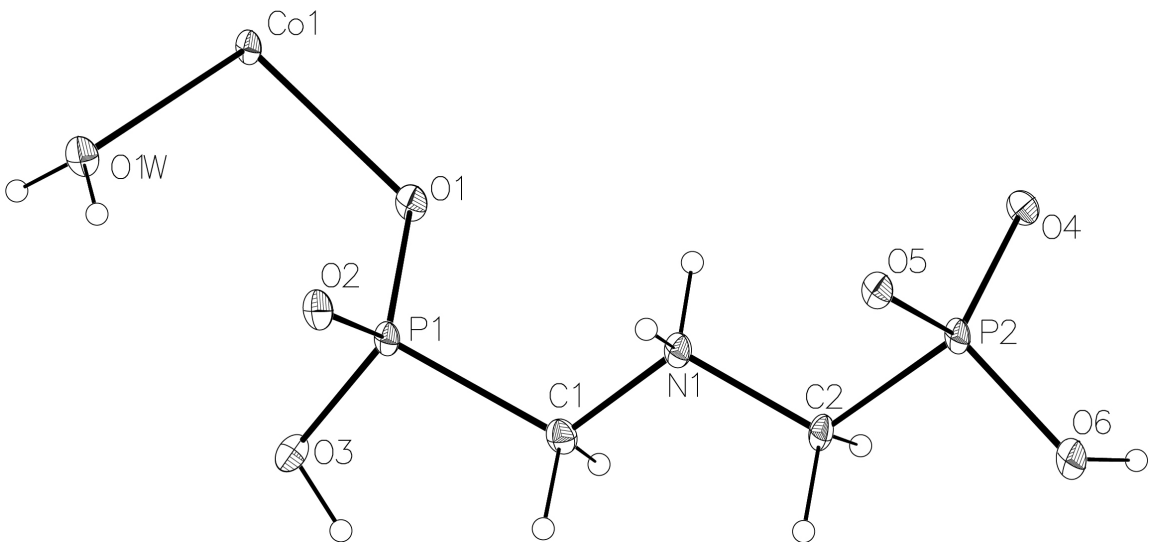

Figure 5. Thermal ellipsoid plot of compound 2. The thermal ellipsoids are at 50% probability.

Table 3. Bond lengths [Å] and angles [°] for compound 2.

Co1-O2[b]	2.062(2)	P2-O4	1.506(2)
Co1-O2[c]	2.062(2)	P2-O5	1.513(2)
Co1-O1[d]	2.097(2)	P2-O6	1.550(2)
Co1-O1	2.097(2)	P2-C2	1.819(3)
Co1-O1W	2.158(2)	P1-O1	1.512(2)
Co1-O1W[d]	2.158(2)	P1-O2	1.502(2)
		P1-O3	1.563(2)
		P1-C1	1.827(3)
		N1-C1	1.489(3)
		N1-C2	1.498(3)
O2[b]-Co1-O2[c]	180	O2-P1-O1	115.3(2)
O2[b]-Co1-O1[d]	89.08(8)	O2-P1-O3	109.7(2)
O2[c]-Co1-O1[d]	90.92(8)	O1-P1-O3	109.5(2)
O2[b]-Co1-O1	90.92(8)	O2-P1-C1	110.2(2)
O2[c]-Co1-O1	89.08(8)	O1-P1-C1	109.2(2)
O1[d]-Co1-O1	180	O3-P1-C1	102.3(2)
O2[b]-Co1-O1W	89.98(8)	O4-P2-O5	113.4(2)
O2[c]-Co1-O1W	90.02(7)	O4-P2-O6	113.1(1)
O1[d]-Co1-O1W	86.58(7)	O5-P2-O6	110.3(1)
O1-Co1-O1W	93.42(7)	O4-P2-C2	110.9(1)
O2[b]-Co1-O1W[d]	90.02(7)	O5-P2-C2	105.5(2)
O2[c]-Co1-O1W[d]	89.98(8)	O6-P2-C2	102.8(1)
O1[d]-Co1-O1W[d]	93.42(7)	P1-O1-Co1	124.7(1)
O1-Co1-O1W[d]	86.58(7)	P1-O2-Co1[a]	134.0(1)
O1W-Co1-O1W[d]	180	C1-N1-C2	112.2(2)
		N1-C2-P2	112.3(2)
		N1-C1-P1	114.4(2)

Symmetry transformations used to generate equivalent atoms: a: x+1,y,z;
b: -x-1,-y+2,-z+1; c: x-1,y,z; d: -x-2,-y+2,-z+1

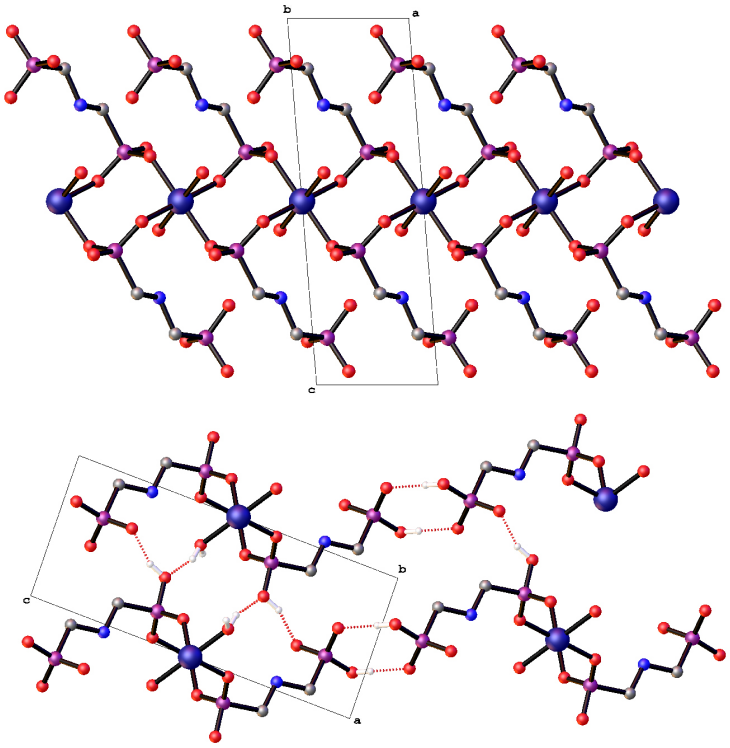

Figure 6. Compound 2 viewed down the *b*-axis (top) showing the 1-D chains. Looking down the *a*-axis (bottom) shows the supramolecular hydrogen bonded structure formed by the chains.

$Co(HO_3PCH_2NH(CH_3)CH_2PO_3H)_2$ (3)

Compound 3 has connectivity nearly isostructural to a related manganese compound. A thermal ellipsoid plot of the asymmetric unit of compound 3 can be seen in Figure 7. Comparing the two structures one can see the coordination and connectivity in the sheets are identical; however, the manganese system contains solvated water molecules while compound 3 is anhydrous. Compound 3 crystallizes in the space group $P2_1/c$ (no. 14) with the cell parameters given in Table 1. Bond lengths and angles are given in Table 4. The structure is 2-D sheets extending to a 3-D supramolecular hydrogen-bonded structure.

The Co(1) is bridged to four symmetry related cobalt ions through O-P-O bridges. This connectivity results in 2-D sheets of edge-shared 16-membered rings as shown in Figure 8. The ligand loses one proton per phosphonic acid group, whereas the amine remains fully protonated. Coordination occurs to the cobalt through only three of its six available oxygen atoms. The protonated amine forms hydrogen bonds with phosphonate oxygens within a given layer, {N(1)-H(1N1)···O(4) 2.886(3) Å, 146(3)°} and {N(1)-H(1N1)···O(1) 2.855(3) Å, 127(3)°}. Also, internally H(4A) hydrogen bonds to O(6), {P(1)-(O3)-H(4A)···O(6), 2.635(3) Å, 163(3)°}. The layers are held together by a network of free O-P-O-H interconnected hydrogen bonded dimers, {P(2)-(O5)-H(5A)···O(6), 2.566(3) Å, 172(2)°} as shown in Figure 9.

The layers of this compound lie in the *bc*-plane. When viewed down the *c*-axis (Figure 9) one can see the zig-zag of hydrogen bonds that hold the layers together;

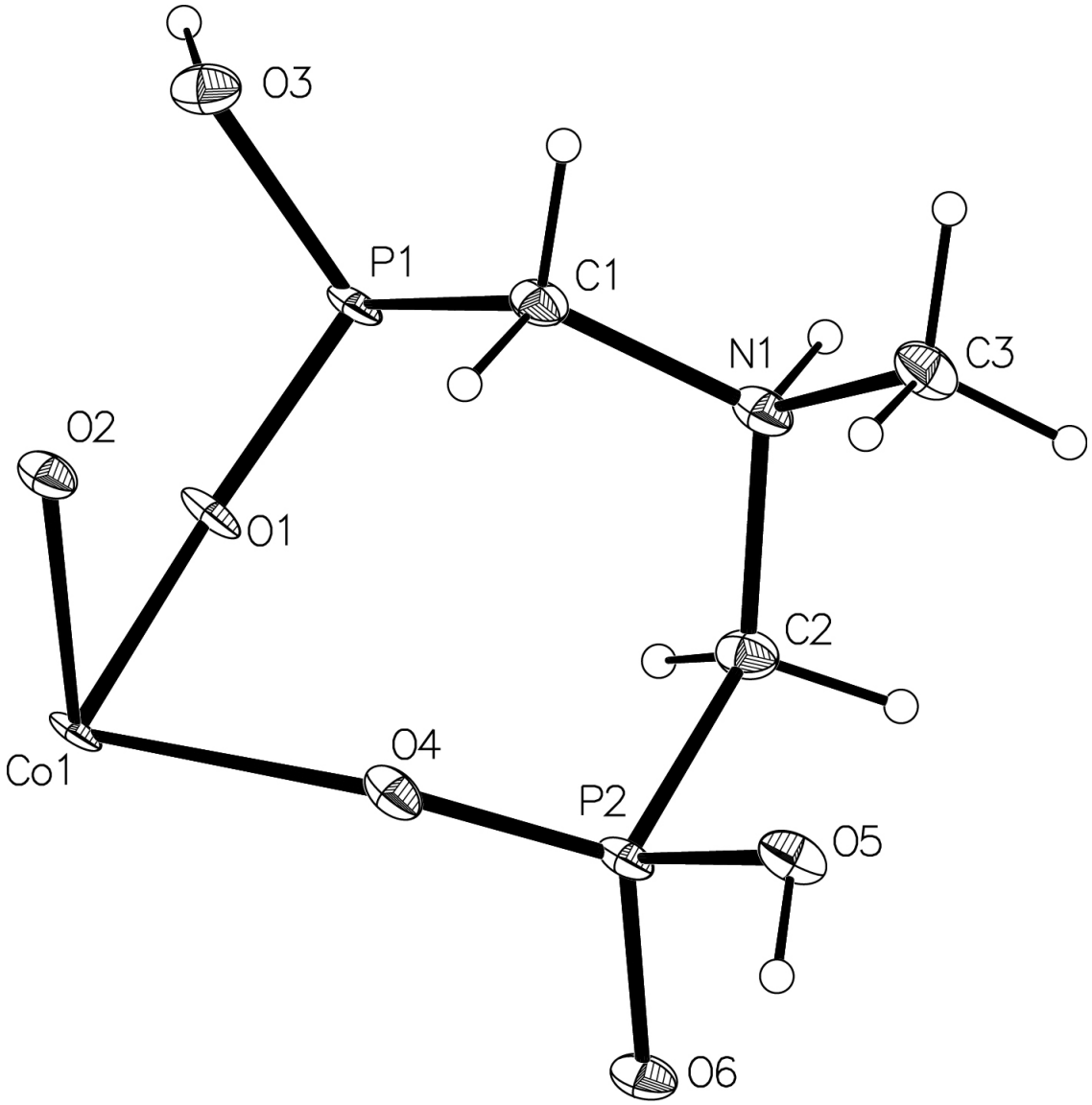

Figure 7. Thermal ellipsoid plot of compound 3. The thermal ellipsoids are at 50% probability.

Table 4. Bond lengths [Å] and angles [°] for compound 3.

Co1-O1[a]	2.056(2)	P2-O4	1.502(2)
Co1-O1	2.056(2)	P2-O6	1.521(2)
Co1-O4[a]	2.132(2)	P2-O5	1.568(2)
Co1-O4	2.132(2)	P2-C2	1.815(3)
Co1-O2	2.141(2)	N1-C3	1.503(4)
Co1-O2[a]	2.141(2)	N1-C1	1.505(4)
P1-O2[b]	1.503(2)	N1-C2	1.509(4)
P1-O1	1.506(2)		
P1-O3	1.577(2)		
P1-C1	1.838(3)		
O1[a]-Co1-O1	180	O2[b]-P1-O1	114.2(1)
O1[a]-Co1-O4[a]	92.71(8)	O2[b]-P1-O3	112.1(1)
O1-Co1-O4[a]	87.29(8)	O1-P1-O3	110.2(2)
O1[a]-Co1-O4	87.29(8)	O2[b]-P1-C1	109.6(2)
O1-Co1-O4	92.71(8)	O1-P1-C1	108.3(2)
O4[a]-Co1-O4	180	O3-P1-C1	101.7(2)
O1[a]-Co1-O2	87.43(8)	O4-P2-O6	115.9(1)
O1-Co1-O2	92.57(8)	O4-P2-O5	111.1(1)
O4[a]-Co1-O2	96.33(8)	O6-P2-O5	111.0(1)
O4-Co1-O2	83.67(8)	O4-P2-C2	111.9(2)
O1[a]-Co1-O2[a]	92.57(8)	O6-P2-C2	102.6(1)
O1-Co1-O2[a]	87.43(8)	O5-P2-C2	103.5(2)
O4[a]-Co1-O2[a]	83.67(8)	P1-O1-Co1	140.2(1)
O4-Co1-O2[a]	96.33(8)	P2-O4-Co1	137.5(1)
O2-Co1-O2[a]	180	P1[c]-O2-Co1	138.4(1)
		C1-N1-C2	114.2(2)
		N1-C1-P1	111.7(2)
		N1-C2-P2	119.6(2)

Symmetry transformations used to generate equivalent atoms:
a: -x+1,-y,-z; b: x,-y+1/2,z-1/2; c: x,-y+1/2,z+1/2

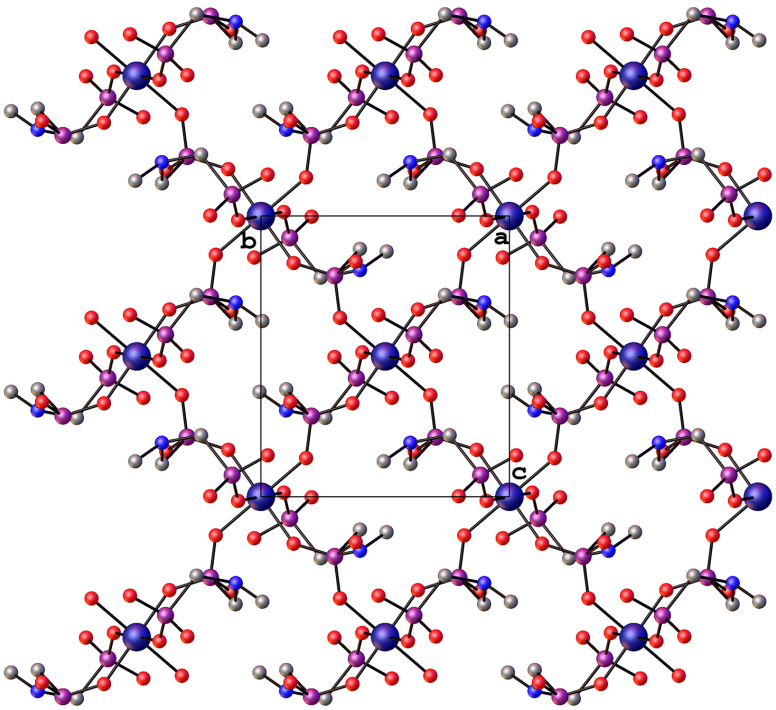

Figure 8. Compound 3 viewed down the *a*-axis. Notice the edge shared 16-membered rings made of four cobalt atoms and four phosphorus atoms. Contrast to compound 1 (Figure 3) and note how the ligands do not bridge the rings in 3 as they do in 1.

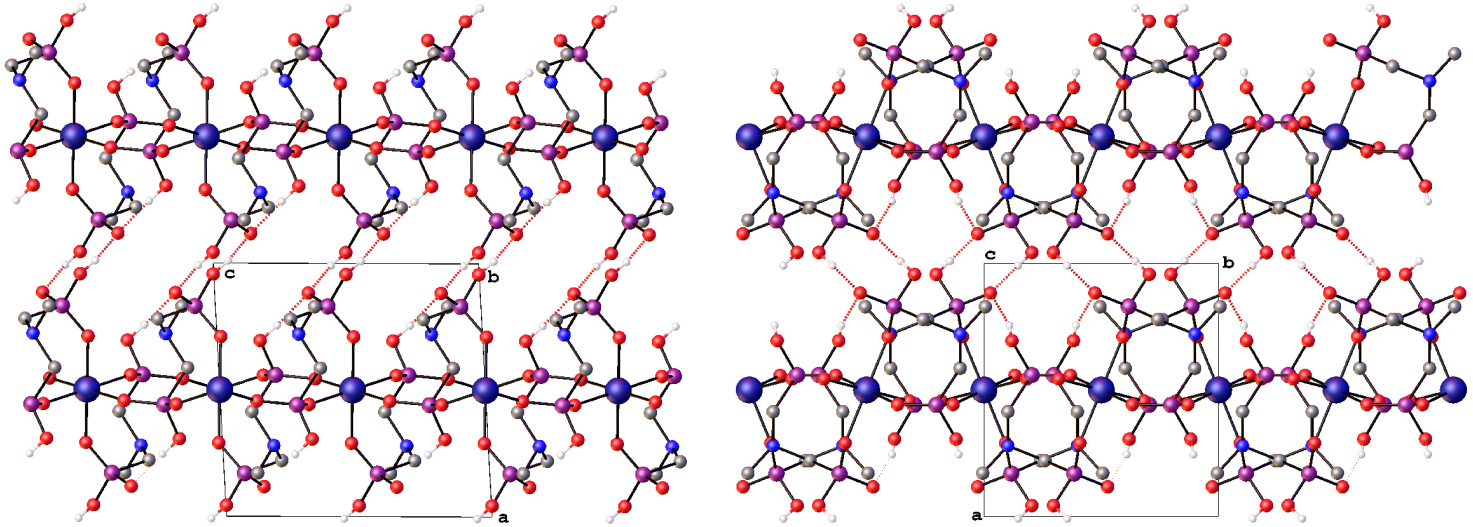

Figure 9. The interlayer hydrogen bonding in compound 3. Viewed down the *b*-axis (left) and the *c*-axis (right). Notice in the right the hydrophilic pockets that surround the hydrogen bonded dimers, unlike those in compound 1 (Figure 4) of hydrophobic nature.

however, unlike the similar compound 1, the hydrogen bonded channels are almost entirely hydrophilic in nature. The arrangement of the layers and the channels formed by the hydrogen bonds may allow for intercalation of amines between the layers. Although the coordination sphere of the cobalt is filled, it may be possible for the amine to replace one or more of the coordinated oxygen atoms, which would result in a major structural change rather than the anticipated intercalation or exfoliation.

$Zn_3(O_3PCH_2NH_2CH_2PO_3)_2$ (4)

Compound 4 is isostructural to the cobalt compound previously reported by Hix.[13] See Appendix B.

$CuClPO_3CH_2NH_2CH_3$ (5)

Compound 5 crystallizes in the space group *C*2/*m* with the cell parameters given in Table 1, the asymmetric unit can be seen in Figure 10. Bond lengths and angles are given in Table 5. The structure is 2-D sheets.

The X-ray crystal structure of compound 5 contains one crystallographically distinct copper ion in a distorted square pyramidal environment with Cu-O bond lengths in the range of 1.928(2)-1.938(2) Å and Cu-Cl bonds in the range of 2.331(2)-2.789(2) Å. The subtle distortion on the copper center is likely due to a Jahn-Teller effect which is common in Cu^{2+} complexes. The phosphorus atom in the ligand is tetrahedrally coordinated with P-O bonds ranging from 1.507(2)-1.524(2) Å. The metal is bonded to all three phosphonate oxygen atoms and two chlorine atoms forming a $CuCl_2O_3$ square

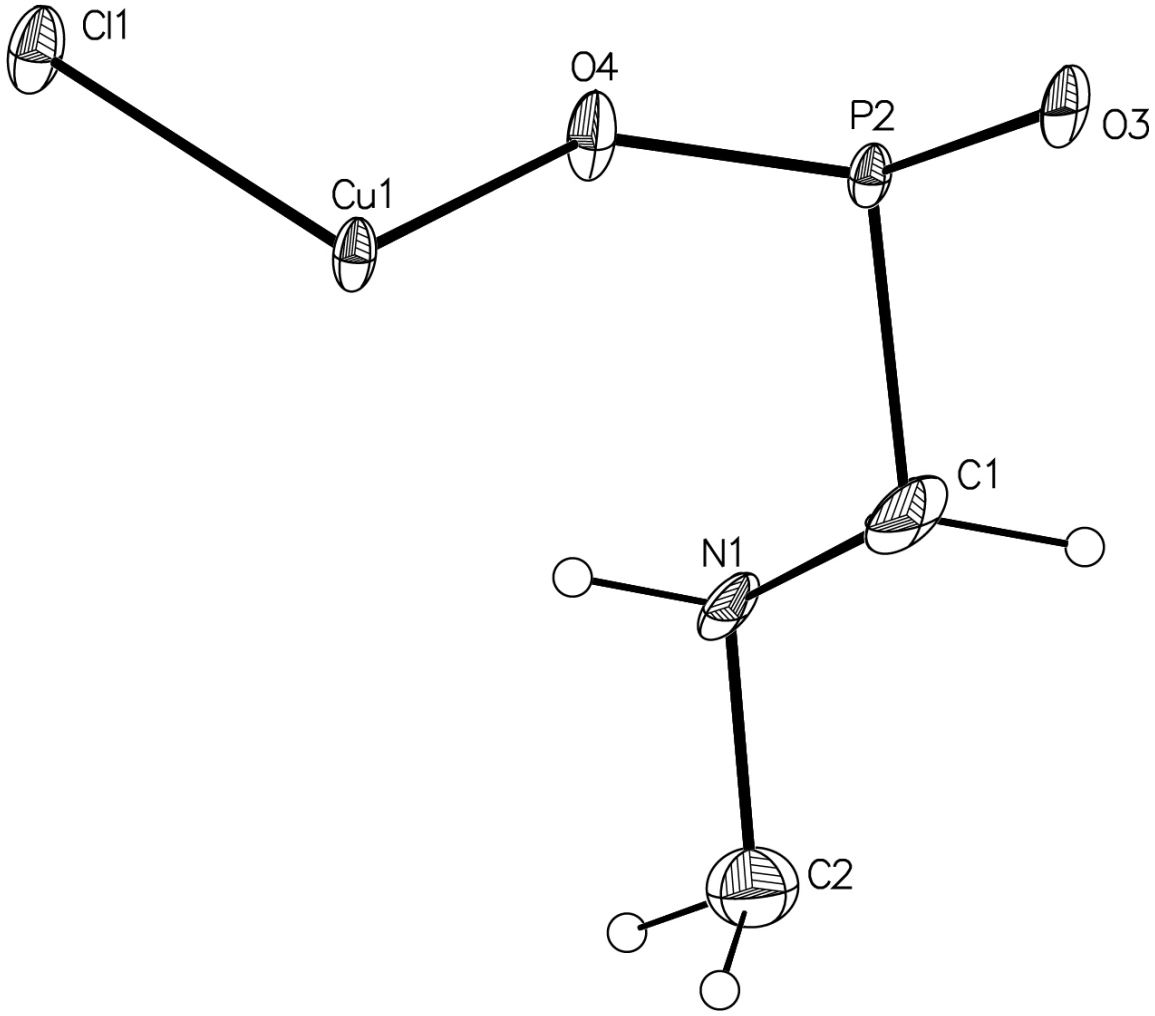

Figure 10. Thermal ellipsoid plot of compound 5. The thermal ellipsoids are at 50% probability.

Table 5. Bond lengths [Å] and angles [°] for compound 5.

Cu1-O2[a]	1.928(2)	P1-O1	1.507(2)
Cu1-O2	1.928(2)	P1-O2	1.524(2)
Cu1-O1	1.938(2)	P1-O2[a]	1.524(2)
Cu1-Cl2	2.331(2)	P1-C1	1.812(3)
Cu1-Cl2[b]	2.789(2)	N1-C1	1.484(3)
		N1-C2	1.493(3)
O2-Cu1-O1	93.72(3)	O1-P1-O2	114.4(2)
O2-Cu1-O2[a]	167.7(2)	O1-P1-O2[a]	114.4(2)
O2-Cu1-Cl2	86.2(2)	O1-P1-C1	107.0(2)
O2-Cu1-Cl2[b]	95.01(2)	O2-P1-O2[a]	106.6(2)
O1-Cu1-O2[a]	93.72(3)	O2-P1-C1	107.0(2)
O1-Cu1-Cl2	179.6(2)	O2[a]-P1-C1	107.0(2)
O1-Cu1-Cl2[b]	87.4(2)	P1-O1-Cu1	138.3(2)
O2[a]-Cu1-Cl2	86.2(2)	P1-O2-Cu1[c]	139.0(2)
O2[a]-Cu1-Cl2[b]	95.01(2)	N1-C1-P1	112.3(2)
Cl2-Cu1-Cl2[b]	93.01(2)	C1-N1-C2	113.9(2)

Symmetry transformations used to generate equivalent atoms: a: x, -y, z; b: -x, -y, -z; c: -x+1/2,-y+1/2,-z+2

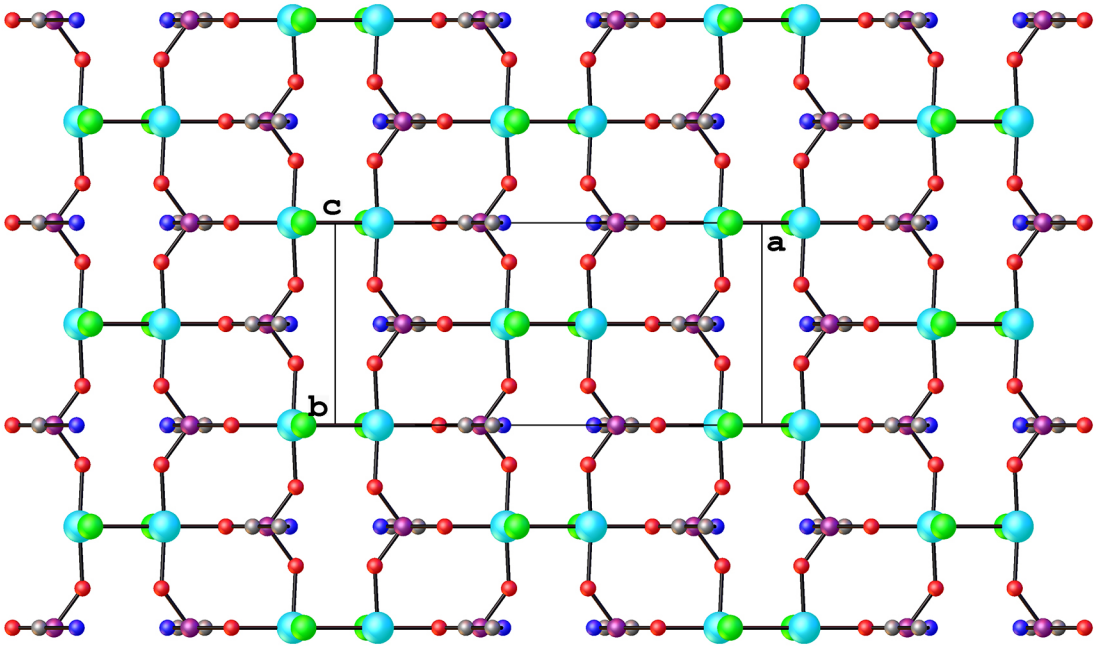

Figure 11. Compound 5 viewed down the *c*-axis. This clearly shows the Cu-O-P-O ladders running along the *b*-axis which are bridged by chlorine atoms along the *a*-axis.

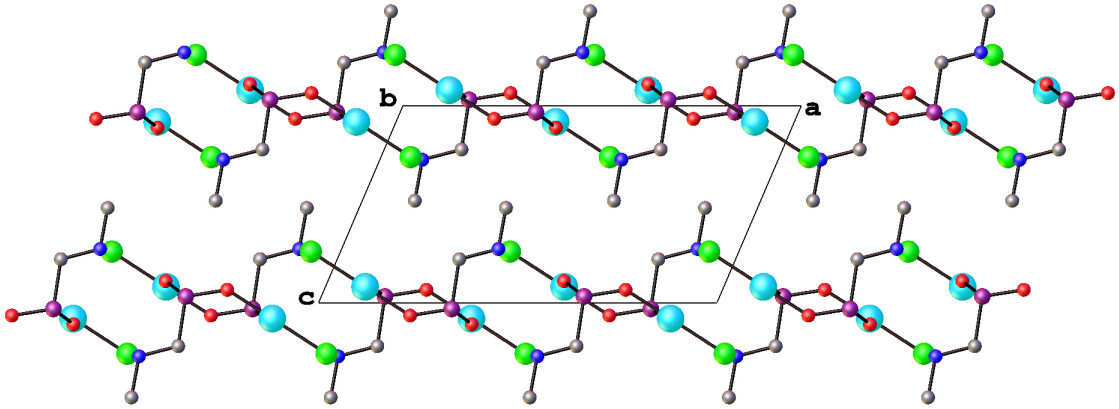

Figure 12. Compound 5 viewed down the *b*-axis. This shows how the methyl groups on the amine interdigitate and only allow weak intereactions to hold the layers together.

pyramid. The backbone of the structure is made up of linear ladders formed by Cu-O-P-O 8-membered rings which are edge shared (Figure 11). The fourth coordination site of the copper, to form the basal plane, is filled by a chlorine atom. These ladders are subsequently bridged together by the bound chlorine atoms interacting with the apex of the neighboring copper atom square pyramid. It bridges through a long Cu-Cl bond of 2.789(2) Å compared to the Cu-Cl bond in the basal plane which is 2.331(2) Å. The ligand loses both protons from the phosphonic acid, while the amine remains fully protonated. The protonated amine forms hydrogen bonds with phosphonate oxygens within the layer {N(1)-H(1A)···O(2) 2.896(2) Å, 139°}. The layer is decorated with pendant CH_3 groups from the secondary amine which interdigiate with protruding chlorine atoms from the layer as shown in Figure 12. The layers appear to be held together only by weak hydrophobic and van der Waals forces.

Infrared Spectroscopy

All five title compounds were studied by IR spectroscopy. The spectra are shown in Figure 13. All five compounds show similarly well characterized bands in the infrared. Various features between 3000 and 2900 cm^{-1} can be assigned to the aliphatic C-H stretching vibrations. The corresponding CH_2 deformation bands appear from 1490 to 1400 cm^{-1}. Both compounds 3 and 5 show characteristic CH_3 bends at 1450 cm^{-1}. The region between 2860 and 2300 cm^{-1} is complicated as it contains both medium bands associated with the PO-H stretching vibrations as well as characteristic NH_2^+ N-H stretching vibrations. In compound 4 the NH_2^+ stretching vibrations are more defined

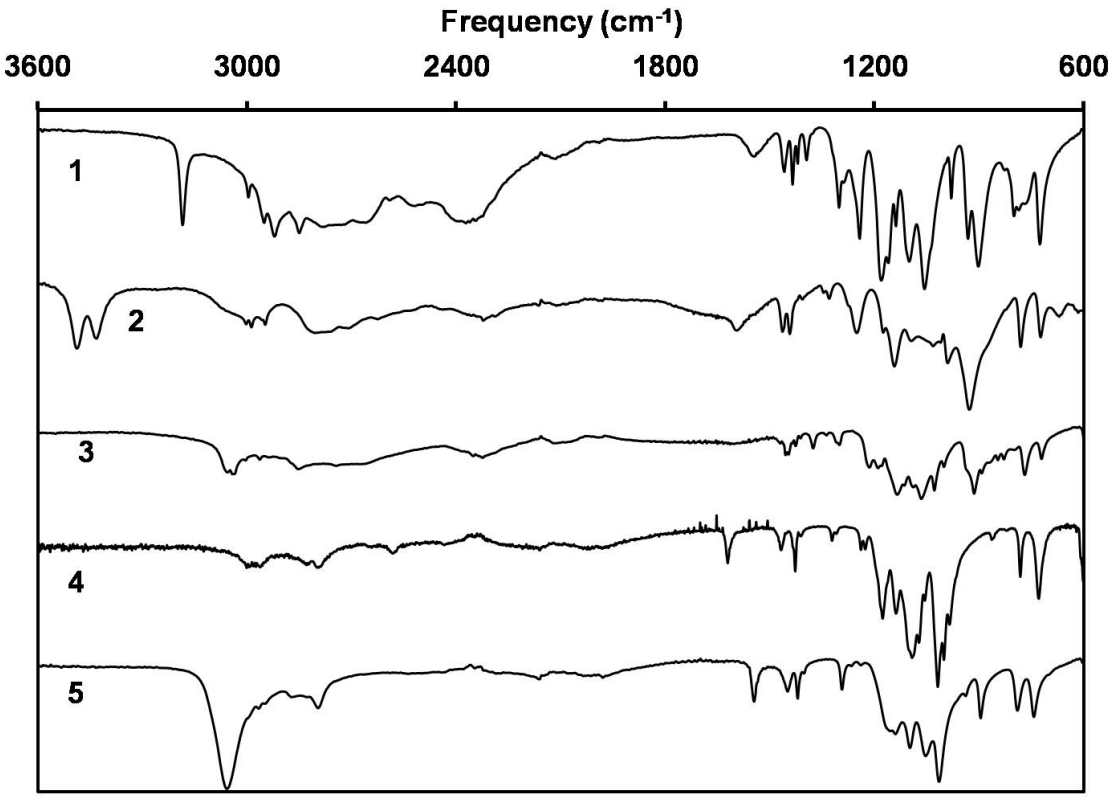

Figure 13. IR spectra of compounds 1 through 5.

and show sharp features at 2827, 2787, and 2577 cm^{-1}. The broad bands at 2112 (1), 2160 (2), 2106 (3), 2100 (4), and 2160 (5) cm^{-1} belong to the NH_2^+ (NH^+ in 3) N-H stretches as well. This along with the NH_2 deformation bands at 1541 (1), 1589 (2), 1620 (4), and 1544 (5) cm^{-1} agrees with the crystallographic assignment of the protonation of the secondary amine. This deformation is not present in compound 3 as it is a tertiary ammonium. The rest of the sharp bands between 1400 and 725 cm^{-1} are overlapping stretching vibrations associated with N-C (1300 – 1000 cm^{-1}) and the various stretches associated with the CPO_3 tetrahedra (1200–725 cm^{-1}).

In compounds 1, 2, and 3, there are strong features between 3600 and 3000 cm^{-1} which are indicative of strong chelate hydrogen bonds. These arise from POH···O hydrogen bond O-H stretches (1, 2, and 3) as well as metal bound water (MOH···O) hydrogen bond O-H stretches (2). All of the tentative assignments agree with previous results reported for iminophosphonate and alkylphosphonate containing complexes.[81, 87, 88]

Thermal Analyses

Thermogravimetric analyses (TGA) of the cobalt materials are very complicated as the starting Co:P ratios do not match the ratios in the typical stable phosphate materials which are expected as the end decomposition products. Also, the decompositions appear to not be complete even at 1000 °C, evidenced by a gradual loss continuing at this high temperature. All TGA can be found in Appendix B.

The TGA of compound 1 shows a series of overlapping weight losses starting at 300 °C and continuing to 800 °C. Over this range there are three processes occurring: the

condensation of the hydrogen phosphonate groups, the pyrolysis of the organic group, and the oxidation and loss of P_2O_5. Due to the complicated decomposition of this compound and a likely mixture of final products, it is difficult to calculate the accuracy of the losses. X-ray analysis of the pyrolysis product shows that it contains $Co(PO_3)_2$; however, the observed loss of 47.19% is not enough for complete conversion to $Co(PO_3)_2$.

TGA of compound 2 shows a similar loss compared to that of the previously reported compound 6; however, close inspection shows that the total weight loss is greater and the initial loss of the bound waters happens above 200 °C compared to the other compound which occurs below 200 °C. The PXRD of the final product confirms the presence of $Co(PO_3)_2$ as the only crystalline phase. The final weight loss of 54% does not match the expected loss of 56.8% confirming that the decomposition is not complete at 1000 °C.

TGA of compound 3 shows a series of overlapping weight losses starting at 300 °C and continuing to 800 °C Over this range there are three processes occurring: the condensation of the hydrogen phosphonate groups, the pyrolysis of the organic group, and the oxidation and loss of P_2O_5. The final weight loss of 59.5% is greater than that would be expected for an end product of $Co(PO_3)_2$ (56.2%). The observed loss can only be explained if the end product is not exclusively $Co(PO_3)_2$. We hypothesize a mixture of $Co(PO_3)_2$ and CoO.

TGA of compound 4 shows a gradual loss starting at 200 °C and continuing to the decomposition of the organic portion. The final product is most likely an equal mix-

ture of $Zn(PO_3)_2$ and $Zn_2P_2O_7$ as evidenced by a total weight loss of 13.01% which is in close agreement to the calculated loss of 12.02%.

TGA of compound 5 shows a weight loss beginning at about 230 °C followed by a brief oxidation at 500 °C before final decomposition to the end product $Cu_2P_2O_7$ as evidenced by a total weight loss of 32.08% which is in close agreement to the calculated loss of 32.21%.

Magnetic Measurements

Magnetic susceptibility measurements of complexes 1, 2 and 5 were performed as outlined in Chapter II.

$Co(HO_3PCH_2NH_2CH_2PO_3H)_2$ (1)

The value of χT at 300 K is 3.2 emu·K·mol^{-1} for compound 1, which is higher than the expected value for an isolated Co^{2+} ion with S = 3/2 and g = 2.0 (χCoT = 1.875 emu·K·mol^{-1}) which is not unexpected given the anisotropic nature of these ions due to spin-orbit coupling which leads to g values greater than 2. (Figure 14).[89] The χT value continuously decreases from room temperature and reaches a minimum of 1.2 emu·K·mol^{-1} at 12 K then increases to 15.5 emu·mol^{-1} K at 3.5 K and finally decreases again. The temperature dependence of $1/\chi$ between 300 and 20 K approximates Curie-Weiss behavior with C = 3.55 emu·K·mol^{-1} and θ = -33 K. The negative sign of the Curie-Weiss constant indicates antiferromagnetic interactions between Co^{2+} centers as well as spin-orbit coupling.

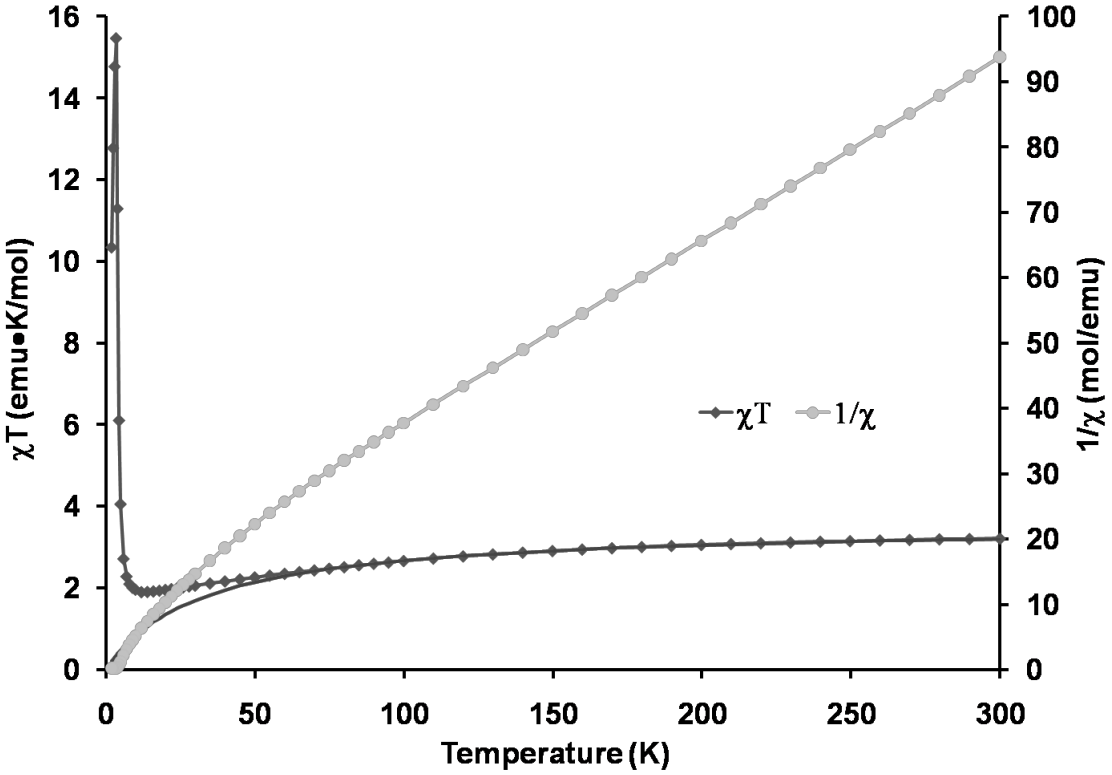

Figure 14. The temperature dependence of χT (♦) and of the inverse susceptibility $1/\chi$ (●) for compound 1. The solid line corresponds to the best fit to the Curie-Weiss law.

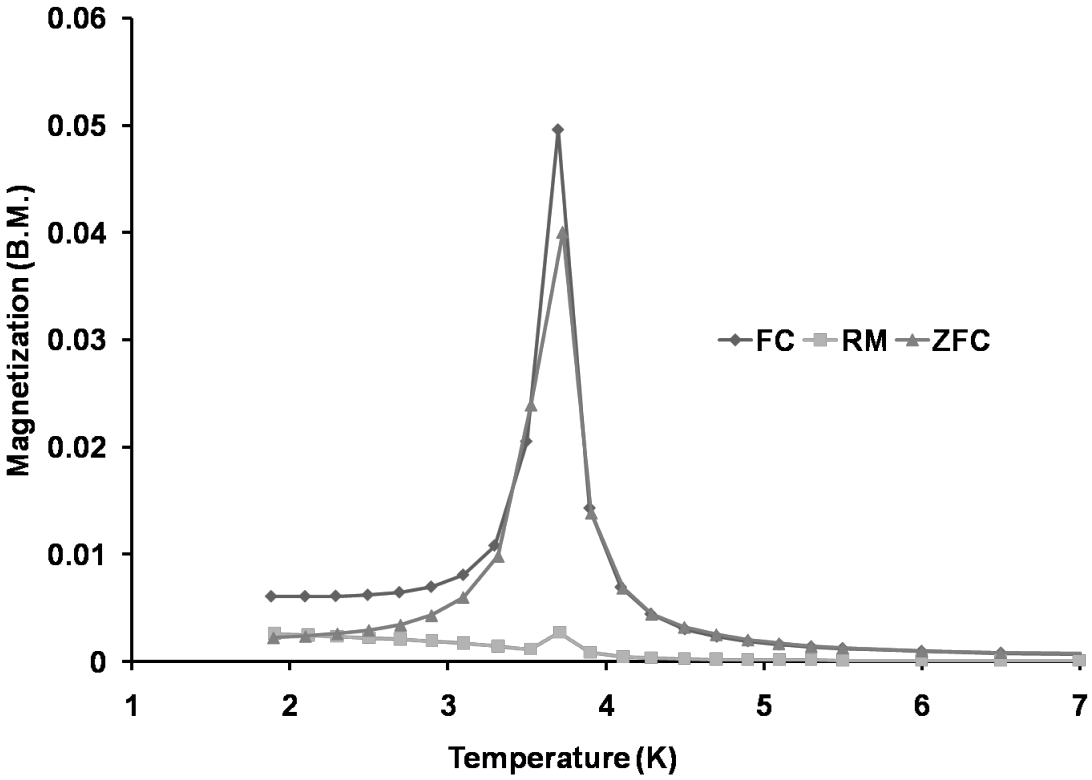

Figure 15. FC, ZFC and remnant magnetization for compound 1. The applied DC magnetic field is 10 Oe.

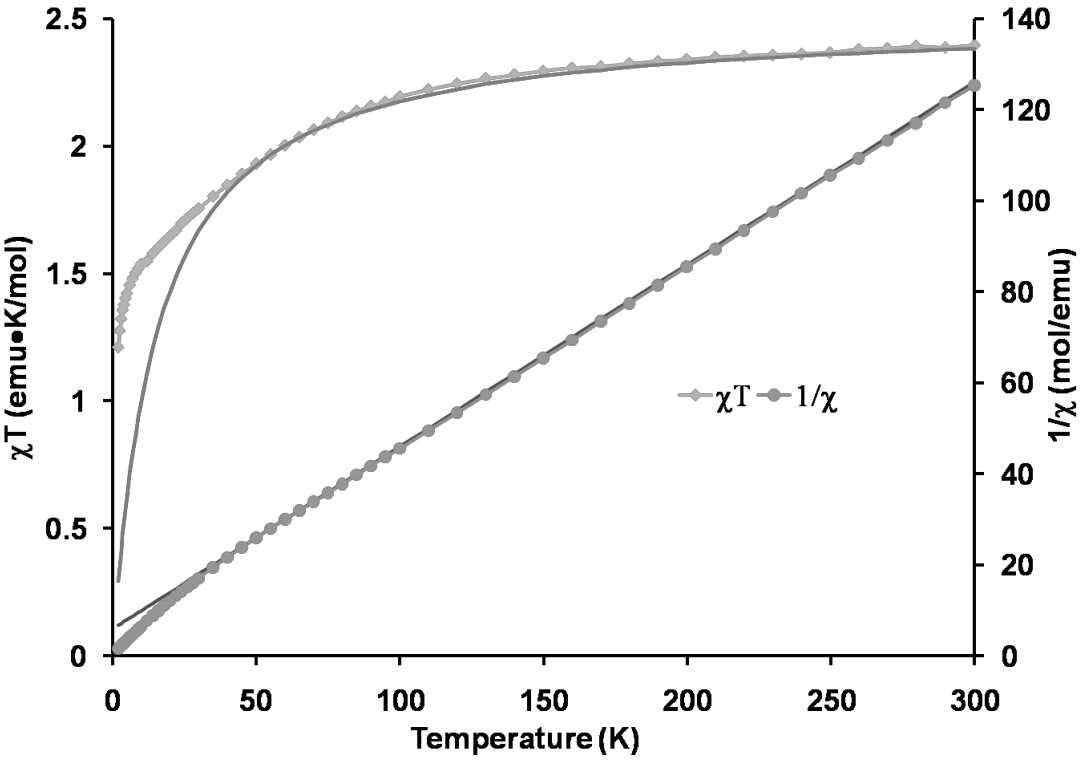

Figure 16. The temperature dependence of χT (♦) and of the inverse susceptibility 1/χ (●) for compound 2. The solid line corresponds to the best fit to the Curie-Weiss law.

A long-range weak ferromagnetic ordering was observed at 3.7 K as deduced from the divergence between the zero-field cooled (ZFC) and field cooled (FC) measurements (Figure 15). The ordering was verified by AC magnetic measurements and a narrow hysteresis loop was observed at 1.8 K. The full magnetic data can be seen in Appendix B.

$Co(H_2O)_2(HO_3PCH_2NH_2CH_2PO_3H)_2$ (2)

The value of χT at 300 K is 2.4 emu·K·mol^{-1} for compound 2, ($\chi_{Co}T$ = 1.875 emu·K·mol^{-1}, S = 3/2, g = 2.0) (Figure 16) which decreases upon lowering the temperature to reach a minimum of 1.2 emu·K·mol^{-1} at 2 K. The temperature dependence of $1/\chi$ between 300 and 30 K approximates Curie-Weiss behavior with C = 2.5 emu·K·mol^{-1} and θ = -15 K. The fact that the Weiss constant is smaller than that of 1 may indicate the absence of antiferromagnetic interactions between Co^{2+} centers and that the Weiss constant is due only to spin-orbital coupling. Field-dependent magnetization at 1.8 K is fitted to a Brillouin function for spin S = 1/2 and g = 3.6, which is typical for an isolated Co^{2+} ion. No long-range magnetic phase transition was observed. The data are included in Appendix B.

$CuClPO_3CH_2NH_2CH_3$ (5)

The χT and χ vs. T plots for one Cu^{2+} ion for compound 5, are shown in Figure 17. The value of χ_m is 0.0012 emu·mol^{-1} at room temperature and increases smoothly to a maximum of 0.0022 emu·mol^{-1} at 65 K and finally decreases to 0.0012 emu·mol^{-1} at 2

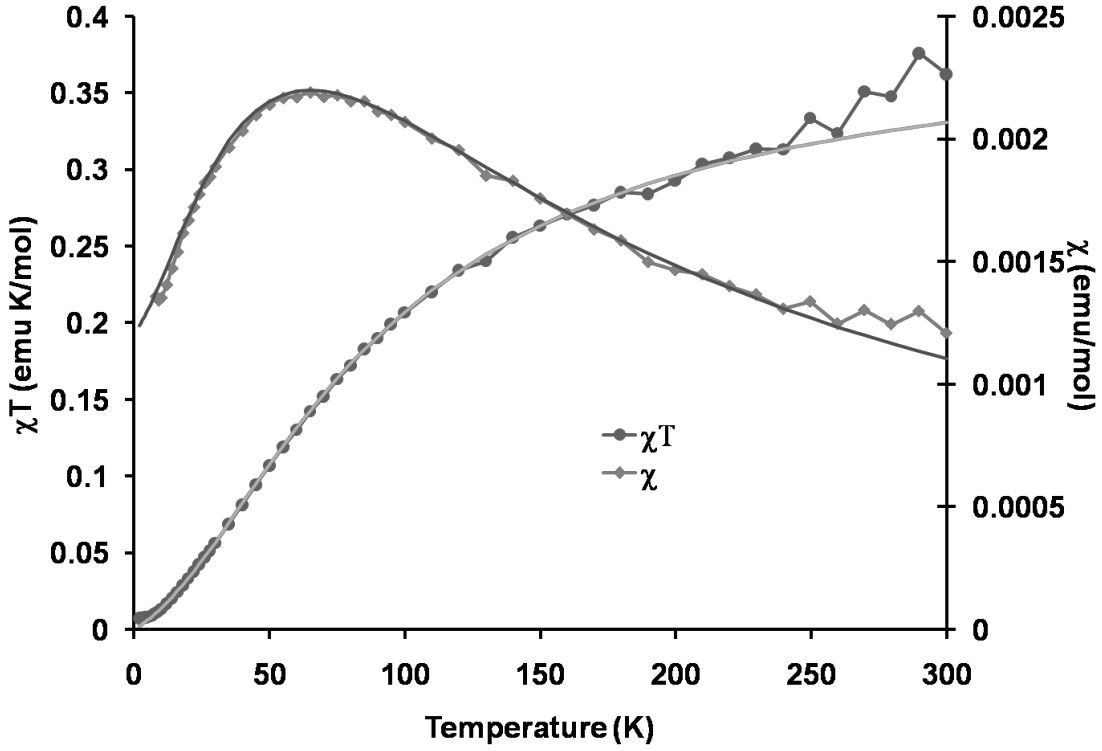

Figure 17. Temperature dependence of χT (•) and χ (♦) for compound 5. The solid and dashed lines correspond to the best fit to an $S = 1/2$ chain model.

K. The value of χT at 300 K is 0.36 emu·K·mol^{-1}, which is lower than the expected value for a spin-only case (χCuT = 0.375 emu·K·mol^{-1}, S = 1/2, g = 2.0). The χT value continuously decreases from room temperature and reaches a minimum of 0.0074 emu·K·mol^{-1} at 2 K. The decrease of χT upon cooling indicates the presence of antiferromagnetic interactions between Cu^{2+} centers. Well-isolated Cu^{2+} chains are the dominant magnetic units in this material. The magnetic data was fit to a simple 1-D chain model[90] (the Hamiltonian is written as $H = -J_iJ_{i-1}$) which produced a good fit to the experimental data over the whole temperature range with the parameters g = 2.06, J = -36 cm^{-1}.

Discussion

The application of combinatorial synthesis allows for investigation of new solvent systems with minimal effort or waste of materials. By running multiple conditions for the same reaction system, the chances of failed reactions can be reduced and the systems can be investigated more thoroughly. The system of IBMPA with various chloride salts of divalent metals has been explored systematically. This ligand was chosen as the system had been thoroughly investigated in water in the past. Although the use of ionic liquids as a new solvent has increased drastically in the past few years, there has been almost no work involving its use in the synthesis of metal phosphonate materials. This work was initiated to explore the use of a mixed solvent system containing water and a hydrophobic ionic liquid [BdMIM][BF_4]. To the best of our knowledge, this is the first time the synthesis of metal phosphonates has been investigated using a mixed system of

this kind, and only the second time ionic liquids have been used at all (ignoring eutectic mixtures).[91]

Cobalt turned out to be interesting as there were already several compounds reported in the literature, the 2-D $Co[NH_2(CH_2PO_3H)_2]_2(H_2O)_2$,[81] and $Co[NH_2(CH_2PO_3H)(CH_2PO_3)](H_2O)_2{\cdot}H_2O$[71] and the 3-D $Co_3[NH(CH_2PO_3)_2]_2$,[13] and yet two additional compounds were obtained. While the same reaction system has been employed with Cu^{2+}, Mn^{2+}, and Zn^{2+}, cobalt produced the best results. Manganese resulted in poorly crystalline solids that have not yet been fully characterized. Cu^{2+} has produced a mixture of compounds which we are still investigating as they too were poorly crystalline. It is interesting that zinc produced compound 4 from every single reaction irrespective of conditions. The amphoteric nature of zinc in aqueous systems may be a factor in this, as it has already been shown that pH plays an extremely important role in phosphonate synthesis. The reactions done with cobalt result in only monodeprotonation of the ligand, retaining its protonated amine as well; however, with zinc only the proton remains on the amine.

The combination of a hydrophobic ionic liquid and water as a solvent in hydroionothermal synthesis proved interesting. At moderate concentrations of metal in water, the system is biphasic; while at lower concentrations the system appears to be homogenous. After reactions, the biphasic systems contain the solid product under the ionic liquid with apparently no metal dissolved in it, with the aqueous solution of unreacted metal ions above.

Compound 5 was the only compound able to be obtained in a pure form when only the ionic liquid was used as a solvent. This compound is the product of an unexpected cleavage of the C-N bond in the ligand converting N-methyliminobis-(methylphosphonic acid) to N-methyliminomethylphosphonic acid. This type of reaction has been reported in the literature: $[Ba_3(O_3PCH_2NH_2CH_2PO_3)_2(H_2O)_4]\cdot 3H_2O$[73] was the result of *in situ* decomposition of $(H_2O_3PCH_2)_2NCH_2C_6H_4COOH$ and $Cu_3[(O_3PCH_2)_2NH_2]_2$[82] was the result of *in situ* decomposition of nitrilotris(methylphosphonic acid).

Compound 3 is the result of an effort to compare the IBMPA with its simplest analogue MIBMP. Other ligands are being investigated as are other ionic liquids to be used in similar combinatorial studies. A better understanding of the effect of the biphasic system utilized in the synthesis of hybrid materials still needs to be obtained.

Conclusion

While several of the reaction systems investigated herein resulted in compounds which had previously been reported, the isolation of five new compounds through the addition of an ionic liquid to an aqueous reaction system is astounding. The use of ionic liquids as a solvent, or co-solvent in the synthesis of hybrid materials allows for a limitless ability to tune solvent systems to ones needs. In this chapter we have merely reported a simple example of this in hopes that it may bring to light a new powerful tool for use in the synthesis of phosphonate based coordination polymers.

CHAPTER IV

SYSTEMATIC INVESTIGATION OF ZINC ALKYLBISPHOSPHONATES

Introduction

Recent review papers have highlighted the similarities and contrasts between carboxylic and phosphonic acids in their use as organic linkers for MOFs. What is most evident is the difference in the number of compounds falling into these two similar classes, with carboxylate MOFs vastly outnumbering phosphonates.[9, 66] Structural knowledge has been a cornerstone to MOF synthesis and the development of the field; therefore, crystalline materials have been preferred. The difference between the carboxylates and the phosphonates has been not only the ability to form crystalline materials, but also to design bonding models; both of which are a virtual guarantee for carboxylates, and subsequently both being difficult for phosphonates. For the latter class, what is interesting is the number of times authors have made claims for rational design, and furthermore structural limitations based off ligand shape and size.[92, 93] No class has been more subject to these generalizations than the alkylbisphosphonates. It has, in the past, been suggested that the chain length determines the structural type.

Herein a series of compounds is presented, which are all made with zinc acetate dihydrate as a starting material and with just four ligands of similar length, $H_2O_3PC_nH_{2n}PO_3H_2$ (n = 3 – 6) (H_4Ln). It is shown that neither the metal nor the chain length has much effect on the structure type, but rather the conditions have the greatest effect. The use of zinc in metal phosphonates often proves interesting as zinc easily

adopts a number of coordination modes, namely tetrahedral or octahedral, although five coordinate is not uncommon. We have discovered that zinc alkylbisphosphonates can be divided into several different families, each of which is based upon a different isoreticular structural archetype. The families will be referred to as zinc alkylphosphonate gate (ZAG), zinc alkylphosphonate cation (ZAC), zinc alkylphosphonate tunnel (ZAT), zinc alkylphosphonate sheet (ZAS), and zinc alkylphosphonate layer (ZAL) compounds. With the exception of one of the presented families (ZAC), there does appear to be a trend of odd versus even chain length adopting a given structural type.

Experimental

Synthesis of Zinc Alkyl Gate Compounds (ZAG-4,6)(Zn(**H_2Ln**)·2H_2O)In a typical experiment Zn(Oac)$_2$·2H_2O (0.1 mmol in 2 mL ddi H_2O), in a 20 mL glass scintillation vial, was adjusted to a pH of ~1.8 using glacial acetic acid. In a separate vial the alkylbisphosphonic acid (H_4L4,6) (0.2 mmol) was dissolved in 2 mL of ddi H_2O and was subsequently layered on top of the zinc acetate solution and set undisturbed for two days to allow for crystal growth. The resulting large colorless crystals were filtered and washed with ethanol and dried at room temperature.

Alternatively, the alkylbisphosphonic acid (1.12 mmol in 5 mL ddi H_2O) was adjusted to a pH of 2.0 using 0.01 M NaOH. To this was added ZnSO4·7H_2O (2.04 mmol in 5 mL ddi H_2O). The resulting mixture was shaken and left to stand for 48 hours undis-

turbed. The resulting large colorless crystals were filtered and washed with ethanol and dried at room temperature.

Synthesis of Zinc Alkyl Tunnel Compounds (ZAT-3,5)(Zn_3(**H_2Ln**)(**Ln**)$_2$(H_2O)$_4$

In a typical experiment $Zn(Oac)_2 \cdot 2H_2O$ (0.3 mmol in 3 mL ddi H_2O), in a 20 mL glass scintillation vial, was adjusted to a pH of 1.8 using glacial acetic acid. In a separate vial the alkylbisphosphonic acid (H_4L3,5) (0.2 mmol) was dissolved in 3 mL of ddi H_2O and was subsequently layered on top of the zinc acetate solution and set undisturbed for two days to allow for crystal growth. The resulting colorless needles were filtered and washed with water and dried at room temperature.

Synthesis of Zinc Alkyl Sheet Compounds (ZAS-3,5)(Zn(**H_2Ln**))

In a typical experiment: into a 25 mL PTFE lined steel pressure vessel were added $Zn(Oac)_2 \cdot 2H_2O$ (0.15 mmol) and the alkylbisphosphonic acid (H_4L3,5) (0.15 mmol). To this was added 0.5 mL ddi H_2O and 0.5 mL glacial acetic acid. The pressure vessel was sealed and heated for four days at 140 °C. The resulting colorless crystals were filtered and washed with ddi H_2O and dried at room temperature.

*Synthesis of Zinc Alkyl Cation Compounds (ZAC-4,5,6) (Zn_2(**H_2Ln**)(**Ln**)·$Zn(H_2O)_6$·H_2O·$HO_2C_2H_3$)*

In a typical experiment $Zn(Oac)_2 \cdot 2H_2O$ (1.2 mmol in 3 mL ddi H_2O), in a 20 mL glass scintillation vial, was adjusted to a pH of 1.8 using glacial acetic acid. In a separate

vial the alkylbisphosphonic acid (H_4L4,5,6) (0.5 mmol) was dissolved in 3 mL of ddi H_2O and was subsequently layered on top of the zinc acetate solution and set undisturbed for two weeks to allow for crystal growth. The reaction produced a mixture of products, long colorless needles of the type ZAT (in the L5 case) form as well as the ZAC smaller blade-like colorless crystals.

*Synthesis of Zinc Alkyl Layered Compounds (ZAL-5,6)(Zn_2(**L5**)) and (Zn_3(**H_2L6**)(**L6**))*

In a typical experiment: into a 25 mL PTFE lined steel pressure vessel were added $Zn(Oac)_2 \cdot 2H_2O$ (0.15 mmol) and the alkylbisphosphonic acid (H_4L5,6) (0.15 mmol). To this was added 0.5 mL ddi H_2O and 0.5 mL glacial acetic acid. The pressure vessel was sealed and heated for four days at 140 °C. The resulting colorless crystals were filtered and washed with ddi H_2O and dried at room temperature.

Single Crystal X-ray Diffraction

Single Crystal X-ray Diffraction for ZAT-5, ZAC-4, ZAC-5, ZAG-4, and ZAG-6 were collected at 110(2) K on a Bruker APEX II diffractometer as outlined in Chapter II. Data for the remaining compounds were collected at 100(2) K on Beamline 11.3.1 at the ALS, LBNL. The space groups were determined to be *Pmmn, C*2*/c, P*2$_1$*/n, P*2$_1$*/c, C*2*/c,* and $P\bar{1}$ for ZAT, ZAG, ZAS, ZAC, ZAL-5, and ZAL-6 respectively Crystal parameters and information pertaining to data collection and refinement for all structures are summarized in Table 6, Table 7, and Table 8. Important bonding distances and angels are listed in further tables in this chapter..

Table 6. Crystallographic data for ZAG-4, ZAG-6, ZAS-3, and ZAS-5.

Sample	**ZAG-4**	**ZAG-6**	**ZAS-3**	**ZAS-5**
Chemical formula	$ZnP_2O_8C_4H_{14}$	$ZnP_2O_8C_6H_{18}$	$ZnP_2O_6C_3H_8$	$ZnP_2O_6C_5H_{12}$
Formula mass	317.46	345.51	267.40	295.46
Crystal system	monoclinic	monoclinic	monoclinic	monoclinic
Space group	*C*2/*c*	*C*2/*c*	$P2_1/n$	$P2_1/n$
λ (Å)	0.71073	0.71073	0.77490	0.77490
a (Å)	18.485(3)	20.388(4)	8.595(7)	8.651(2)
b (Å)	8.2738(15)	8.2663(13)	5.056(4)	5.0283(12)
c (Å)	8.2600(15)	8.1857(13)	18.096(15)	22.598(5)
β (deg.)	114.461(2)	102.720(13)	93.344(9)	93.046(3)
Z	4	4	4	4
V (Å^3)	1149.9(4)	1345.7(4)	785.1(11)	981.6(4)
Temperature (K)	150(2)	120(2)	100(2)	100(2)
Density (g/cm^3)	2.433	1.705	2.262	1.999
Measured reflections	5775	7120	14326	13137
Unique reflections	1133	1395	2032	2853
Parameters	69	84	109	127
Restraints	0	1	0	0
R_{int}	0.0204	0.0691	0.0541	0.0534
θ range (deg.)	2.75 - 25.99	2.67 - 26.48	4.38 - 31.56	3.81 - 33.07
R_1, wR_2 all data	0.0190, 0.0468	0.0520, 0.0856	0.0327, 0.0794	0.0479, 0.0936
S (GooF) all data	1.120	1.037	1.084	1.049
Max/min res. Dens. (e/Å^3)	0.304/-0.284	0.322/-0.483	0.501/-0.710	0.779/-0.974

Table 7. Crystallographic data for ZAT-3, ZAT-5, ZAL-5, ZAL-6.

Sample	**ZAT-3**	**ZAT-5**	**ZAL-5**	**ZAL-6**
Chemical formula	$Zn_3P_4O_{16}C_6H_{22}$	$Zn_3P_4O_{16}C_{10}H_{30}$	$Zn_2P_2O_6C_5H_9$	$Zn_3P_4O_{12}C_{12}H_{26}$
Formula mass	670.23	726.33	357.80	682.38
Crystal system	orthorhombic	orthorhombic	monoclinic	triclinic
Space group	*Pmmn*	*Pmmn*	*C2/c*	$P\bar{1}$
λ (Å)	0.77490	0.71073	0.77490	0.77490
a (Å)	19.397(3)	24.408(4)	21.775(4)	8.658(11)
b (Å)	27.620(5)	27.827(5)	4.8267(8)	9.935(16)
c (Å)	5.1655(9)	5.1509(7)	9.5273(17)	12.95(3)
α (deg.)	90.00	90.00	90.00	100.56(13)
β (deg.)	90.00	90.00	95.233(2)	104.59(16)
γ (deg.)	90.00	90.00	90.00	90.81(12)
Z	4	4	4	2
V (Å^3)	2767.4(8)	3498.5(10)	997.2(3)	1058(3)
Temperature (K)	100(2)	110(2)	100(2)	100(2)
Density (g/cm^3)	1.609	1.379	2.383	2.142
Measured reflections	28084	13383	4590	5344
Unique reflections	3019	3009	1291	2825
Parameters	142	161	69	280
Restraints	0	0	0	0
R_{int}	0.0803	0.1288	0.0437	0.0532
θ range (deg.)	2.57 - 29.13	0.83 - 24.71	4.10 - 31.57	3.17 - 24.90
R_1, wR_2 all data	0.0492, 0.1236	0.0913, 0.1582	0.0350, 0.0917	0.1095, 0.2313
S (GooF) all data	1.048	1.022	1.090	1.034
Max/min res. Dens. (e/Å^3)	1.796/-0.907	0.611/-0.926	0.785/-1.072	3.088/-1.876

Table 8. Crystallographic data for ZAC-4, ZAC-5, and ZAC-6.

Sample	**ZAC-4**	**ZAC-5**	**ZAC-6**
Chemical formula	$Zn_5P_6O_{26}C_{12}H_{42}$	$Zn_5P_6O_{26}C_{17}H_{52}$	$Zn_5P_6O_{28}C_{20}H_{58}$
Formula mass	1115.23	1217.24	1259.33
Crystal system	monoclinic	triclinic	monoclinic
Space group	$P2_1/c$	$P1$	$P2_1/c$
λ (Å)	0.71073	1.5418	0.77490
a (Å)	10.5536(9)	10.349(2)	13.045(2)
b (Å)	17.3130(11)	17.038(4)	17.192(3)
c (Å)	10.3937(7)	23.070(4)	10.3905(18)
α (deg.)	90.00	90.0	90.00
β (deg.)	99.502	94.574(10)	96.914(3)
γ (deg.)	90.00	90.0	90.00
Z	2	2	2
V (Å^3)	1873.0(2)	4054.9(14)	2313.3(7)
Temperature (K)	110(2)	110(2)	100(2)
Density (g/cm^3)	1.977	1.830	1.808
Measured reflections	20167	4417	23278
Unique reflections	3290	4417	6217
Parameters	224	653	314
Restraints	0	3	31
R_{int}	0.1128		0.0596
θ range (deg.)	1.96 - 25.02	1.92 - 53.21	2.89 - 32.07
R_1, wR_2 all data	0.1171, 0.2950	0.2779, 0.4342	0.0822, 0.1261
S (GooF) all data	0.997	1.949	0.999
Max/min res. Dens. (e/Å^3)	9.447/-1.326	2.079/-1.387	1.471/-0.975

Data for ZAC-4 and ZAC-5 were very poor and showed signs of twinning and stacking faults which were not fully resolved. The structural features present were enough to determine they are in fact part of the same family as ZAC-6; however, the crystallographic data are not good quality.

Results

Syntheses

A systematic investigation was needed to fully understand how alkylbisphosphonates can be used to design porous framework materials. This work aimed to investigate if isoreticular structures can be designed with divalent alkylbisphosphonates, and will cover the range of alkyl spacers using the ligand H_4Ln, n = 3 to 6. Two techniques were utilized in investigating this system: (i) varying the pH of the reaction, (ii) varying the metal-to-ligand starting ratios.

The first technique is adapted from the procedure used by Clearfield et al.[33] The metal salt was dissolved in a minimal amount of water and its pH adjusted to different amounts, then a solution of the ligand dissolved in a minimal amount of water was layered on top. This procedure differs from that reported by Clearfield and coworkers in that it layers the two solutions whereas they mixed the two solutions and placed them on a shaker for 24 - 72 hours. The metal-to-ligand ratio was initially fixed at 2:1. Since these conditions worked well in the previously studied Cu^{2+} H_4L5 derivative, the first reactions were set up with Zn^{2+} and the H_4L5 ligand.

The second technique was simply to fix the pH and to vary the metal-to-ligand starting ratio. The same process was followed with the metal being dissolved in a minimal amount of water, pH adjusted to a fixed amount (~1.8), and then a solution of the ligand dissolved in a minimal amount of water was layered on top.

In both cases once a new structure appeared with a given synthetic condition, the conditions were adjusted to produce a phase pure product. After the optimal conditions were determined then the ligand chain length was changed in an attempt to synthesize the same structural architecture with longer (or shorter) linkers.

Crystal Structures

All of the compounds presented contain tetrahedrally coordinated zinc atoms in which all of the coordination sites are phosphonate oxygen atoms. The Zn – O bond lengths range from 1.878(2) – 2.018(5) Å which is in good agreement with previously reported zinc phosphonate materials. The PO_3C tetrahedral in these structures all contain P – O bond distances of 1.495(2) – 1.590(2) Å. The large range in the P – O bonds can be attributed to the presence of protons on some of the oxygen atoms which results in an elongation of the P –O bond compared to a chelated or double-bonded oxygen atom.

Several of the presented compounds also have octahedrally coordinated zinc atoms in which some or all of the sites are water molecules. The Zn – O(w) bond lengths range from 2.027(3) – 2.165(5) Å.

Zinc Alkyl Gate (ZAG-4,6)

In 2003, Ruibiao Fu and coworkers presented a series of divalent phosphonates using H_4L4 including the compound ZAG-4.[94] Further investigation shows that this same compound had previously been synthesized by Dierdra Arnold at Texas A&M

University and was presented in her Masters thesis with PXRD structural analysis.[95] Both of these previous reports were in agreement of the structure of ZAG-4.

Much like ZAG-4, ZAG-6 consists of 1-D chains which are hydrogen bonded together into 2-D supramolecular sheets and cross-linked by the alkyl linkers to form a 3-D network. Figure 18 shows the asymmetric unit. ZAG-6 crystallizes in the space group *C*2/*c* (No. 15) with the cell parameters given in Table 6. Bond lengths and angles are given in Table 9.

The Zn(1) center is bridged to four symmetry-related zinc ions through O-P-O bridges in two directions to form a 1-D chain of 8-membered rings, and through full ligand bridges in the other two directions to link the 1-D chains together into a 3-D network as shown in Figures 19 and 20. The ligand only loses one proton per phosphonic acid, and there are two interstitial water molecules (which are related by symmetry) hydrogen bonded between the inorganic chains. Together with the water molecules, the 1-D chains are hydrogen bonded together to form a 2-D supramolecular sheet through hydrogen bonds, {P(2)-O(3)-H(3C)···O(1W) 2.5445(19) Å, 162(2)°}, {O(1W)-H(1W)···O(3) 2.8010(19) Å, 178(3)°}, and {O(1W)-H(2W)···O(2) 2.8010(19) Å, 171(2)°}. A localized diagram of this hydrogen bonded network is shown in Figure 21. When viewed down the *c*-axis (Figure 22) one can see the diamond shaped channels of interstitial water molecules that lie between the inorganic chains and the wine-rack or child safety-gate topology.

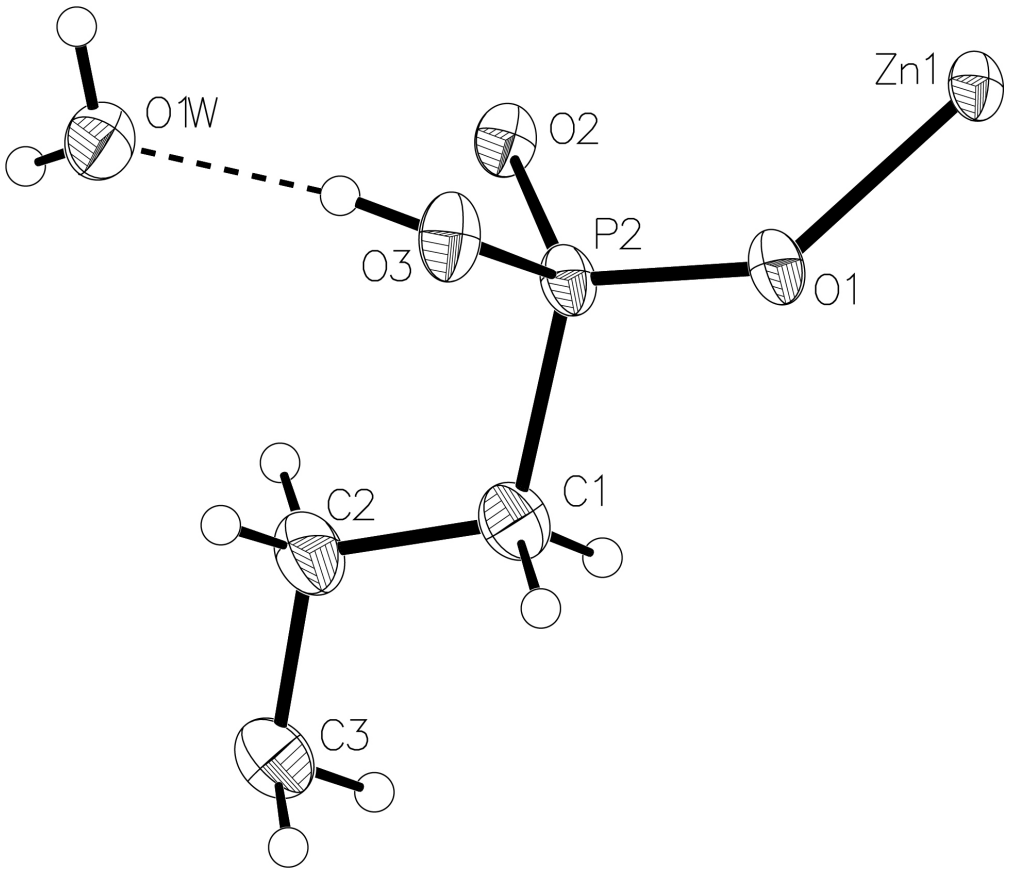

Figure 18. Thermal ellipsoid plot of ZAG-6.The thermal ellipsoid probabilities are at 50%.

Table 9. Selected bond lengths [Å] and angles [°] for ZAG-4 (left) and ZAG-6 (right).

Zn1-O1[a]	1.9309(13)	Zn1-O1[a]	1.926(2)
Zn1-O2	1.9458(12)	Zn1-O2	1.945(2)
Zn1-O1	1.9309(13)	Zn1-O1	1.926(2)
Zn1-O2[a]	1.9458(12)	Zn1-O2[a]	1.945(2)
P1-O1	1.5048(13)	P2-O1	1.501(2)
P1-O2[b]	1.5226(13)	P2-O2[c]	1.521(2)
P1-O3	1.5718(14)	P2-O3	1.566(2)
P1-C1	1.7844(18)	P2-C1	1.786(4)
O1-Zn1-O1[a]	114.93(8)	O1-Zn1-O1[a]	113.72(14)
O1-Zn1-O2	107.23(5)	O1-Zn1-O2	111.26(9)
O1[a]-Zn1-O2	109.40(5)	O1[a]-Zn1-O2	106.49(10)
O1-Zn1-O2[a]	109.40(5)	O1-Zn1-O2[a]	106.49(10)
O1[a]-Zn1-O2[a]	107.23(5)	O1[a]-Zn1-O2[a]	111.26(9)
O2-Zn1-O2[a]	108.50(8)	O2-Zn1-O2[a]	107.52(13)
O1-P1-O2[b]	114.83(7)	O1-P2-O2[c]	114.64(13)
O1-P1-O3	106.65(7)	O1-P2-O3	106.66(13)
O1-P1-C1	109.32(8)	O1-P2-C1	109.24(16)
O2[b]-P1-O3	107.93(7)	O2[c]-P2-O3	108.56(13)
O2[b]-P1-C1	110.34(8)	O2[c]-P2-C1	109.89(15)
O3-P1-C1	107.45(8)	O3-P2-C1	107.58(16)
P1-O1-Zn1	131.64(8)	P2-O1-Zn1	132.17(15)
P1[d]-O2-Zn1	133.95(8)	P2[c]-O2-Zn1	134.07(14)

Symmetry transformations used to generate equivalent atoms: a: -x+1,y,-z+3/2;
b: x,-y+1,z-1/2; c: -x+1,-y+1,-z+1; d: x,-y+1,z+1/2

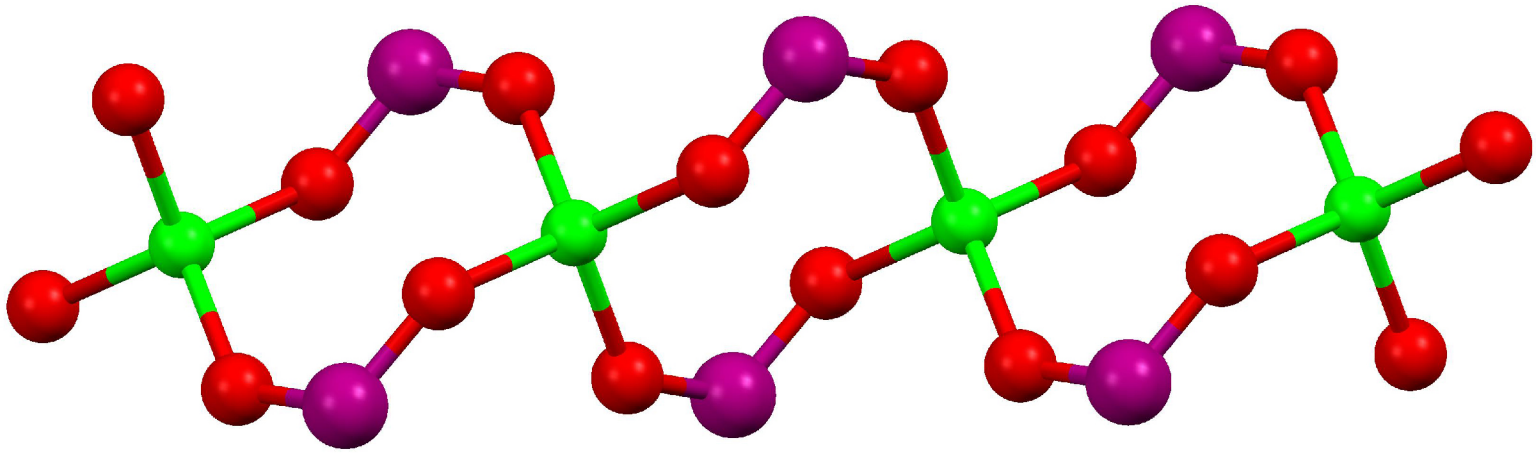

Figure 19. Corner shared 8-membered Zn-O-P-O rings which make up the 1-D inorganic chain unit of ZAG-6.

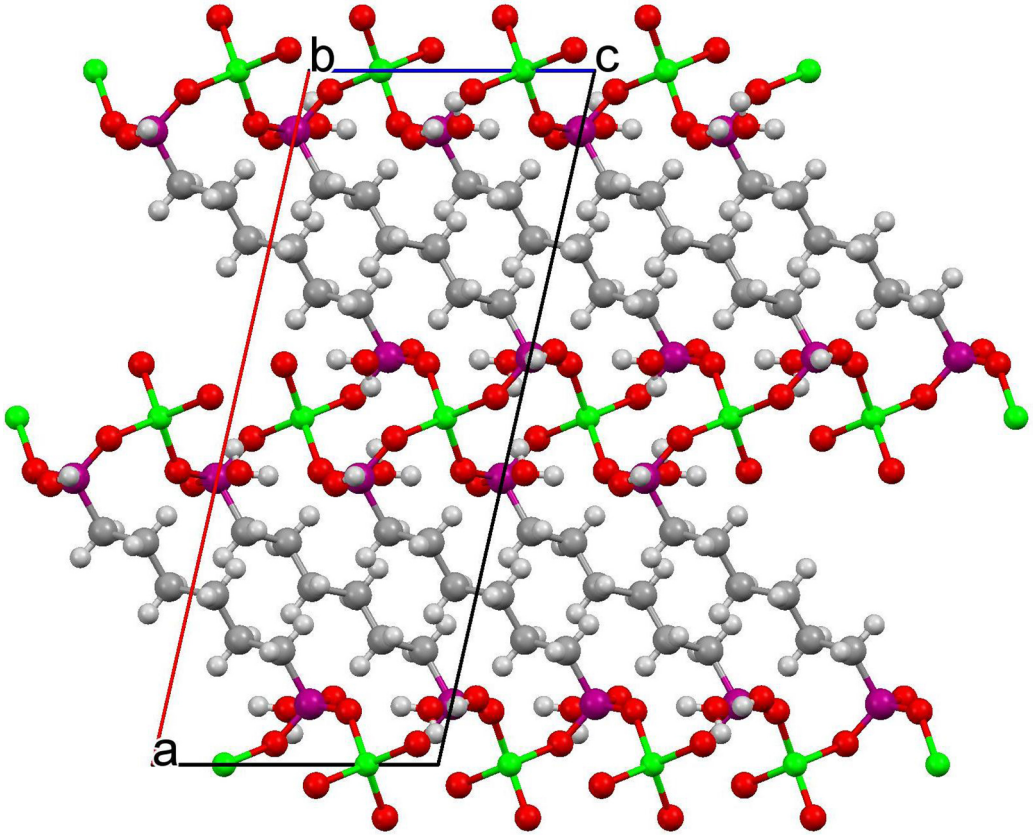

Figure 20. ZAG-6 viewed along the *b*-axis showing the cross-linking of the 1-D chains to form the 3-D network.

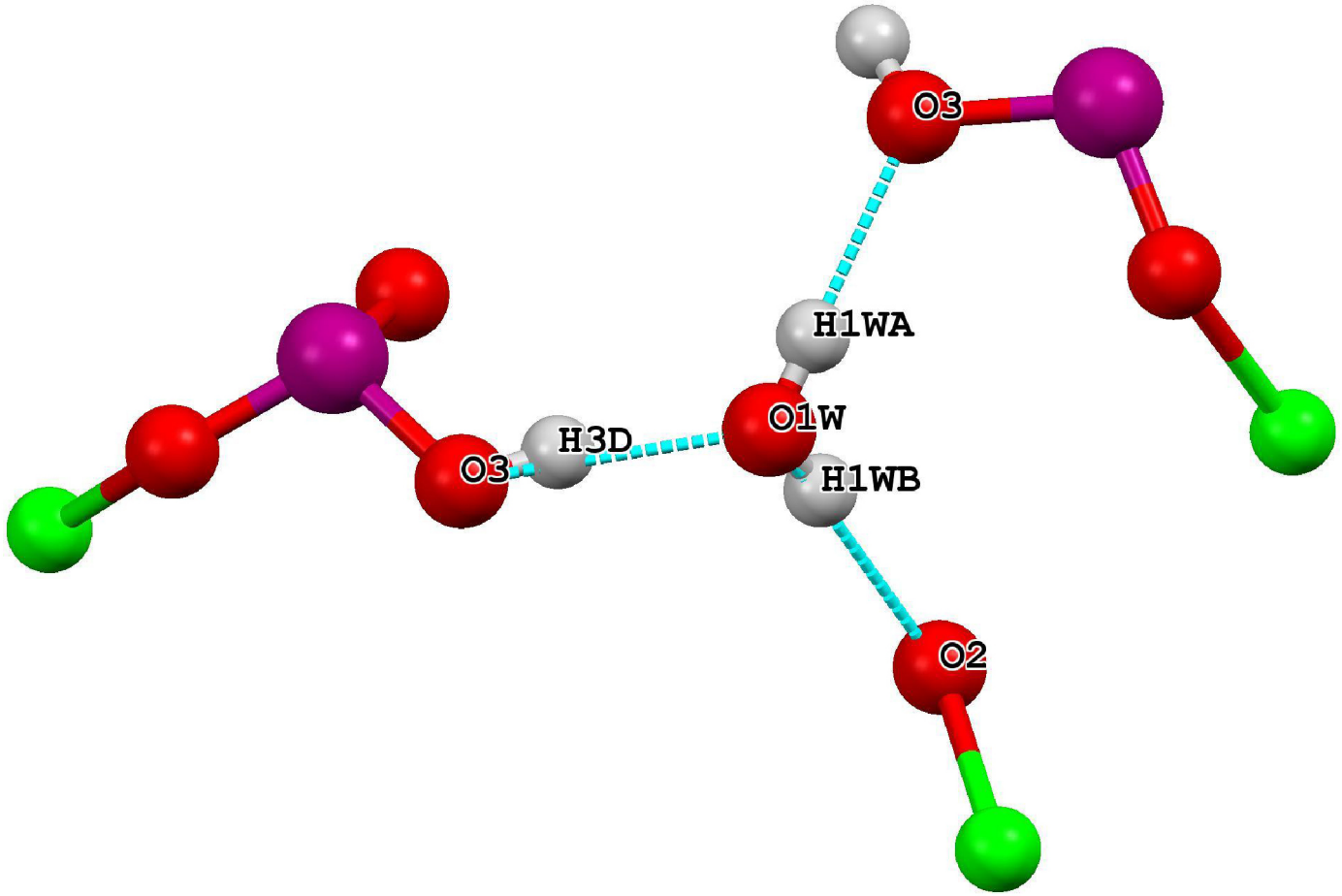

Figure 21. Localized hydrogen bonding scheme of ZAG-6 showing the interconnection between 1-D chains via the interstitial water molecule.

Identical reaction conditions with supplementation of H_4L4 for H_4L6 results in the production of ZAG-4 which has an identical topology to that of ZAG-6. It consists of the same 1-D chains hydrogen bonded into 2-D sheets which are further cross-linked into a 3-D network. ZAG-4 crystallizes in the space group *C*2/*c* (No. 15) with slightly different cell parameters due to different orientation of the unit cell to provide the most conventional β-angle. Our structure of ZAG-4 also agrees with those independently determined by Fu and Arnold. Figures 23 and 24 show side by side comparisons of ZAG-4 and ZAG-6.

Zinc Alkyl Tunnel (ZAT-3,5)

ZAT-3 consists of 1-D chains which are cross-linked in one direction by octahedral tetraaqua zinc centers and in the other direction by the alkyl chain to form a 3-D network with a large and a small 1-D channel. The asymmetric unit is shown in Figure 25. ZAT-3 crystallizes in the space group *Pmmn* (no. 59) with the cell parameters given in Table 7. Bond lengths and angles are given in Table 10.

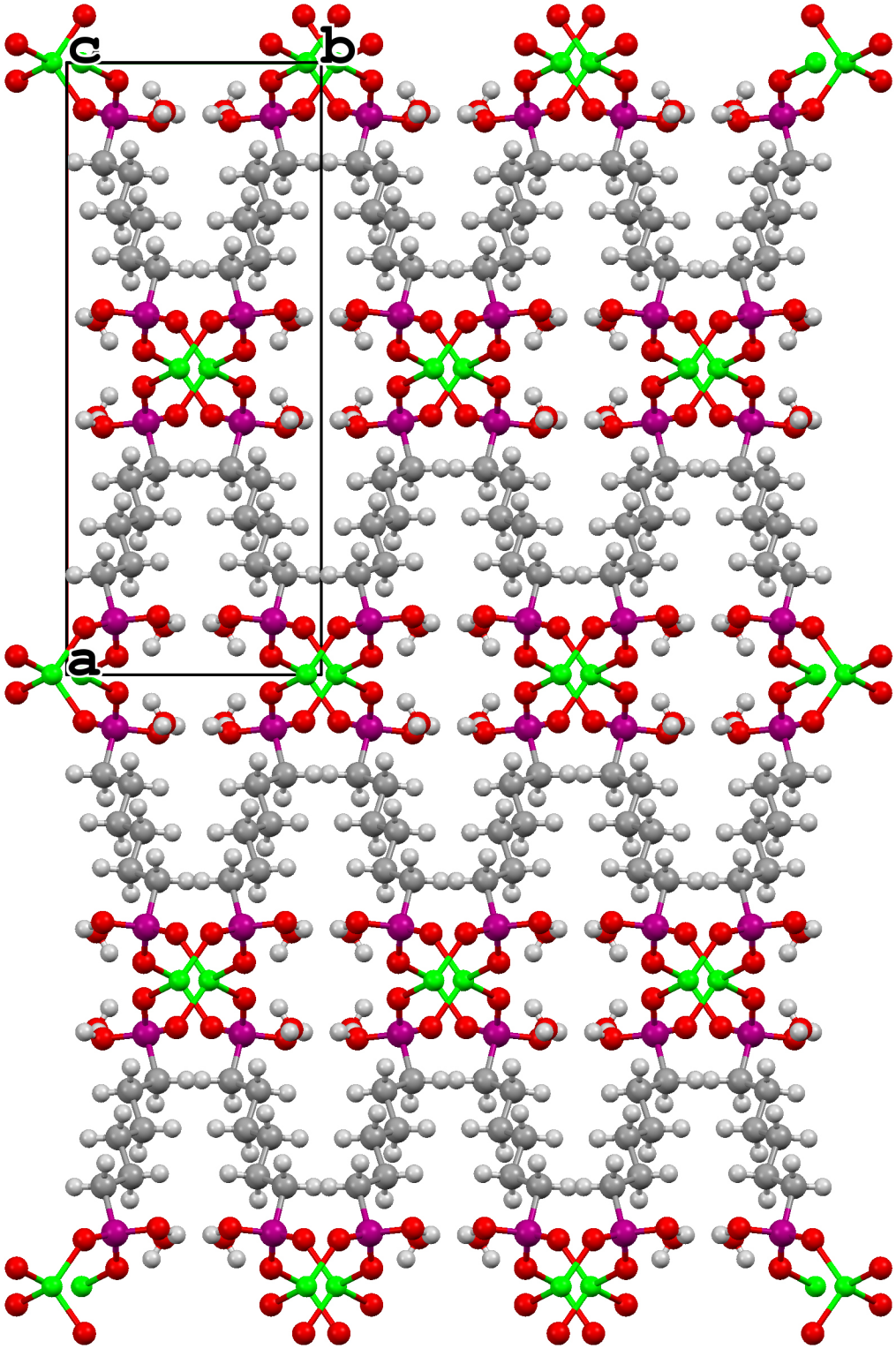

Figure 22. ZAG-6 viewed down the *c*-axis showing the diamond shaped channels.

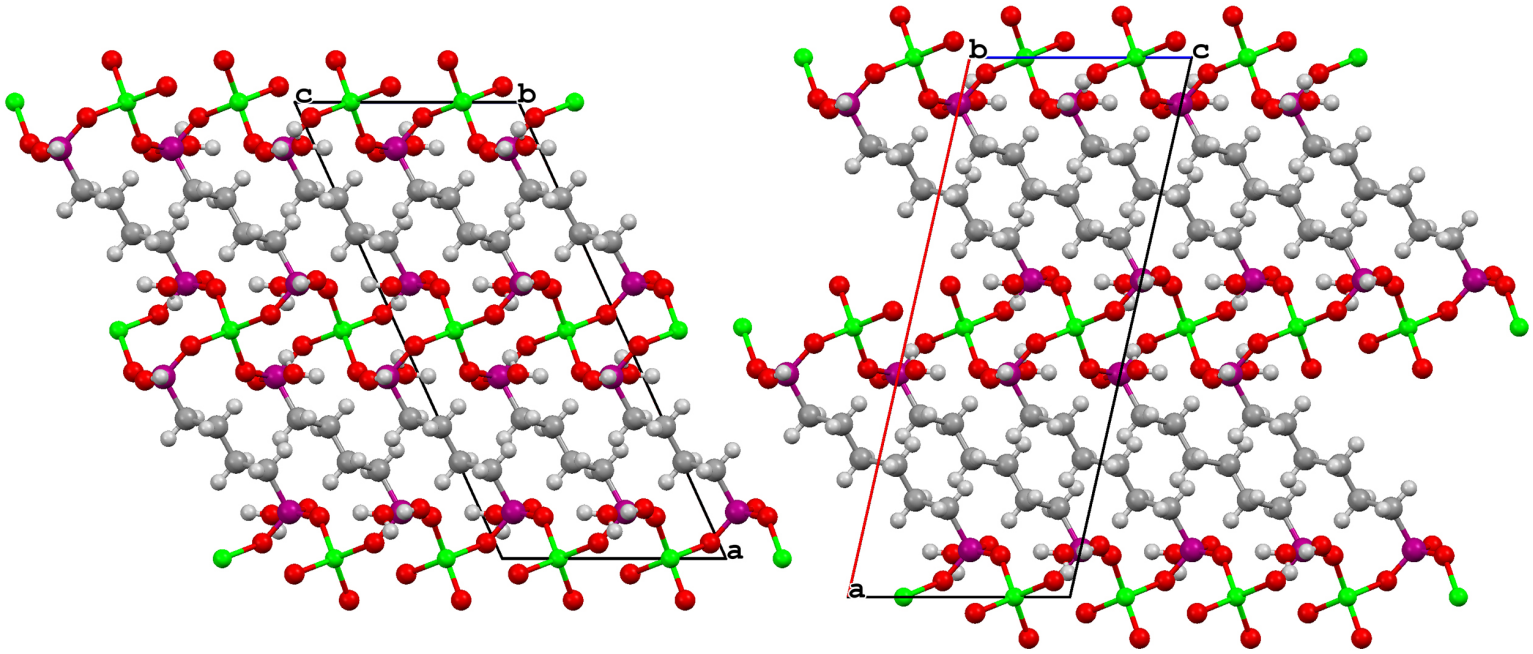

Figure 23. Side by side comparison of ZAG-4 (left) and ZAG-6 (right) viewed down the *b*-axis. The different cell directions are due to conventional unit cell conformity. The unit cells are related by the transformation matrix 1 0 2 0 -1 0 0 0 -1.

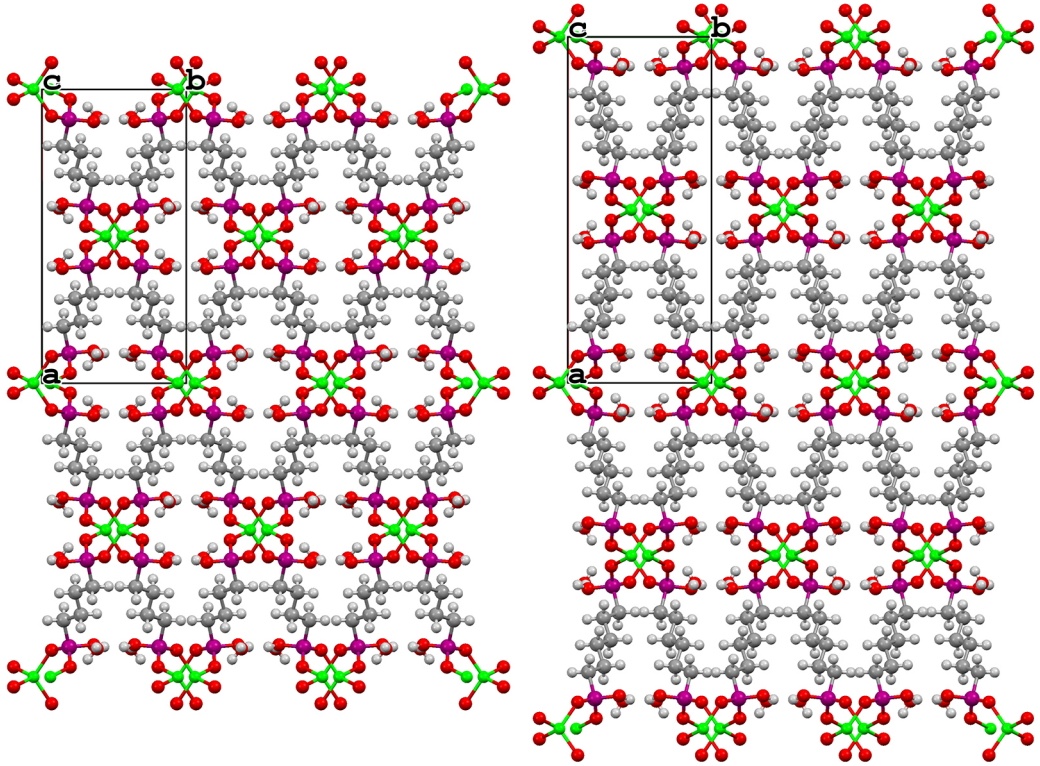

Figure 24. Side by side comparison of ZAG-4 (left) and ZAG-6 (right) viewed down the *c*-axis.

The Zn(1) center is tetrahedrally coordinated by four phosphonate oxygen atoms and is bridged to four symmetry related Zn(1) centers through O-P-O bridges to form a 1-D chain of 8-membered Zn-O-P-O rings as shown in Figure 26. These 1-D chains are bridged together by an octahedral Zn(2) via a Zn-O-P-O-Zn-O-P-O linkage to form 24 membered rings as shown in Figure 27. The Zn(1) center is further bridged to 12 symmetry related Zn(1) centers through three symmetry related completely deprotonated full ligand bridges. The Zn(1) is even further bridged to two symmetry related Zn(2) centers through both an O-P-O bridge and a partially deprotonated ligand bridging across its length. The last bridge for the Zn(1) center comes through the partially deprotonated, full ligand which bridges to one last Zn(1) center which totals 19 zinc atoms to which a single Zn(1) is bridged to. This effectively amounts to 2-D sheets of 8- and 24-membered rings being cross-linked by the alkyl linkers. In total there are two symmetry independent zinc atoms and two independent ligands, one which is fully deprotonated and one in which each phosphonate group is monoprotonated. This total arrangement results in a metal:ligand ratio of 3:2. Contained in this connective array is one intra-chain hydrogen bond, {O(3)-H(3)···O(4), 2.582(4) Å, 170(2)°}. This connectivity results in a large 3-D

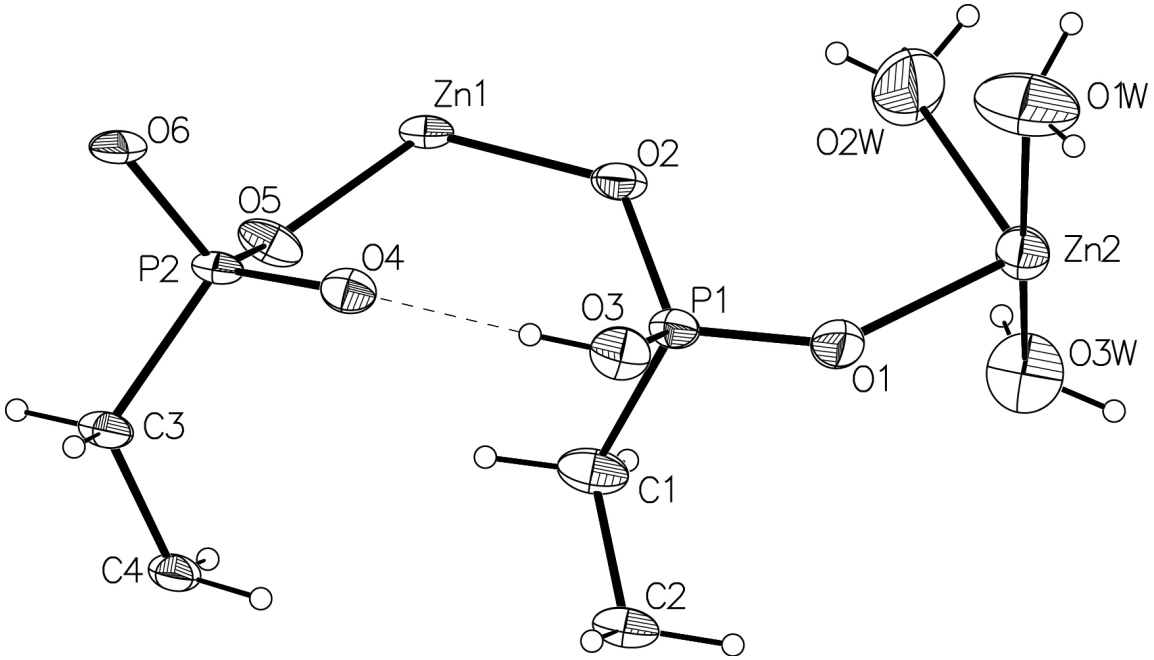

Figure 25. Thermal ellipsoid plot of ZAT-3.The thermal ellipsoids are at 50% probability.

Table 10. Selected bond lengths [Å] for ZAT-3.

Zn1-O4[a]	1.966(2)	Zn2-O1	2.002(3)
Zn1-O2	1.957(2)	Zn2-O1[c]	2.002(3)
Zn1-O5	1.923(2)	Zn2-O3W	2.101(5)
Zn1-O6[b]	1.921(2)	Zn2-O2W	2.131(3)
P1-O1	1.496(3)	Zn2-O2W[c]	2.131(3)
P1-O2[b]	1.519(2)	Zn2-O1W[c]	2.165(5)
P1-O3	1.575(3)	P2-O4	1.545(2)
P1-C1	1.789(4)	P2-O5	1.514(2)
		P2-O6	1.526(3)
		P2-C3	1.794(3)

Symmetry transformations used to generate equivalent atoms: a: x, y, z+1;
b: -x+1, -y+2, -z+1 c: x, -y+3/2, z

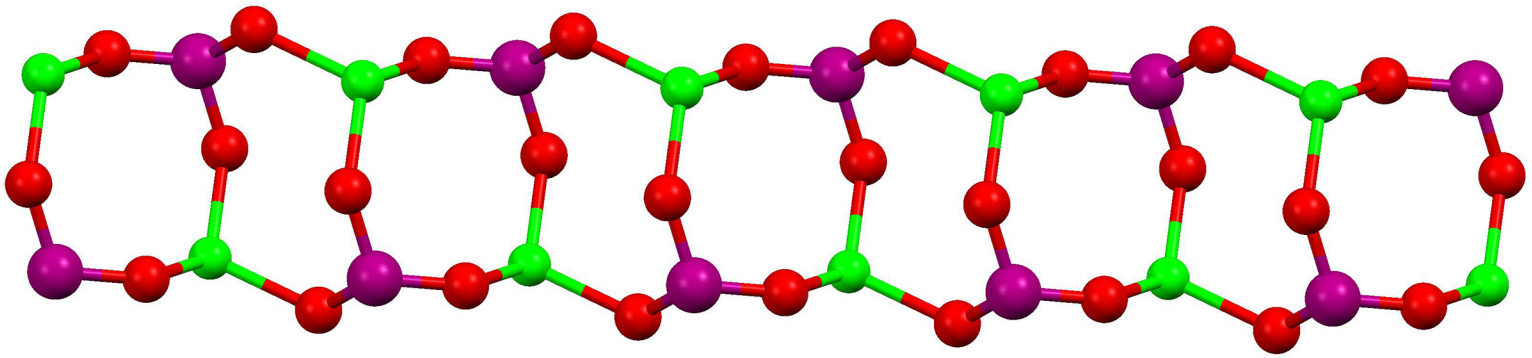

Figure 26. Edge shared fused 8-membered Zn-O-P-O rings that make up the 1-D inorganic chain of ZAT-3

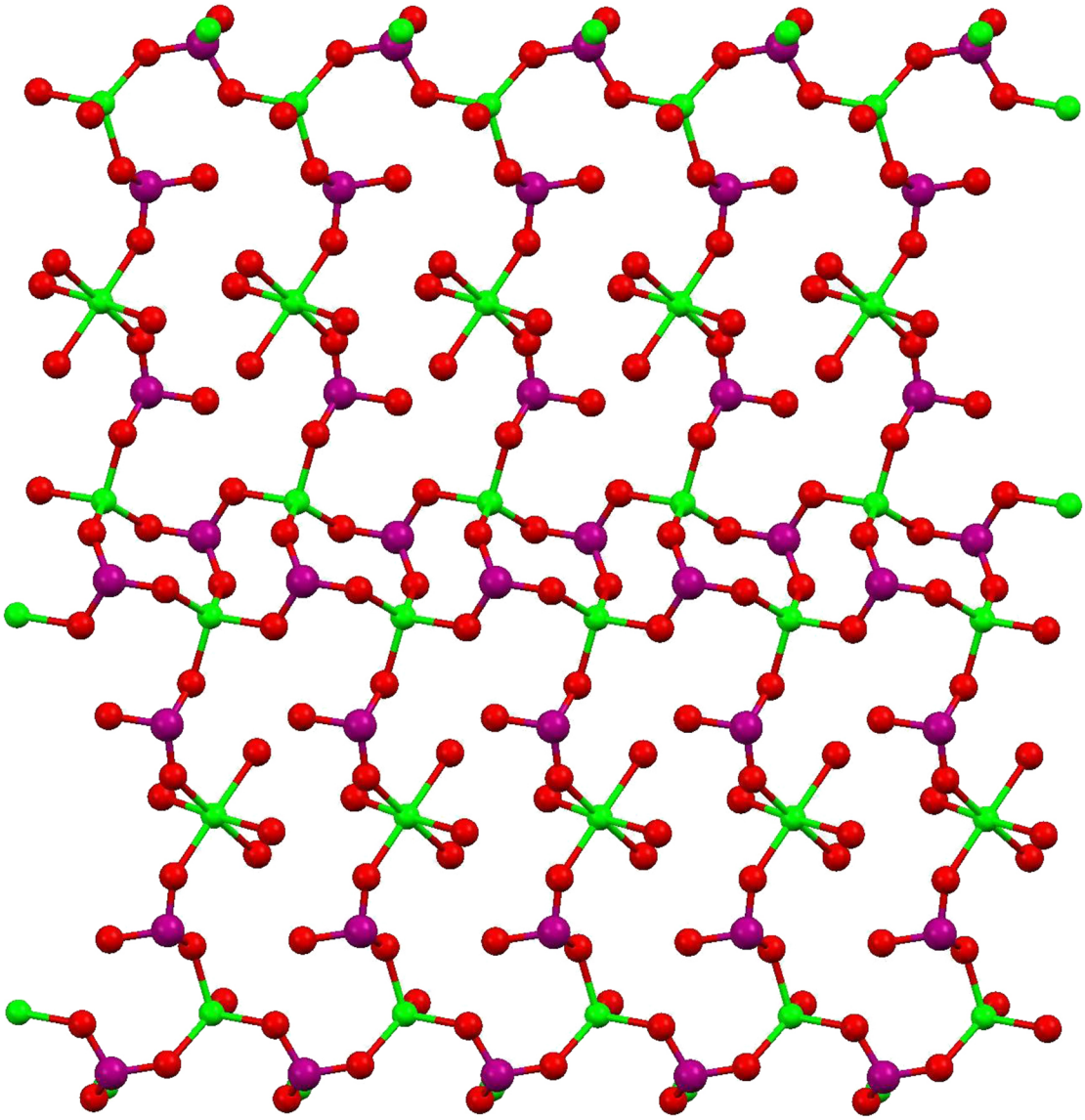

Figure 27. Fused 8-member and 24-member rings which make up the 2-D sheets of ZAT-3. Notice the tetrahedral zinc atoms form 1-D chains which are crosslinked by the octahedral zinc atoms.

framework which contains 1-D tunnels of ~0.7 nm in diameter and parallel much smaller 1-D tunnels as shown in Figure 28. The contents of this tunnel have not been determined but are most likely a mixture of water and acetic acid, or just water.

Identical reaction conditions with supplementation of H_4L5 for H_4L3 results in the production of ZAT-5 which has an identical topology to that of ZAT-3. ZAT-5 crystallizes in the space group *Pmmn* (No. 59) with slightly different cell parameters due to the increase in the chain length. The large tunnel in ZAT-5 is ~1.3 nm in diameter and also contains unknown solvent molecules as in ZAT-3. Figures 29 and 30 show side by side comparisons of ZAT-3 and ZAT-5.

Zinc Alkyl Sheet (ZAS-3,5)

In 1999, Clearfield and coworkers presented a pair of zinc frameworks made with H_4L3, one of which was ZAS-3.[34] This compound was synthesized via a very different procedure and was solved via PXRD at room temperature. We have solved the structure of ZAS-3 and ZAS-5 via single crystal X-ray diffraction at low temperature.

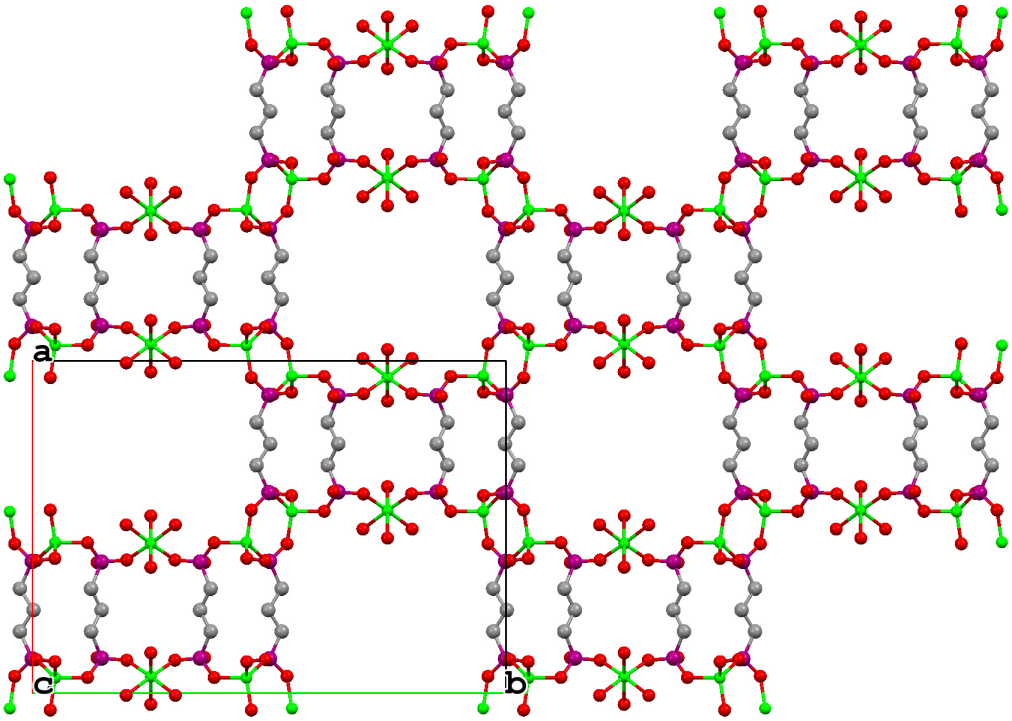

Figure 28. ZAT-3 viewed down the *c*-axis showing the two different 1-D channels. Hydrogen atoms have been omitted for clarity. The solvent in the pores have been removed using the SQUEEZE algorithm.

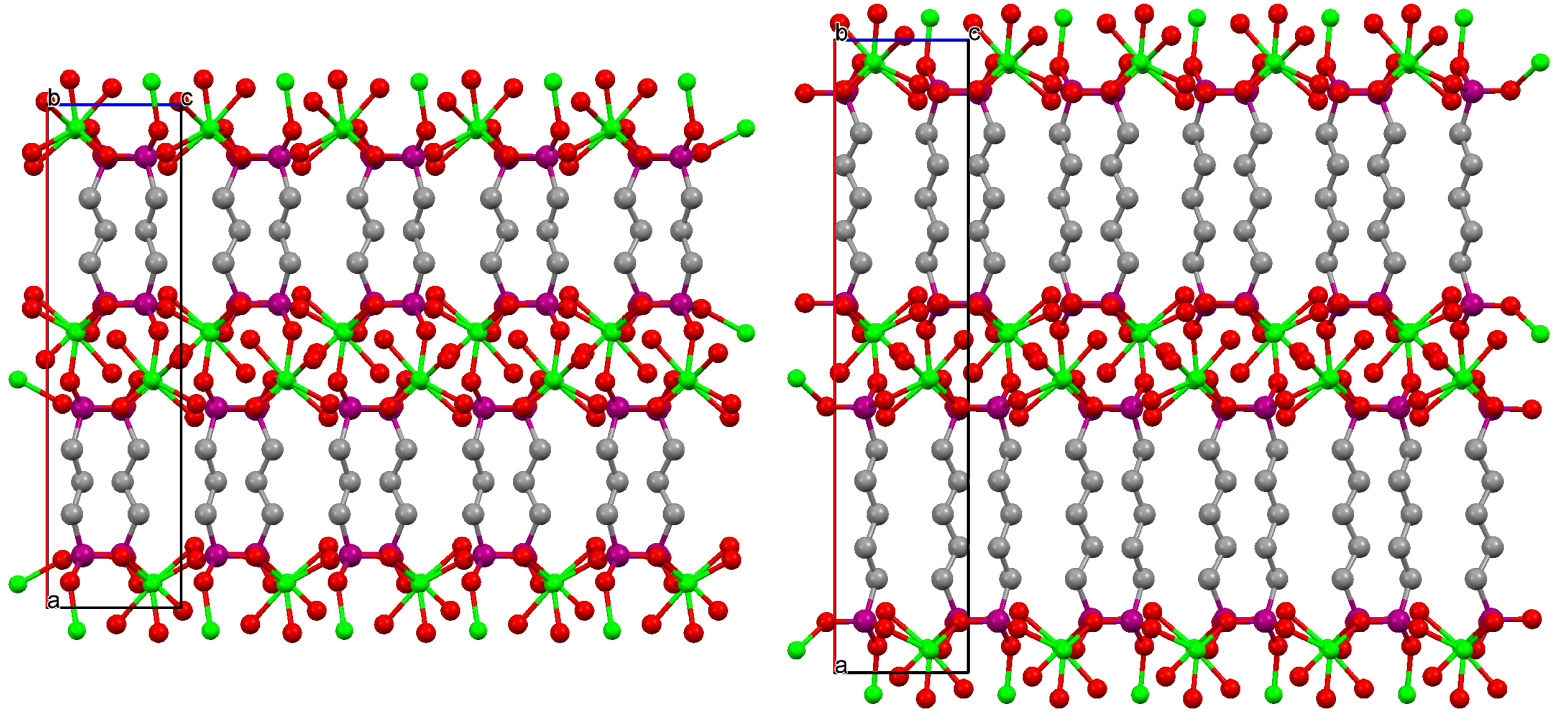

Figure 29. ZAT-3 (left) and ZAT-5 (right) viewed down the *b*-axis showing the alkyl pillars bridging together the 2-D sheets. Hydrogen atoms have been removed for clarity.

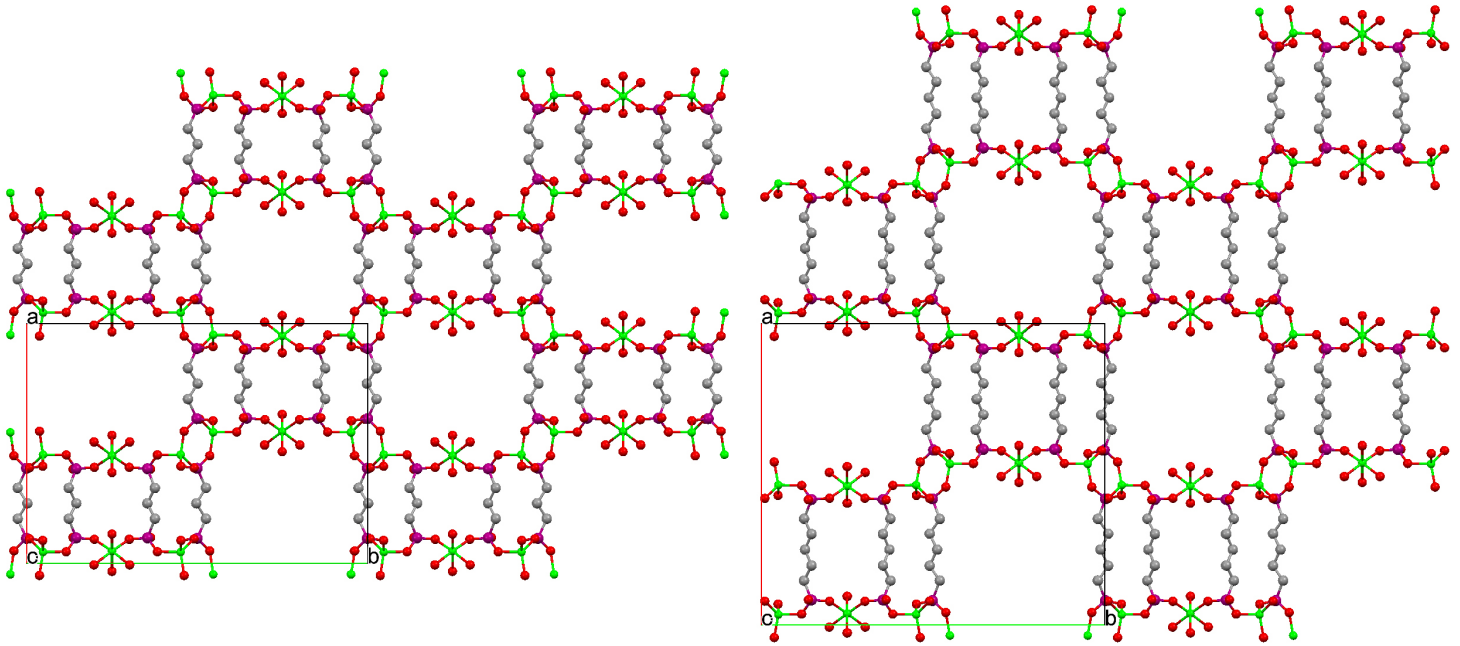

Figure 30. ZAT-3 (left) and ZAT-5 (right) as viewed down the *c*-axis showing the various 1-D tunnels. Hydrogen atoms have been omitted for clarity. Solvent molecules have been removed using the SQUEEZE algorithm.

ZAS-3 consists of 1-D inorganic chains which are cross-linked in two directions by the alkyl chains to form 2-D slabs which are hydrogen bonded together to form a supramolecular 3-D network. The asymmetric unit is shown in Figure 31. ZAS-3 crystallizes in the space group $P2_1/n$ (no. 14) with the cell parameters given in Table 6. Bond lengths and angles are given in Table 11.

ZAS-3 contains one symmetry independent zinc atom and one H_4L3 ligand, in which each phosphonate group only has one deprotonated hydroxyl group. This combination results in a metal:ligand ratio of 1:1. The Zn(1) center is bridged to four symmetry related Zn(1) centers through O-P-O bridges to form 1-D chains of 12-membered Zn-O-P-O linkages as shown in Figure 32. The Zn(1) centers are further bridged to six symmetry related Zn(1) centers through full ligand bridges, resulting in a total of 10 Zn(1)-Zn(1) bridges. This connectivity forms 2-D slabs as shown in Figure 33. Neighboring slabs are further hydrogen bonded together through a pair of P-O-H···O interactions, {P(1)-O(1)-H(6)···O(4) 2.632(3) Å, 157(2)°} and {P(2)-O(5)-H(5A)···O(1) 2.699(3) Å, 150(3)°} which are depicted in Figure 34. The chains run parallel to the *b*-axis and hydrogen bond into 2-D supramolecular sheets in the *ab*-plane.

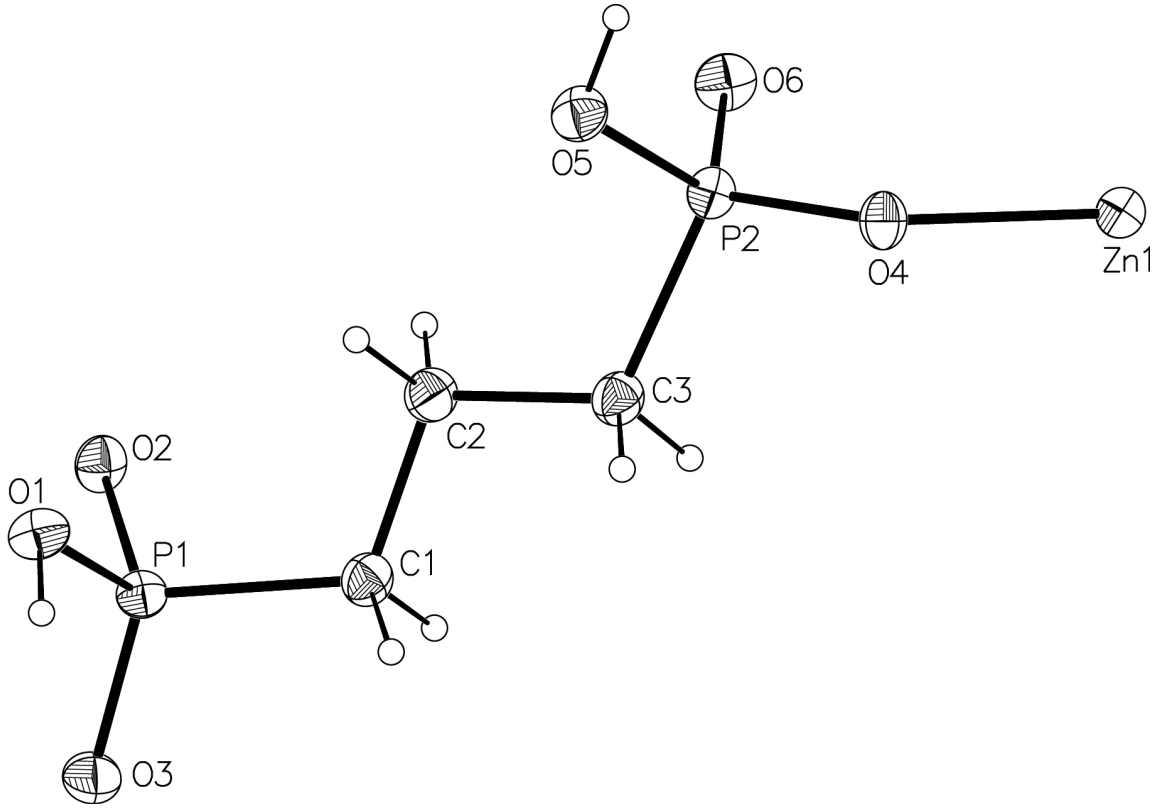

Figure 31. Thermal ellipsoid plot of ZAS-3.The thermal ellipsoids are at 50% probability.

Table 11. Selected bond lengths [Å] for ZAS-3 (left) and ZAS-5(right).

Zn1-O3	1.912(2)	Zn1-O3	1.915(2)
Zn1-O6	1.916(2)	Zn1-O6	1.915(2)
Zn1-O2	1.941(2)	Zn1-O2	1.946(2)
Zn1-O4[b]	1.956(2)	Zn1-O5	1.955(2)
P1-O1	1.587(2)	P1-O1	1.590(2)
P1-O2	1.505(2)	P1-O2	1.504(2)
P1-O3[a]	1.499(2)	P1-O3[c]	1.495(2)
P1-C1	1.792(3)	P1-C1	1.787(3)
P2-O4	1.521(2)	P2-O4	1.573(2)
P2-O5	1.571(2)	P2-O5	1.518(2)
P2-O6[b]	1.497(2)	P2-O6[d]	1.498(2)
P2-C3	1.780(3)	P2-C5	1.787(3)

Symmetry transformations used to generate equivalent atoms: a: x,y-1,z;
b: -x+3/2,y-1/2,-z+1/2; c: x,y+1,z,; d: -x+3/2,y+1/2,-z+1/2

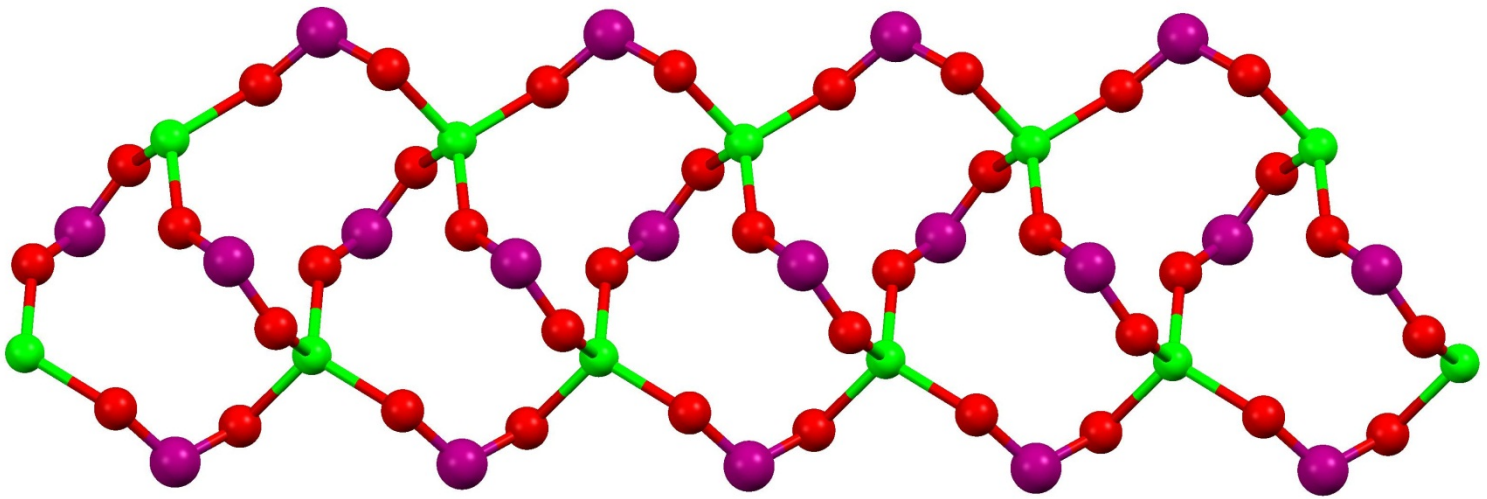

Figure 32. Fused 12-member rings which form the tube-like 1-D chain of ZAS-3.

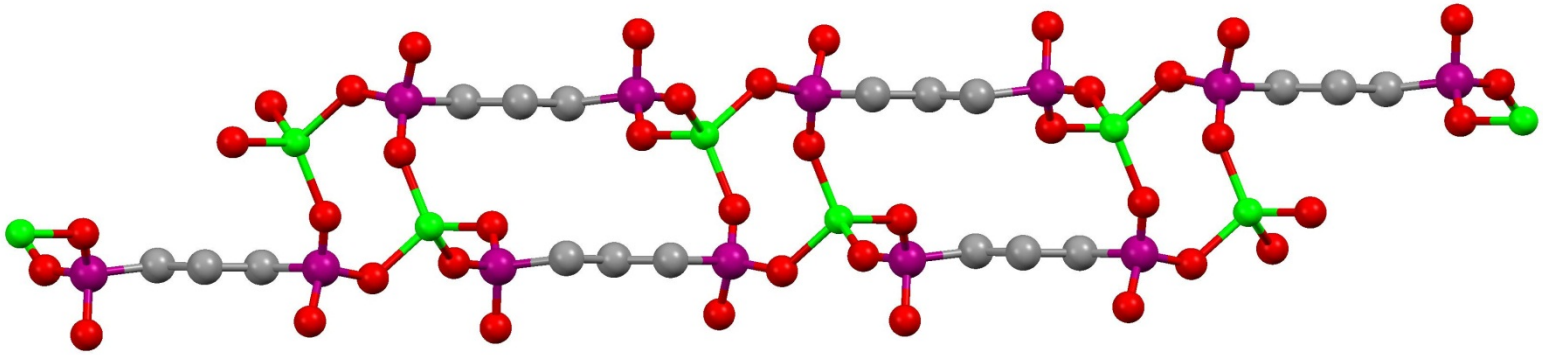

Figure 33. The 1-D chains of ZAS-3 are bridged by pairs of H_4L3 linkers to form a 2-D slab.

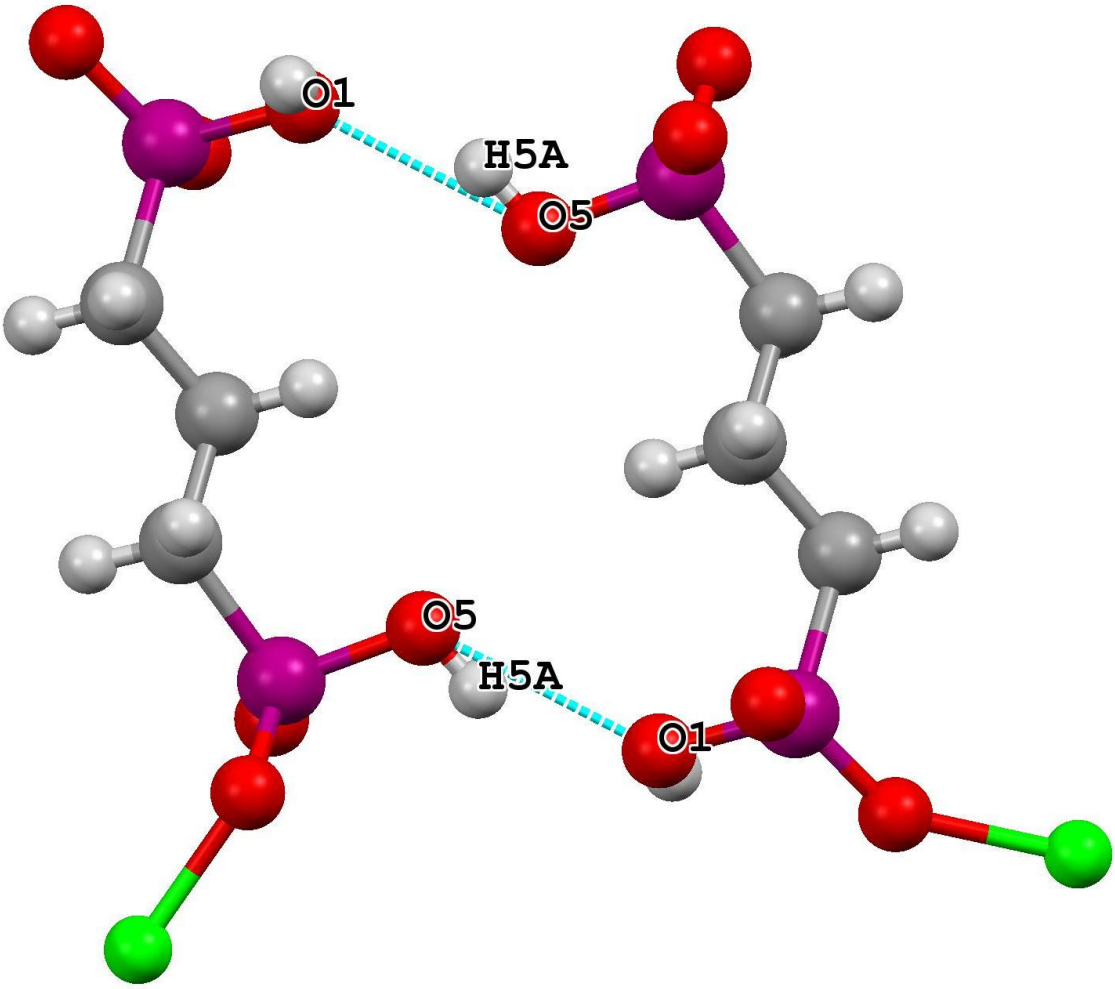

Figure 34. Localized H-bonding in ZAS-3. This shows how neighboring slabs are connected to form the supramolecular 3-D network.

Identical reaction conditions with supplementation of H_4L5 for H_4L3 results in the production of ZAS-5 which has an identical topology to that of ZAS-3. ZAS-5 crystallizes in the space group $P2_1/n$ (No. 14) with slightly different cell parameters due to the increase in the chain length. Figure 35 shows side by side comparisons of ZAS-3 and ZAS-5.

Zinc Alkyl Cation (ZAC-4, 5, 6)

In similar work, using 2-methylpiperazine as a template, Fu and coworkers were able to obtain two related compounds $(C_5H_{14}N_2)Zn_4(O_3P(CH_2)_nPO_3)_2(HO_3P(CH_2)_n)$-$PO_3H)$ where n = 2 and 4.[96] These compounds are structured with a double layer of tetrahedrally coordinated zinc centers bridged by phosphonate linkages connected to form 8-membered and 16-membered rings. The edges of these rings are shared, forming larger 24-membered rings. The double layers are cross-linked together by the alkylbis-(phosphonic acid) and the large 24-membered rings contain a fully protonated 2-methylpiperazine for charge balance.

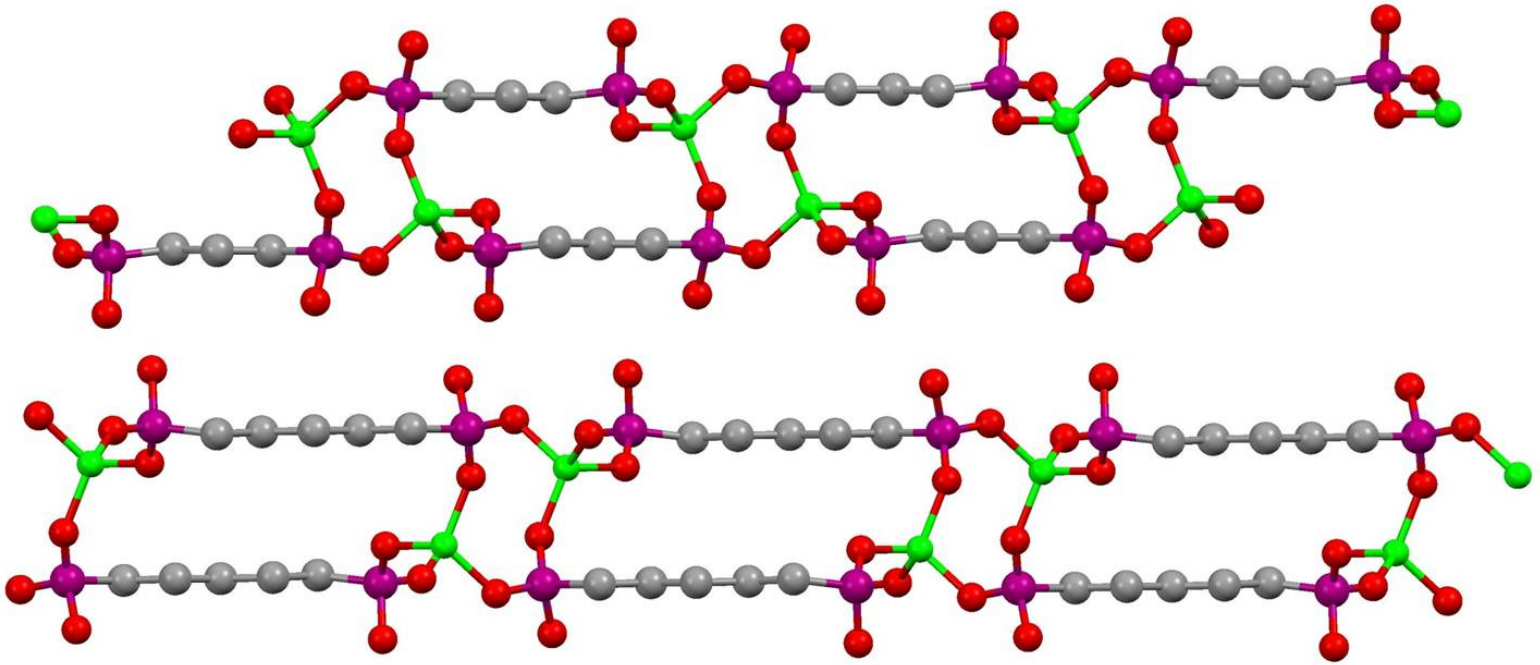

Figure 35. ZAS-3 (top) and ZAS-5 (bottom) slabs.

The ZAC-6 asymmetric unit is shown in Figure 36. ZAC-6 crystallizes in the space group $P2_1/c$ (no. 14) with the cell parameters given in Table 8. Bond lengths are given in Table 12.

ZAC-6 consists of a similar double layer of tetrahedrally coordinated zinc centers as in the compound presented by Fu. The layer is composed of a 1-D tube of fused 8-membered rings as shown in Figure 37. The linkages in the chain are alternating "chair" and "boat" type. These chains are linked together by pairs of O-P-O bridges which combine to form 16-membered rings to form corrugated layers as shown in Figure 38. The top down view of these layers show that the chains and bridges are edge shared to form larger 24-membered rings as shown in Figure 39. The difference from Fu's compound is that the charge balance is obtained by the inclusion of a $Zn(H_2O)_6^{2+}$ ion, in the center of the 24-membered rings instead of a 2-methylpiperazine. The layer viewed down the *a*-axis shows these rings as well as the encapsulated ion as shown in Figure 40.

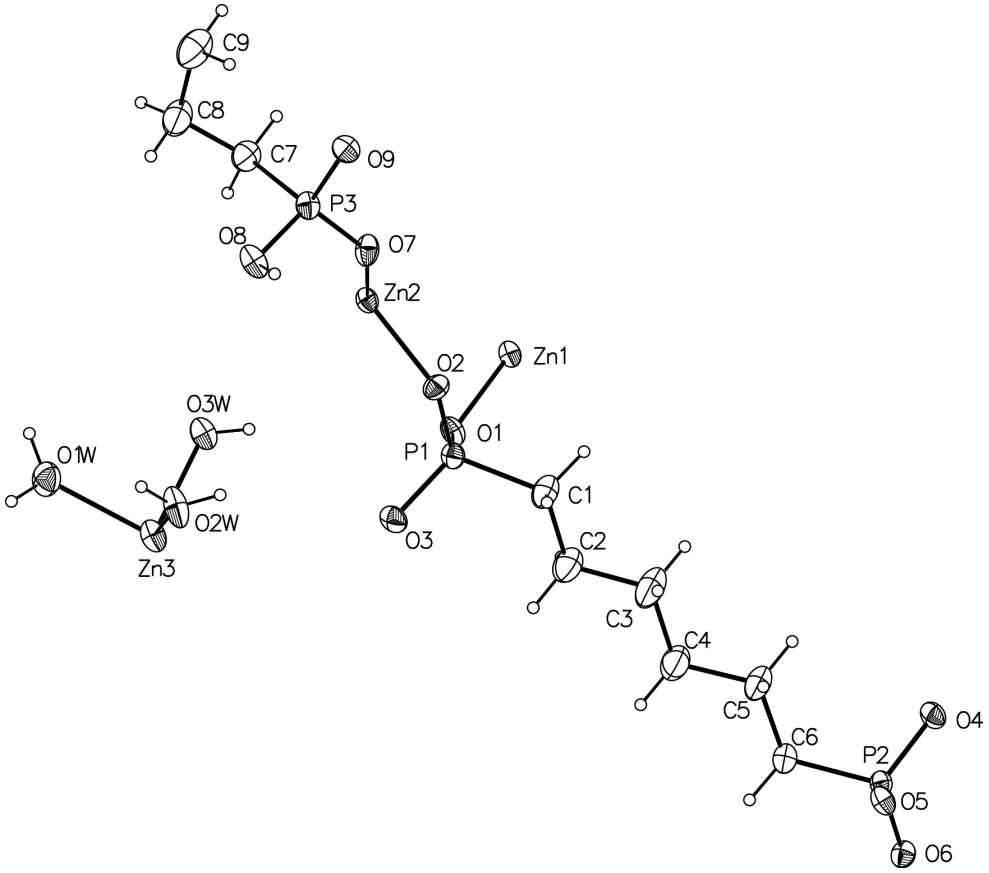

Figure 36. Thermal ellipsoid plot of ZAC-6. The thermal ellipsoids are at 50% probability. The acetic acid and water molecule have been omitted for clarity.

Table 12. Selected bond lengths [Å] for ZAC-6.

Zn1-O1	1.932(3)	Zn3-O1W	2.109(3)
Zn1-O6[b]	1.934(3)	Zn3-O2W	2.027(3)
Zn1-O3[a]	1.925(3)	Zn3-O3W	2.094(3)
Zn1-O9[c]	1.951(3)	Zn3-O1W[e]	2.109(3)
Zn2-O2	1.969(3)	Zn3-O2W[e]	2.027(3)
Zn2-O4[d]	1.916(3)	Zn3-O3W[e]	2.094(3)
Zn2-O5[b]	1.932(3)	P2-O4	1.523(3)
Zn2-O7	1.953(3)	P2-O5	1.533(3)
P1-O1	1.524(3)	P2-O6	1.535(3)
P1-O2	1.540(3)	P2-C6	1.794(4)
P1-O3	1.528(3)	P3-O7	1.520(3)
P1-C1	1.777(5)	P3-O8	1.564(3)
		P3-O9	1.515(3)
		P3-C7	1.779(5)

Symmetry transformations used to generate equivalent atoms: a: x,-y+3/2,z-1/2; b: x+1,y,z; c: -x+1,y+1/2,-z+1/2; d: x+1,-y+3/2,z+1/2; e: x,-y+3/2,z+1/2

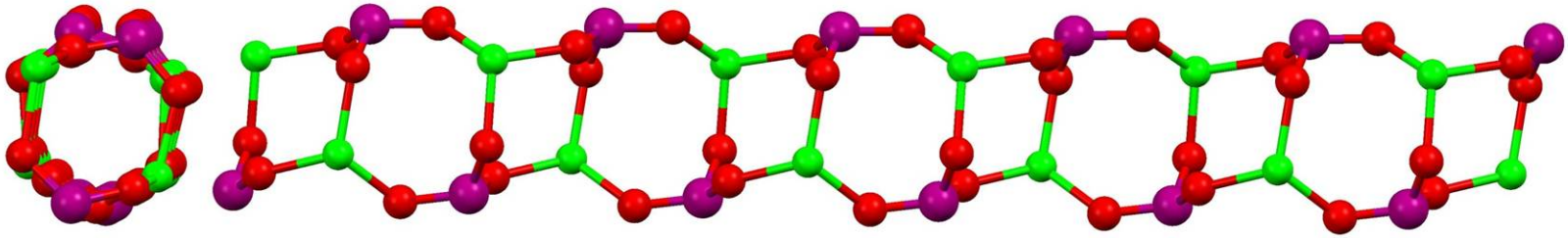

Figure 37. The 1-D tube-like chain of ZAC-6. The left image is viewed down the chain showing how it forms a tube, the right image is viewed perpendicular to the chain showing the 8-membered linkages. The linkages alternate between "boat" and "chair" conformation.

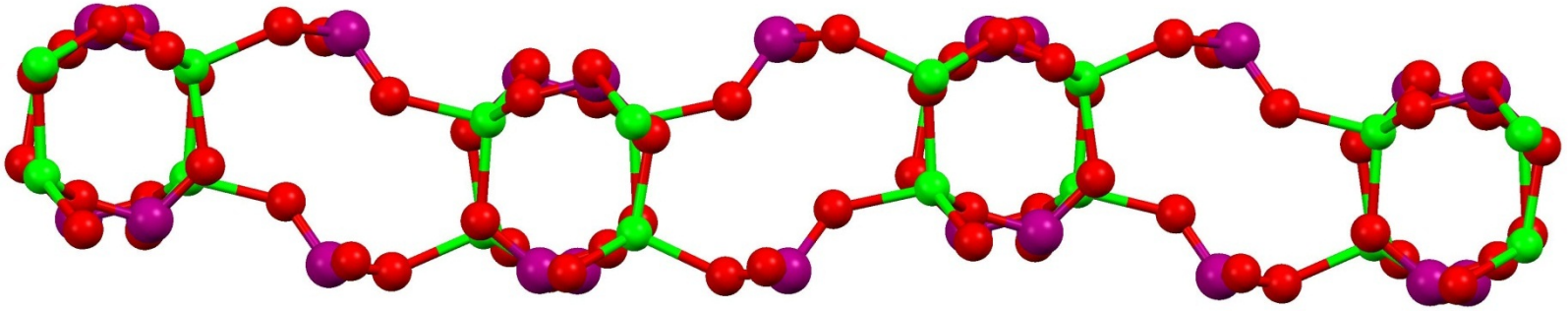

Figure 38. ZAC-6 viewed down parallel 1-D tubes showing how they are bridged via O-P-O pairs to form new 16-membered rings that bridge to form the 2-D sheet.

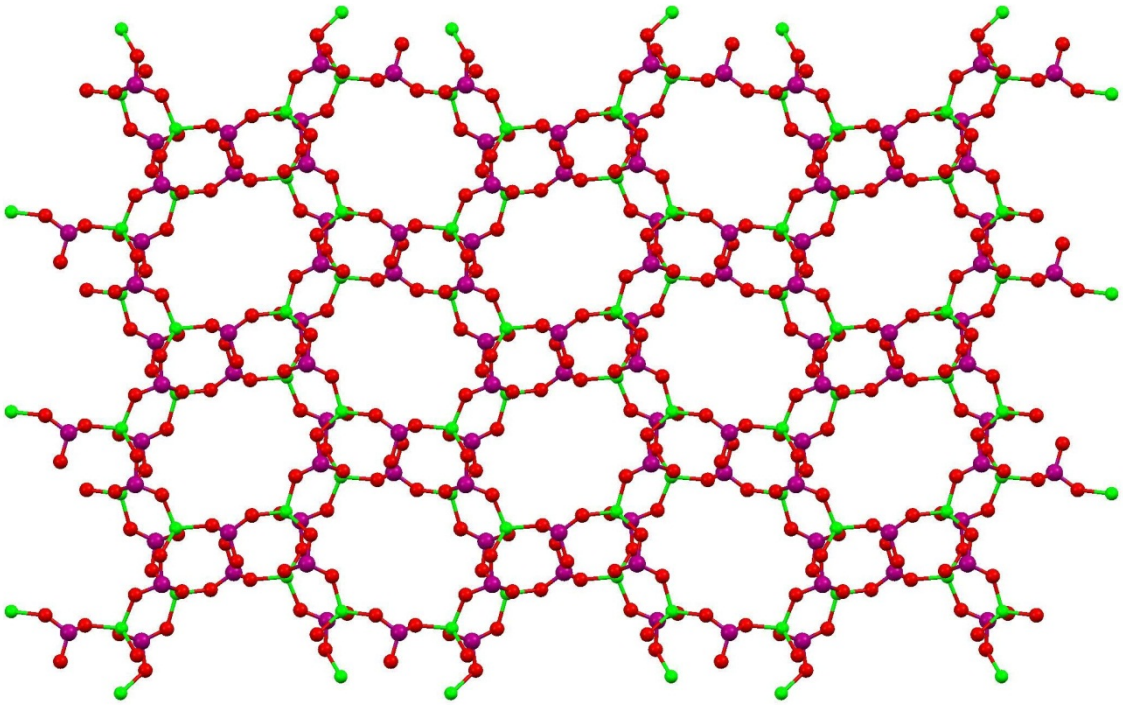

Figure 39. ZAC-6 viewed down the *a*-axis showing the 24-membered rings.

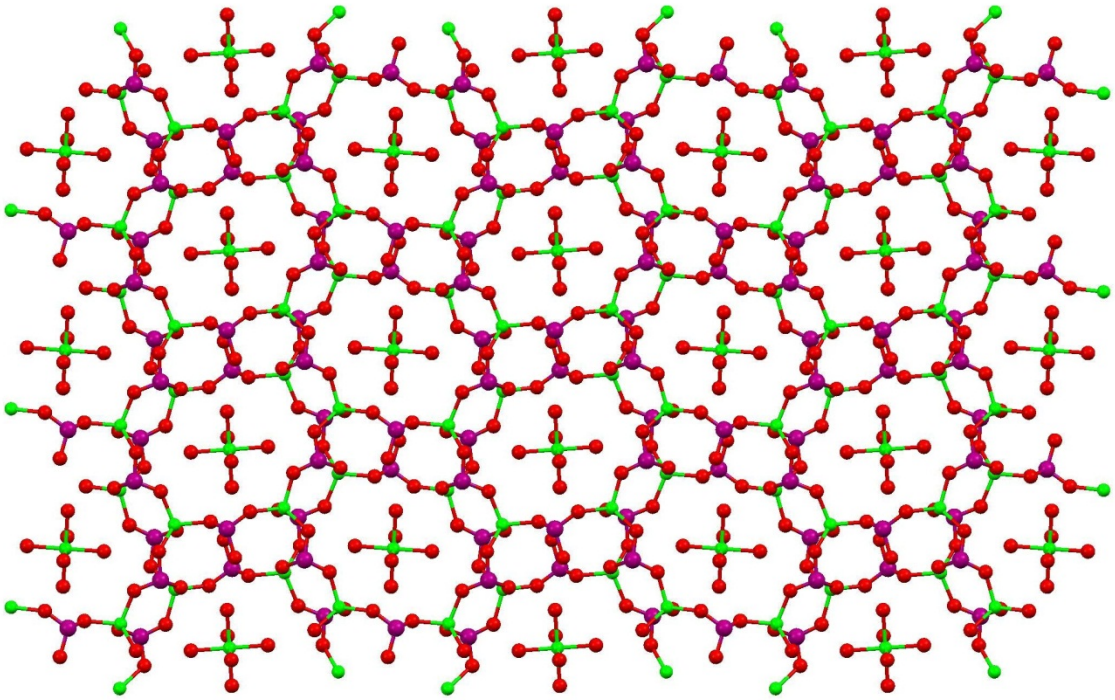

Figure 40. ZAC-6 viewed down the *a*-axis showing the encapsulated $Zn(H_2O)_6^{2+}$ in the 24-membered rings.

The double layers are connected together by a pair of symmetry independent bisphosphonic acid linkers; one linker is fully deprotonated and the other has one proton per phosphonic acid group. Figure 41 shows that due to the corrugation of the layer, the fully deprotonated ligand is in a normal alkyl chain conformation and the partially deprotonated ligand is disordered over two positions due to a distortion in the torsional angles of the central carbon atoms.

The 1-D channels which run along the *a*-axis that are formed by the 24-membered rings contain the $Zn(H_2O)_6^{2+}$ ions as well as one water molecule and one acetic acid molecule.

Identical reaction conditions with supplementation of H_4L4 and H_4L5 for H_4L6 results in the production of ZAC-4 and ZAC-5 which have an identical topology to that of ZAC-6. ZAC-5's parameters have not been finalized and are presented in the space group *P*1 (No. 1). ZAC-4 crystallizes in the space group $P2_1/c$ (No. 15) and does not contain acetic acid. Figure 42 show side by side comparisons of ZAC-4 and ZAC-6.

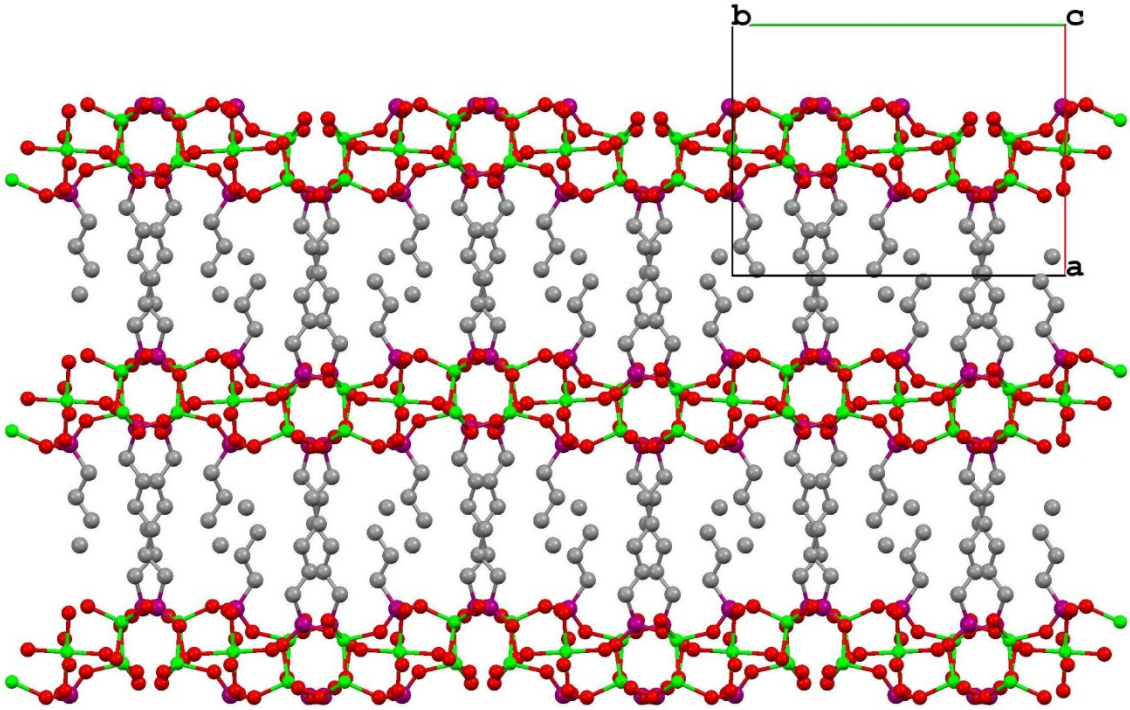

Figure 41. ZAC-6 viewed down the *c*-axis. Note how the corrugation in the layers results in one alkyl chain being in a normal conformation and the other being disordered over two positions due to a distortion in the chain.

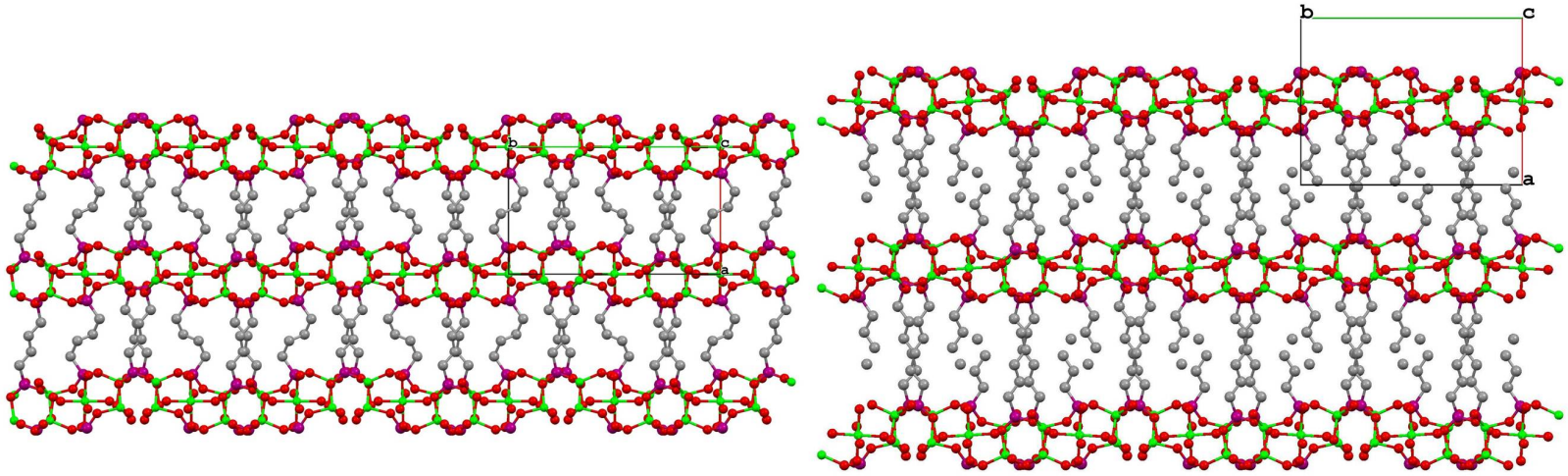

Figure 42. ZAC-4 (left) and ZAC-6 (right) viewed down the *c*-axis.

Zinc Alkyl Layer (ZAL-5,6)

ZAL-5 and ZAL-6 are not isoreticular compounds; however, both of these compounds are stuffed pillared compounds of zinc alkylbisphosphonates so they have been combined together for this section. They are synthesized via identical methods with only the ligand differing.

ZAL-5 consists of 2-D inorganic sheets which are pillared by the H_4L5 ligand to form a 3-D stuffed pillared compound. Figure 43 shows the asymmetric unit which contains one zinc atom and half of a fully deprotonated ligand. ZAL-5 crystallizes in the space group *C*2/*c* (No. 15) with the cell parameters given in Table 7. Bond lengths and angles are given in Table 13.

The Zn(1) center is connected to eight symmetry related Zn(1) atoms through O-P-O bridges and one additional Zn(1) through a pair of oxo-bridges. This connectivity results in a series of edge shared 4- 8- 10- and 12-membered rings which come together to form a complex 2-D layer in the *bc*-plane as shown in Figure 44. The layers are cross-linked by the L5 linker completing the 3-D framework as shown in Figure 45 as viewed down the *b*-axis.

ZAL-6 consists of 2-D inorganic sheets which are pillared as well to form a 3-D stuffed layered compound. ZAL-6 crystallizes in the space group $P\bar{1}$ (No. 2) with the cell parameters given in Table 7. The asymmetric unit consists of three different tetrahedral zinc centers and one L6 and two half H_4L6 ligands. The whole ligand is fully deprotonated while the two half ligands each only have one proton per phosphonate. One of

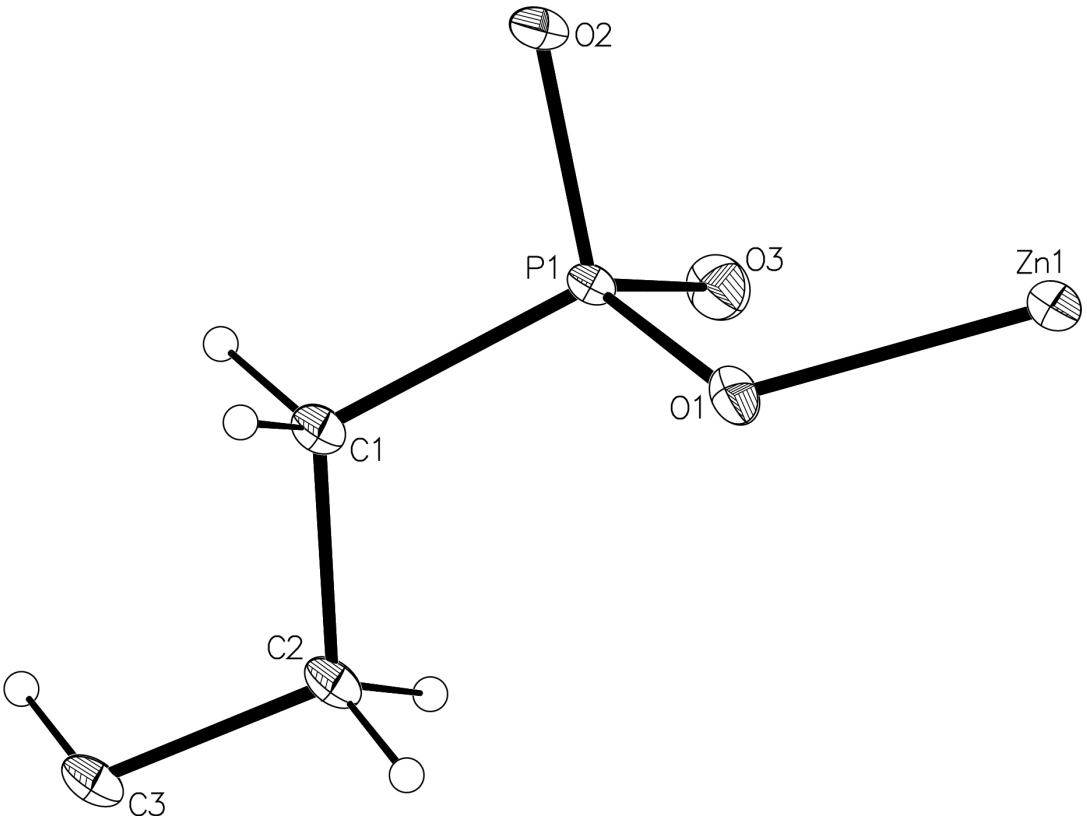

Figure 43. Thermal ellipsoid plot of ZAL-5.The thermal ellipsoids are at 50% probability.

Table 13. Selected bond lengths [Å] and angles [°] for ZAL-5.

Zn1-O3	1.878(2)	P1-O1	1.528(2)
Zn1-O1	1.9295(18)	P1-O2^{c}	1.5530(19)
Zn1-O2	1.9971(19)	P1-O3^{b}	1.517(2)
Zn1-O2^{a}	2.0031(18)	P1-C1	1.792(3)
O3-Zn1-O1	112.99(9)	O3^{b}-P1-O1	111.78(11)
O3-Zn1-O2^{a}	120.13(8)	O3^{b}-P1-O2^{c}	107.87(11)
O1-Zn1-O2^{a}	109.23(8)	O1-P1-O2^{c}	109.84(10)
O3-Zn1-O2	112.95(8)	O3^{b}-P1-C1	110.91(12)
O1-Zn1-O2	115.61(8)	O1-P1-C1	109.50(12)
O2^{a}-Zn1-O2	82.83(8)	O2^{c}-P1-C1	106.80(11)
P1-O1-Zn1	118.18(12)	Zn1^{a}-O2-Zn1	97.17(8)
P1^{c}-O2-Zn1^{a}	136.22(11)	P1^{d}-O3-Zn1	146.92(13)
P1^{c}-O2-Zn1	126.39(11)		

Symmetry transformations used to generate equivalent atoms: a: -x+1/2,-y+1/2,-z+1; b: x,-y,z-1/2; c: -x+1/2,-y-1/2,-z+1; d: x,-y,z+1/2

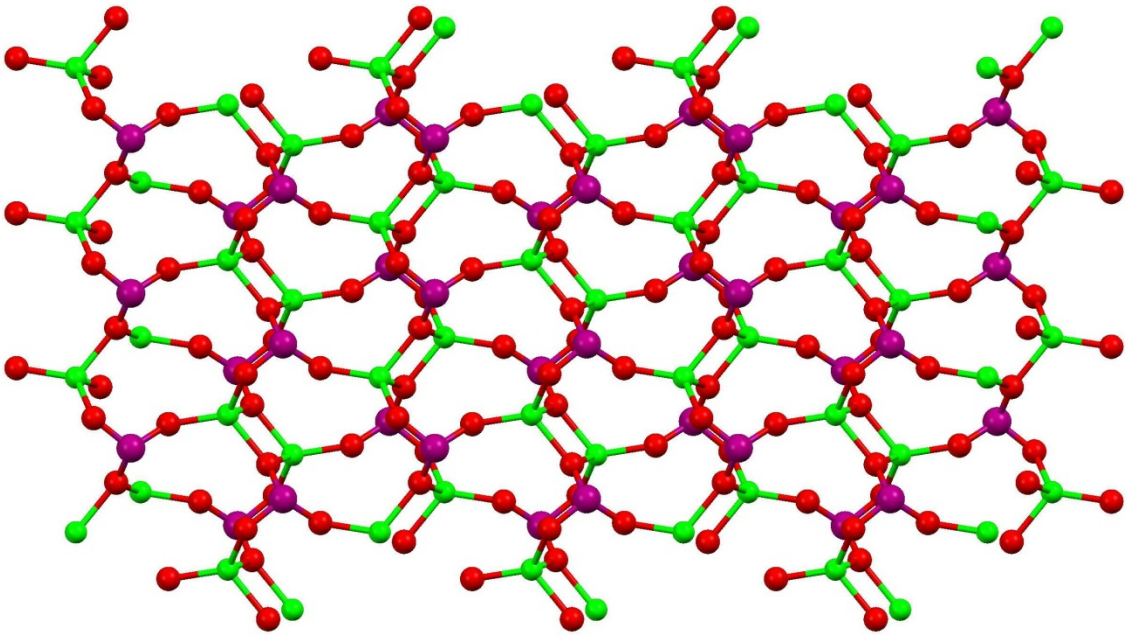

Figure 44. ZAL-5 viewed down the *a*-axis showing the 2-D layer.

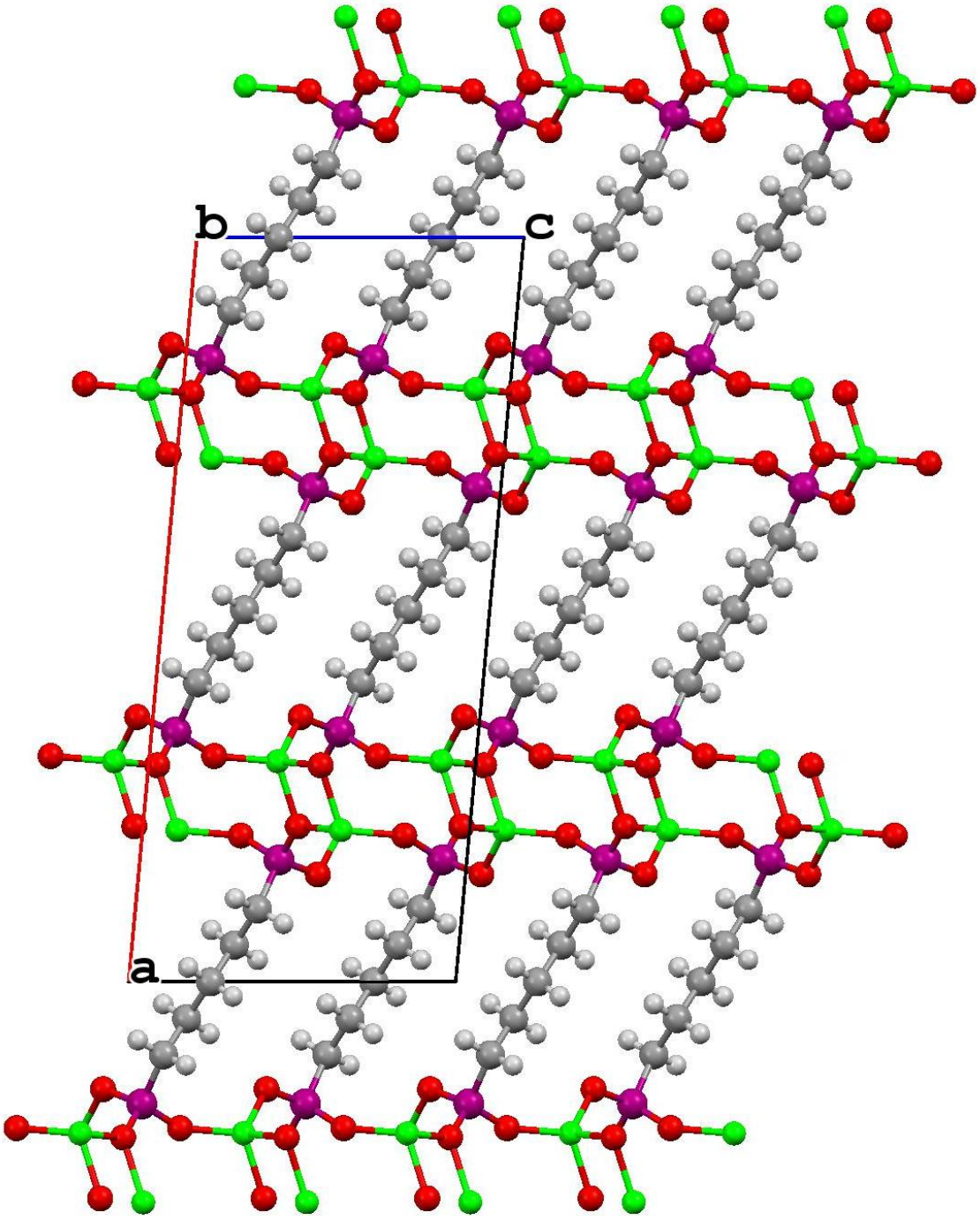

Figure 45. ZAL-5 viewed down the *b*-axis showing the ligand pillars linking together the 2-D sheets to form the 3-D network.

the half ligands is in a standard alkyl chain conformation, as is the fully deprotonated one and the other half ligand is kinked in a corkscrew manner as shown in Figure 46. The layer is constructed by 1-D chains of fused 8- and 10-memebered rings as shown in Figure 47 which are further bridged to form the 2-D sheet by pairs of O-P-O bridges as shown in Figures 48 and 49.

Discussion

Similar to our work with zinc, Zubieta and coworkers have reported a series of related vanadium compounds synthesized by systematically increasing the length of the alkyl spacers. They found that for n = 2 to 5 there are isoreticular structures in which the inorganic layers are identical, but the stacking between them varies slightly due to the conformation of the odd or even numbered chains. After n = 5, the structural type changes to that of pillared slab structures from n = 6 to 8; and for n = 9 the structure obtained is a condensed double layer. While the construction of the vanadyl frameworks has been noticeably different from that of the later transition metals due to the bonded oxide, it is interesting to note the similarities between the n = 3 to 5 compounds for V and Cu. In the copper phosphonate structures, a water molecule takes the place of the vanadyl oxygen atom, resulting in a similar coordination environment.

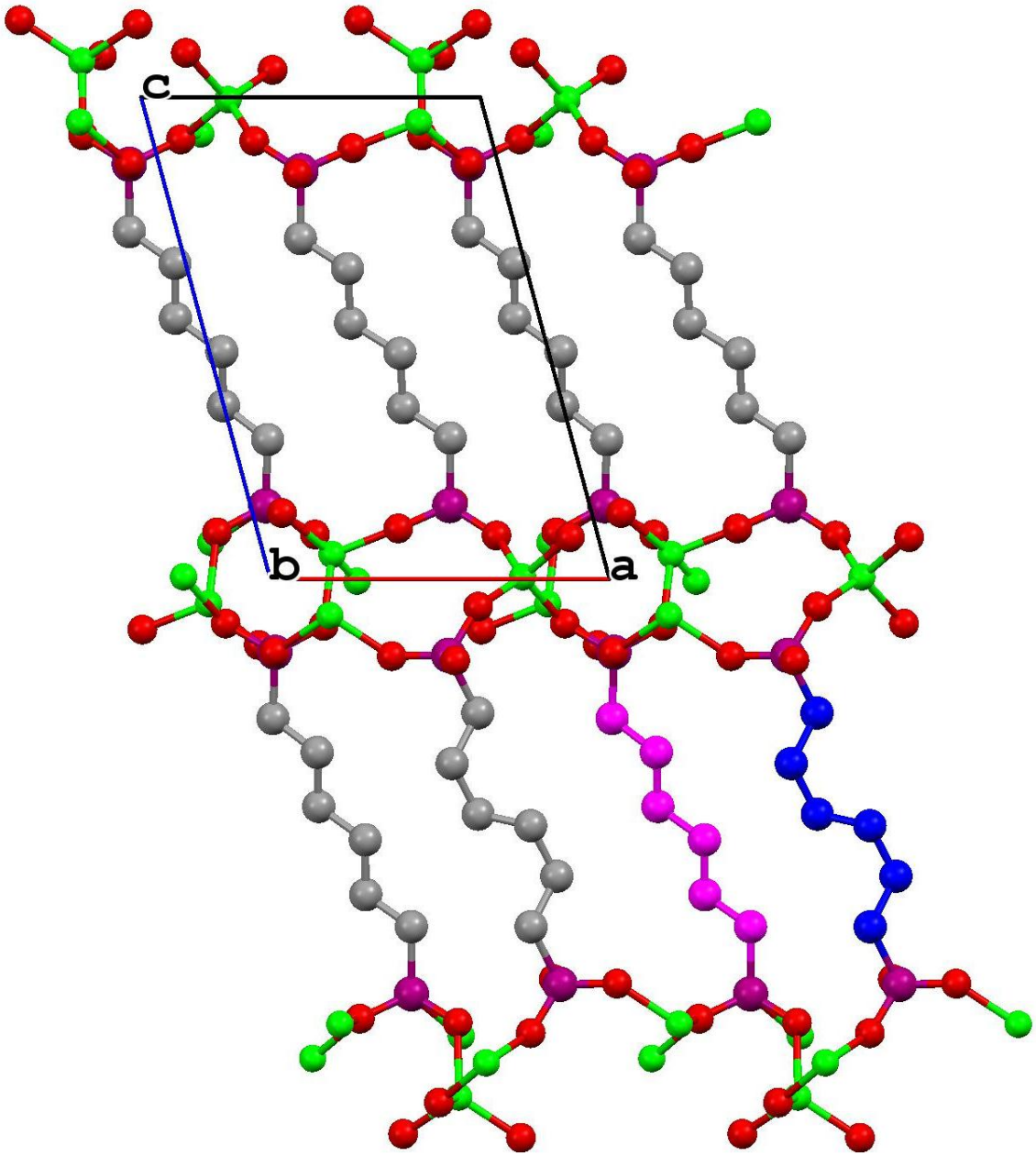

Figure 46. ZAL-6 viewed down the *b*-axis. Notice the two different conformations of the alkyl chain, normal (magenta) and kinked (blue).

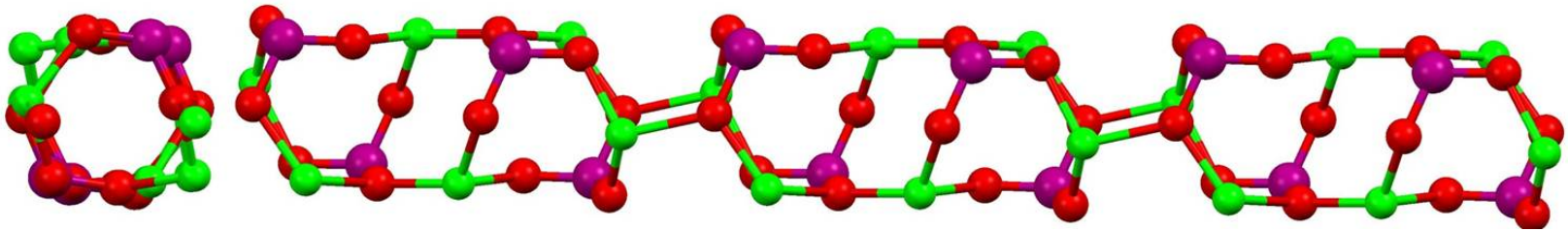

Figure 47. 1-D chain in ZAL-6 looking down the tube (left) and along the chain (right).

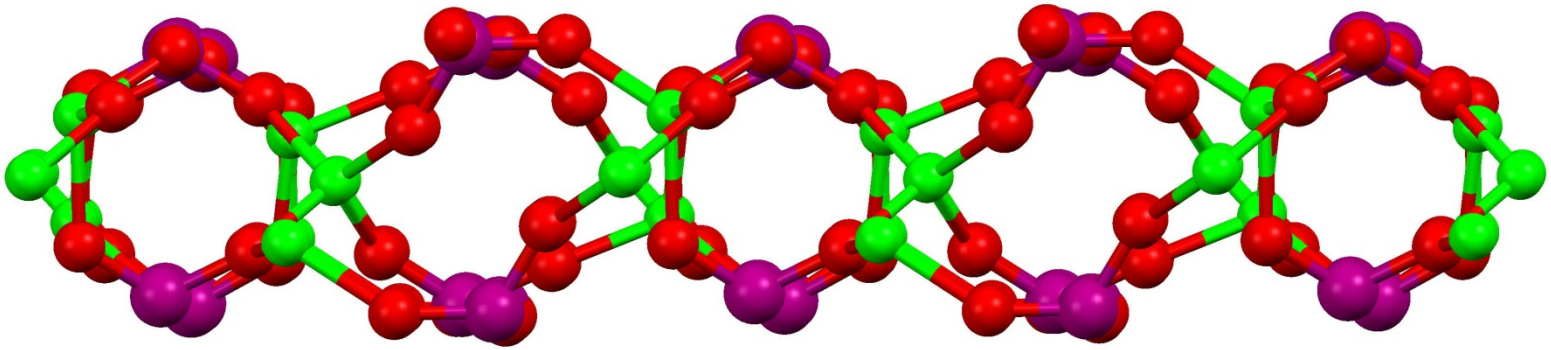

Figure 48. ZAL-6 viewed down the 1-D tubes showing the pairs of O-P-O bridges between neighboring chains.

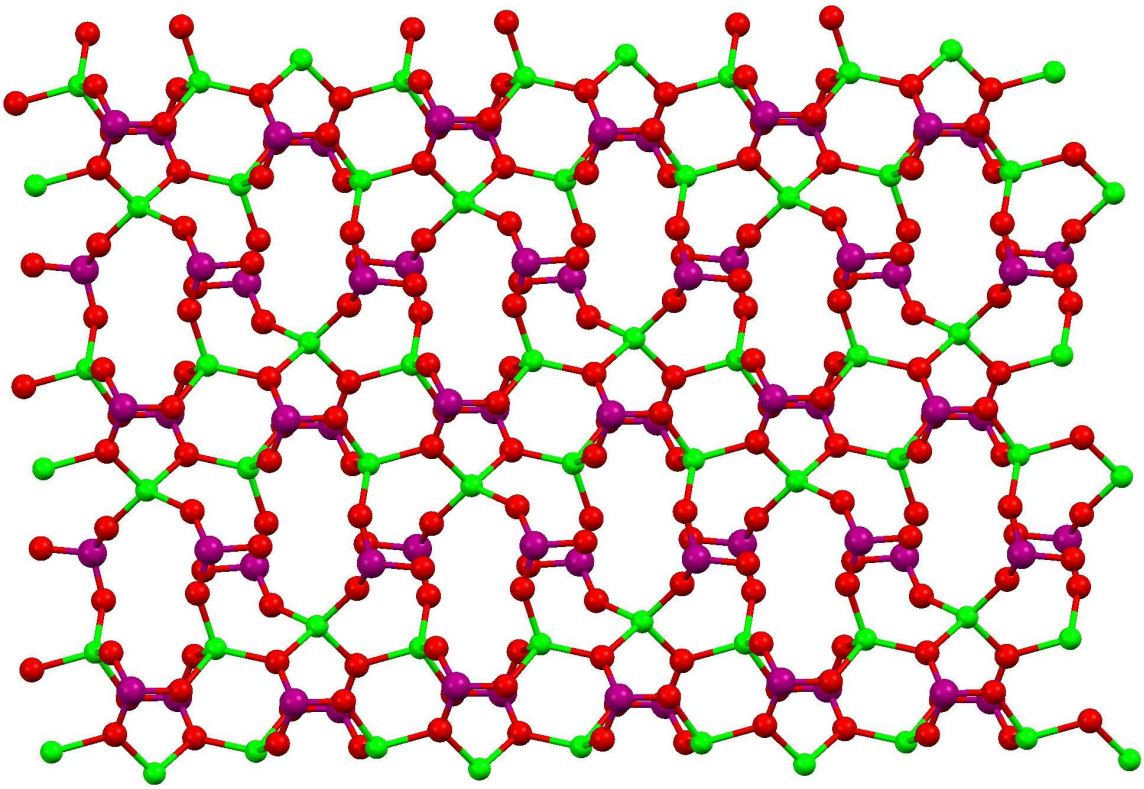

Figure 49. The 2-D layer of ZAL-6 viewed down the *a*-axis. Notice the 1-D tubes running left to right starting at the top and bridged by pairs of O-P-O groups to the neighboring chains.

Attfield and coworkers recently reported a series of gallium diphosphonates in which they attempted to systematically vary the chain length from n = 3 to 10. The results of their research combined with our own confirm that the structures of these compounds are quite diverse; however, identical reaction conditions can produce some materials which appear to be capable of isoreticular extension while others appear to be limited by the conformation of the ligands.

What our work has shown is that unlike the previous systematic investigations our results do not suggest that structural type is limited to the length of the alkyl linker (i.e. Zubieta's study where the structural types are grouped by chain length). We show here for example that the H_4L5 linker is involved in four different structural archetypes, ZAT, ZAS, ZAC, and ZAL. There are no instances of zinc H_4L5 structures in the literature to date, which suggests that the use of these alkylphosphonates has stalled in current research. The diversity of the structures we have presented here should be cause for reconsideration as to the usefulness of these flexible linkers.

One of the common features between these families is the inclusion of monodeprotonated phosphonic acid groups. This results in all of the compounds, except for ZAL-5, containing 1-D inorganic chain building units. In a few cases (ZAT, ZAC, and ZAL) these 1-D chains are further cross-linked to form layers; however, it is the 1-D chains which show some of the most unique structural diversity. The simplest of the chains are found in the ZAG family which contains corner-fused 8-membered rings. Stepping up in complexity are the ZAT chains which have edge fused 8-membered rings forming a ladder type arrangement. The ZAC family has 1-D chains which are formed

by edge fused 8-membered rings as well, except in this case the rings alternate between "chair" and "boat" conformation. The ZAS family has chains made of fused 12-membered rings. And lastly ZAL-6 has a mixture of fused 8- and 10-membered rings. Figure 50 shows a side by side comparison of all of these 1-D chains.

Several of these families contain ordered channels of hydrogen bonds which may be useful for proton conduction pathways; ZAT in particular may be useful for this purpose because the substitution of the octahedral metal may allow for the ability to tune proton conduction. The ZAG family has shown interesting properties under isostatic pressure (which is discussed in Chapter VI) which may lead to the development of new pressure switch or sensing materials.

It is interesting to note that in all of the presented structures, there exist tetrahedrally coordinated zinc centers. This fact leads to the presumption that there may be even more structural variations with zinc centers that are octahedral and even other coordinations.

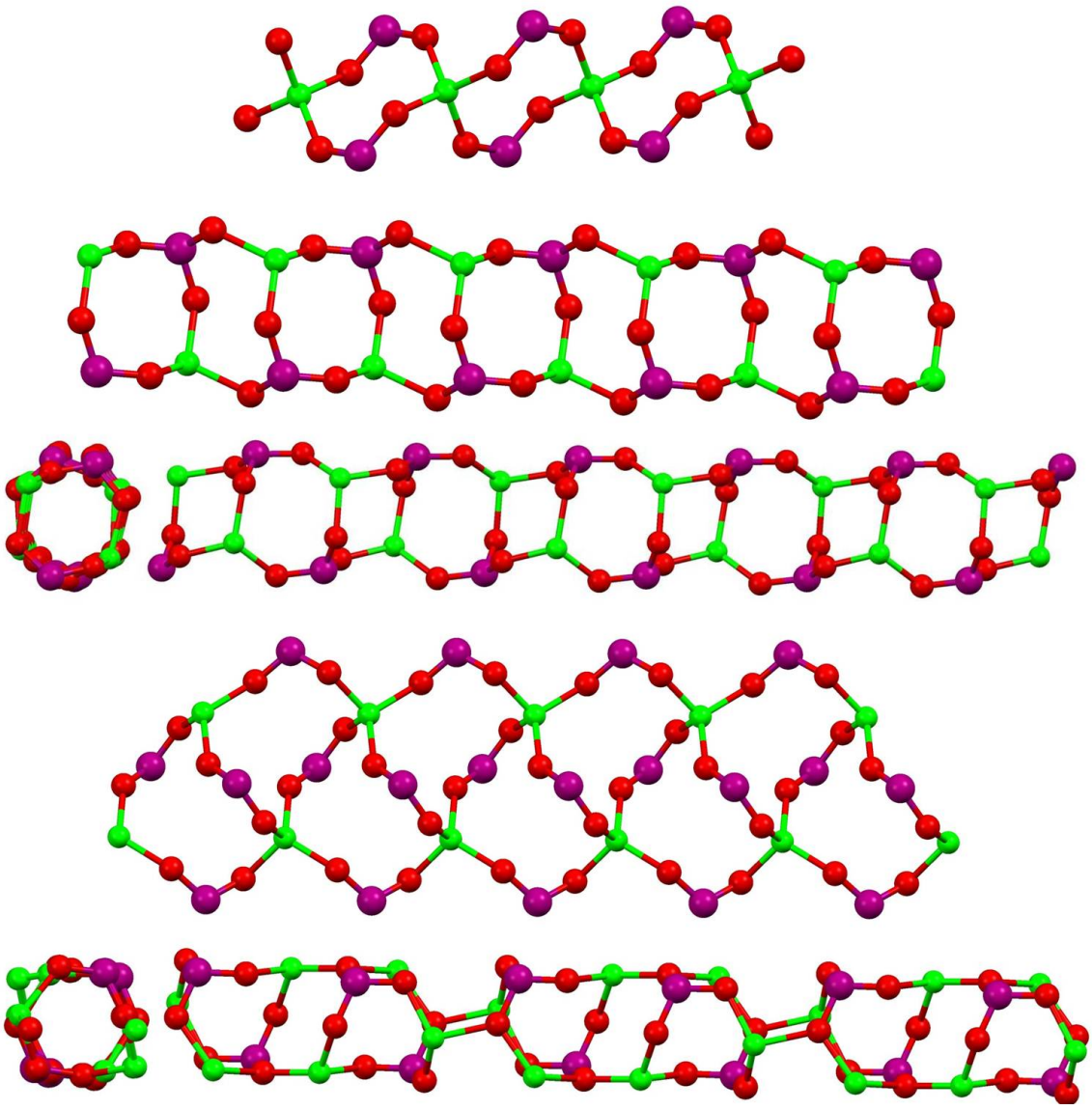

Figure 50. Comparison of the 1-D chain building units in ZAG, ZAT, ZAC, ZAS, and ZAL-6. (From top to bottom, respectively)

Conclusion

Rigid carboxylic and phosphonic acids have played an important role in the development of porous MOFs for gas storage and separation; however, the huge diversity of structures that can be obtained with alkylbisphosphonic acids suggests that the narrow framing of rigid ligands may be missing potentially useful materials. While permanent porosity may be a challenge with these materials, there exist a number of other potential applications in piezo- and thermofunctionality. Chapter VI will delve into the structure-property relationships of the ZAG family under high applied pressure.

CHAPTER V

STRUCTURAL CHANGES THROUGH THERMALLY INDUCED DEHYDRATION*

Introduction

As outlined in the previous chapters, we have dedicated over a decade to the research of phosphonate coordination chemistry.[9, 12] In this dissertation we have presented alkylphosphonates and iminophosphonates; however, there are many other types of ligands both rigid and flexible which have been utilized in the past. This chapter deals with recent work conducted utilizing BBMP.[97] In the past few years a number of compounds with similar ligand types have been published by the Clearfield group.[98] Work utilizing N-(phosphonmethyl)-aza-18-crown-6 ether resulted in macrocyclic leaflet compounds whose structure featured a central stem to which azacrown ethers are bonded.[99] Reaction of pyridylphosphonic acids provided insight into the effects of free pyridyl groups on the coordination environment of various divalent metals, Cu, Mn, Zn, and Sn. The Cu, Mn, and Zn reactions yielded compounds of different dimensionality, a 3D open framework copper complex, a 2D layered Mn complex in which there are two types of ligated Mn atoms, and a dimeric Zn molecule with ZnO_2Cl_2 tetrahedra and a $Zn_2O_4P_2$ 8-membered ring core.[100] In some cases the pyridyl nitrogen atoms are protonated forming H-bonds to phosphonate oxygen atoms and together with PO-H hydrogen bonds form supramolecular structures. In contrast, Sn^{2+} alone resulted in a large variety of structural types including 1-D chains and 2-D layers depending on the nitrogen position on the pyridyl ring.[65]

---

*Zon, J.; Kong, D.; Gagnon, K.; Perry, H.; Holliness, L.; Clearfield, A., *Dalton Transactions* **2010**, *39* (45), 11008-11018. – Reproduced by permission from The Royal Society of Chemistry. http://pubs.rsc.org/en/content/articlelanding/2010/dt/c0dt00676a.

Work with both benzenediyl-1,4-bis(methylphosphonic acid) and bipiperidine-N,N'-bis(methylphosphonic acid) yielded 3D layered compounds with Co^{2+} in which the layers are crosslinked by the organic linkers.[69]

Some related derivatives are the ligand BBMP and 1,3,5-tris(methylphosphonic acid) (BTMP) which are two conformationally flexible ligands. The crystal structure of BTMP has been determined by Jaffres et al.[101] The molecule surprisingly has all three methyl phosphonic acid groups located on the same side of the benzene ring. Also, this conformation results in formation of a dimer which leads to an uneven distribution of the protons. The BBMP ligand was recently synthesized and utilized in the creation of two isostructural compounds with Co^{2+} and Mn^{2+} and one additional compound with Cu^{2+}. This chapter will discuss the Co^{2+} and Mn^{2+} compounds in detail.

With the recent attractiveness of magnetic switch and sensor materials, there has been an increase in the research of magnetic materials which have properties that are sensitive to external stimuli, such as temperature and pressure.[42-45, 102] Very subtle changes to molecule structure, including packing, desolvation, and change in coordination environment can effectively modify the magnetic properties of a coordination polymer.[49, 103-107] One of the most attractive methods for causing changes the magnetic properties of a material is to induce changes in the dimensionality of the material.[108-110] (i.e. changing from a 0-D to 1-D or 2-D material, etc.). One major problem this method is that large changes in structure typically result in destruction of crystallinity, so determining the result of the structural transition is not straight-forward. There have been a few studies which have successfully managed single-crystal-to-single-crystal transfor-

mations, and thus have had successful structural analysis;[46, 110-113] there have been several other studies which have utilized PXRD to follow the structural transformation.[114]

In this chapter we present two isostructural compounds made with BBMP, one with Co^{2+} and one with Mn^{2+}. The Co compound undergoes a two stage dehydration which has been followed via single crystal X-ray diffraction. The Co compound has had its magnetic properties probed at each state of hydration.

Experimental

Synthesis of CoBBMP-4H_2O and MnBBMP-4H_2O M($HO_3PC_{14}H_{12}PO_3H$)(H_2O)$_4$·2H_2O

These preparations were carried out in the same way. The metal perchlorates, M(ClO_4)$_2$·6H_2O, 0.5 mmol were dissolved in 1 ml of water. BBMP (0.5 mmol) was dissolved in a minimum of ethanol and 1 ml of water added. Trimethylamine, as 40% water solution, was added dropwise until the pH was 5.0. The metal perchlorate solution was then added and the mixture stirred for 12 h. This mixture was then heated at 90–100 ◦C for 24 h in a PTFE lined pressure vessel. The yield was usually about 0.15 g or ~65%.

Single Crystal X-ray Diffraction

Data were collected at 110 K on a Bruker Smart CCD-1000 platform diffractometer equipped with Mo-Kα (λ = 0.71073 Å) radiation for the as synthesized Co and MnBBMP-4H_2O structures. Data collection and reduction were performed as outlined in the introduction.

Data for the dehydrated structures were collected on a modified Bruker APEX-II diffractometer at the ALS, LBNL (λ = 0.77490 Å). Data for CoBBMP-2H_2O were collected while heating a crystal of CoBBMP-4H_2O to 400 K on an Oxford Systems cryostream. CoBBMP-4H_2O was mounted at 100 K on a MiTeGen kapton pin and was heated to 400 K at a rate of 150 K/hr. Data were not collected at 400 K but actually closer to 380 K utilizing a hemisphere of data in 540 frames taken at 1.0 ° intervals in ω with an exposure time of 1 sec/frame. Data for CoBBMP was collected at 400 K utilizing the same parameters. CoBBMP-4H_2O was mounted on a MiTeGen kapton pin at 400 K and held for 30 minutes before the start of data collection. The crystallographic data for these compounds are summarized in Table 14.

Magnetic Measurements

Magnetic susceptibility measurements were performed on polycrystalline samples at 1000 Oe in a plastic bag. Several measurements were performed on a single sample of CoBBMP-4H_2O. The first set of measurements was run over the temperature range of 2 – 300K. Next, the sample was heated to 350 K before being cooled to 2 K while measuring. Then the sample was heated to 400 K before being cooled to 2 K. After this, the sample was removed and allowed to rehydrate. The sample was reloaded into a gel capsule and measurements were rerun over the temperature range of 2 – 300 K. The sample was heated to 375 K before being cooled to 2 K while measuring. Then the sample was finally heated to 400 K before being cooled one last time 2 K with measurement.

Table 14. Crystallographic data for MnBBMP-4H_2O, CoBBMP-4H_2O, CoBBMP-2H_2O, and CoBBMP.

Sample	**MnBBMP-4H_2O**	**CoBBMP-4H_2O**	**CoBBMP-2H_2O**	**CoBBMP**
Chemical formula	$MnO_{12}P_2C_{14}H_{26}$	$CoO_{12}P_2C_{14}H_{26}$	$Co_2O_{16}P_4C_{28}H_{26}$	$CoO_6P_2C_{14}H_{14}$
Formula mass	503.23	507.22	862.24	399.12
Crystal system	monoclinic	monoclinic	monoclinic	monoclinic
Space group	$P2_1/c$	$P2_1/c$	Pc	$P2_1/c$
λ (Å)	0.71073	0.71073	0.77490	0.77490
a (Å)	16.365(4)	16.268(5)	14.121(14)	13.749(15)
b (Å)	8.7437(19)	8.678(3)	8.604(8)	9.169(10)
c (Å)	14.866(3)	14.730(4)	14.573(14)	14.538(16)
β (deg.)	98.025(8)	97.952(5)	105.623(13)	111.891(1)
Z	4	4	2	4
V (Å^3)	2106.5(8)	2059.5	1705(3)	1701(3)
Temperature (K)	110(2)	110(2)	380(8)	400(2)
Density (g/cm^3)	1.587	1.636	1.680	1.559
Unique reflections	4728	3609	4622	2853
θ range (deg.)	1.26 - 27.52	2.53 - 25.00	3.03 - 25.00	2.98 - 30.26
R_1, wR_2 all data	0.00420, 0.1105	0.0424, 0.1113	0.1671, 0.3188	0.2037, 0.2937
S (GooF) all data	1.107	1.144	1.041	1.133
Max/min res. Dens. (e/Å^3)	1.607/-0.471	1.431/-0.616	2.977/-1.155	0.748/-0.520

*Data for CoBBMP-2H_2O and CoBBMP are rather poor due to the rapidly changing temperature over the course of the data collection, the twinning due to a change in symmetry, and crystal degradation.

Table 15. Some bond lengths [Å] for MnBBMP-4H_2O (left) and CoBBMP-4H_2O (right).

Mn1-O4	2.0942(14)	Co1-O1	2.029(2)
Mn1-O3W	2.1487(14)	Co1-O3W	2.067(2)
Mn1-O6W	2.1798(2)	Co1-O5W	2.069(2)
Mn1-O4W	2.1808(15)	Co1-O4W	2.098(2)
Mn1-O1	2.2050(14)	Co1-O4	2.157(2)
Mn1-O5W	2.2842(15)	Co1-O6W	2.162(2)
P1-O1	1.5183(14)	P1-O1	1.498(2)
P1-O2	1.5796(14)	P1-O2	1.576(2)
P1-O3	1.5072(14)	P1-O3	1.526(2)
P1-C1	1.808(2)	P1-C1	1.814(3)
P2-O4	1.4996(14)	P2-O4	1.520(2)
P2-O5	1.5739(14)	P2-O5	1.579(2)
P2-O6	1.5246(14)	P2-O6	1.502(2)
P2-C3	1.808(2)	P2-C5	1.805(3)

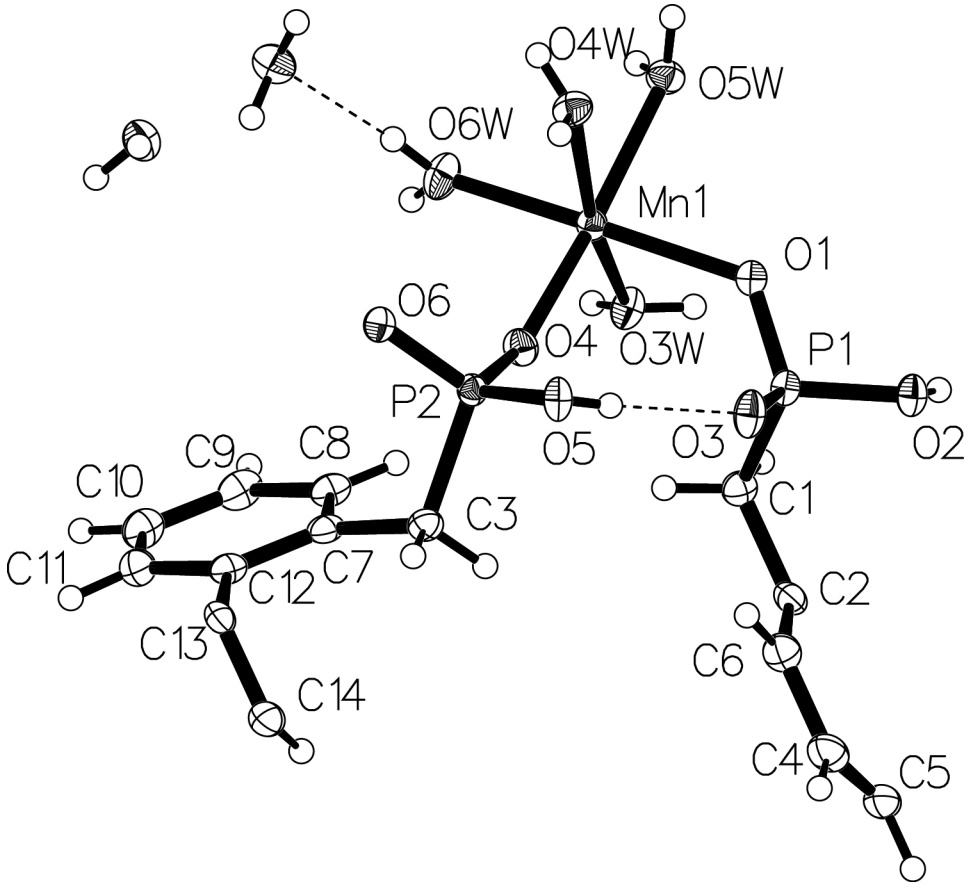

Figure 51. Thermal ellipsoid plot of MnBBMP-4H_2O.The thermal ellipsoids are at 50% probability.

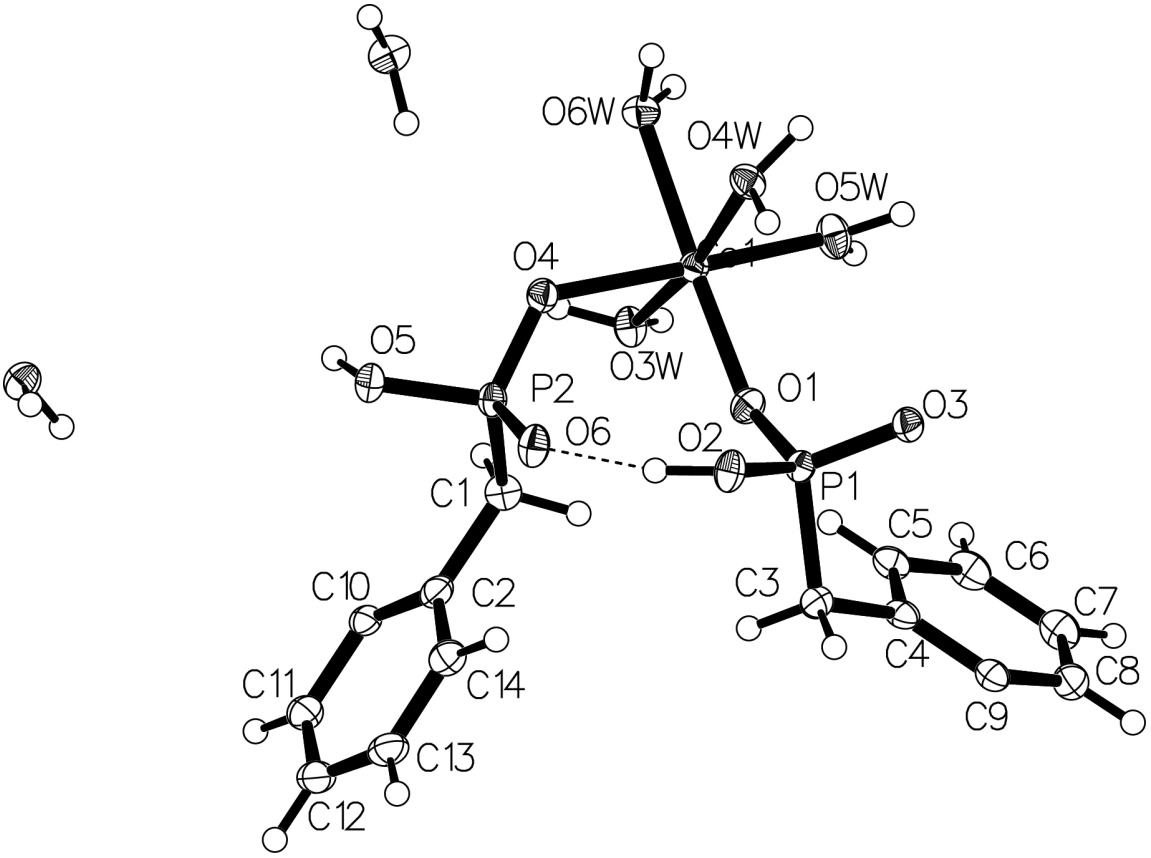

Figure 52. Thermal ellipsoid plot of CoBBMP-4H_2O.The thermal ellipsoids are at 50% probability.

Results

Structure of Mn and CoBBMP-4H_2O

The cobalt and manganese compounds are isostructural of composition $M(HO_3PC_{14}H_{12}PO_3H)(H_2O)_4 \cdot 2H_2O$. Bond distances and angles are given in Table 15. The space group is $P2_1/c$ with unit cell dimensions given in Table 14. The number scheme utilized in structure solution is provided in Figure 51 (Mn) and Figure 52 (Co). The M^{2+} is six coordinate being bonded to two phosphonate groups, through one oxygen atom from each group, and four water molecules.

The phenyl rings are rotated about each other at an angle of 74 degrees allowing the biphenyl group to bridge across cobalt ions. This arrangement results in ligand bridged rows of M^{2+} chains running parallel to the *b*-axis (Figure 53) and separating the metal atoms the length of the *b*-axis. The chains have three of their four water molecules pointing alternately up and down in the *c*-axis direction. This arrangement allows for extensive hydrogen bonding between water molecules in one chain with the non-bonded phosphonate oxgen atoms of another chain (Figure 54). There are also a number of hydrogen bonds between the water molecules and the protonated phosphonate oxygen atoms and also between water molecules. The bunching of the phosphonate groups towards each other pushes the phenyl rings to the outside creating a double layer of phenyl rings which are rather close, enough to develop π-π interactions, further aiding to create a stable supramolecular structure. The two columns of phenyl rings in the center of the

unit cell (Figure 54) constitute a hydrophobic region wheras the water molecules around the M^{2+} create a hydrophilic region.

The Co-O bond distances have two short (2.029(2), 2.067(2) Å), two medium length (2.096(2) and 2.098(2) Å), and two long (2.157(2) and 2.161(2) Å) values (Table 15). The same sequence holds for the Mn structure but with slightly larger M-O values due to the increased size of Mn^{2+} (Table 15). In the phosphonate tetrahedra, the protonated P-O distances are longer than the other P-O bond distances as is common for partially protonated phosphonate groups. The shortest hydrogen bonds are between the phosphonate groups as donor and acceptor (O5-H···O3, 2.557(3) Å and O2-H···O6, 2.566(3) Å).

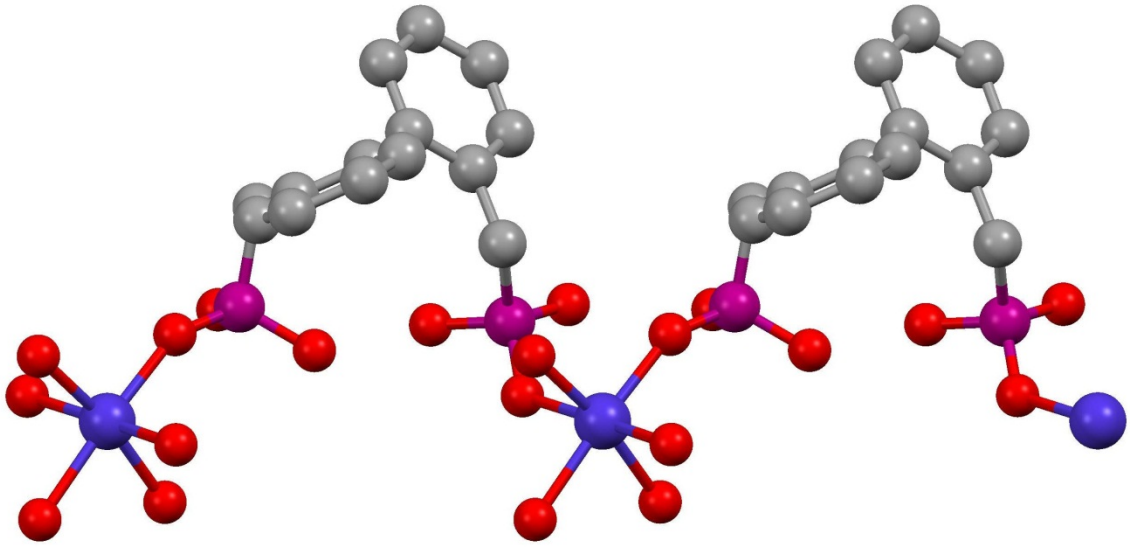

Figure 53. Representation of CoBBMP-4H_2O chains running along the *b*-axis showing the ligand bridged 0-D cobalt octahedra.

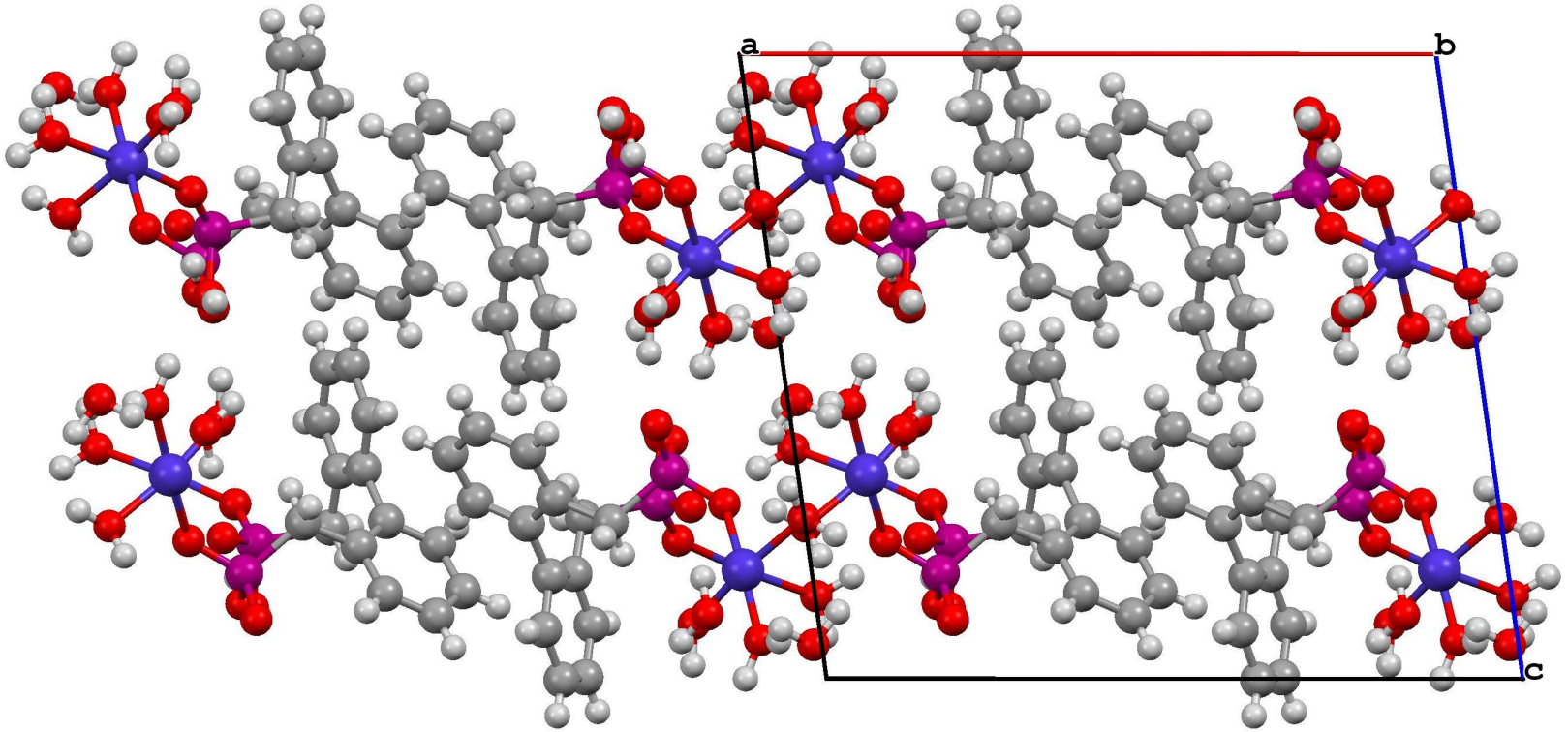

Figure 54. The unit cell of CoBBMP-4H_2O as viewed down the *b*-axis. This shows the arrangement of the hydrogen bonded array between phosphonic acid groups and water molecules in the *bc*-plane. Also note the alternating array of hydrophobic and hydrophilic groups from left to right along the *a*-axis

Thermal Analysis

Because of the water content of CoBBMP-4H_2O it was of interest to determine the weight losses upon heating. In the case of the CoBBMP-4H_2O compound the TGA was run at both 1 °C and 10 °C per minute (Figure 55). Both runs gave much the same result. At a low temperature of 57.9 °C, 3.8 H_2O were lost (10 °C/min) as opposed to 3.7 H_2O at 49.1 °C (1 °C/min). Out of a total of six water molecules in the compound the successive water losses were, for the 1 and 10 °C heating rates, respectively, 5.8, 104.6 °C; 5.6, 91 °C; 6.9, 340.4 °C; 6.9, 350.4 °C. It is likely that over 1 mol of H_2O was lost as adsorbed surface water to amount to approximately 4 mol water lost at 104.6 °C and 6 mol water lost by 350 °C. This is unusual as there are two interstitial water molecules and four coordinated water molecules, meaning that two coordinated waters and the interstitial waters are lost at the same temperature and rather easily. The remaining two coordinated waters remain up to 350 °C. Another sample was heated at the rate of 1 °C/min to 200 °C and held at this temperature for 30 min. The total weight loss was 20.72% or the equivalent of 5.8 H_2O or 6 mols of water. The compound was now bright purple indicating a change of coordination from six to four. On standing overnight the original pink color was restored. The dehydration is reversible.

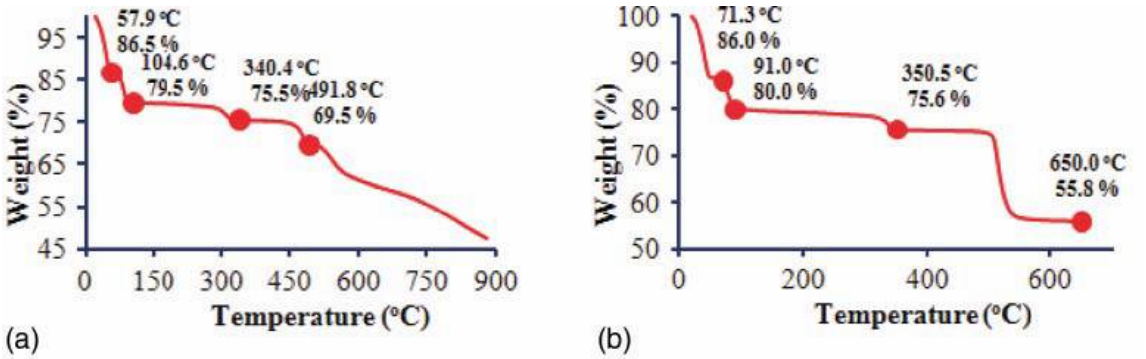

Figure 55. Thermogravimetric analysis curves for CoBBMP-4H_2O run at 10 °C/min (A) and at 1 °C/min (B).

Structure of CoBBMP-2H_2O

The structure of the partially dehydrated CoBBMP-2H_2O compound was determined serendipitously during an experiment to fully dehydrate the compound. Bond distances are given in Table 16. The space group lowers to *Pc* with unit cell dimensions given in Table 14. Figure 56 shows the asymmetric unit and atom labeling scheme. The Co^{2+} is still six coordinate; however, it is bonded to four oxygen atoms from phosphonate groups and two water molecules. There are now two symmetry independent Co centers. Co1 is bridged to Co2 through a pair of oxo-bridges in one direction and a pair of O-P-O bridges in the other direction. This arrangement results in a 1-D inorganic chain of alternating 4- and 8-membered rings. The phenyl rings are rotated about each other at an angle of 74 degrees allowing the biphenyl group to align as pendant groups on the top and bottom of the chain. Each of the two phosphonate groups are monoprotonated, one group provides one oxygen atom to the Co1-Co2 oxo-bridge, the other group provides the Co2-Co1 O-P-O bridge. The 1-D chains continue to run along the *b*-axis as shown in Figure 57. The coordinate water molecules are on Co1 and Co2. The phosphonate oxygen atoms are square planar coordinate on each Co center with the two water molecules filling out the coordination sphere of each metal center making them octahedral. The Co1 and Co2 octahedra are slightly canted (~7 °) with respect to one another. The arrangement of the water molecules and phosphonate oxygen atoms allows for an extended hydrogen bonded array creating a 2-D supramolecular inorganic sheet in the *bc*-plane as shown in Figure 58.

Table 16. Selected bond lengths [Å] for CoBBMP-2H_2O.

Co1-O8	2.004(8)	Co2-O2	2.062(15)
Co1-O3	2.161(15)	Co2-O4W	2.133(17)
Co1-O10[a]	2.223(14)	Co2-O9	2.153(15)
Co1-O6	2.197(14)	Co2-O3W	2.148(19)
Co1-O2W	2.236(15)	Co2-O6[b]	2.174(13)
Co1-O1W	2.268(16)	Co2-O10	2.337(14)
P1-O1	1.558(16)	P2-O4	1.613(15)
P1-O2	1.518(15)	P2-O5	1.519(2)
P1-O3	1.520(15)	P2-O6	1.521(2)
P1-C1	1.78(2)	P2-C14	1.83(2)
P3-O7	1.569(2)	P4-O10	1.455(14)
P3-O8	1.520(2)	P4-O11	1.490(16)
P3-O9	1.536(16)	P4-O12	1.546(17)
P3-C15	1.75(3)	P4-C28	1.82(2)

Symmetry transformations used to generate equivalent atoms: a: x, y-1, z;
b: x, y+1, z

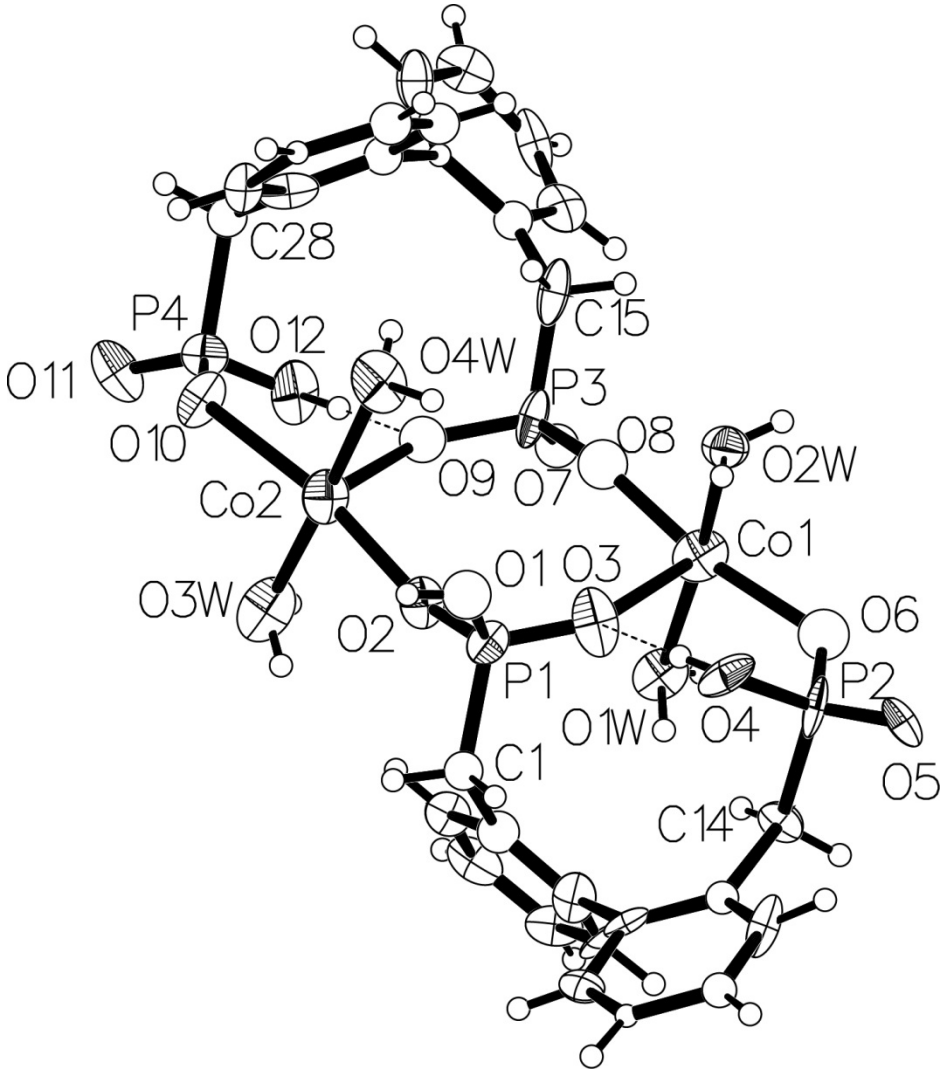

Figure 56. Thermal ellipsoid plot of CoBBMP-2H_2O.The thermal ellipsoids are at 50% probability.

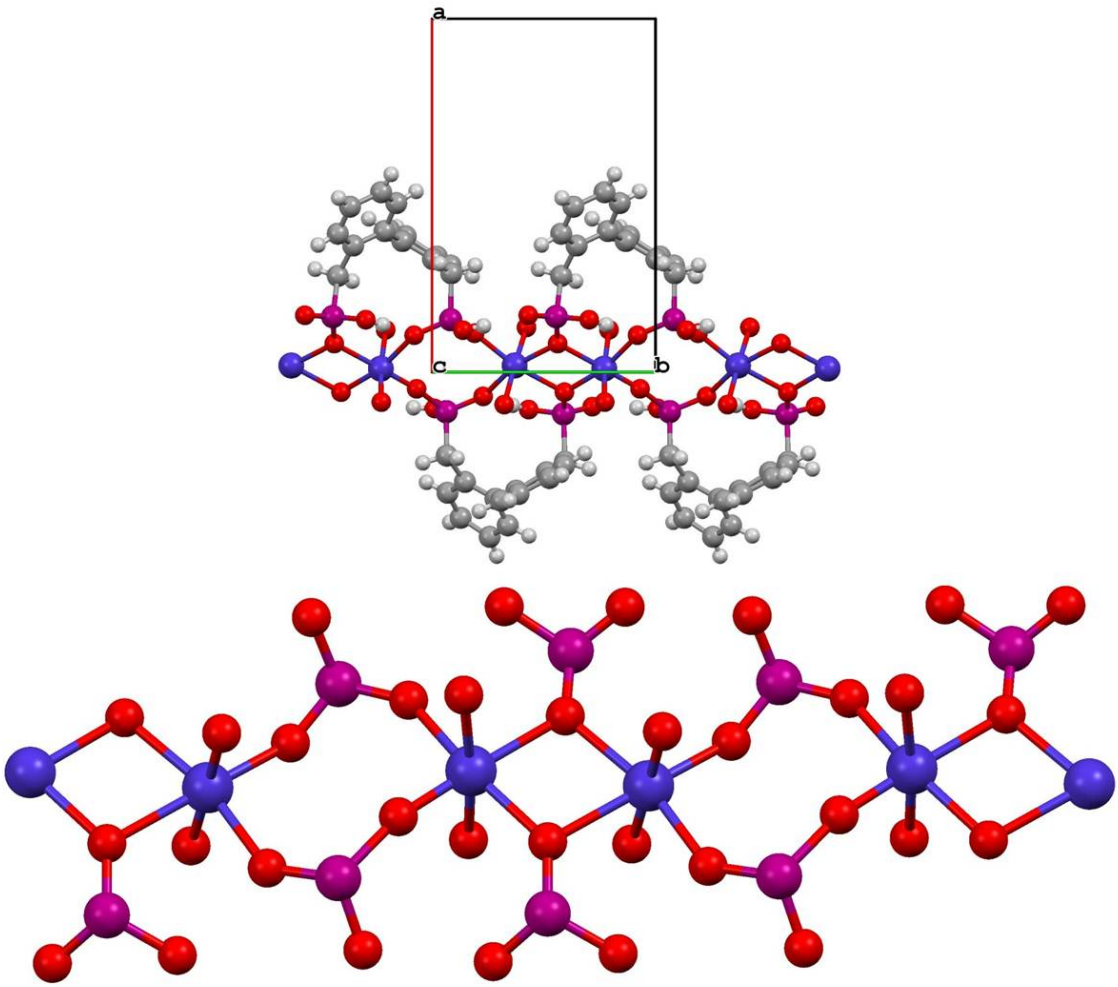

Figure 57. CoBBMP-2H_2O showing the pendant ligand arrangement as well as the composition of the 1-D inorganic chain.

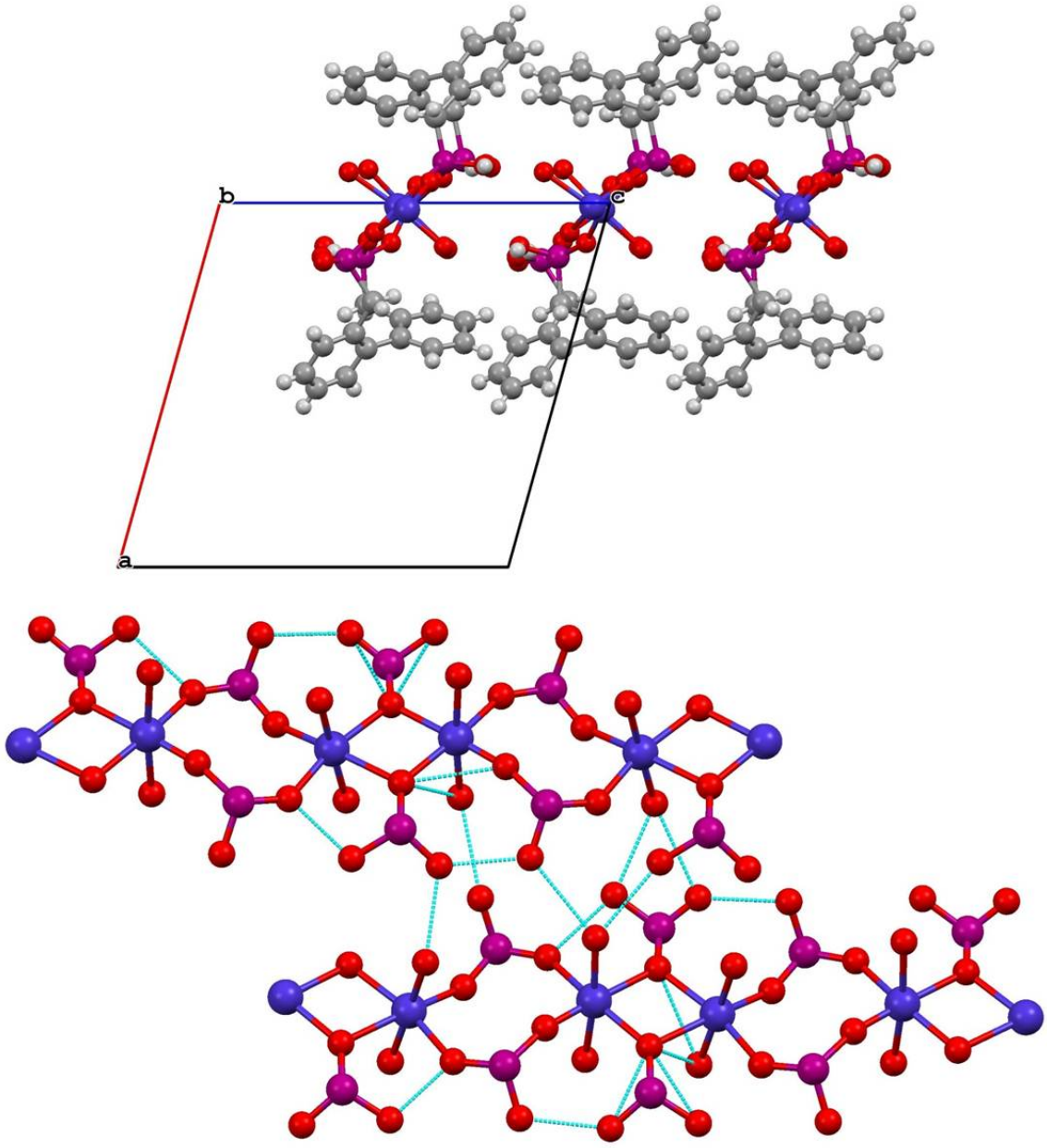

Figure 58. CoBBMP-2H_2O arrangement showing the neighboring 1-D chains as viewed down the *b*-axis (top) and top down showing a few of the hydrogen bonding interactions (bottom).

The Co1-O bond distances have two short (2.004(8), 2.161(15) Å), two medium length (2.223(14) and 2.197(14) Å), and two long (2.236(15) and 2.268(15) Å) values (Table 16). The Co2-O bond distances are not as easily divided. There is definitely one longer bond at 2.337(14) Å but the remainder all fall in the range of 2.062(15) – 2.174(13) Å as shown in Table 16. The confidence in these bond distances is rather low as the data for CoBBMP-2H_2O is rather poor given the nature of the experiment, the loss of symmetry and the resultant twinning; however, the connectivity is most likely correct and agrees rather well with the thermal analysis. The interstitial water molecules are completely gone as are two of the bound waters. The cobalt centers are also now directly bridged to each other as opposed to being isolated in the original structure. This should provide an interesting situation to study magnetically. CoBBMP-4H_2O is a 1-D chain with isolated 0-D inorganic units; after losing the two bound water molecules and the interstitial water molecules the coordination polymer becomes a 1-D chain which is composed of a 1-D inorganic unit.

Structure of CoBBMP

The structure of the fully dehydrated CoBBMP compound was determined via single-crystal-to-single-crystal dehydration at 400 K. The crystal was severely damaged during the experimental process in which it began to peel like a banana as shown in Figure 59. Despite this damage, the structure was determined with reasonable confidence in connectivity. Bond distances are given in Table 17. The symmetry of the system returned and the space group is once again $P2_1/c$ with unit cell dimensions given in Table 14. Figure 60 shows the asymmetric unit and atom labeling scheme.

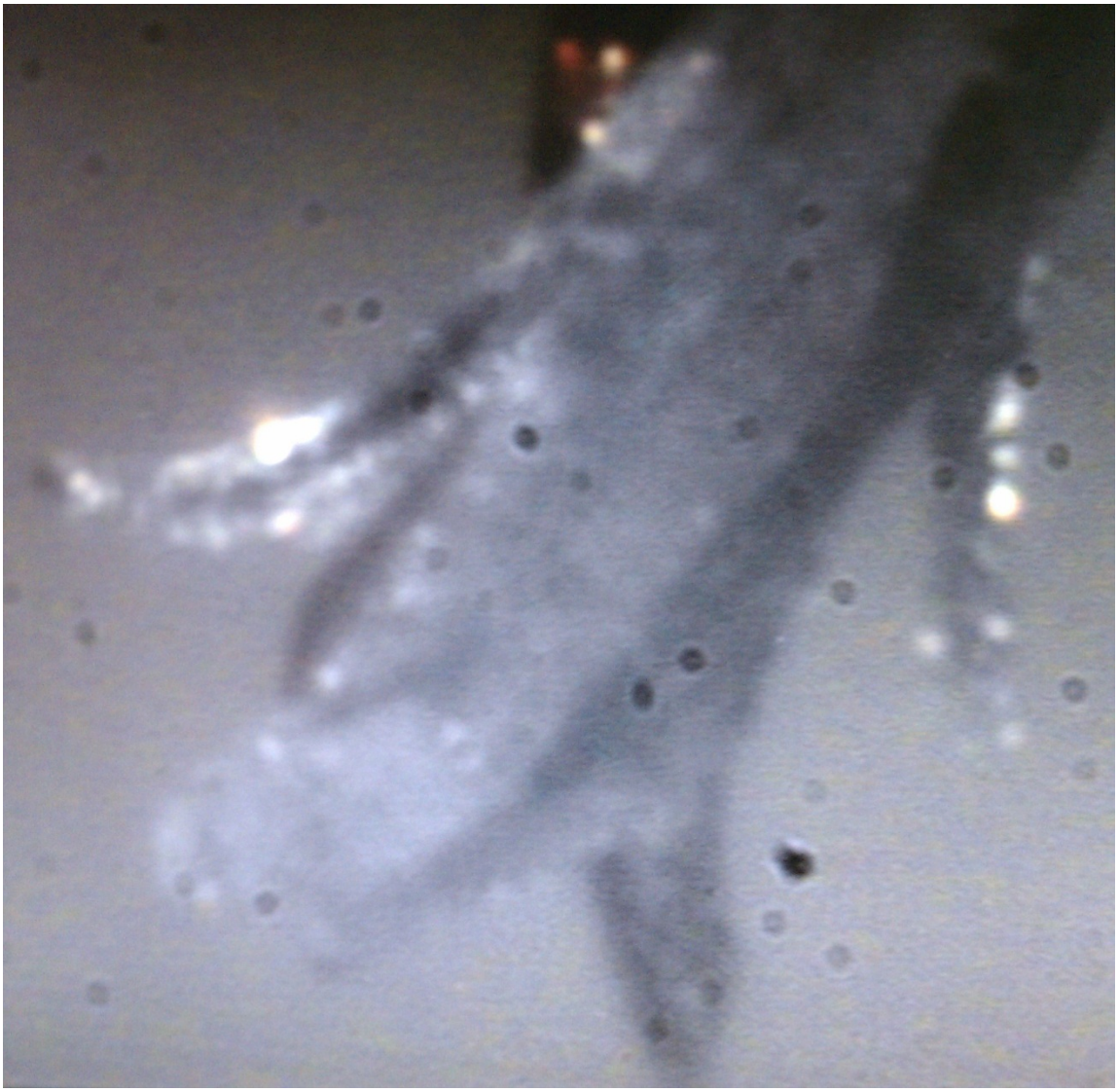

Figure 59. Photo of the crystal of CoBBMP after dehydration, which has begun to peel like a banana.

Table 17. Selected bond lengths [Å] for CoBBMP.

Co1-O2	1.983(8)	P2-O4	1.490(7)
Co1-O3	1.985(8)	P2-O5[a]	1.506(8)
Co1-O4	1.996(7)	P2-O6	1.564(7)
Co1-O5	2.018(8)	P2-C14[a]	1.779(13)
P1-O2	1.481(8)	P1-O1	1.574(8)
P1-O3[b]	1.481(7)	P1-C1	1.778(13)

Symmetry transformations used to generate equivalent atoms: a: -x+1,y+1/2,-z+1/2; b: -x+1,-y+1,-z

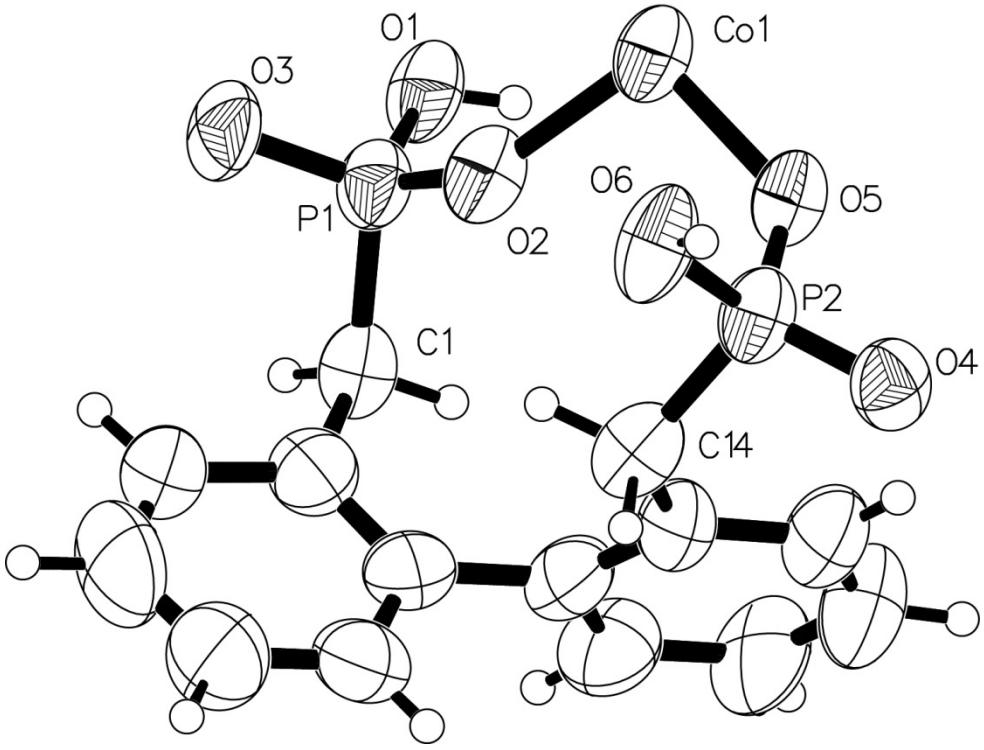

Figure 60. Thermal ellipsoid plot for CoBBMP.The thermal ellipsoid probability is at 50%.

The Co^{2+} has changed to four coordinate with only phosphonate oxygen atoms arranged in a tetrahedral fashion. There is one Co center in the asymmetric unit which is bridged to a symmetry related Co in one direction by a pair of O-P-O linkages and to two other symmetry related Co centers by single O-P-O bridges. This arrangement results in a 2-D inorganic sheet which is made up of 8- and 24-membered rings in the *bc*-plane. The 24-membered rings have four protonated phosphonate oxygen atoms protruding into the center of them as shown in Figure 61. The phenyl rings have reduced the angle they are rotated about each other by, to about 72 degrees, which is still surprisingly close to the original value of 74 degrees. The 2-D inorganic layer is decorated on its surfaces by the biphenyl ligands as shown in Figure 62.

The Co-O bond distances have two short (1.983(8), 1.985(8) Å) and two longer (1.996(7) and 2.018(8) Å) values (Table 17). The connectivity is most likely correct and agrees rather well with the thermal analysis. The change in coordination from octahedral to tetrahedral agrees well with the color change from pink to dark purple that is witnessed upon heating of the sample. The new coordination environment of the cobalt atoms should provide an interesting situation to study magnetically. CoBBMP-4H_2O is a 1-D chain with isolated 0-D inorganic units; after losing the two bound water molecules and the interstitial water molecules the coordination polymer becomes a 1-D chain which is built by a 1-D inorganic unit. Finally after losing the remaining two water molecules the system becomes a 2-D layered compound composed of a 2-D inorganic sheet of tetrahedral cobalt centers.

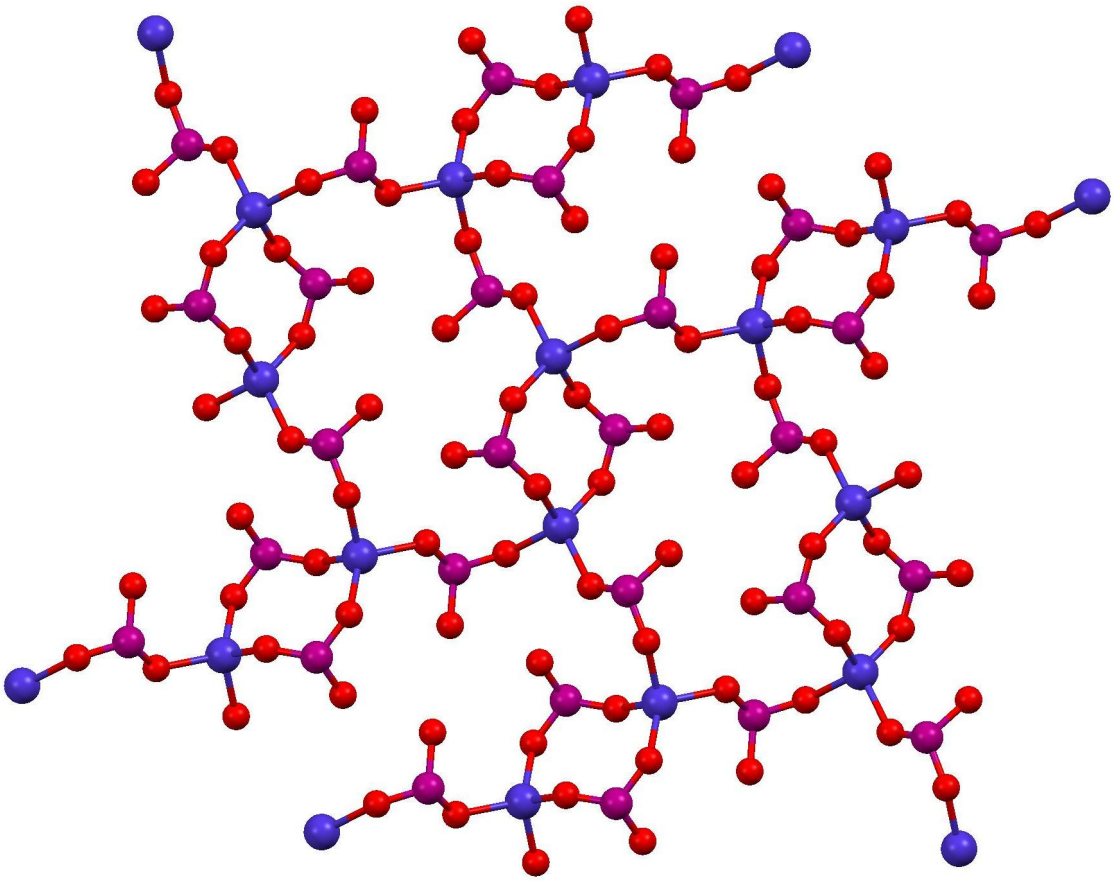

Figure 61. CoBBMP viewed perpendicular to the 2-D inorganic layer showing the fused 8- and 24- memebered rings.

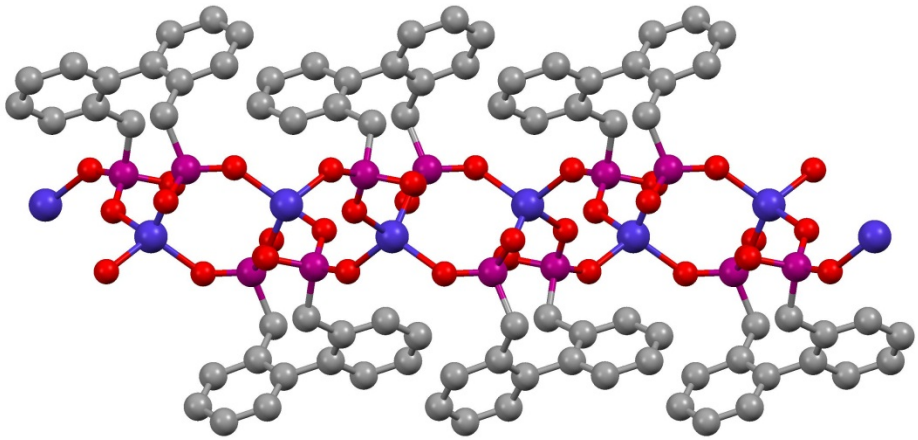

Figure 62. CoBBMP viewed down the *b*-axis showing the inorganic layer and how the biphenyl groups decorate the surface

Magnetic Measurements

CoBBMP-4H_2O

The value of χT at 300 K is 3.1 emu·K·mol^{-1} for CoBBMP-4H_2O (S = 3/2 and g = 2.7) (Figure 63), which is higher than the expected value for an isolated Co^{2+} ion with S = 3/2 and g = 2.0. ($\chi_{Co}T$ = 1.875 emu·K·mol^{-1}) which is not unexpected given the anisotropic nature of these ions due to spin-orbit coupling, which leads to g values greater than 2.[89] The χT value continuously decreases from room temperature and reaches a minimum of 1.9 emu·K·mol^{-1}. The temperature dependence of $1/\chi$ between 300 and 40 K approximates Curie-Weiss behavior with C = 3.4 emu·K·mol^{-1} and θ = -25 K. Field dependent magnetization at 1.8 K is fitted to a Brillouin function for spin S = 1/2 and g= 4.3 (Figure 64).

CoBBMP dehydrated at 350 K

The value of χT at 300 K is 3.3 emu·K·mol^{-1} for the sample (S = 3/2 and g = 2.7) (Figure 65), which is higher than expected for an isolated Co^{2+} ion with S = 3/2 and g = 2.0 ($\chi_{Co}T$ = 1.875 emu·K·mol^{-1}) which is not unexpected given the anisotropic nature of these ions due to spin orbit coupling, which leads to g values greater than 2. Differently than CoBBMP-4H_2O, χT decreases steadily to a minimum from room temperature to 18 K where it reaches a minimum at 2.4 emu·K·mol^{-1} before increasing slowly to a maximum at 2.99 emu·K·mol^{-1} at 2 K. This data has not been fit yet; however, it is clear that there is a positive value of the Weiss constant showing the presence of a ferromagnetic

component. The field dependent magnetization at 1.8 K deviates from a fit for S = 1/2, g = 4.3 and θ = 0.5 (Figure 66). Unfortunately, modeling is still required for this system and it has not been confirmed that this is the magnetic data for CoBBMP-$2H_2O$.

CoBBMP

The value of χT at 300 K is 2.5 emu·K·mol^{-1} for CoBBMP (S = 3/2 and g = 2.35) (Figure 67), which is higher than expected for an isolated Co^{2+} ion with S = 3/2 and g = 2.0 ($\chi_{Co}T$ = 1.875 emu·K·mol^{-1}). χ_m starts at 0.0085 emu/mol before raising to a maximum value of 0.2165 emu/mol at 3 K before dropping down to 0.2099 emu/mol at 2K. This data is fit rather well by Curie-Weiss law down to 4K with C = 2.6 emu·K·mol^{-1} and θ = -6.5 K. The negative sign of the Curie-Weiss constant indicates antiferromagnetic interactions between Co^{2+} centers. The field dependent magnetization at 1.8 K is fit up to 12000 Oe with parameters of S = 1/2, g = 4.3 emu·K·mol^{-1}, and θ = -6.5 K; however, the magnetization deviates positively with further applied field showing the antiferromagnetic interactions nicely. (Figure 68). One nice feature about this data is that the decrease in g and Curie constants are in favor of a change to T_d Co^{2+} centers.

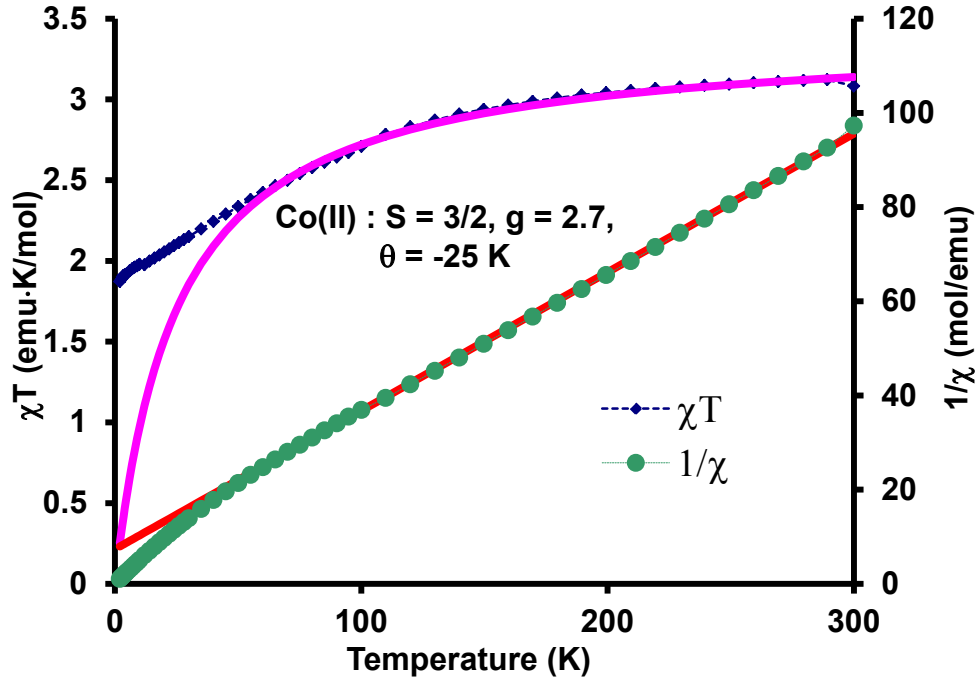

Figure 63. The temperature dependence of χT (♦) and of the inverse susceptibility $1/\chi$ (●) for CoBBMP-4H_2O. The solid line corresponds to the best fit to the Curie-Weiss law.

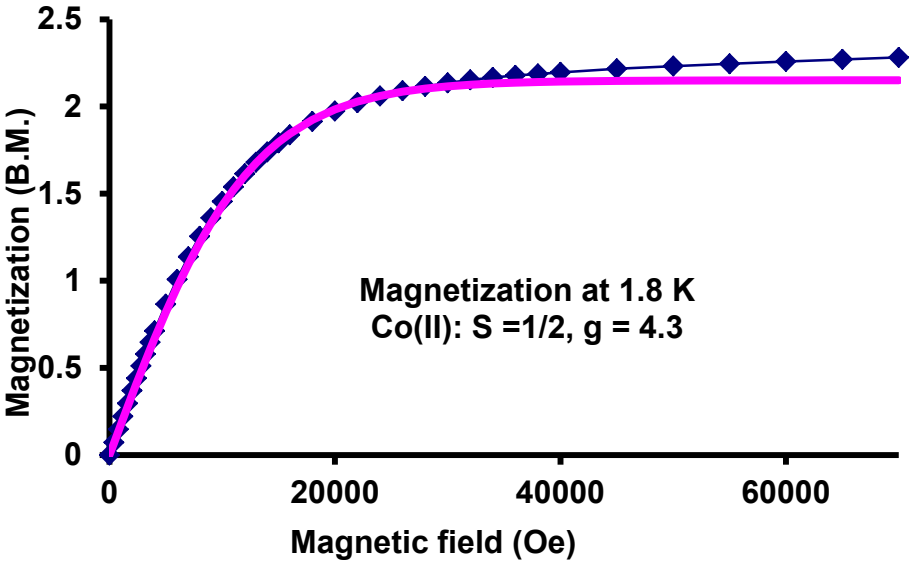

Figure 64. Field dependence of the bulk magnetization of CoBBMP-4H_2O.

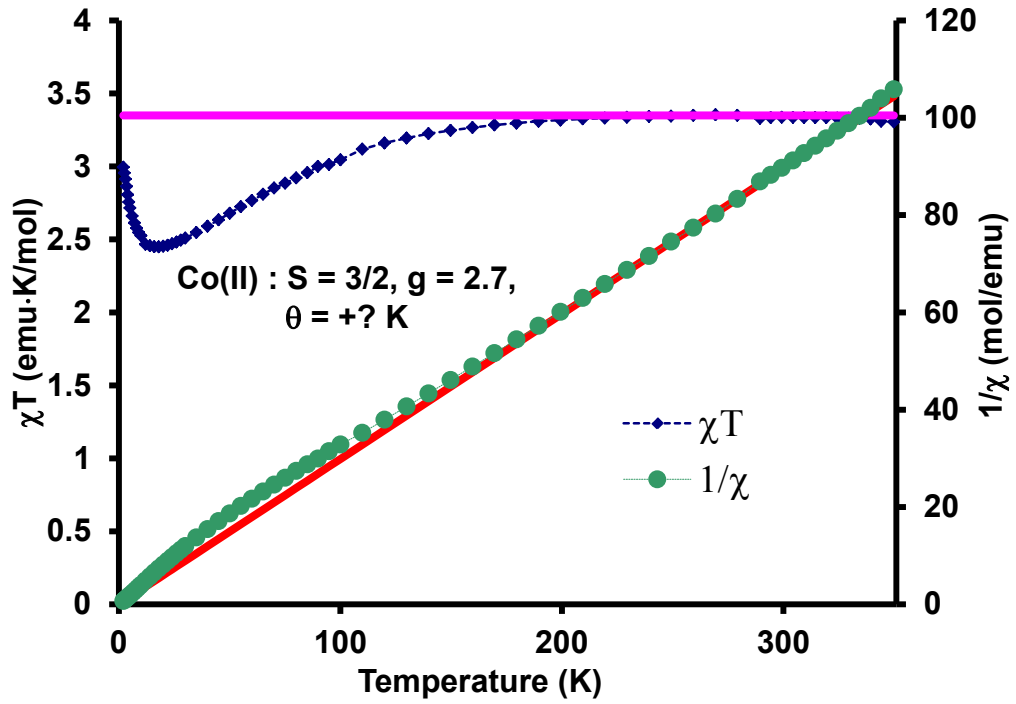

Figure 65. The temperature dependence of χT (♦) and of the inverse susceptibility 1/χ (●) for the 350 K data. The solid line corresponds to the best fit to the Curie-Weiss law.

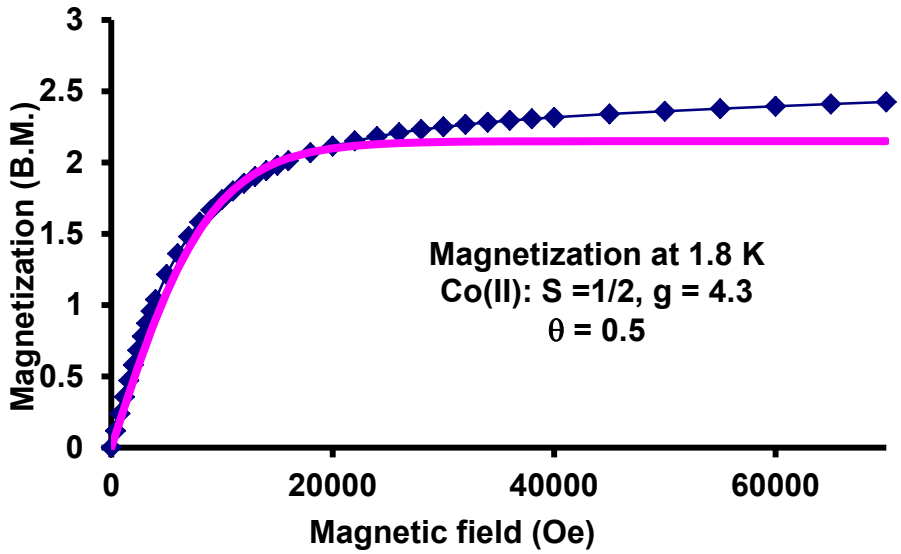

Figure 66. Field dependence of the bulk magnetization of the 350 K data.

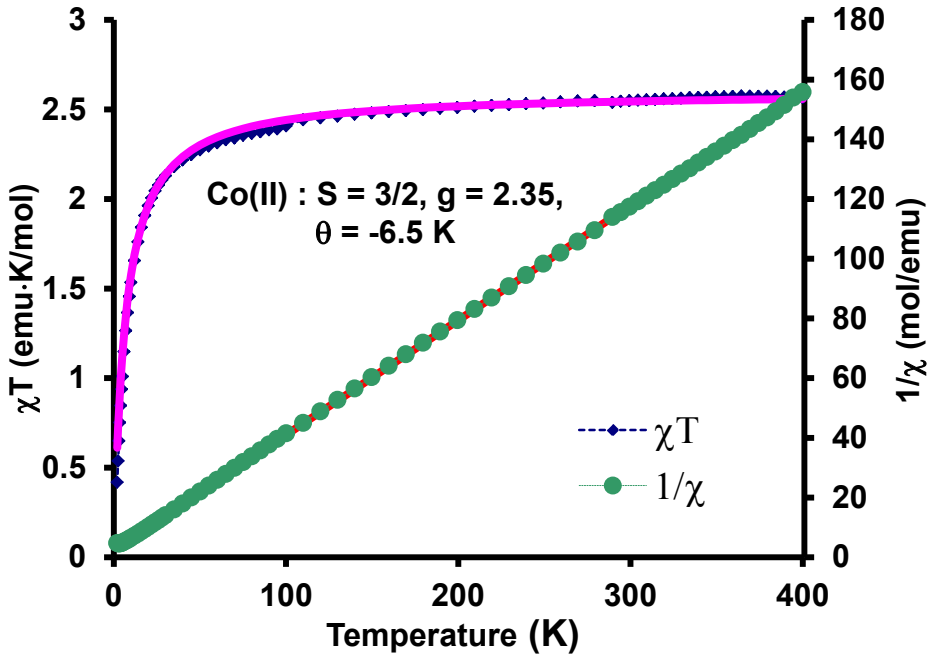

Figure 67. The temperature dependence of χT (♦) and of the inverse susceptibility 1/χ (●) for CoBBMP. The solid line corresponds to the best fit to the Curie-Weiss law.

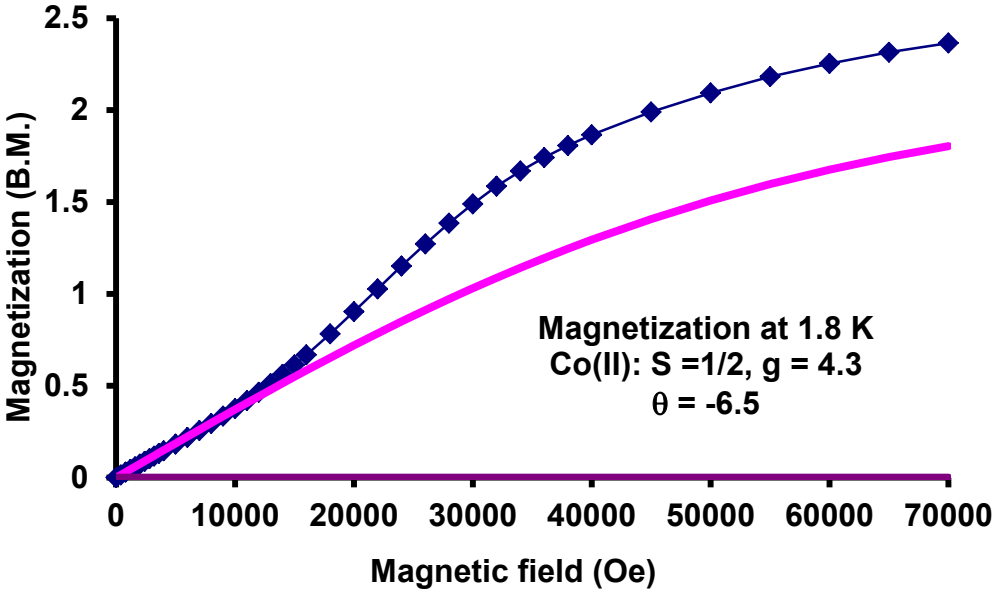

Figure 68. Field dependence of the bulk magnetization of CoBBMP. This clearly shows the antiferromagnetic characteristics.

Discussion

The flexibility of BBMP has shown the real strength of conformationally flexible ligands as evidenced by the drastic differences between the structures during the dehydration of a cobalt compound. While the biphenyl backbone barely moves from structure to structure the methylphosphonic acid groups adjust significantly. The torsional angles defined by P2-C1-C2-C10 and P1-C3-C4-C9 (in the CoBBMP-4H_2O structure) change from 124.6°, 117.4° to -106.5°, -109.9° to -152.4°, -104.7° respectively for the 4H_2O, 2H_2O, and 0H_2O structures (the naming scheme is different from structure to structure, but the same atoms in the ligand were selected for torsion measurements). One of the major changes between the structures is the Co-Co distance which starts at around 7 Å, and shrinks to 3.5 Å before settling at 4.7 Å at the shortest distances in each of the structures. The reversibility of this dehydration is what is most interesting; the system goes through some very large structural changes and still reverses the entire hydration process, picking up the four coordination waters as well as the two interstitial water molecules.

Conclusion

Conformationally flexible phosphonic acids such as BBMP allow for the ability to study large structural changes due to thermally induced dehydration via single-crystal-to-single-crystal transformation. Single crystal X-ray diffraction provides the simplest means of determining structure in crystalline materials, so single-crystal-to-single-crystal transformations are desirable. The ability of transition metal compounds to undergo

large coordination environment changes is an attractive characteristic for materials with variable magnetic properties. Presented in this chapter was just one example of a material which reversibly changes from a paramagnetic compound through a ferromagnetic intermediate to an antiferromagnetic compound.

CHAPTER VI

STRUCTURAL CHANGES UNDER HIGH PRESSURE*

Introduction

MOFs have revolutionized the field of crystal engineering, and stand to potentially revolutionize the field of solid-state chemistry.[37-41] The narrow definition of these materials is still under debate; however, the broad definition includes compounds exhibiting some level of dimensionality that are composed of metal-ions or cluster building units extended through coordinated organic linkers. Examples include carboxylates, phosphonates, and imidizoles to name a few.[66, 115, 116] Similar to any other class of solid-state materials, these new compounds exhibit a wide variety of unique chemical properties attractive for a diversity of applications from ion-exchange to gas storage/separations. Now that these compounds have presented themselves as being useful for engineering applications, more information is needed as to the mechanical properties and limitations. This information will lead to a variety of beneficial applications including pressure switches, smart body armor, pressure sensors, or shock absorbing materials.

As mentioned in Chapter I, a recent review paper presented a number of cases where mechanical properties of hybrid materials had been investigated; however, that number was relatively small compared with the number of MOFs published to date.[50] Many of these cases were computational. Of the few experimental studies that have been conducted, very interesting properties have been uncovered. The study of crystalline

---

*Reproduced with permission from Gagnon, K. J.; Beavers, C. M.; Clearfield, A., *J. Am. Chem. Soc.* **2013**, *135* (4), 1252-1255. Copyright American Chemical Society 2013.

compounds under isostatic pressure loading has yielded remarkable results.[50, 51] One relevant find here has been on the role of hydrogen bonding in extended minerals, Parise and coworkers conducted a number of neutron scattering experiments on various hydrous minerals under pressure to show that the H-O bond lengths do not change; however, O···O distances do and the H atom positions may rearrange. One role they propose as being very relevant is that of the H···H repulsion. Chapman and coworkers have shown that the compressibility of crystalline MOFs can be affected by guest inclusion and that the porosity of these materials can be modified by treating them first with small pressures.[52, 53] Moggach and coworkers have shown the effects of pressure on single crystalline porous frameworks, and the structural changes associated with forcing solvent into the pores.[52, 53] The main application front for MOFs has been around gas storage and the under-standing of how these structures change with applied pressure will be important if these materials are to have any industrial viability.

Although a few pressure studies have been conducted on MOFs, to the best of our knowledge, they have been conducted on rigid, highly-porous or non-porous materials. The common factor between the examples is the rigidity of the linker. As presented in Chapter IV there is a large diversity of structures associated with the use of alky chains in metal phosphonates. One of these materials we presented in Chapter IV and named it as ZAG-4. The name ZAG comes from the likeness of the structure, when viewed down the *c*-axis, to a collapsible pet or child safety gate (Figure 69). Herein we investigate the effect of isostatic pressure (0 - ~10 GPa) on the flexible framework ZAG-4.

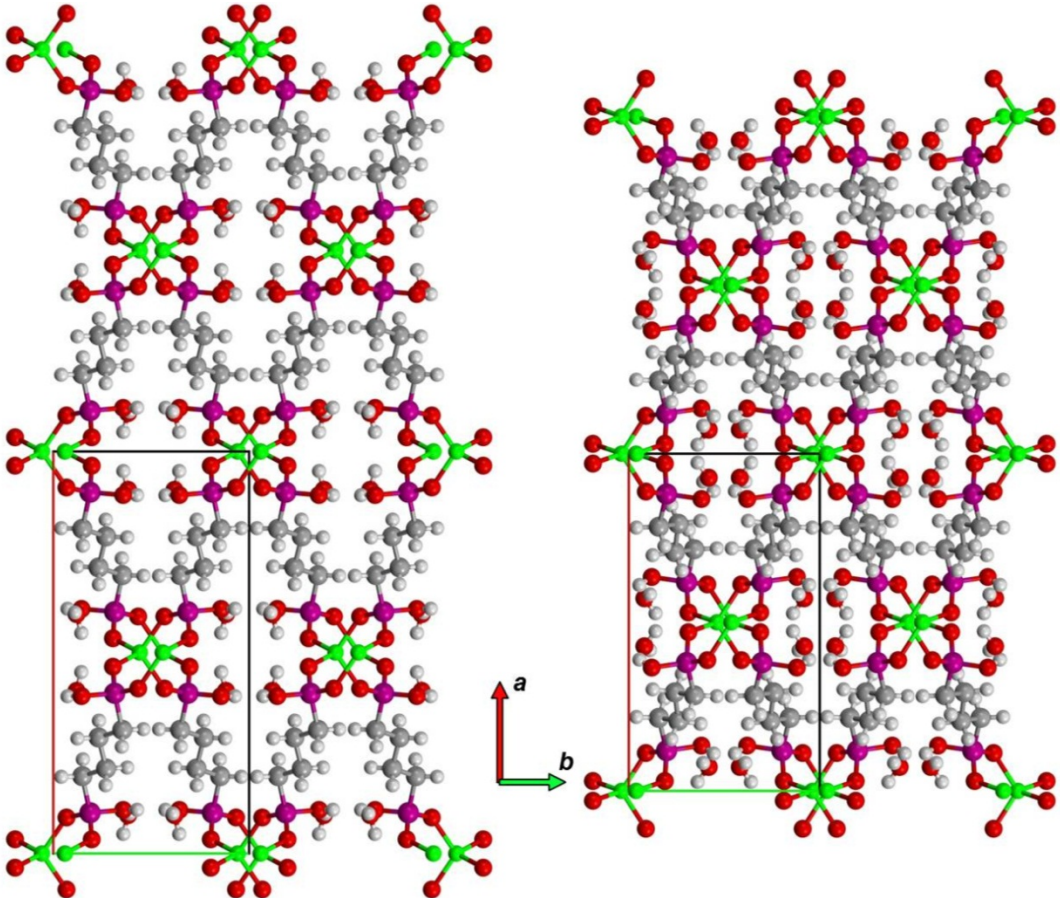

Figure 69. ZAG-4 as viewed down the *c*-axis for the ambient (left) and 7.32(7) GPa (right) structures.

This framework was chosen because it is a chemically robust member of a family of related zinc alkyl frameworks. ZAG-4 can be described as being composed of corner fused Zn-O-P-O 8-membered rings into a 1-D chain which is hydrogen bonded in one direction to neighboring chains and cross-linked in the other direction by the butane linker. The hydrogen bonded channel is filled with two water molecules per formula unit. Furthermore, we investigate ZAG-6 under a few applied pressures; however, no systematic investigation was carried out due to equipment difficulties.

Experimental

The pressure dependent studies of ZAG-4 and ZAG-6 were conducted on a single crystal, for each sample, of dimensions ~175 x 60 x 40 μm. The samples were loaded into a Merrill-Bassett-type DAC with Bohler-Almax cut diamonds, with culets of 600 μm in tungsten-carbide backing seats, and a tungsten gasket with hole diameter of 350 μm. The pressure medium used was a 4:1 methanol/ethanol mixture. The crystal was first affixed to the surface of the diamond culet using silicon vacuum grease before the gasket was set in place. A small amount of ruby powder was added for pressure calibration and the methanol/ethanol added before closing the DAC. The cell was pressurized initially and was allowed to stabilize for a period of 3 hours before data collection.

Data collection was performed on Beamline 11.3.1 at the ALS at LBNL. *In situ* diffraction experiments were performed using synchrotron radiation (λ = 0.60480 Å (ZAG-4, ZAG-6) and 0.67020 Å (ZAG-6 6.9 GPa)) on a modified Bruker APEX-II diffractometer system. To maximize the amount of data obtained in the experiments, three

data sets were run at each pressure with a rotation of the DAC by 120 degrees resulting in three total datasets per pressure. Each data set included a series of phi and omega scans at 3 seconds per frame. The pressure of the cell was monitored between each data set for pressure stability and to make sure there was no methanol/ethanol leakage leading to pressure loss. The pressure was monitored via ruby fluorescence stimulated by a 100W 447 nm diode, measured via fiber-optic coupled to a Princeton Instruments Acton 300i spectrometer following the methods established previously in the literature.[117] Data for ZAG-4 were collected at pressures of 1.65(10), 2.81(9), 5.69(3), and 7.32(7) GPa. The pressure within the DAC was raised to 9.9(2) GPa (as calculated from the ruby fluorescence measured); however, during data collection, the gasket failed under this pressure and the pressure fluid escaped until stabilizing at 5.0 GPa. The cell was then unloaded and the crystal was removed and cleaned under oil before being remounted on a MiTeGen® kapton pin for data collection at room temperature. Data for ZAG-6 were collected at pressures of ~2.8, 4.3, and 6.9 GPa systematic studies were not conducted on one single crystal of ZAG-6 due to instrumentation issues. Appendix A contains more information on the DAC, its design and construction.

Results

ZAG-4 Systematic Pressure Studies

ZAG-4 is considerably resilient under isostatic conditions, with respect to crystallinity. The framework continues to diffract with decreasing intensity, but with rela-

tively little peak broadening. The volume decreases 27% over 7.3 GPa with the largest change of 11.5% occurring over the first 1.7 GPa of pressure. This is accompanied by an increase in density of 36%. The largest contributing factor to this change is the increase of the β angle from 113.837(2) to 123.227(8)°. All of the relative cell parameters with respect to the ambient parameters against applied pressure are shown in Figure 70. Figure 71 shows a plot of the change in volume with respect to pressure. From this curve we can ascertain that the change in volume is best fit by a fourth order Birch-Murnaghan equation of state, Table 18 shows the breakdown of the results of several equations of state calculations from the program eosfit.[118] Table 19 shows the packing index for each pressure.

Some of the largest changes in the structure are located in the inorganic 1-D chain. This is first observed by the greater than 10% decrease in the *c*-axis which contains this chain; however, inspection of the 8-membered chain-link provides a more complete explanation as shown in Figure 72. Figures 72A and 72B, which are representations of this 8-memembered ring at ambient pressure (A) and 7.32(7) GPa (B), clearly show that the distortion of the ring is due to an opening of the O1-Zn1-O2′ angle resulting in the Zn1-Zn1′ distance reducing from 4.245(1) to 3.754(1) Å. Figures 72C and 72D shows that the chair-type conformation of these rings is retained. While Figure 72 shows the localized deformation of a given link in the inorganic chain, Figure 73 shows that the long-range structure of the inorganic chain does not change substantially.

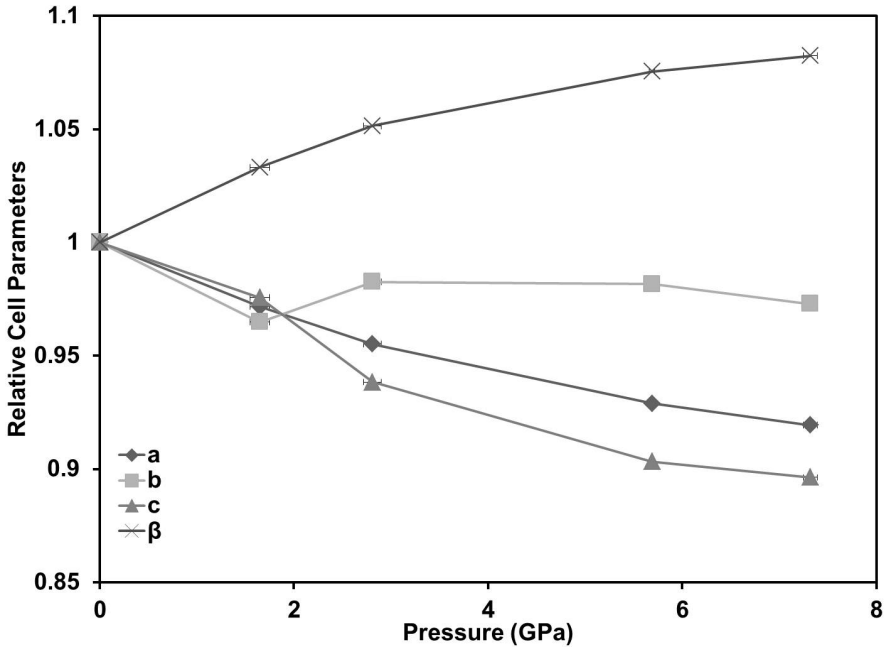

Figure 70. Experimental relative lattice parameter variation observed with respect to increase in pressure. Vertical error bars are contained within the markers.

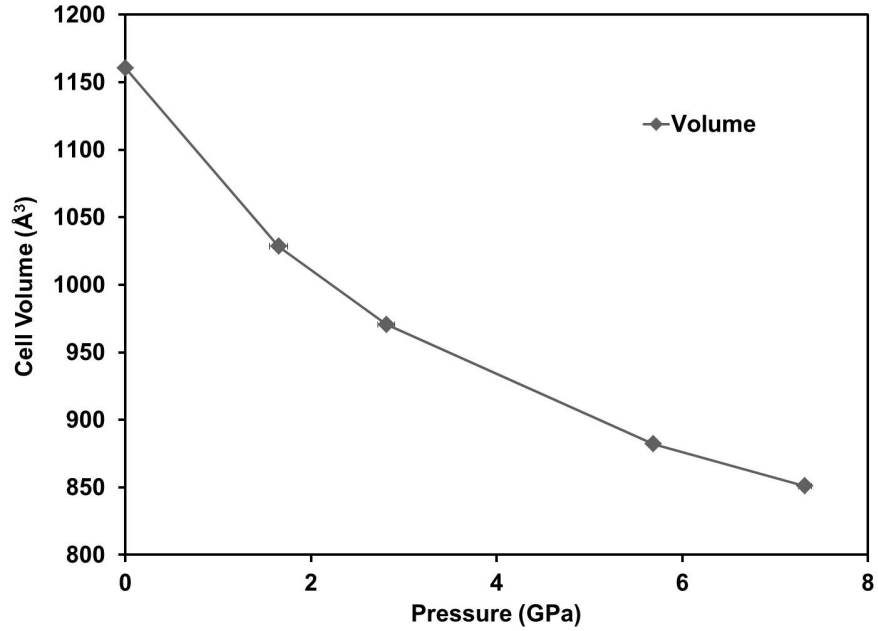

Figure 71. Experimental unit cell volume variation observed with respect to increase in pressure. This is best fit by a fourth order Birch-Murnaghan equation of state with K_0 = 11.66, K′ = 1.976, and K" = 1.3776. Vertical error bars are contained within the markers.

Table 18. Results of equation of state calculations from eosfit.

	V_o	K_o	K'	K''	X^2w	$delP_{max}$
M	1160.173	9.38236	5.21098	-	1.049	0.077
BM2	1159.283	12.15152	4	-	12.7517	0.332
BM3	1160.174	8.73766	6.51476	-1.45664	0.9408	0.099
BM4	1160.096	11.66431	1.97567	1.3776	0.049	0.015
NS2	1158.199	16.09971	2	-	45.903	-0.585
NS3	1160.166	7.46254	10.24467	-10.3476	3.5833	0.134
NS4	1160.096	12.95447	-0.73121	3.21682	0.1571	0.027
V	1160.189	8.59717	6.71975	-	1.994	0.108

*Murnaghan, Birch-Murnaghan (2nd, 3rd and 4th order), Natural Strain (2nd, 3rd, and 4th order) and Vinet

Table 19. K. P. I's for ZAG-4 at each pressure.

	Ambient	1.65(10) GPa	2.81(9) GPa	5.69(3) GPa	7.32(7) GPa	Ambient post
K. P. I.*	69.7%	76.5%	80%	86.5%	87.5%	69.8%

*As calculated by the program Platon.

Further inspection of the inorganic chain shows that from ambient pressure up to the applied pressure of 7.32(7) GPa the chain actually expands in the *b*-axis direction a little over 0.2 Å. This is quite substantial as it amounts to a change of approximately 2% on the *b*-axis. Initially, from ambient to 1.65(10) GPa this chain compresses about 0.3 Å, on increasing to 2.81(9) GPa, the chain begins to expand nearly 0.1 Å and continues to expand through 7.32(7) GPa.

One factor we have yet to explain is the changing linear compressibility of the *b*-axis. This direction lies perpendicular to the inorganic chains and contains all of the hydrogen bonding between the included water molecule and the free P-OH groups. Across the presented pressures, the shortest hydrogen bond (O3-H3···O1W) decreases from 2.557(3) to 2.37(2) Å. While the positions of the hydrogen atoms in these bonds are questionable, the interatomic distances are not. It is clear that the caged water molecules collapse inward to fill free space as best they can; however, the existence of the hydrogen atoms on the caged water molecules, as well as the hydroxide, reduces the amount of room available and limits the amount of compression. Following the aforementioned O3-H3···O1W distance, it is seen that the water molecules moves closer, shortening the distance from 2.557(3) to 2.460(9) Å initially, a change of 0.097 Å. Further pressure increases change this distance to 2.404(10), 2.406(10), and 2.37(2) Å, respectively. Taking into account the error on these values, there is compression from 1.65 to 2.81 GPa; however, the distance does not change with further applied pressure. This channel of hydrogen bonds combined with the expansion of the lateral direction of the inorganic chain

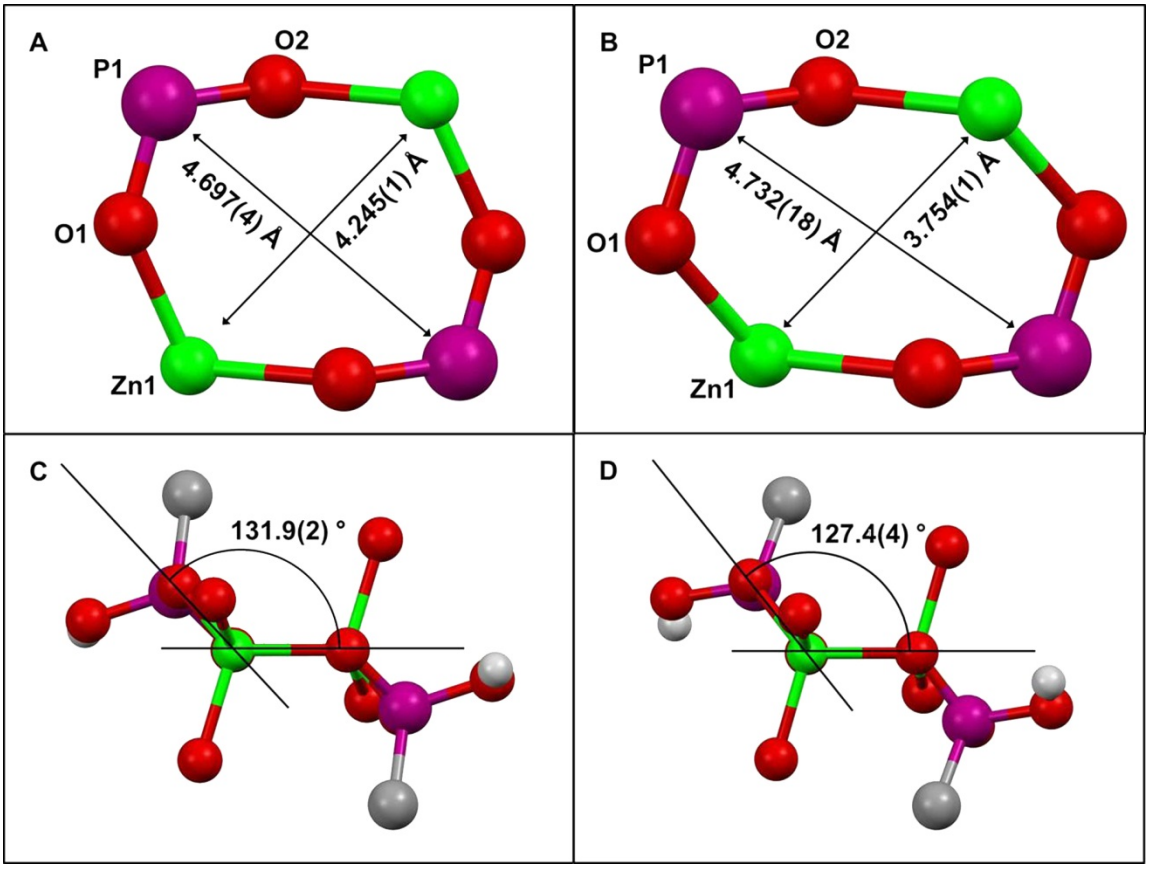

Figure 72. Representations for ZAG-4 of the 8-membered chain-link at ambient pressure (A, C) and 7.32(7) GPa (B, D) both showing the ring (top) and the chair-like conformation (bottom). The solid black lines in the bottom represent calculated mean planes. The O1-Zn1-O2′ internal angle increases from 109.54(8) – 114.7(3) °. ′: -x+1,-y+1,-z+2.

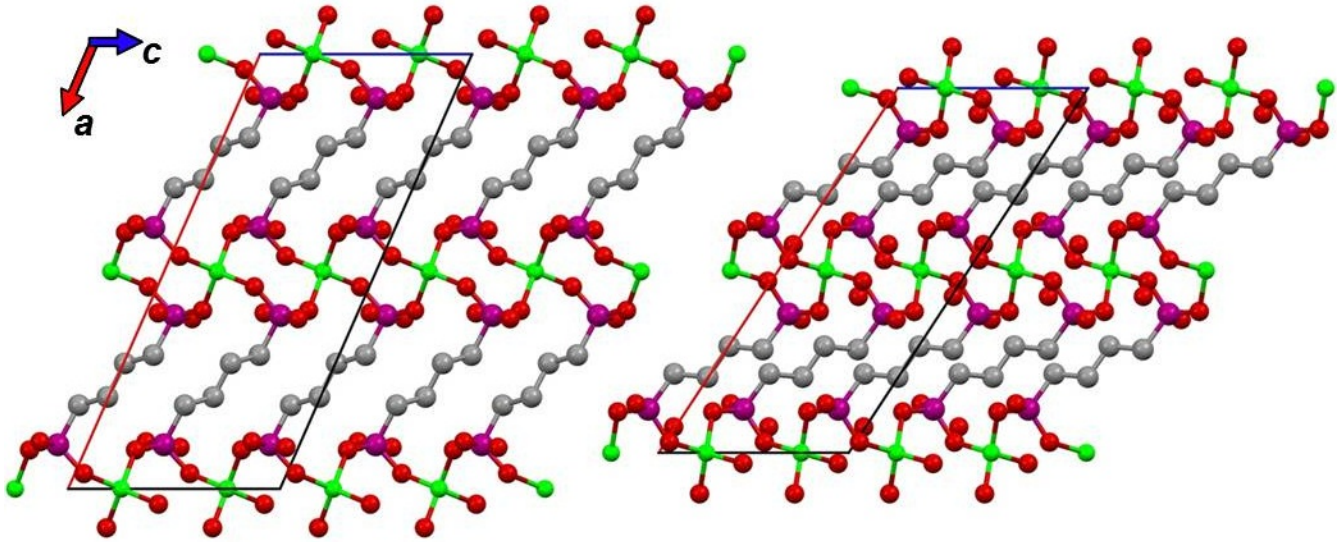

Figure 73. View down the *b*-axis of the ambient (left) and 7.32(7) GPa (right) ZAG-4 structures.

explains why there is an initial decrease followed by an increase with a relative stand-still along the *b*-axis. Initially this hydrogen bonded channel compresses, as does the inorganic chain, but then begins to push back strongly as the collective force of the hydrogen bonding strengthens, and the inorganic chain expands as well. To the best of our knowledge, we propose that it is the combination of these two structural features that causes the *b*-axis to compress and expand over the pressures presented.

This phenomena is not new, in 1998 Baughman and coworkers identified structures containing a "wine-rack" topology were among those predicted to exhibit negative linear compressibility.[119] While "wine-rack" describes the topology, "gate" does better to describe the mechanism. Cheetham and coworkers recently investigated this phenomenon in a zinc formate hybrid material, which they stated had been the first hybrid framework to the best of their knowledge reported showing negative linear compressibility.[120] In Cheetham's report, the negative linear compressibility results in an axis change of less than 1% over the applied pressure range of 0 – 1 GPa.

Herein, we report that over the pressure range of 1.65 – 2.81 GPa the negative linear compressibility results in a change of axis length of almost 2% (increasing from 8.000(2) to 8.147(2) Å). Furthermore, the axis decreases less than 0.5% over the next 3 GPa of applied pressure (8.147(2) to 8.139(2) Å). As Cheetham and coworkers point out, this type of material is attractive for a variety of piezoresponsive applications such as pressure sensors, 'smart' body armor, pressure switches, and shock absorbing materials.[121, 122] It is the inclusion of the caged water molecules in this compound that provides the unique axis compression character.

Despite the very large relative decreases in volume and the various cell parameters, after raising the pressure to 9.9 GPa and upon rapid removal of pressure, the process proves to be completely reversible with all cell parameters returning to values within reasonable error of the ambient pressure room-temperature data. Table 20 shows the unit-cell parameters and crystal information for all pressures and the return to ambient pressure after the experiment. It is interesting to note that the quality of the crystal is maintained such that when the gasket failed at 9.9 GPa, during data collection, the expansion of the cell could be followed across the 3 hours of data collection.

Table 20. Cell parameters and crystallographic information for ZAG-4 at different pressures.

Pressure	Ambient	1.65(10) GPa	2.81(9) GPa	5.69(3) GPa	7.32(7) GPa	Ambient*
Space Group	*C*2/*c* (15)	*C*2/*c* (15)	*C*2/*c* (15)	*C*2/*c* (15)	*C*2/*c* (15)	*C*2/*c* (15)
Lambda (Å)	0.60480	0.60480	0.60480	0.60480	0.60480	0.60480
a (Å)	18.515(4)	17.991(2)	17.685(2)	17.1996(19)	17.023(2)	18.55(2)
b (Å)	8.291(2)	8.000(2)	8.147(2)	8.139(2)	8.066(3)	8.272(5)
c (Å)	8.265(2)	8.0643(6)	7.7557(6)	7.4651(6)	7.4078(8)	8.261(5)
β (°)	113.837(2)	117.609(6)	119.697(6)	122.431(6)	123.227(8)	113.790(6)
V ($Å^3$)	1160.5(5)	1028.5(3)	970.6(3)	882.0(3)	850.9(3)	1160.1(13)
ρ (g/cm^3)	1.817	2.050	2.172	2.391	2.478	1.818
Reflections	1770	762	721	693	547	1713
Parameters	69	64	65	69	69	69
R_{int}	0.0453	0.0439	0.0537	0.0638	0.0630	0.0619
R_1/wR_2	0.0458/0.0960	0.0450/0.0963	0.0456/0.1125	0.0639/0.1369	0.0742/0.1580	0.0495/0.1137
θ Range	5.14 – 25.69	3.77 – 25.20	3.74 – 24.83	3.79 – 25.54	2.43 – 25.64	5.13 – 25.58

*Data taken on the single crystal which was removed from DAC after being brought to 9.9(2) GPa.
All unit cells for data taken on pressurized samples are reported as unconventional representations utilizing the transformation matrix 1 0 2 0 -1 0 0 0 -1. This was done to maintain the same orientation as in the ambient structure.

ZAG-6 Pressure Studies

The pressure studies of ZAG-6 were met by a series of equipment challenges which resulted in only a handful of measurements that could be made with minimal confidence. In spite of this, many common features can be seen in the analysis of the data that was collected. The volume decreases over 26% over 6.9 GPa. This is accompanied by over a 27% increase in density. The largest contributing factor to this change is the decrease of the *a*-axis from 23.186(5) Å to 19.782(4) Å (~15%). Figure 74 shows a side by side comparison of ZAG-6 at ambient pressure and 6.9 GPa. All of the relative cell parameters with respect to the ambient parameters against applied pressure are shown in Figure 75. One strange point is that there appears to be little change in the cell parameters from 0 to 2.8 GPa, I suspect that this is due to experimental error; however, the results of this data are after four independent pressure measurements. Further measurements at these pressures and pressures around this point are necessary to confirm the results. Figure 76 shows a plot of the change in volume with respect to pressure. Unfortunately, unlike with the ZAG-4 compound, there are not enough data points to attempt a fit of this curve.

Some of the largest changes in the structure are located in the inorganic 1-D chain, although not as large as in ZAG-4. The *c*-axis decreases 6% compared to the greater than 10% in ZAG-4. Many of the same changes are seen in ZAG-6 that are seen in ZAG-4 as shown in Figure 77. Figures 77A and 77B show the 8-membered rings at ambient pressure (A) and 6.9 GPa (B). Similar to ZAG-4, the Zn1-Zn1' distance

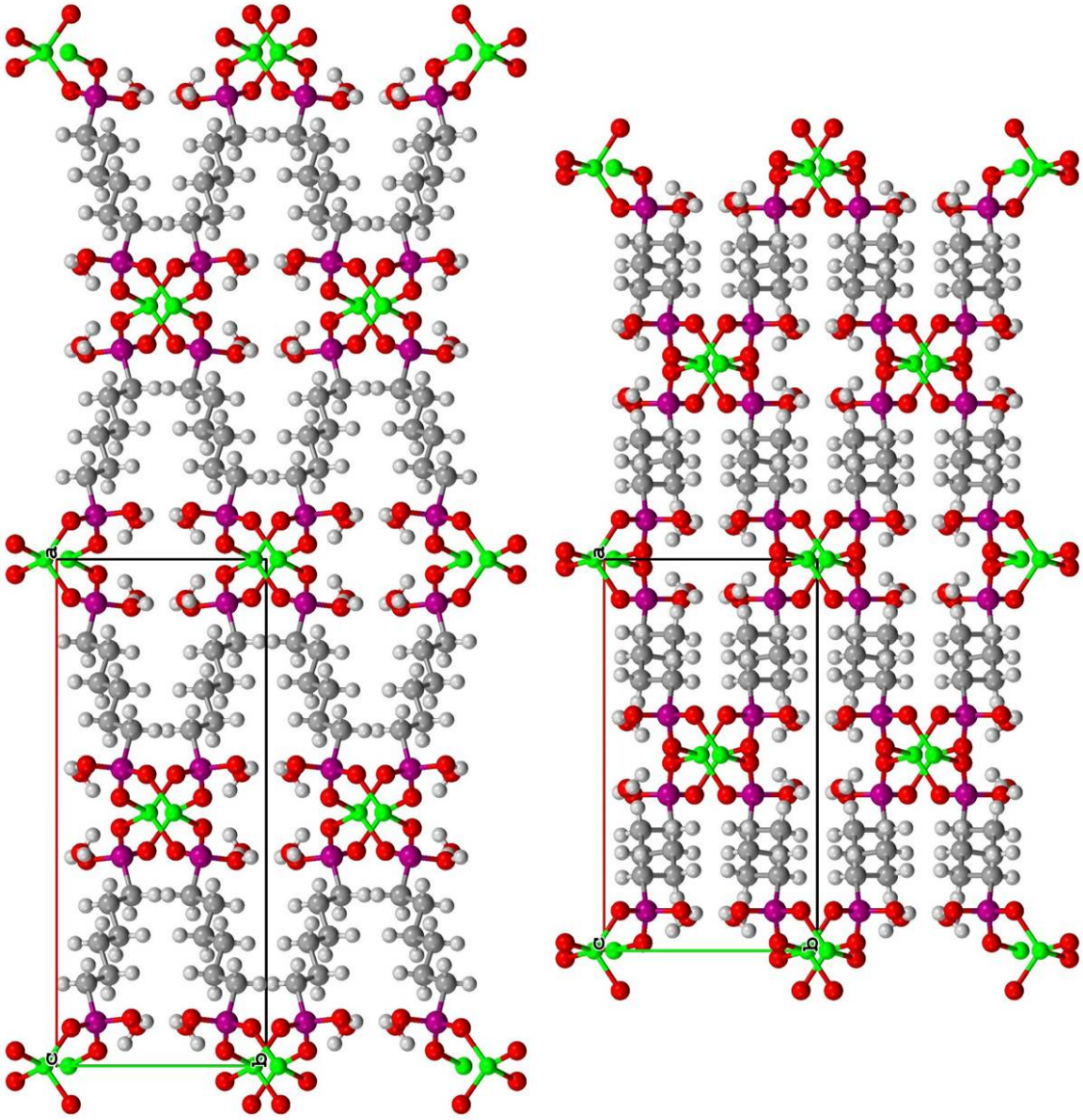

Figure 74. ZAG-6 as viewed down the *c*-axis for the ambient (left) and 6.9 GPa (right) structures.

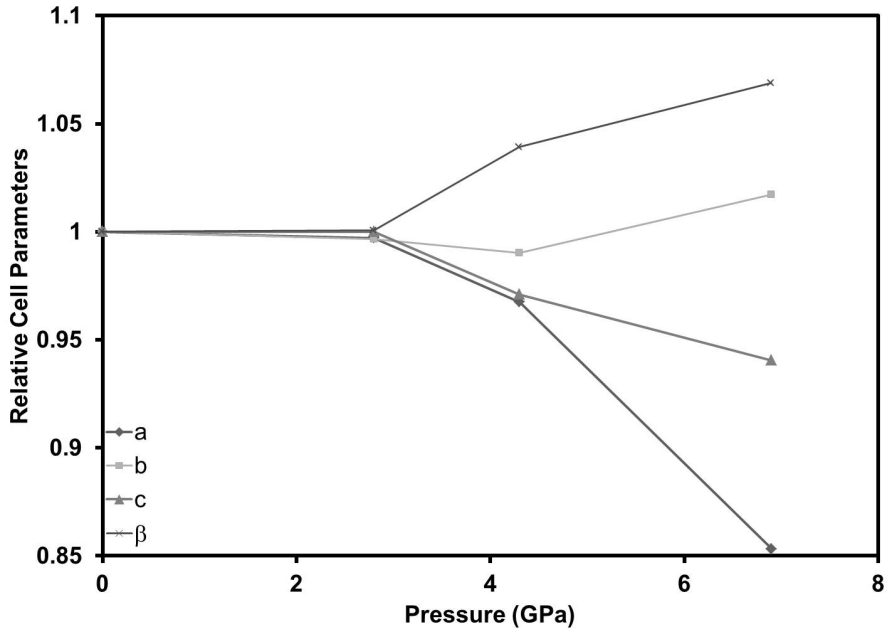

Figure 75. Experimental relative lattice parameter variation observed with respect to increase in pressure for ZAG-6.

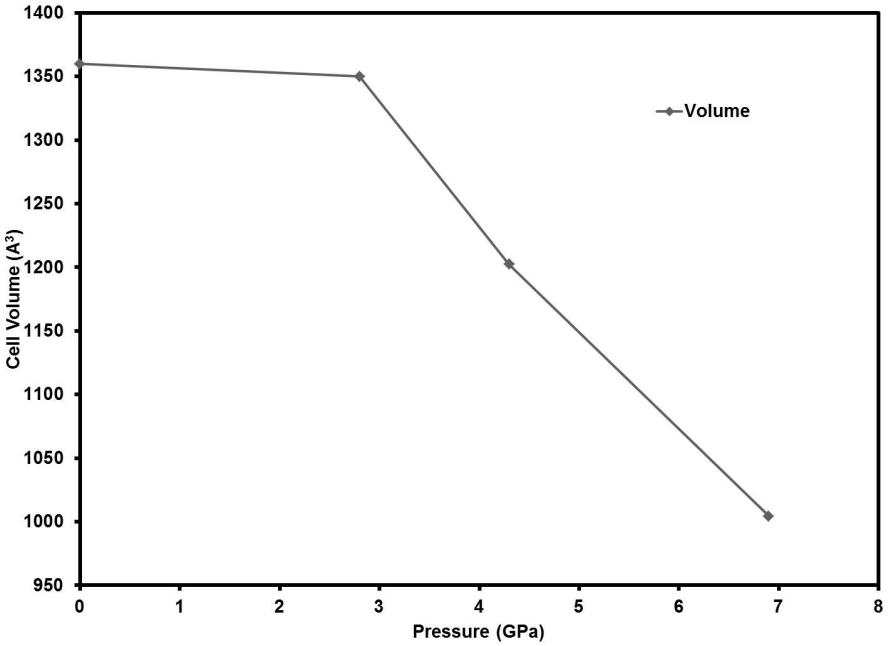

Figure 76. Experimental unit cell volume variation observed with respect to increase in pressure for ZAG-6.

reduces from 4.2117(4) to 3.9354(6) Å. Figures 77C and 77D shows that the chair-type conformation of the rings is retained. While Figure 77 shows the localized deformation of a given link in the inorganic chain, Figure 78 shows that the long-range structure of the inorganic chain does not change substantially. One major difference between ZAG-4 and ZAG-6 can be seen in Figure 79 which shows that the alkyl chain of ZAG-6 begins to distort via a cork-screw kinking mechanism. This results in a significantly larger decrease in the *a*-axis than in ZAG-4, ~15% compared to ~8%.

Further inspection of the inorganic chain shows that from ambient pressure up to the applied pressure of 6.9 GPa the chain actually expands in the *b*-axis direction almost 0.3% or just under 0.2 Å. As with ZAG-4 this expansion is close to 2% of the *b*-axis, which is very close to how much the *b*-axis expands across this temperature. A systematic study of this compound would help determine the extent to which the negative linear compressibility presents itself in the ZAG-6 compound. Unlike ZAG-4 the hydrogen bonds between the framework and O1W only change slightly from 2.528 to 2.500 Å. Table 21 lists the cell parameters for ZAG-6 for the various applied pressures at which data were collected.

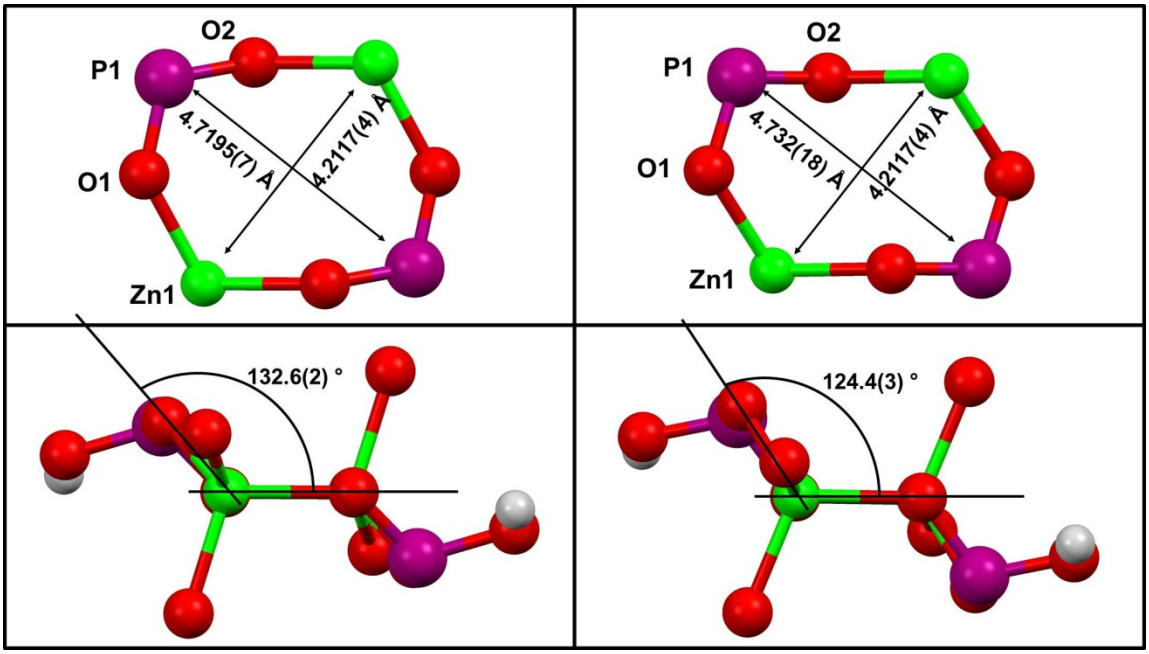

Figure 77. Representations of the 8-membered chain-link in ZAG-6 at ambient pressure (A, C) and 6.9 GPa (B, D) both showing the ring (top) and the chair-like conformation (bottom). The solid black lines in the bottom represent calculated mean planes.

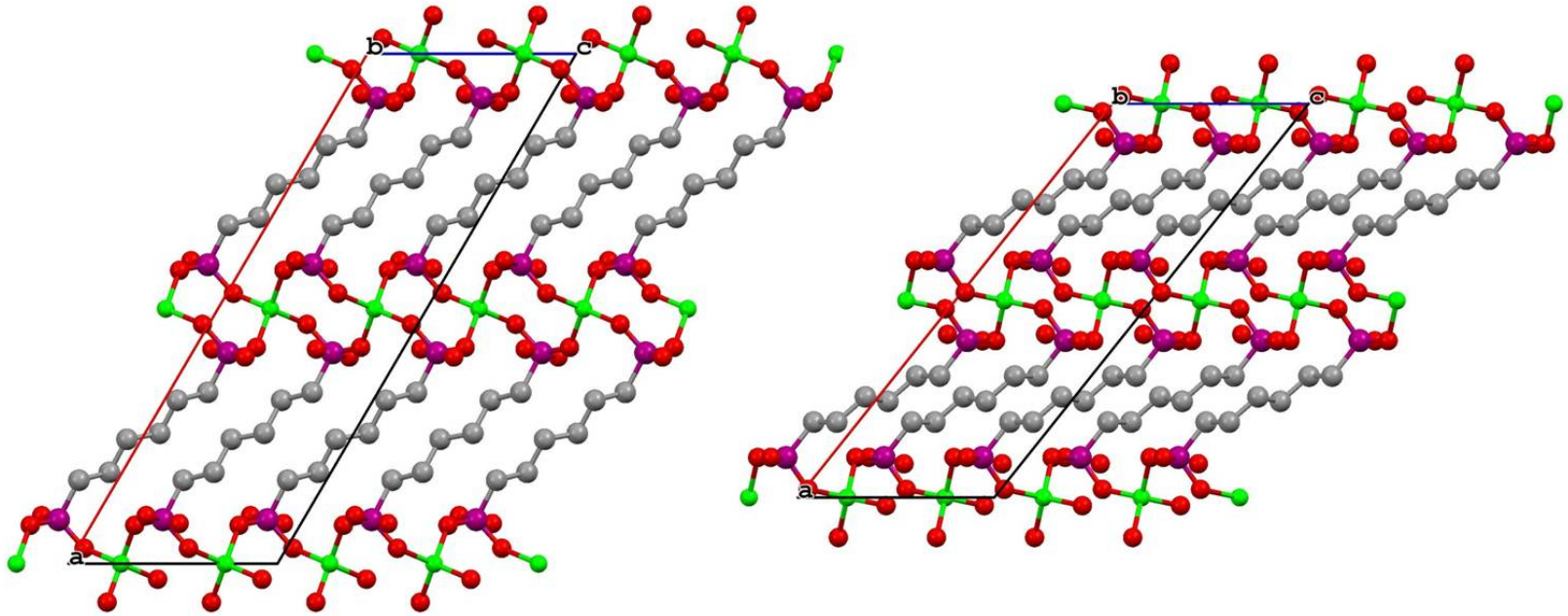

Figure 78. View down the *b*-axis of ZAG-6 of the ambient (left) and 6.9 GPa (right) structures.

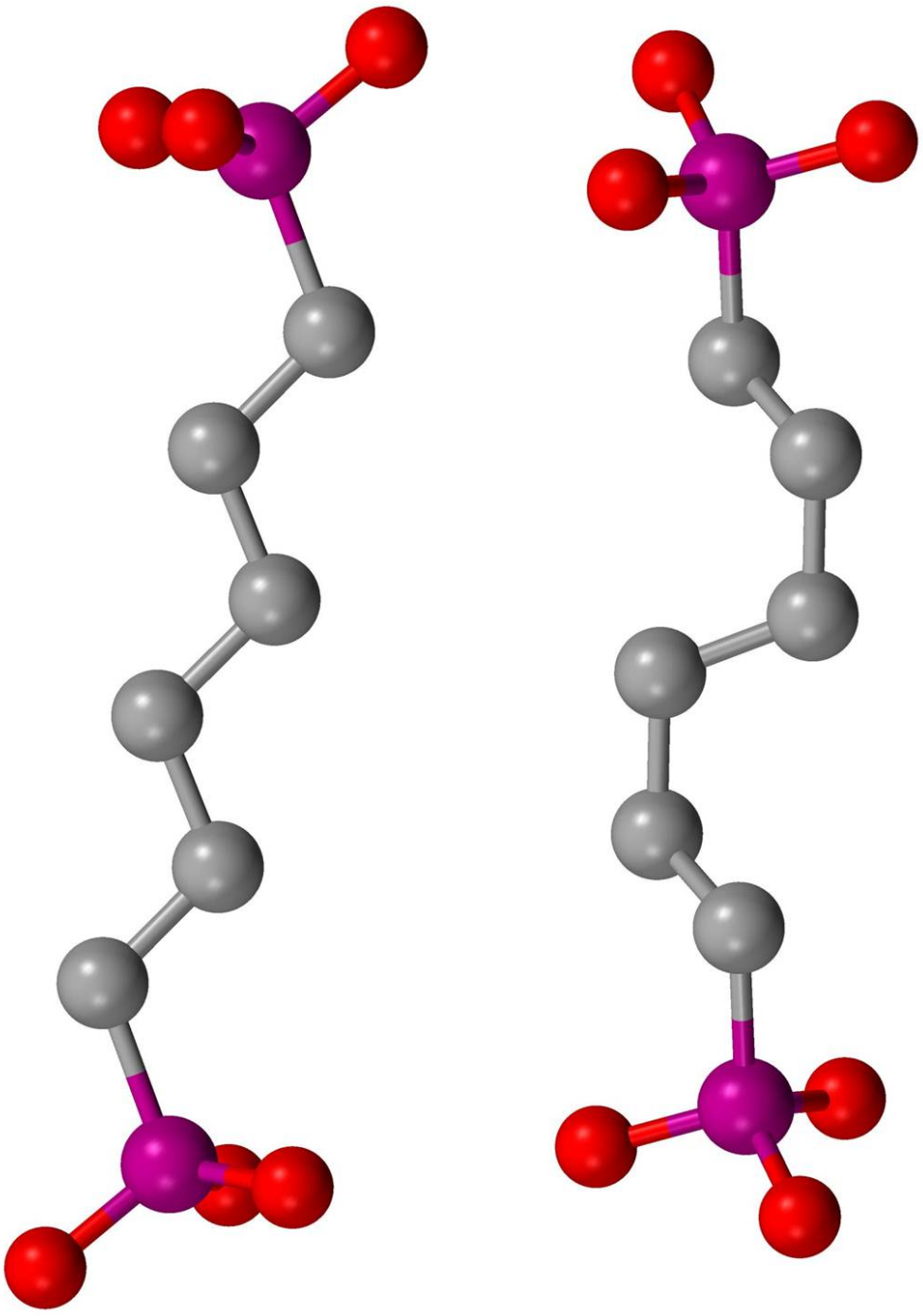

Figure 79. Side by side comparison of the alkyl chain conformations in ZAG-6 in the ambient pressure (left) and at 6.9 GPa (right).

Table 21. Cell parameters and crystallographic information for ZAG-6 at different pressures.

Pressure	Ambient	2.8 GPa	4.3 GPa	6.9 GPa
Space Group	*C*2/*c* (15)	*C*2/*c* (15)	*C*2/*c* (15)	*C*2/*c* (15)
Lambda (Å)	0.60480	0.60480	0.60480	0.60480
a (Å)	23.186(5)	23.120(5)	22.433(8)	19.782(4)
b (Å)	8.2881(16)	8.2591(10)	8.207(2)	8.430(3)
c (Å)	8.2031(16)	8.2037(10)	7.9648(18)	7.7146(12)
β (°)	120.389(2)	120.467(13)	125.12(3)	128.672(12)
V (Å^3)	1359.8(5)	1350.2(4)	1199.3(6)	1004.4(4)
ρ (g/cm^3)	1.688	1.700	1.914	2.159
Reflections	3093	1249	617	698
Parameters	78	78	78	78
R_{int}	0.0700	0.0781	0.0505	0.0989
R_1/wR_2	0.0596/0.1282	0.0676/0.2046	0.0854/0.1430	0.0917/0.1962
θ Range	5.03 – 29.66	3.00 – 25.61	2.72 – 26.03	3.46 – 28.70

All unit cells for data taken on pressurized samples are reported as unconventional representations utilizing the transformation matrix 1 0 2 0 -1 0 0 0 -1. This was done to maintain the same orientation as in the ZAG-4 structures.

Discussion

There are several factors that differ between ZAG-4 and ZAG-6; however, both systems exhibit negative linear compressibility and more than likely largely anisotropic materials properties. The biggest difference between ZAG-4 and ZAG-6 is the change in alkyl chain conformation that occurs in ZAG-6. When pressure is applied to a system, structurally, the weakest points will change first. With ZAG-4 the shorter alkyl chain is more resistant to changes in the torsional angles and the inorganic chain and the water molecules make the largest changes. It appears that in ZAG-6 the alkyl chain is significantly more susceptible to pressure induced changes and allows for the inorganic portion to be better stabilized.

Taking everything into account, one can see how frameworks similar to the one presented herein may find their use as a new class of piezoelectric or piezomagnetic materials. By carefully studying the structural effects of pressure on these hybrid materials one can begin to design new systems which may exhibit unique properties. It has been suggested that there are benefits to using hybrid materials over those that are either purely organic or inorganic. They provide compounds that are often the best of both worlds, per se. In the compounds we have presented here, the alkyl chains provide a spring-like cushion to stabilize the compression of the system allowing for large distortions in the metal coordination environment, without destruction of the material.

Conclusion

We have demonstrated that the flexibility of an alkyl chain supported MOF can result in dramatic elastic behavior of a single crystal. ZAG-4 is highly compressible with reversibility possible within the regime of 10 GPa while maintaining single crystal quality. The axis orthogonal to the *bc*-plane exhibits remarkable compressibility of nearly 17%, while the inorganic chain direction also compresses over 10%. Despite these large compressions in the *a*- and *c*-axes, the *b*-axis exhibits both positive and negative linear compressibility. Further investigation is necessary to determine the upper bound of the reversible nature of this material. Future studies will include the systematic pressure study of the ZAG-6 compound, as well as a full series of nanoindentation experiments on both ZAG-4 and ZAG-6 to determine more fully the mechanical properties of these materials. Calculations on both ZAG-4 and ZAG-6 are also being performed to confirm the experimental data as well as to probe the anisotropy of the mechanical properties. We hope through these studies to better understand the changing linear compressibility of the *b*-axis in ZAG-4 and in ZAG-6 as well. Through these future studies and similar studies on related compounds, we may unveil that phosphonate MOFs and related compounds may exhibit interesting piezoelectric and piezomagnetic properties while withstanding remarkable mechanical external forces, and may find applications in piezoresponsive materials.

CHAPTER VII

SUMMARY

This work has given a series of examples of how conformationally flexible phosphonic acids can be utilized to construct a large variety of metal phosphonates. Chapter III showed how ionic liquids can be utilized to access a variety of new structural types when used as a supplement to hydrothermal synthesis. Zinc when combined with various alkylbis(phosphonic acids) resulted in five new families of compounds with increasing complexity of 1-D building units as described in Chapter IV. Chapter V and VI showed how external stimuli such as temperature and pressure can result in structural changes useful for sensor and switch materials. Specifically Chapter V showed how the conformational flexibility of the BBMP ligand allows for drastic structural change throughout dehydration, which resulted in a paramagnetic material becoming antiferromagnetic. Chapter VI addressed how the flexibility of an alkyl chain constructed MOF can survive high applied external pressures and could find uses as highly anisotropic materials for pressure sensors and switches.

REFERENCES

1. Clearfield, A., *Curr. Opin. Solid State Mater. Sci.* **1996,** *1* (2), 268-278.
2. Lee, J.; Farha, O. K.; Roberts, J.; Scheidt, K. A.; Nguyen, S. T.; Hupp, J. T., *Chem. Soc. Rev.* **2009,** *38* (5), 1450-1459.
3. Li, J.-R.; Kuppler, R. J.; Zhou, H.-C., *Chem. Soc. Rev.* **2009,** *38* (5), 1477-1504.
4. Chae, H. K.; Siberio-Pérez, D. Y.; Kim, J.; Go, Y.; Eddaoudi, M.; Matzger, A. J.; O'Keeffe, M.; Yaghi, O. M., *Nature* **2004,** *427* (6974), 523-527.
5. Eddaoudi, M.; Kim, J.; Rosi, N.; Vodak, D.; Wachter, J.; O'Keeffe, M.; Yaghi, O. M., *Science (New York, N.Y.)* **2002,** *295* (5554), 469-472.
6. Férey, G., *Science (New York, N.Y.)* **2001,** *291* (5506), 994-995.
7. Férey, G.; Mellot-Draznieks, C.; Serre, C.; Millange, F., *Acc. Chem. Res.* **2005,** *38* (4), 217-225.
8. Kim, J.; Chen, B.; Reineke, T. M.; Li, H.; Eddaoudi, M.; Moler, D. B.; O'Keeffe, M.; Yaghi, O. M., *J. Am. Chem. Soc.* **2001,** *123* (34), 8239-8247.
9. Gagnon, K. J.; Perry, H. P.; Clearfield, A., *Chem. Rev.* **2011,** *112* (2), 1034-1054.
10. Wang, Z.; Cohen, S. M., *Chem. Soc. Rev.* **2009,** *38* (5), 1315-1329.
11. Colombo, V.; Galli, S.; Choi, H. J.; Han, G. D.; Maspero, A.; Palmisano, G.; Masciocchi, N.; Long, J. R., *Chem. Sci.* **2011,** *2* (7), 1311-1319.
12. Clearfield, A., *Dalton Trans.* **2008,** (44), 6089-6102.
13. Turner, A.; Jaffres, P.-A.; MacLean, E. J.; Villemin, D.; McKee, V.; Hix, G. B., *Dalton Trans.* **2003,** (7), 1314-1319.

14. Fan, J.; Shu, M.-H.; Okamura, T.-a.; Li, Y.-Z.; Sun, W.-Y.; Tang, W.-X.; Ueyama, N., *New J. Chem.* **2003,** *27* (9), 1307-1309.

15. Menelaou, M.; Dakanali, M.; Raptopoulou, C. P.; Drouza, C.; Lalioti, N.; Salifoglou, A., *Polyhedron* **2009,** *28* (15), 3331-3339.

16. Parnham, E. R.; Drylie, E. A.; Wheatley, P. S.; Slawin, A. M. Z.; Morris, R. E., *Angew. Chem.* **2006,** *118* (30), 5084-5088.

17. Sheu, C.-Y.; Lee, S.-F.; Lii, K.-H., *Inorg. Chem.* **2006,** *45* (5), 1891-1893.

18. Shi, F.-N.; Trindade, T.; Rocha, J. o.; Paz, F. A. A., *Cryst. Growth Des.* **2008,** *8* (11), 3917-3920.

19. Lin, Z.; Wragg, D. S.; Warren, J. E.; Morris, R. E., *J. Am. Chem. Soc.* **2007,** *129* (34), 10334-10335.

20. Liu, H.-S.; Lan, Y.-Q.; Li, S.-L., *Cryst. Growth Des.* **2010,** *10* (12), 5221-5226.

21. Morris, R. E., *Chem. Commun.* **2009,** (21), 2990-2998.

22. Parnham, E. R.; Morris, R. E., *J. Am. Chem. Soc.* **2006,** *128* (7), 2204-2205.

23. Morris, R. E., *Ionothermal Synthesis of Zeolites and Other Porous Materials*. Wiley-VCH Verlag GmbH & Co. KGaA: 2010; p 87-105.

24. Xie, Z.-L.; Feng, M.-L.; Li, J.-R.; Huang, X.-Y., *Inorg. Chem. Commun.* **2008,** *11* (10), 1143-1146.

25. Gagnon, K. J.; Prosvirin, A. V.; Dunbar, K. R.; Teat, S. J.; Clearfield, A., *Dalton Trans.* **2012,** *41* (14), 3995-4006.

26. Le Bideau, J.; Payen, C.; Palvadeau, P.; Bujoli, B., *Inorg. Chem.* **1994,** *33* (22), 4885-4890.

27. Maeda, K.; Akimoto, J.; Kiyozumi, Y.; Mizukami, F., *Angew. Chem., Int. Ed. Engl.* **1995,** *34* (11), 1199-1201.

28. Maeda, K.; Akimoto, J.; Kiyozumi, Y.; Mizukami, F., *J. Chem. Soc., Chem. Commun.* **1995,** (10), 1033-1034.

29. Maeda, K.; Kiyozumi, Y.; Mizukami, F., *Angewandte Chemie International Edition in English* **1994,** *33* (22), 2335-2337.

30. Lohse, D. L.; Sevov, S. C., *Angew. Chem., Int. Ed. Engl.* **1997,** *36* (15), 1619-1621.

31. Gao, Q.; Guillou, N.; Nogues, M.; Cheetham, A. K.; Férey, G., *Chem. Mater.* **1999,** *11* (10), 2937-2947.

32. Yuan, Z.; Clegg, W.; Attfield, M. P., *J. Solid State Chem.* **2009,** *182* (11), 3049-3054.

33. Poojary, D. M.; Zhang, B.; Clearfield, A., *J. Am. Chem. Soc.* **1997,** *119* (51), 12550-12559.

34. Poojary, D. M.; Zhang, B.; Clearfield, A., *Chem. Mater.* **1999,** *11* (2), 421-426.

35. Arnold, D. I.; Ouyang, X.; Clearfield, A., *Chem. Mater.* **2002,** *14* (5), 2020-2027.

36. Riou, D.; Ferey, G., *J. Mater. Chem.* **1998,** *8* (12), 2733-2735.

37. Barthelet, K.; Marrot, J.; Riou, D.; Férey, G., *Ang. Chem. Int. Ed.* **2002,** *41* (2), 281-284.

38. Yaghi, O. M.; O'Keeffe, M.; Ockwig, N. W.; Chae, H. K.; Eddaoudi, M.; Kim, J., *Nature* **2003,** *423* (6941), 705-714.

39. Maeda, K., *Micropor. Mesopor. Mater.* **2004,** *73* (1-2), 47-55.

40. Rowsell, J. L. C.; Millward, A. R.; Park, K. S.; Yaghi, O. M., *J. Am. Chem. Soc.* **2004,** *126* (18), 5666-5667.

41. Special Issue on Metal-Organic Frameworks. In *Chem. Rev.*, **2012**, *112*, 673-1268.

42. Kepert, C. J., *Chem. Commun.* **2006,** (7), 695-700.

43. Kitagawa, S.; Kitaura, R.; Noro, S.-i., *Angew. Chem. Int. Ed.* **2004,** *43* (18), 2334-2375.

44. Zhang, B.; Wang, Z. M.; Kurmoo, M.; Gao, S.; Inoue, K.; Kobayashi, H., *Adv. Funct. Mater.* **2007,** *17* (4), 577-584.

45. Wang, Z.; Zhang, B.; Fujiwara, H.; Kobayashi, H.; Kurmoo, M., *Chem. Commun.* **2004,** (4), 416-417.

46. Lee, E. Y.; Suh, M. P., *Angew. Chem. Int. Ed.* **2004,** *43* (21), 2798-2801.

47. Ovcharenko, V. I.; Fokin, S. V.; Kostina, E. T.; Romanenko, G. V.; Bogomyakov, A. S.; Tretyakov, E. V., *Inorg. Chem.* **2012,** *51* (22), 12188-12194.

48. Zhang, Y.-J.; Liu, T.; Kanegawa, S.; Sato, O., *J. Am. Chem. Soc.* **2009,** *131* (23), 7942-7943.

49. Nihei, M.; Han, L.; Oshio, H., *J. Am. Chem. Soc.* **2007,** *129* (17), 5312-5313.

50. Tan, J. C.; Cheetham, A. K., *Chem. Soc. Rev.* **2011,** *40* (2), 1059-1080.

51. Parise, J. B., *Rev. Mineral. Geochem.* **2006,** *63* (1), 205-231.

52. Chapman, K. W.; Halder, G. J.; Chupas, P. J., *J. Am. Chem. Soc.* **2008,** *130* (32), 10524-10526.

53. Chapman, K. W.; Halder, G. J.; Chupas, P. J., *J. Am. Chem. Soc.* **2009,** *131* (48), 17546-17547.

54. Graham, A. J.; Allan, D. R.; Muszkiewicz, A.; Morrison, C. A.; Moggach, S. A., *Angew. Chem. Int. Ed.* **2011,** *50* (47), 11138-11141.

55. Ogborn, J. M.; Collings, I. E.; Moggach, S. A.; Thompson, A. L.; Goodwin, A. L., *Chemical Science* **2012,** *3* (10), 3011-3017.

56. Gagnon, K. J.; Beavers, C. M.; Clearfield, A., *J. Am. Chem. Soc.* **2013,** *135* (4), 1252-1255.

57. Mao, J.-G.; Wang, Z.; Clearfield, A., *Inorg. Chem.* **2002,** *41* (9), 2334-2340.

58. *SAINT Frame integration software*, v7.60a; Bruker AXS, Inc., Madison, WI: 2008.

59. Sheldrick, G. M. *SADABS, Program for Absorption Correction of Area Detector Frames*, Bruker AXS, Inc., Madison, WI.: 2008.

60. Sheldrick, G., *Acta Crystallographica Section A* **2008,** *64* (1), 112-122.

61. *TOPAS General Profile and Structure Analysis Software for Powder Diffraction Data*, v4.2; Bruker AXS, Karlsruhe, Germany: 2009.

62. Pawley, G., *J. Appl. Crystallogr.* **1981,** *14* (6), 357-361.

63. Shi, F.-N.; Trindade, T.; Rocha, J.; Paz, F. A. A., *Cryst. Growth Des.* **2008,** *8* (11), 3917-3920.

64. Welton, T., *Chem. Rev.* **1999,** *99* (8), 2071-2084.

65. Perry, H.; Zon, J.; Law, J.; Clearfield, A., *J. Solid State Chem.* **2010,** *183* (5), 1165-1173.

66. Shimizu, G. K. H.; Vaidhyanathan, R.; Taylor, J. M., *Chem. Soc. Rev.* **2009,** *38* (5), 1430-1449.

67. Colodrero, R. M. P.; Cabeza, A.; Olivera-Pastor, P.; Papadaki, M.; Rius, J.; Choquesillo-Lazarte, D.; García-Ruiz, J. M.; Demadis, K. D.; Aranda, M. A. G., *Cryst. Growth Des.* **2011,** *11* (5), 1713-1722.

68. Demadis, K. D.; Katarachia, S. D.; Raptis, R. G.; Zhao, H.; Baran, P., *Cryst. Growth Des.* **2006,** *6* (4), 836-838.

69. Perry, H. P.; Gagnon, K. J.; Law, J.; Teat, S.; Clearfield, A., *Dalton Trans.* **2012,** *41* (14), 3985-3994.

70. Chuang, Y.-H.; Liu, H.; O'Connor, C. J.; Zubieta, J., *Inorg. Chem. Commun.* **2008,** *11* (10), 1205-1208.

71. Yang, B.-P.; Prosvirin, A. V.; Zhao, H.-H.; Mao, J.-G., *J. Solid State Chem.* **2006,** *179* (1), 175-185.

72. Yang, B.-P.; Mao, J.-G., *Inorg. Chem.* **2005,** *44* (3), 566-571.

73. Bauer, S.; Müller, H.; Bein, T.; Stock, N., *Inorg. Chem.* **2005,** *44* (25), 9464-9470.

74. Yang, B.-P.; Sun, Z.-M.; Mao, J.-G., *Inorg. Chim. Acta* **2004,** *357* (5), 1583-1588.

75. Kong, D.; McBee, J. L.; Clearfield, A., *Cryst. Growth Des.* **2004,** *5* (2), 643-649.

76. Kong, D.; Li, Y.; Ouyang, X.; Prosvirin, A. V.; Zhao, H.; Ross, J. H.; Dunbar, K. R.; Clearfield, A., *Chem. Mater.* **2004,** *16* (16), 3020-3031.

77. Kong, D.; Li, Y.; Jr., J. H. R.; Clearfield, A., *Chem. Commun.* **2003,** (14), 1720-1721.

78. Mao, J.-G.; Wang, Z.; Clearfield, A., *J. Chem. Soc., Dalton Trans.* **2002,** (23), 4457-4463.

79. Mao, J.-G.; Wang, Z.; Clearfield, A., *Inorg. Chem.* **2002,** *41* (23), 6106-6111.

80. Kilyen, M.; Lakatos, A.; Latajka, R.; Labadi, I.; Salifoglou, A.; Raptopoulou, C. P.; Kozlowski, H.; Kiss, T., *J. Chem. Soc., Dalton Trans.* **2002,** (18), 3578-3586.

81. Jankovics, H.; Daskalakis, M.; Raptopoulou, C. P.; Terzis, A.; Tangoulis, V.; Giapintzakis, J.; Kiss, T.; Salifoglou, A., *Inorg. Chem.* **2002,** *41* (13), 3366-3374.

82. Cabeza, A.; Bruque, S.; Guagliardi, A.; Aranda, M. A. G., *J. Solid State Chem.* **2001,** *160* (1), 278-286.

83. Matczak-Jon, E.; Kurzak, B.; Kamecka, A.; Sawka-Dobrowolska, W.; Kafarski, P., *J. Chem. Soc., Dalton Trans.* **1999,** (20), 3627-3637.

84. Yang, B.-P.; Prosvirin, A. V.; Guo, Y.-Q.; Mao, J.-G., *Inorg. Chem.* **2008,** *47* (5), 1453-1459.

85. Nguyen, T. L. A.; Devic, T.; Mialane, P.; Rivière, E.; Sonnauer, A.; Stock, N.; Demir-Cakan, R.; Morcrette, M.; Livage, C.; Marrot, J. r.; Tarascon, J.-M.; Férey, G. r., *Inorg. Chem.* **2010,** *49* (22), 10710-10717.

86. Altermatt, D.; Brown, I. D., *Acta Crystallographica Section B* **1985,** *41* (4), 240-244.

87. Bakhmutova, E. V.; Ouyang, X.; Medvedev, D. G.; Clearfield, A., *Inorg. Chem.* **2003,** *42* (22), 7046-7051.

88. Subramaniam, V.; Hoggard, P. E., *J. Agric. Food. Chem.* **1988,** *36* (6), 1326-1329.

89. Feng, M.-L.; Prosvirin, A. V.; Mao, J.-G.; Dunbar, K. R., *Chemistry – A European Journal* **2006,** *12* (32), 8312-8323.

90. Estes, W. E.; Gavel, D. P.; Hatfield, W. E.; Hodgson, D. J., *Inorg. Chem.* **1978,** *17* (6), 1415-1421.

91. Byrne, P. J.; Wragg, D. S.; Warren, J. E.; Morris, R. E., *Dalton Trans.* **2009,** (5), 795-799.

92. Attfield, M. P.; Yuan, Z.; Harvey, H. G.; Clegg, W., *Inorg. Chem.* **2010,** *49* (6), 2656-2666.

93. Schmidt, C.; Stock, N., *Inorg. Chem.* **2012,** *51* (5), 3108-3118.

94. Fu, R.-B.; Wu, X.-T.; Hu, S.-M.; Zhang, J.-J.; Fu, Z.-Y.; Du, W.-X., *Polyhedron* **2003,** *22* (19), 2739-2744.

95. Arnold, D. I. The Synthesis and Characterization of Zinc(II) and Copper(II) Diphophonatoalkanes. Texas A&M University, Texas A&M University, 2000.

96. Fu, R.; Huang, X.; Hu, S.; Xiang, S.; Wu, X., *Inorg. Chem.* **2006,** *45* (14), 5254-5256.

97. Zon, J.; Kong, D.; Gagnon, K.; Perry, H.; Holliness, L.; Clearfield, A., *Dalton Trans.* **2010,** *39* (45), 11008-11018.

98. Clearfield, A., *Curr. Opin. Solid State Mater. Sci.* **2002,** *6* (6), 495-506.

99. Krishnamohan Sharma, C. V.; Clearfield, A., *J. Am. Chem. Soc.* **2000,** *122* (7), 1558-1559.

100. Konar, S.; Zoń, J.; Prosvirin, A. V.; Dunbar, K. R.; Clearfield, A., *Inorg. Chem.* **2007,** *46* (13), 5229-5236.

101. Jaffrès, P.-A.; Villemin, D.; Montouillout, V.; Fernandez, C.; Chardon, J.; Sopkova-De Oliveira Santos, J., *Mol. Cryst. Liq. Cryst.* **2002,** *389* (1), 87-95.

102. Halder, G. J.; Kepert, C. J.; Moubaraki, B.; Murray, K. S.; Cashion, J. D., *Science* **2002,** *298* (5599), 1762-1765.

103. Maspoch, D.; Ruiz-Molina, D.; Veciana, J., *J. Mater. Chem.* **2004,** *14* (18), 2713-2723.

104. Cheng, X. N.; Zhang, W. X.; Lin, Y. Y.; Zheng, Y. Z.; Chen, X. M., *Adv. Mater.* **2007,** *19* (11), 1494-1498.

105. Yanai, N.; Kaneko, W.; Yoneda, K.; Ohba, M.; Kitagawa, S., *J. Am. Chem. Soc.* **2007,** *129* (12), 3496-3497.

106. Guillou, N.; Livage, C.; van Beek, W.; Noguès, M.; Férey, G., *Angew. Chem. Int. Ed.* **2003,** *42* (6), 643-647.

107. Niel, V.; Thompson, A. L.; Muñoz, M. C.; Galet, A.; Goeta, A. E.; Real, J. A., *Angew. Chem. Int. Ed.* **2003,** *42* (32), 3760-3763.

108. Haldar, R.; Maji, T. K., *CrystEngComm* **2012,** *14* (2), 684-690.

109. Liu, X.-M.; Wang, B.-Y.; Xue, W.; Xie, L.-H.; Zhang, W.-X.; Cheng, X.-N.; Chen, X.-M., *Dalton Trans.* **2012,** *41* (44), 13741-13746.

110. Ma, C.-B.; Hu, M.-Q.; Chen, H.; Wang, M.; Zhang, C.-X.; Chen, C.-N.; Liu, Q.-T., *CrystEngComm* **2010,** *12* (5), 1467-1473.

111. Cao, M.-L.; Mo, H.-J.; Liang, J.-J.; Ye, B.-H., *CrystEngComm* **2009,** *11* (5), 784-790.

112. Cheng, X.-N.; Zhang, W.-X.; Chen, X.-M., *J. Am. Chem. Soc.* **2007,** *129* (51), 15738-15739.

113. Sarma, D.; Natarajan, S., *Cryst. Growth Des.* **2011,** *11* (12), 5415-5423.

114. Yoshida, Y.; Inoue, K.; Kurmoo, M., *Inorg. Chem.* **2008,** *48* (1), 267-276.

115. Aromí, G.; Barrios, L. A.; Roubeau, O.; Gamez, P., *Coord. Chem. Rev.* **2011,** *255* (5–6), 485-546.

116. Phan, A.; Doonan, C. J.; Uribe-Romo, F. J.; Knobler, C. B.; O'Keeffe, M.; Yaghi, O. M., *Acc. Chem. Res.* **2009,** *43* (1), 58-67.

117. Piermarini, G. J.; Block, S.; Barnett, J. D.; Forman, R. A., *J. Appl. Phys.* **1975,** *46* (6), 2774-2780.

118. Angel, R. J., *Rev. Mineral. Geochem.* **2000,** *41* (1), 35-59.

119. Baughman, R. H.; Stafström, S.; Cui, C.; Dantas, S. O., *Science* **1998,** *279* (5356), 1522-1524.

120. Li, W.; Probert, M. R.; Kosa, M.; Bennett, T. D.; Thirumurugan, A.; Burwood, R. P.; Parinello, M.; Howard, J. A. K.; Cheetham, A. K., *J. Am. Chem. Soc.* **2012,** *134* (29), 11940-11943.

121. Godwin, J. G.; Ge, X.; Stephan, K.; Jurisch, A.; Tullius, S. G.; Iacomini, J., *Proceedings of the National Academy of Sciences* **2010,** *107* (32), 14339-14344.

122. Grima, J. N.; Attard, D.; Caruana-Gauci, R.; Gatt, R., *Scripta Mater.* **2011,** *65* (7), 565-568.

APPENDIX A

NEW EQUIPMENT DESIGNS

The following are the plans for the various pieces of equipment designed and used in the experiments involved in this dissertation. Thanks to William Seward for his help in turning these drawings into fabrications. The drawings are of the parts involved with two different sizes of steel pressure vessels, a 16 chamber 4 x 4 aluminum high pressure vessel, and a modified, smaller, lighter diamond anvil cell.

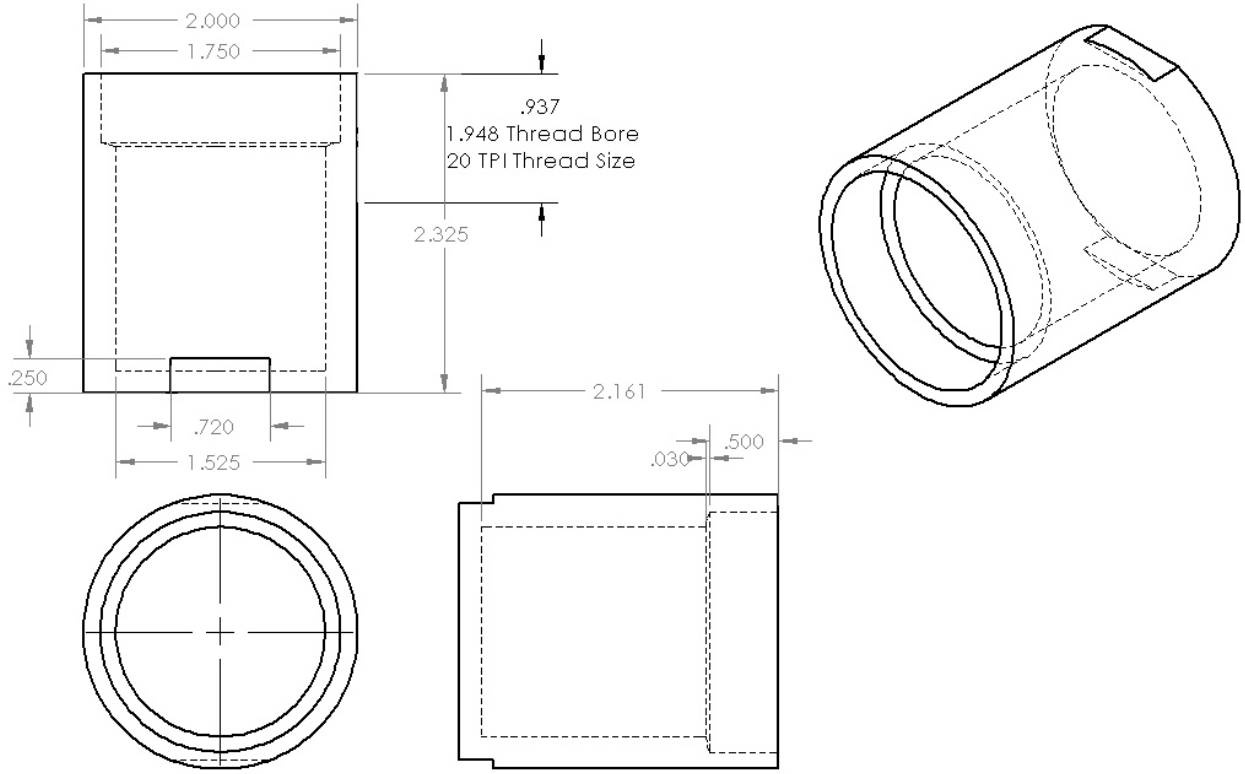

		UNLESS OTHERWISE SPECIFIED:		NAME	DATE
		DIMENSIONS ARE IN INCHES TOLERANCES: FRACTIONAL ± ANGULAR: MACH ± BEND ± TWO PLACE DECIMAL ± THREE PLACE DECIMAL ±	DRAWN		
			CHECKED		
			ENG APPR.		
			MFG APPR.		
		INTERPRET GEOMETRIC TOLERANCING PER:	Q.A.		
		MATERIAL	COMMENTS:		
NEXT ASSY	USED ON	FINISH			
APPLICATION		DO NOT SCALE DRAWING			

TITLE:

SIZE	DWG. NO.	REV
A3	small_vessel_bottom	
SCALE: 1:1	WEIGHT:	SHEET 1 OF 1

5 4 3 2 1

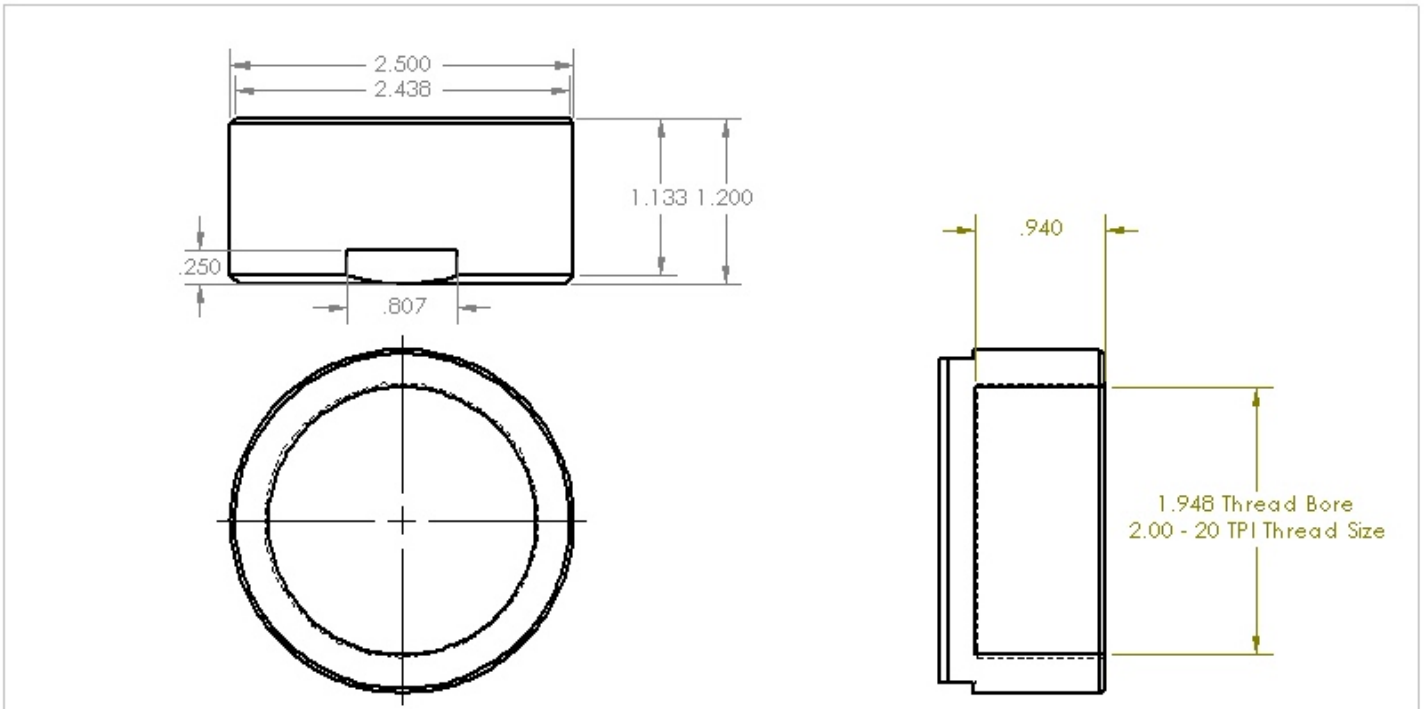

		UNLESS OTHERWISE SPECIFIED:		NAME	DATE
		DIMENSIONS ARE IN INCHES TOLERANCES: FRACTIONAL ± ANGULAR: MACH ± BEND ± TWO PLACE DECIMAL ± THREE PLACE DECIMAL ±	DRAWN		
			CHECKED		
			ENG APPR.		
			MFG APPR.		
			Q.A.		
		PROPERTY DOMYTRIC TOLERANCING PER:	COMMENTS:		
		MATERIAL Stainless 304			
NEXT ASSY	USED ON	FINISH			
APPLICATION		DO NOT SCALE DRAWING			

PROPRIETARY AND CONFIDENTIAL

THE INFORMATION CONTAINED IN THIS DRAWING IS THE SOLE PROPERTY OF <ENTER COMPANY NAME HERE>. ANY REPRODUCTION IN PART OR AS A WHOLE WITHOUT THE WRITTEN PERMISSION OF <ENTER COMPANY NAME HERE> IS PROHIBITED.

TITLE:

small_vessel_lid

SIZE	DWG. NO.	REV
A		

SCALE: 1:1	WEIGHT:	SHEET 1 OF 1

5 4 3 2 1

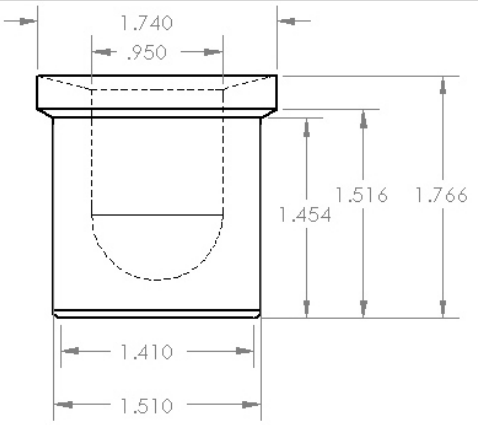

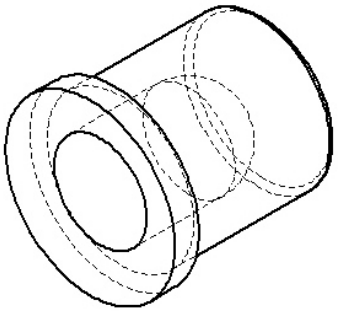

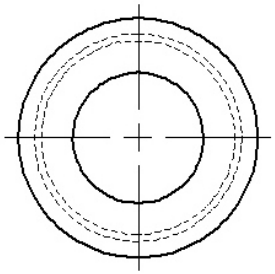

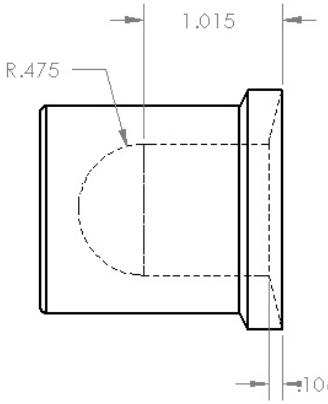

		UNLESS OTHERWISE SPECIFIED:		NAME	DATE
		DIMENSIONS ARE IN INCHES TOLERANCES: FRACTIONAL ± ANGULAR: MACH ± BEND ± TWO PLACE DECIMAL ± THREE PLACE DECIMAL ±	DRAWN		
			CHECKED		
			ENG APPR.		
			MFG APPR.		
		INTERPRET GEOMETRIC TOLERANCING PER:	Q.A.		
		MATERIAL Virgin PTFE	COMMENTS:		
NEXT ASSY	USED ON	FINISH			
APPLICATION		DO NOT SCALE DRAWING			

TITLE:
small_teflon_bottom

SIZE	DWG. NO.	REV
A		
SCALE: 1:1	WEIGHT:	SHEET 1 OF 1

5 4 3 2 1

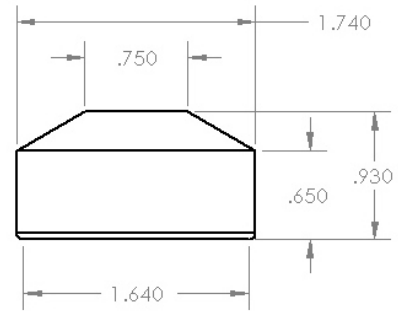

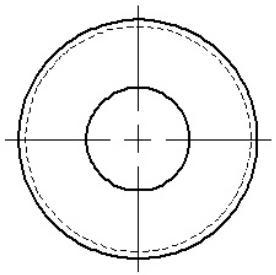

		UNLESS OTHERWISE SPECIFIED:		NAME	DATE
		DIMENSIONS ARE IN INCHES TOLERANCES: FRACTIONAL ± ANGULAR: MACH ± BEND ± TWO PLACE DECIMAL ± THREE PLACE DECIMAL ±	DRAWN		
			CHECKED		
			ENG APPR.		
			MFG APPR.		
			Q.A.		
		INTERPRET GEOMETRIC TOLERANCING PER:	COMMENTS:		
		MATERIAL Virgin PTFE			
NEXT ASSY	USED ON	FINISH			
APPLICATION		DO NOT SCALE DRAWING			

TITLE:

small_teflon_lid

SIZE	DWG. NO.	REV
A		

SCALE: 1:1	WEIGHT:	SHEET 1 OF 1

5 4 3 2 1

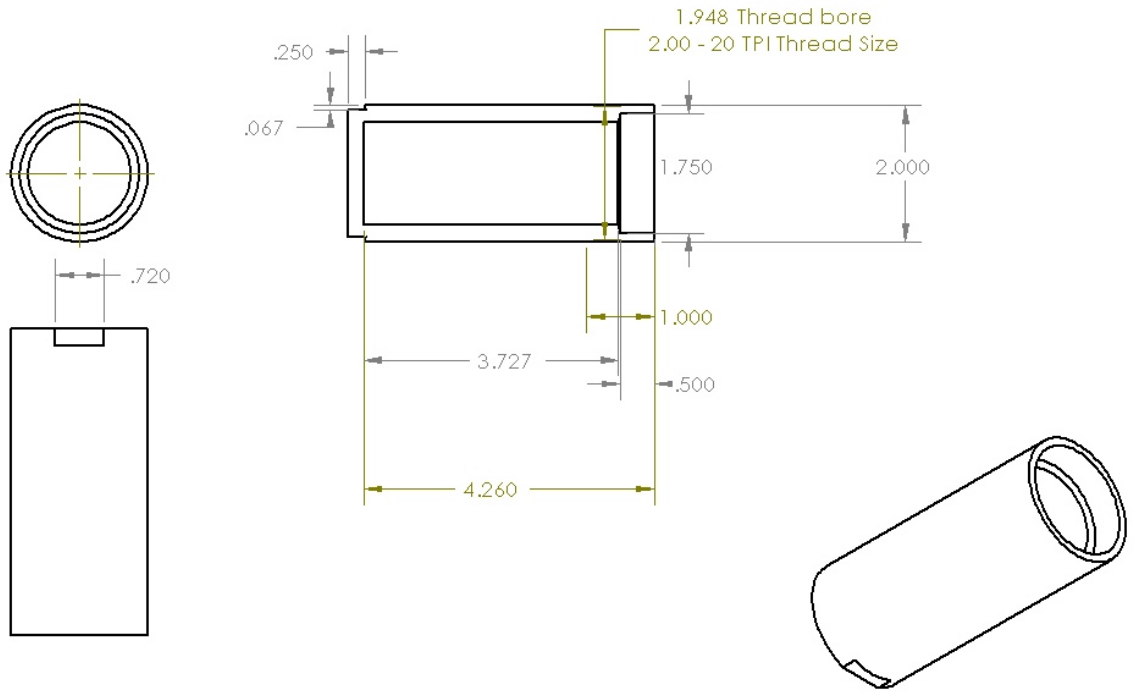

		UNLESS OTHERWISE SPECIFIED:		NAME	DATE
		DIMENSIONS ARE IN INCHES TOLERANCES: FRACTIONAL ± ANGULAR: MACH ± BEND ± TWO PLACE DECIMAL ± THREE PLACE DECIMAL ±	DRAWN		
			CHECKED		
			ENG APPR.		
			MFG APPR.		
		INTERPRET GEOMETRIC TOLERANCING PER:	Q.A.		
		MATERIAL Stainless 304	COMMENTS:		
NEXT ASSY	USED ON	FINISH			
APPLICATION		DO NOT SCALE DRAWING			

TITLE:

tall_vessel_bottom

SIZE	DWG. NO.	REV
A		
SCALE: 1:2	WEIGHT:	SHEET 1 OF 1

5 4 3 2 1

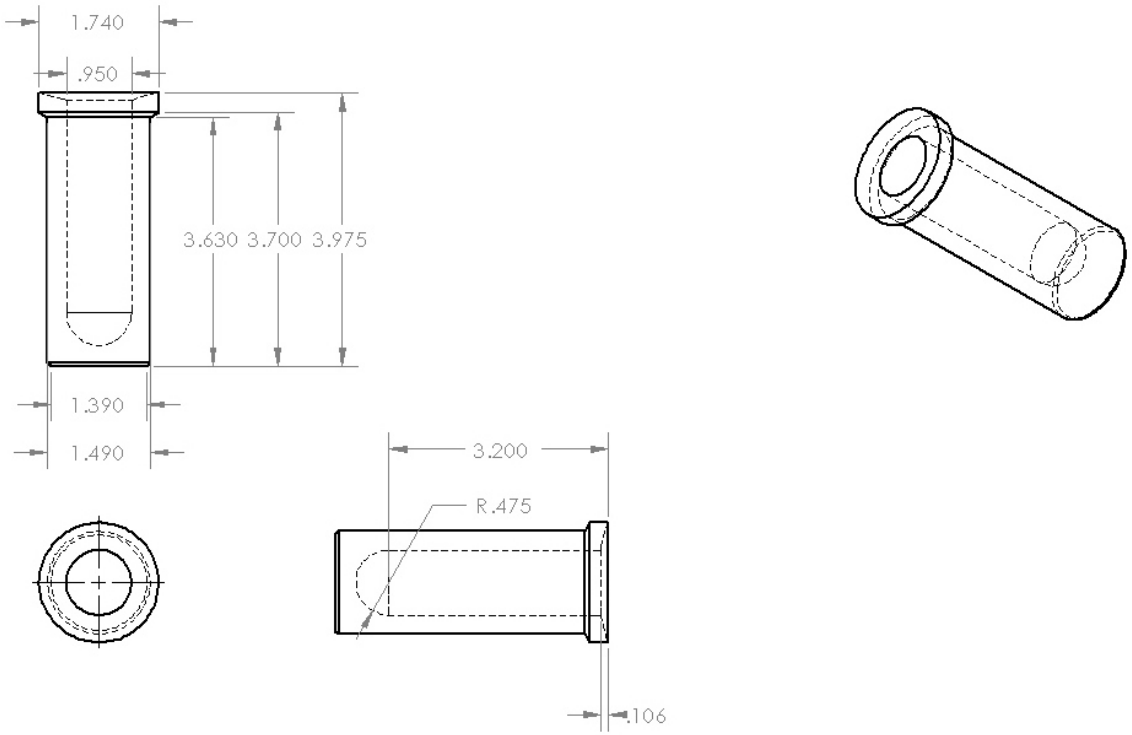

		UNLESS OTHERWISE SPECIFIED:		NAME	DATE
		DIMENSIONS ARE IN INCHES TOLERANCES: FRACTIONAL ± ANGULAR: MACH ± BEND ± TWO PLACE DECIMAL ± THREE PLACE DECIMAL ±	DRAWN		
			CHECKED		
			ENG APPR.		
			MFG APPR.		
		INTERPRET GEOMETRIC TOLERANCING PER:	Q.A.		
		MATERIAL Virgin PTFE	COMMENTS:		
NEXT ASSY	USED ON	FINISH			
APPLICATION		DO NOT SCALE DRAWING			

TITLE:

tall_teflon_bottom

SIZE	DWG. NO.	REV
A		
SCALE: 1:2	WEIGHT:	SHEET 1 OF 1

5 4 3 2 1

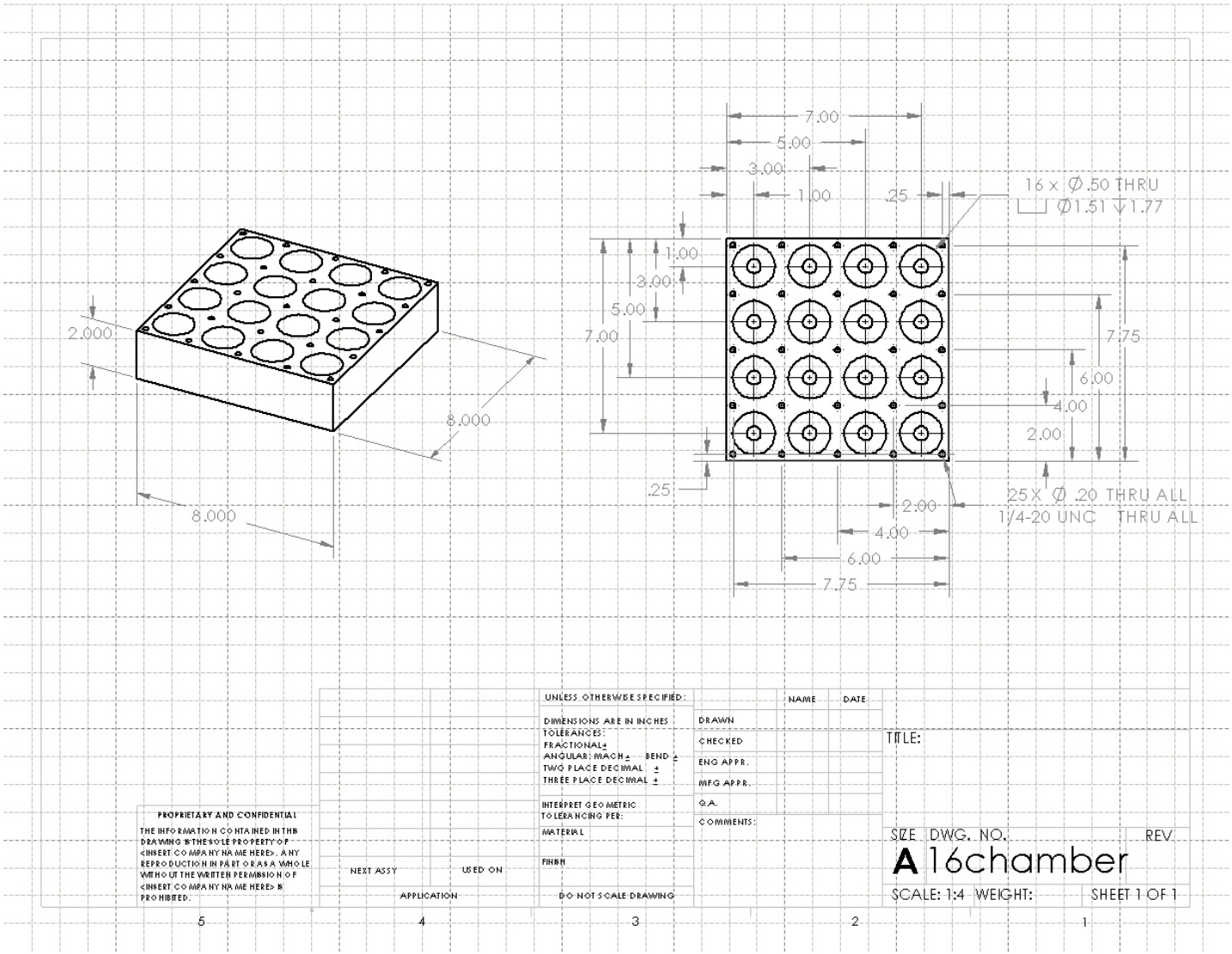
2.000
8.000
8.000
7.00
5.00
3.00
1.00
.25
16 x Ø.50 THRU
⌴ Ø1.51 ↧1.77
1.00
3.00
5.00
7.00
7.75
6.00
4.00
2.00
.25
.25 X Ø .20 THRU ALL
1/4-20 UNC THRU ALL
2.00
4.00
6.00
7.75
UNLESS OTHERWISE SPECIFIED:
NAME
DATE
DIMENSIONS ARE IN INCHES
TOLERANCES:
FRACTIONAL ±
ANGULAR: MACH ± BEND ±
TWO PLACE DECIMAL ±
THREE PLACE DECIMAL ±
INTERPRET GEOMETRIC TOLERANCING PER:
MATERIAL
FINISH
DRAWN
CHECKED
ENG APPR.
MFG APPR.
Q.A.
COMMENTS:
TITLE:
SIZE DWG. NO. REV.
A 16chamber
SCALE: 1:4 WEIGHT: SHEET 1 OF 1
PROPRIETARY AND CONFIDENTIAL
THE INFORMATION CONTAINED IN THIS DRAWING IS THE SOLE PROPERTY OF <INSERT COMPANY NAME HERE>. ANY REPRODUCTION IN PART OR AS A WHOLE WITHOUT THE WRITTEN PERMISSION OF <INSERT COMPANY NAME HERE> IS PROHIBITED.
NEXT ASSY
USED ON
APPLICATION
DO NOT SCALE DRAWING
5
4
3
2
1

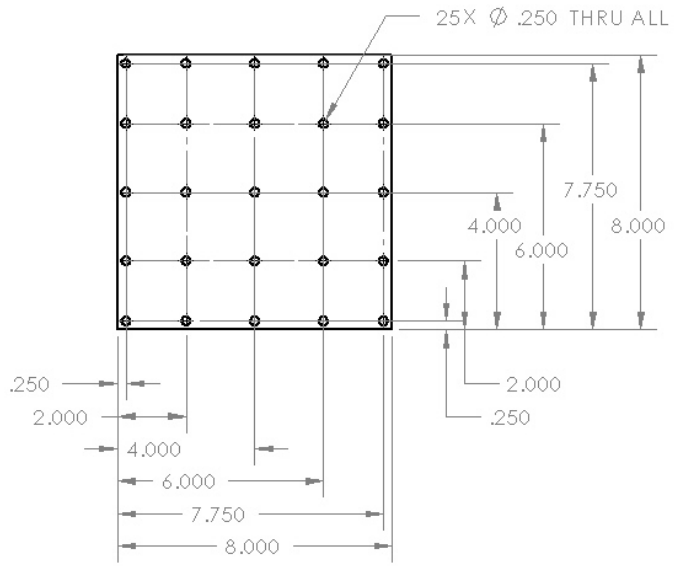

		UNLESS OTHERWISE SPECIFIED:		NAME	DATE
		DIMENSIONS ARE IN INCHES TOLERANCES: FRACTIONAL ± ANGULAR: MACH ± BEND ± TWO PLACE DECIMAL ± THREE PLACE DECIMAL ±	DRAWN		
			CHECKED		
			ENG APPR.		
			MFG APPR.		
			Q.A.		
		INTERPRET GEOMETRIC TOLERANCING PER:	COMMENTS:		
		MATERIAL			
NEXT ASSY	USED ON	FINISH			
APPLICATION		DO NOT SCALE DRAWING			

TITLE:

SIZE	DWG. NO.	REV
A	Aluminum_top	
SCALE: 1:4	WEIGHT:	SHEET 1 OF 1

5 4 3 2 1

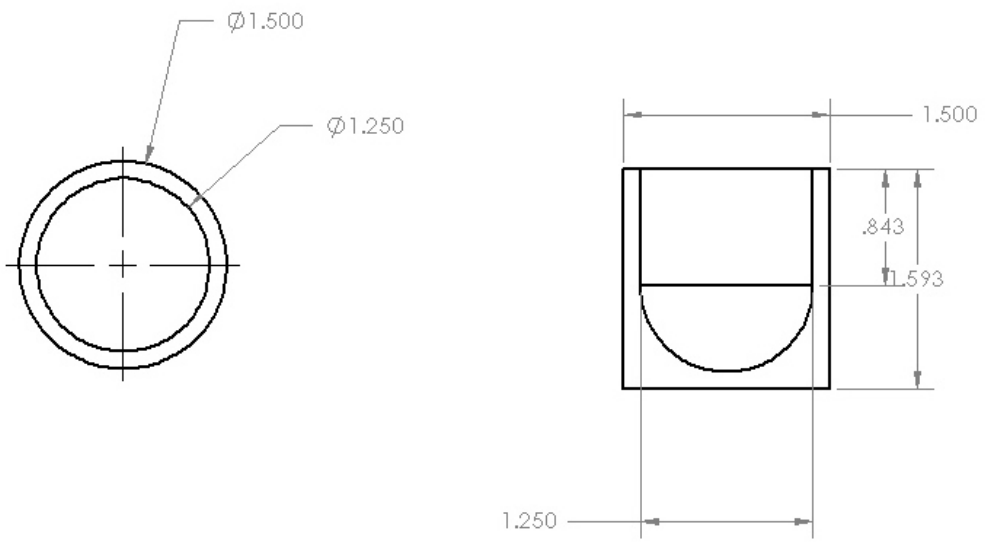

		UNLESS OTHERWISE SPECIFIED:		NAME	DATE
		DIMENSIONS ARE IN INCHES TOLERANCES: FRACTIONAL ± ANGULAR: MACH ± BEND ± TWO PLACE DECIMAL ± THREE PLACE DECIMAL ±	DRAWN		
			CHECKED		
			ENG APPR.		
			MFG APPR.		
		INTERPRET GEOMETRIC TOLERANCING PER:	Q.A.		
		MATERIAL	COMMENTS:		
NEXT ASSY	USED ON	FINISH			
APPLICATION		DO NOT SCALE DRAWING			

PROPRIETARY AND CONFIDENTIAL

THE INFORMATION CONTAINED IN THIS DRAWING IS THE SOLE PROPERTY OF <INSERT COMPANY NAME HERE>. ANY REPRODUCTION IN PART OR AS A WHOLE WITHOUT THE WRITTEN PERMISSION OF <INSERT COMPANY NAME HERE> IS PROHIBITED.

TITLE:

SIZE	DWG. NO.	REV
A	A6_chamb_cup	
SCALE: 1:1	WEIGHT:	SHEET 1 OF 1

5 4 3 2 1

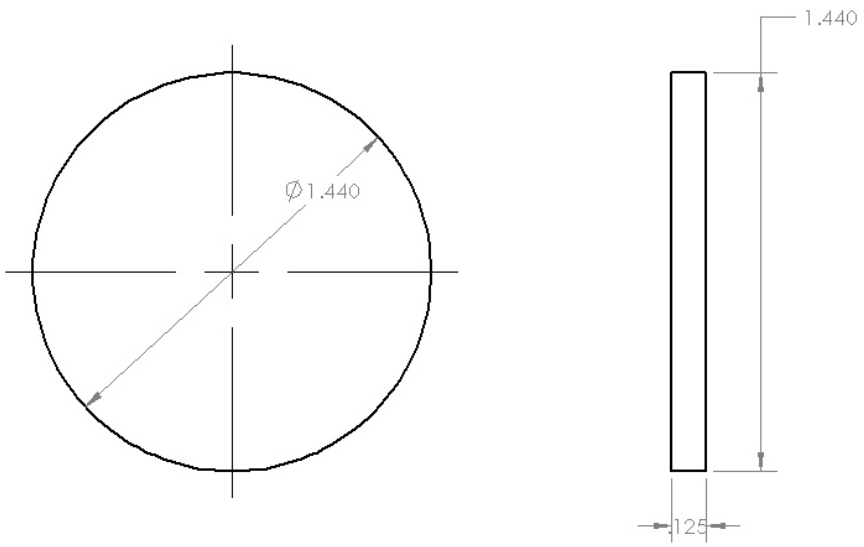

		UNLESS OTHERWISE SPECIFIED:		NAME	DATE
		DIMENSIONS ARE IN INCHES TOLERANCES: FRACTIONAL ± ANGULAR: MACH ± BEND ± TWO PLACE DECIMAL ± THREE PLACE DECIMAL ±	DRAWN		
			CHECKED		
			ENG APPR.		
			MFG APPR.		
		INTERPRET GEOMETRIC TOLERANCING PER:	Q.A.		
		MATERIAL	COMMENTS:		
NEXT ASSY	USED ON	FINISH			
APPLICATION		DO NOT SCALE DRAWING			

TITLE:

SIZE	DWG. NO.	REV
A	hole_plug	
SCALE: 2:1	WEIGHT:	SHEET 1 OF 1

5 4 3 2 1

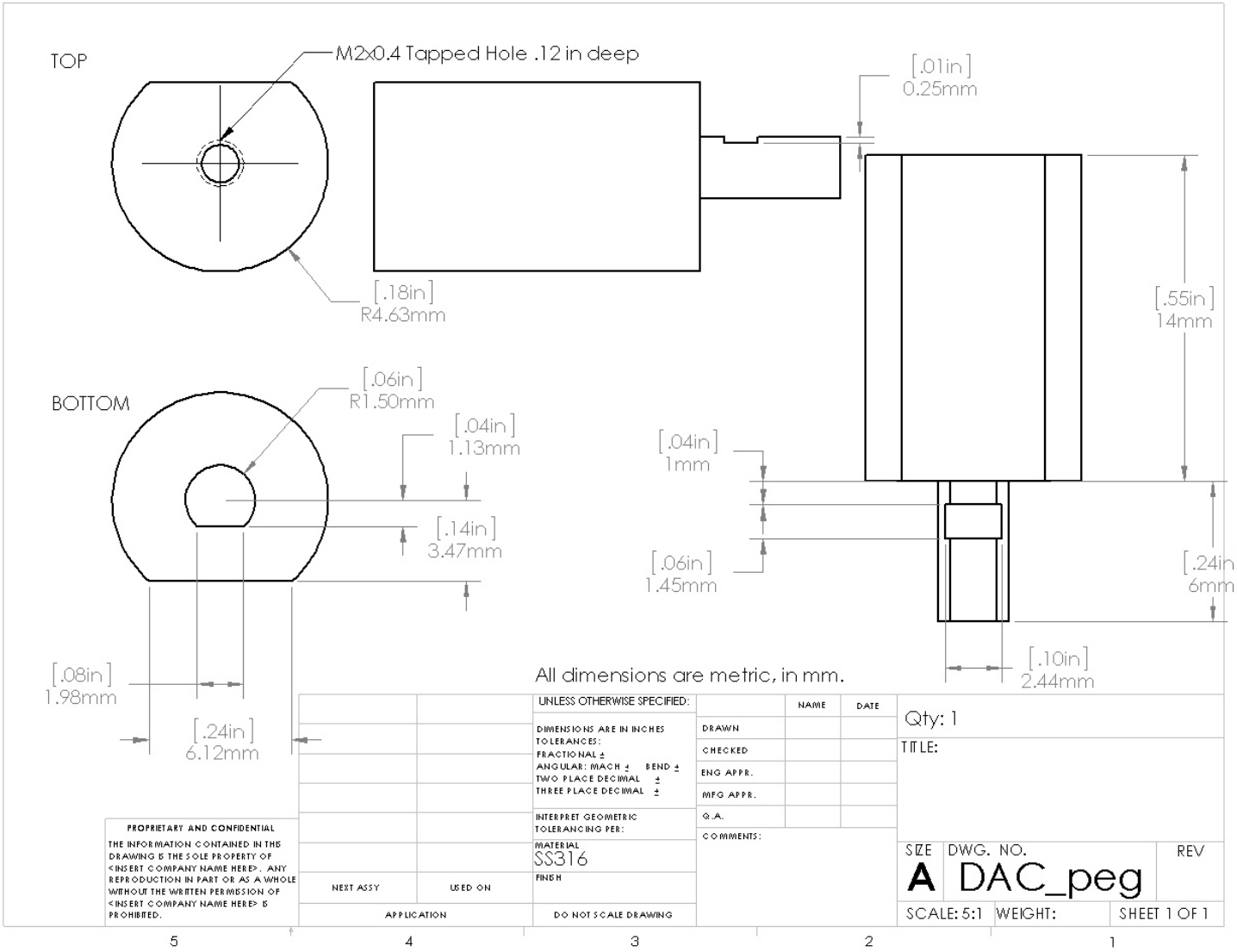
TOP
M2x0.4 Tapped Hole .12 in deep
[.01in]
0.25mm
[.18in]
R4.63mm
[.55in]
14mm
BOTTOM
[.06in]
R1.50mm
[.04in]
1.13mm
[.14in]
3.47mm
[.04in]
1mm
[.06in]
1.45mm
[.24in]
6mm
[.10in]
2.44mm
[.08in]
1.98mm
[.24in]
6.12mm
All dimensions are metric, in mm.
UNLESS OTHERWISE SPECIFIED:
DIMENSIONS ARE IN INCHES
TOLERANCES:
FRACTIONAL ±
ANGULAR: MACH ± BEND ±
TWO PLACE DECIMAL ±
THREE PLACE DECIMAL ±
INTERPRET GEOMETRIC TOLERANCING PER:
MATERIAL
SS316
FINISH
DO NOT SCALE DRAWING
NAME
DATE
DRAWN
CHECKED
ENG APPR.
MFG APPR.
Q.A.
COMMENTS:
Qty: 1
TITLE:
SIZE
A
DWG. NO.
DAC_peg
REV
SCALE: 5:1
WEIGHT:
SHEET 1 OF 1
NEXT ASSY
USED ON
APPLICATION
PROPRIETARY AND CONFIDENTIAL
THE INFORMATION CONTAINED IN THIS DRAWING IS THE SOLE PROPERTY OF <INSERT COMPANY NAME HERE>. ANY REPRODUCTION IN PART OR AS A WHOLE WITHOUT THE WRITTEN PERMISSION OF <INSERT COMPANY NAME HERE> IS PROHIBITED.
5
4
3
2
1

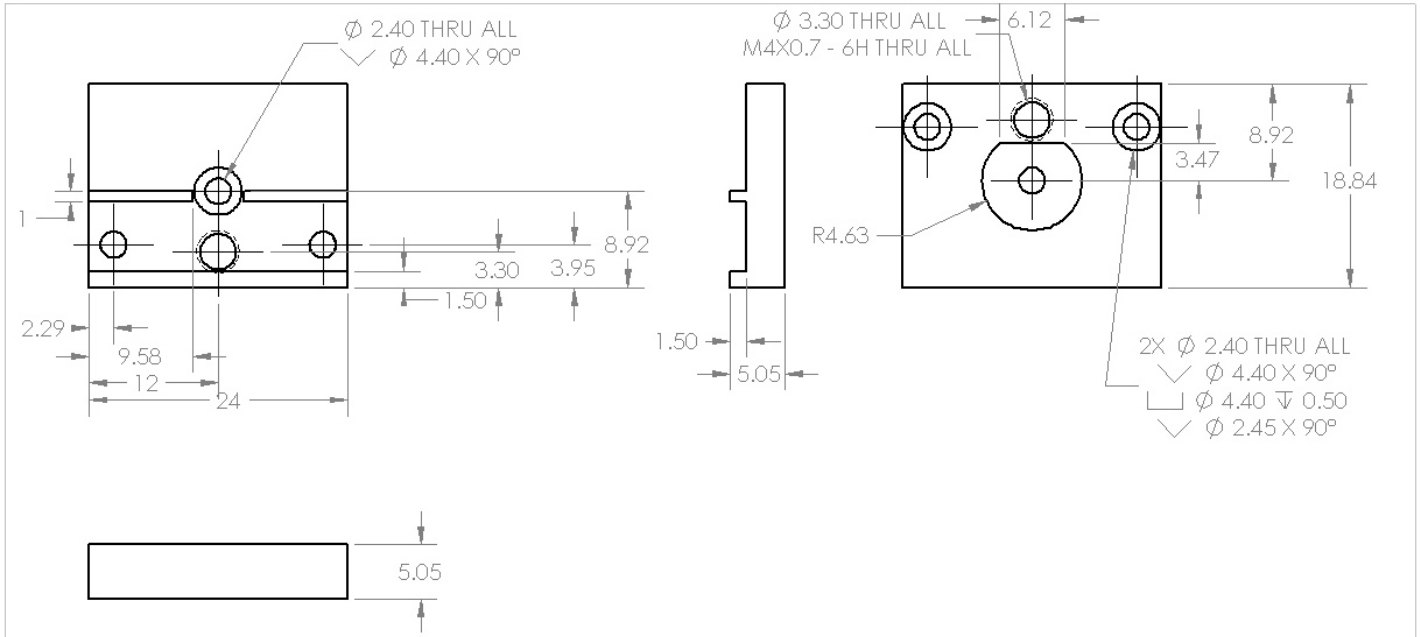

All dimensions are metric in mm.

		UNLESS OTHERWISE SPECIFIED:		NAME	DATE
		DIMENSIONS ARE IN INCHES TOLERANCES: FRACTIONAL ± ANGULAR: MACH ± BEND ± TWO PLACE DECIMAL ± THREE PLACE DECIMAL ±	DRAWN		
			CHECKED		
			ENG APPR.		
			MFG APPR.		
			Q.A.		
		INTERPRET GEOMETRIC TOLERANCING PER:	COMMENTS:		
		MATERIAL Aluminum			
NEXT ASSY	USED ON	FINISH			
APPLICATION		DO NOT SCALE DRAWING			

Qty: 1

TITLE:

SIZE	DWG. NO.	REV
A	DAC base	
SCALE: 2:1	WEIGHT:	SHEET 1 OF 1

5 4 3 2 1

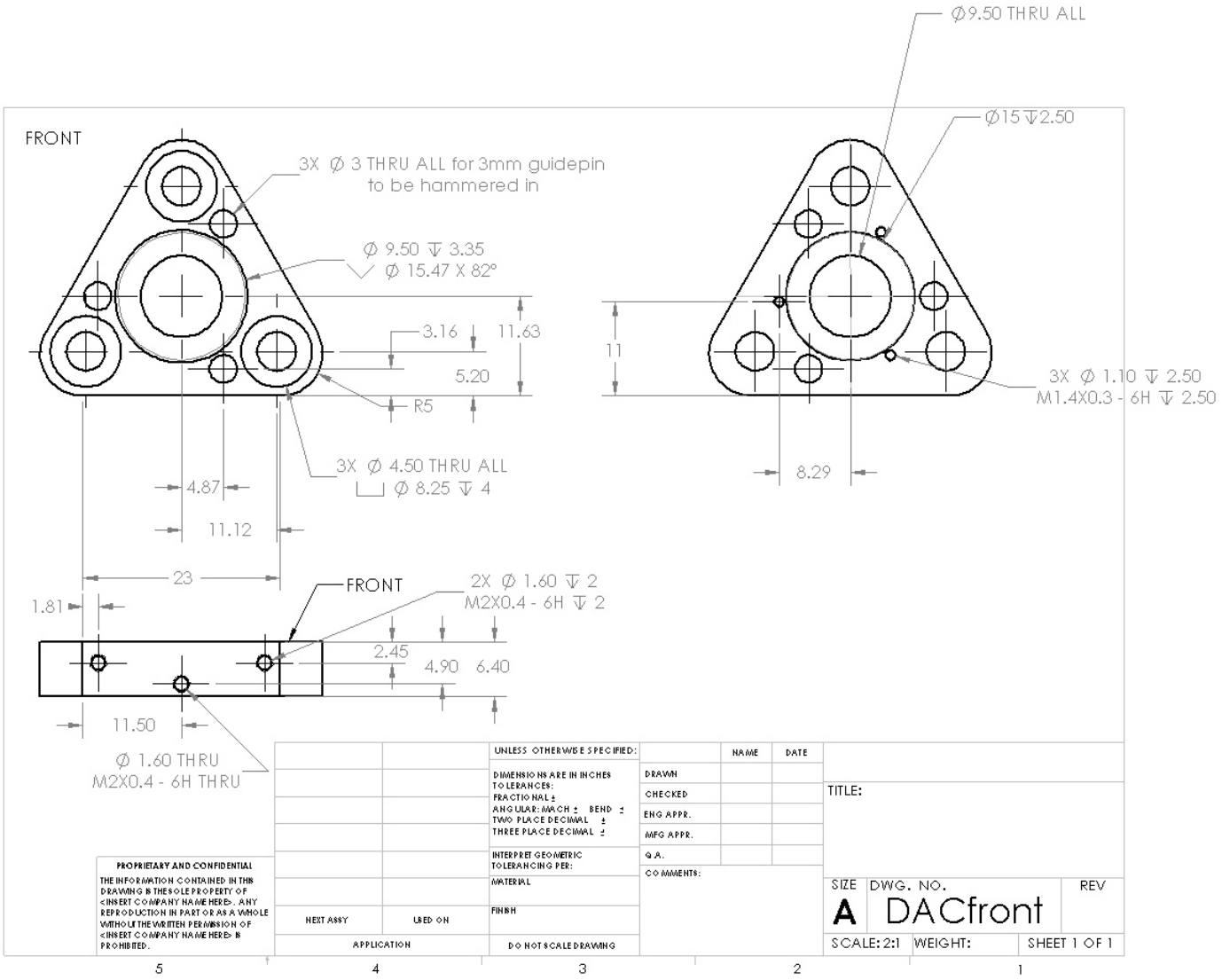
FRONT
3X Ø 3 THRU ALL for 3mm guidepin
to be hammered in
Ø 9.50 ↧ 3.35
Ø 15.47 X 82°
3.16
11.63
5.20
R5
3X Ø 4.50 THRU ALL
⌴ Ø 8.25 ↧ 4
4.87
11.12
23
1.81
FRONT
2X Ø 1.60 ↧ 2
M2X0.4 - 6H ↧ 2
2.45
4.90
6.40
11.50
Ø 1.60 THRU
M2X0.4 - 6H THRU
Ø9.50 THRU ALL
Ø15 ↧2.50
11
3X Ø 1.10 ↧ 2.50
M1.4X0.3 - 6H ↧ 2.50
8.29
UNLESS OTHERWISE SPECIFIED:
DIMENSIONS ARE IN INCHES
TOLERANCES:
FRACTIONAL ±
ANGULAR: MACH ± BEND ±
TWO PLACE DECIMAL ±
THREE PLACE DECIMAL ±
INTERPRET GEOMETRIC
TOLERANCING PER:
MATERIAL
FINISH
DO NOT SCALE DRAWING
NAME
DATE
DRAWN
CHECKED
ENG APPR.
MFG APPR.
Q.A.
COMMENTS:
TITLE:
SIZE
A
DWG. NO.
DACfront
REV
SCALE: 2:1
WEIGHT:
SHEET 1 OF 1
NEXT ASSY
USED ON
APPLICATION
PROPRIETARY AND CONFIDENTIAL
THE INFORMATION CONTAINED IN THIS DRAWING IS THE SOLE PROPERTY OF <INSERT COMPANY NAME HERE>. ANY REPRODUCTION IN PART OR AS A WHOLE WITHOUT THE WRITTEN PERMISSION OF <INSERT COMPANY NAME HERE> IS PROHIBITED.
5
4
3
2
1

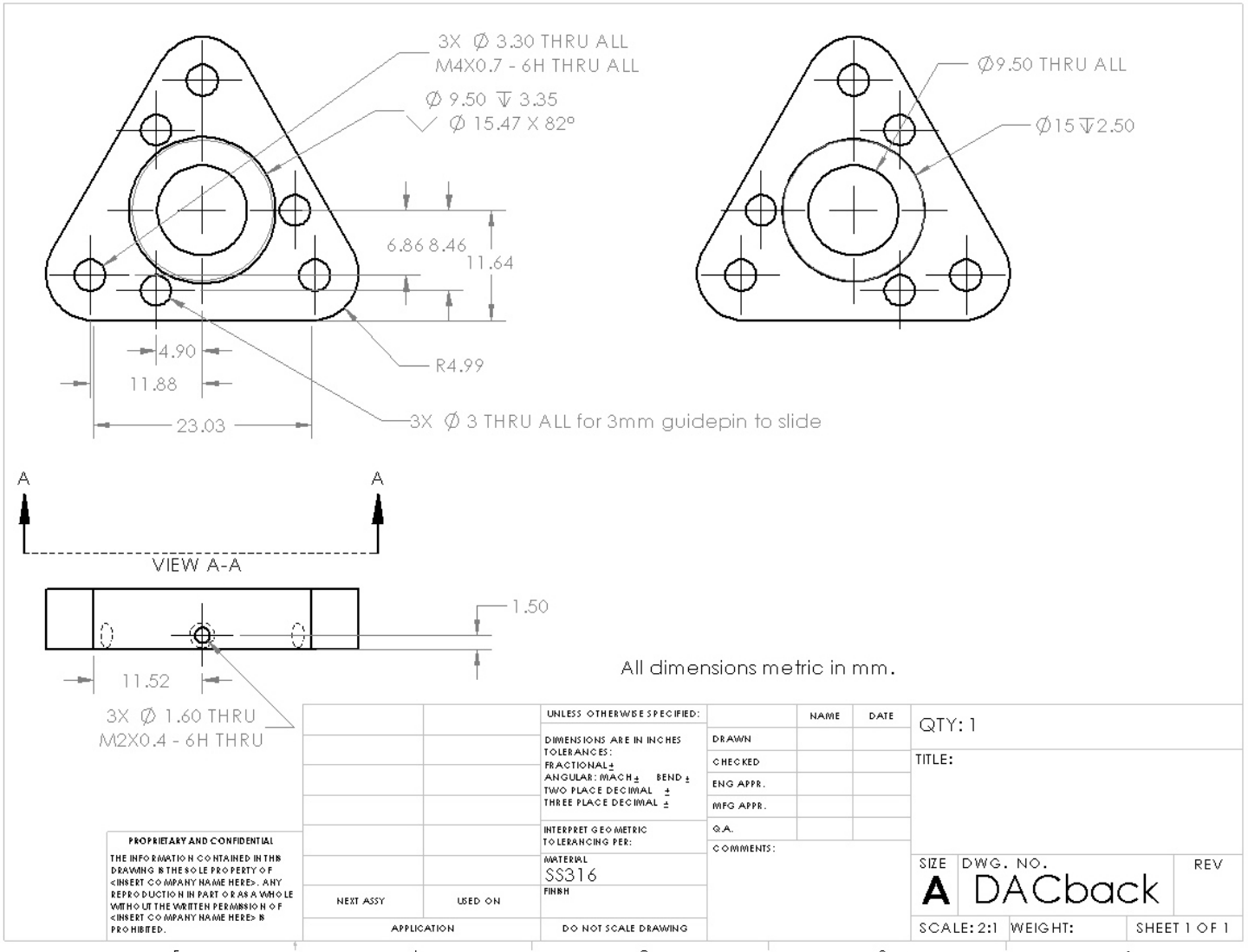
3X Ø 3.30 THRU ALL
M4X0.7 - 6H THRU ALL
Ø 9.50 ↧ 3.35
Ø 15.47 X 82°
6.86 8.46
11.64
4.90
11.88
23.03
R4.99
3X Ø 3 THRU ALL for 3mm guidepin to slide
Ø9.50 THRU ALL
Ø15 ↧2.50
A
A
VIEW A-A
1.50
11.52
3X Ø 1.60 THRU
M2X0.4 - 6H THRU
All dimensions metric in mm.
UNLESS OTHERWISE SPECIFIED:
DIMENSIONS ARE IN INCHES
TOLERANCES:
FRACTIONAL ±
ANGULAR: MACH ± BEND ±
TWO PLACE DECIMAL ±
THREE PLACE DECIMAL ±
INTERPRET GEOMETRIC TOLERANCING PER:
MATERIAL
SS316
FINISH
NEXT ASSY
USED ON
APPLICATION
DO NOT SCALE DRAWING
DRAWN
CHECKED
ENG APPR.
MFG APPR.
Q.A.
COMMENTS:
NAME
DATE
QTY: 1
TITLE:
SIZE
A
DWG. NO.
DACback
REV
SCALE: 2:1
WEIGHT:
SHEET 1 OF 1
PROPRIETARY AND CONFIDENTIAL
THE INFORMATION CONTAINED IN THIS DRAWING IS THE SOLE PROPERTY OF <INSERT COMPANY NAME HERE>. ANY REPRODUCTION IN PART OR AS A WHOLE WITHOUT THE WRITTEN PERMISSION OF <INSERT COMPANY NAME HERE> IS PROHIBITED.
5
4
3
2
1

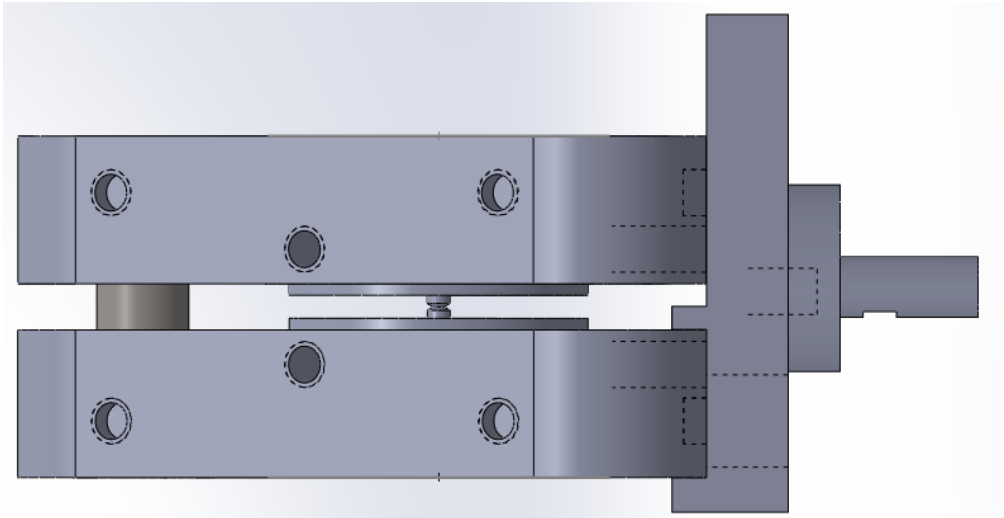

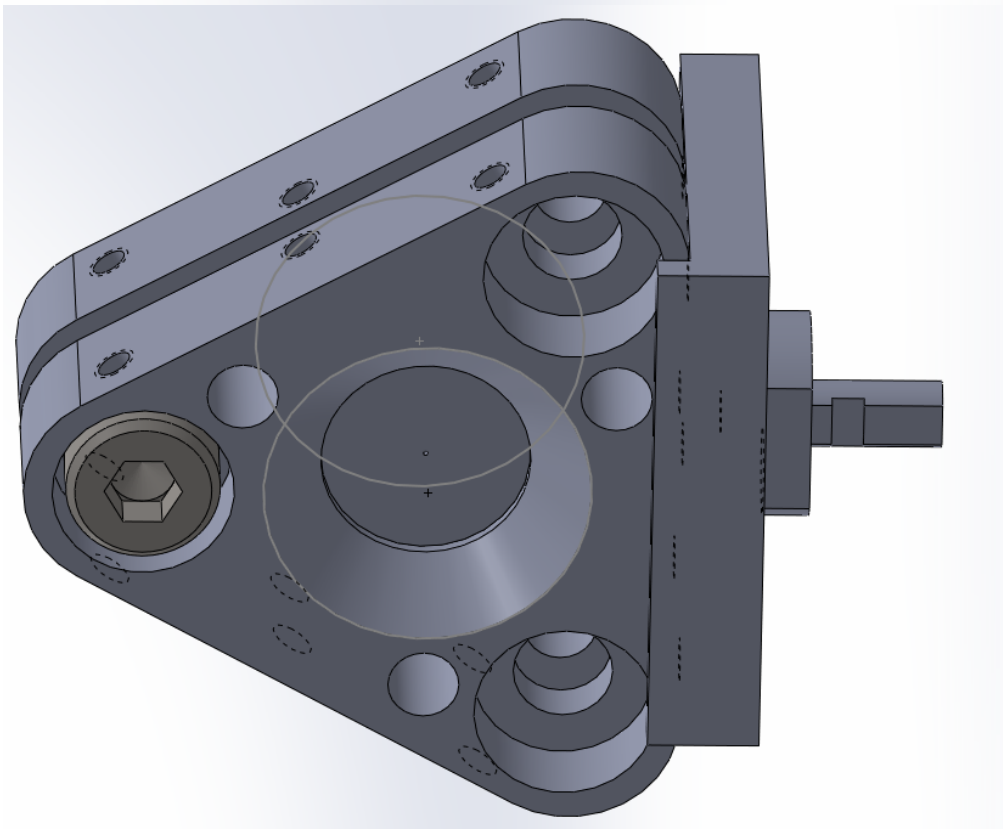

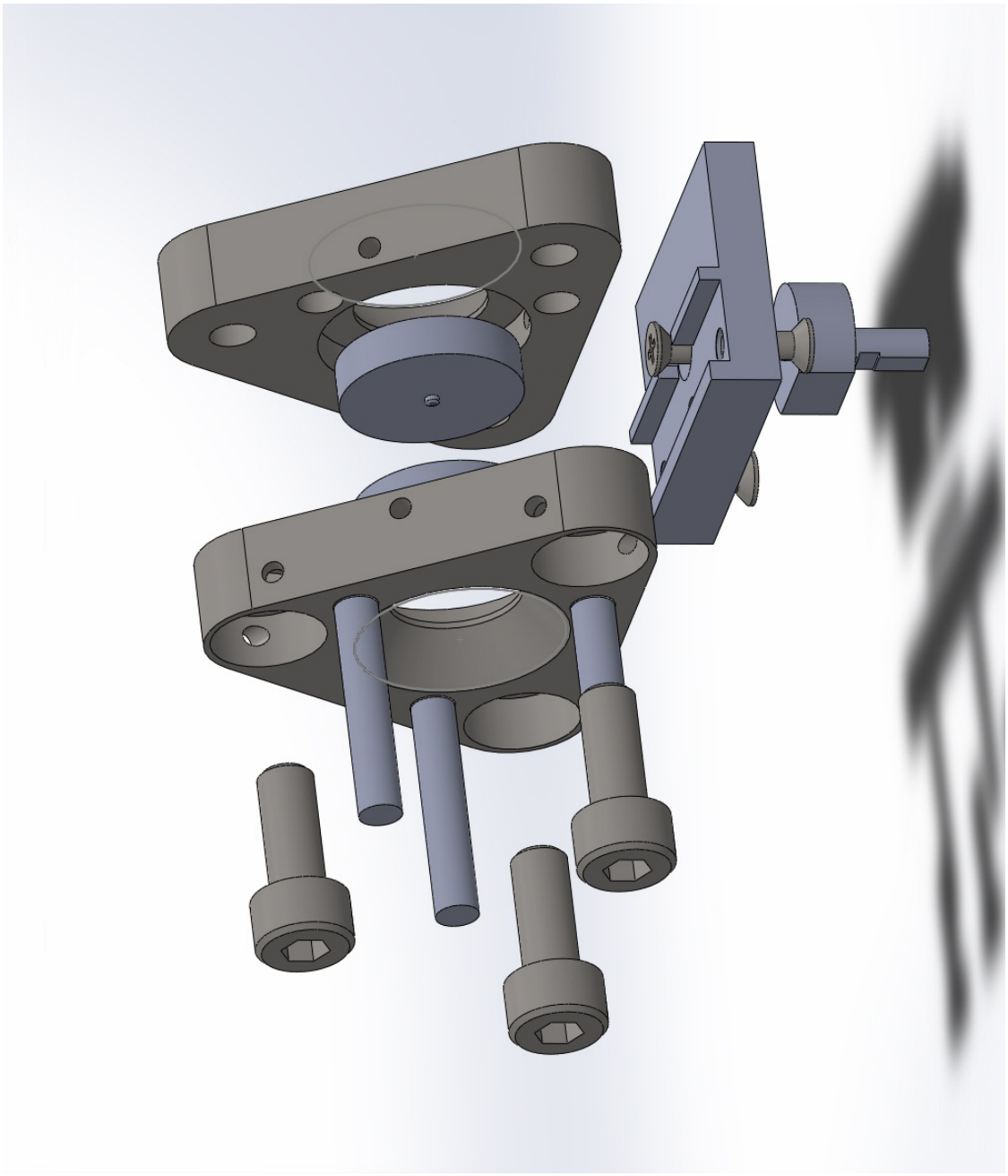

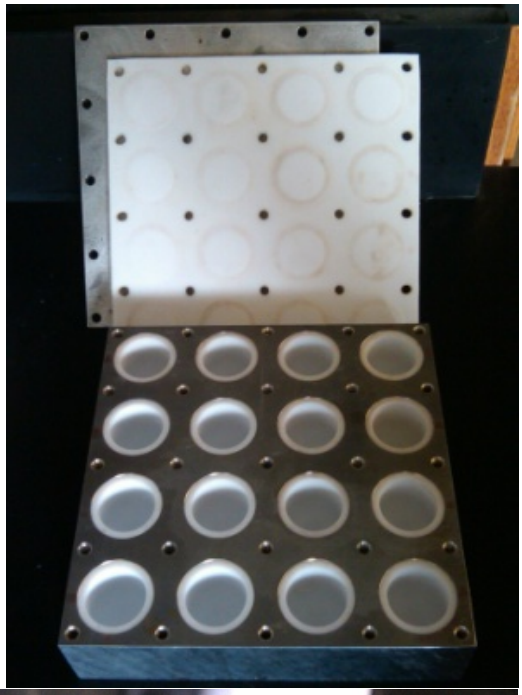

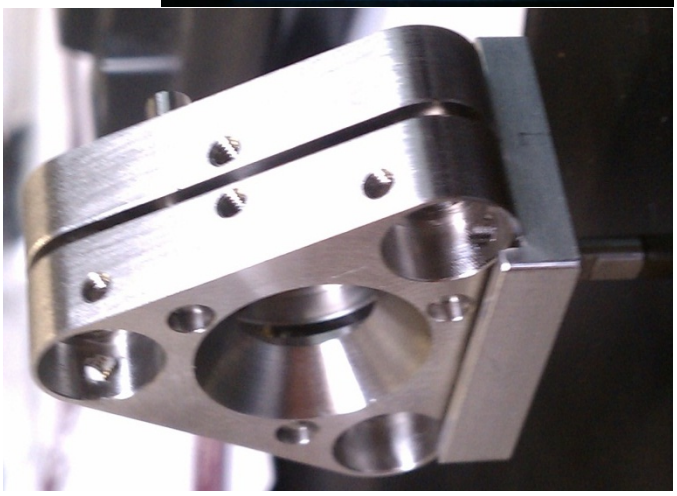

APPENDIX B

CHAPTER IV SUPPLEMENTARY INFORMATION

Table B1.Result of the Rietveld refinement of 4.

molecular formula	$Zn_3[NH_2(CH_2PO_3)_2]_2$
formula weight	600.21
crystal system	orthorhombic
a, Å	10.6881(2)
b, Å	13.3129(2)
c, Å	5.4266(2)
a, deg	90.00
b, deg	90.00
g, deg	90.00
V, Å3	772.14
space group	P 2_12_12
Z	2
D_{calc}, g cm^{-3}	2.59
q range, deg	8.0 - 57.0
T (K)	298(2)
l, Å	1.542
Chebychev background polynomial order	5
R_{exp} (%)	8.700
R_{wp} (%)	15.044
R_p (%)	11.824

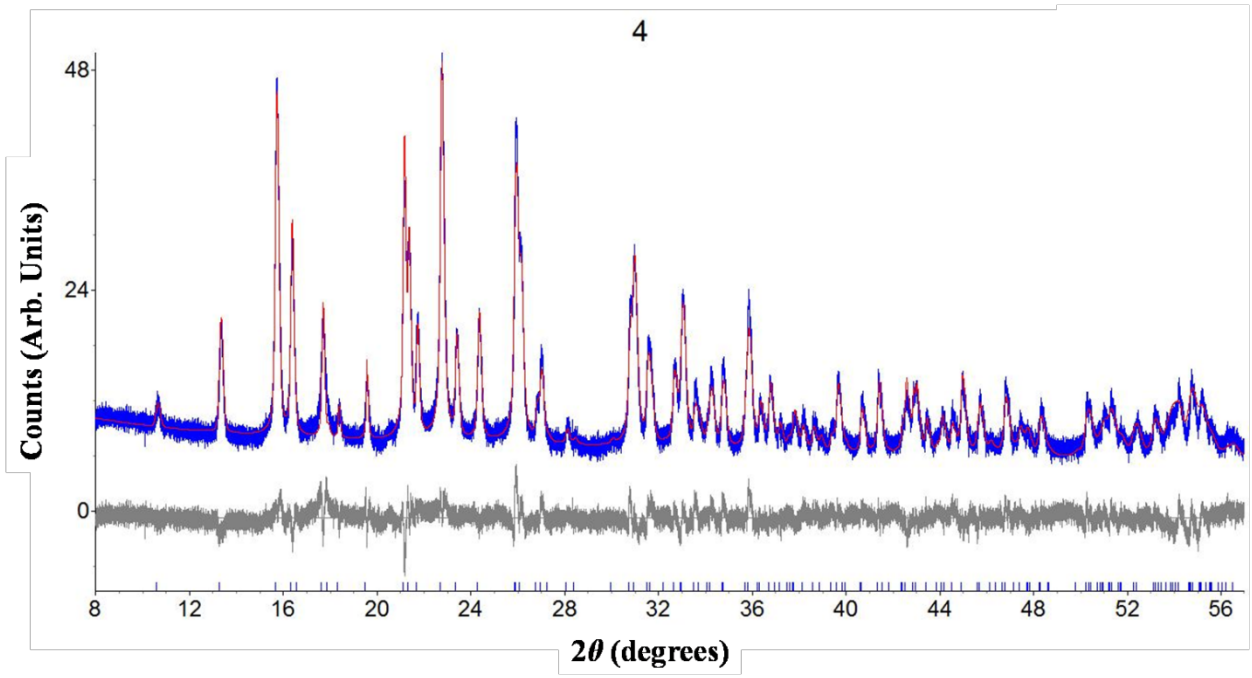

Figure B1 Rietveld plot for 4 of experimental (blue) calculated (red) and difference (gray).

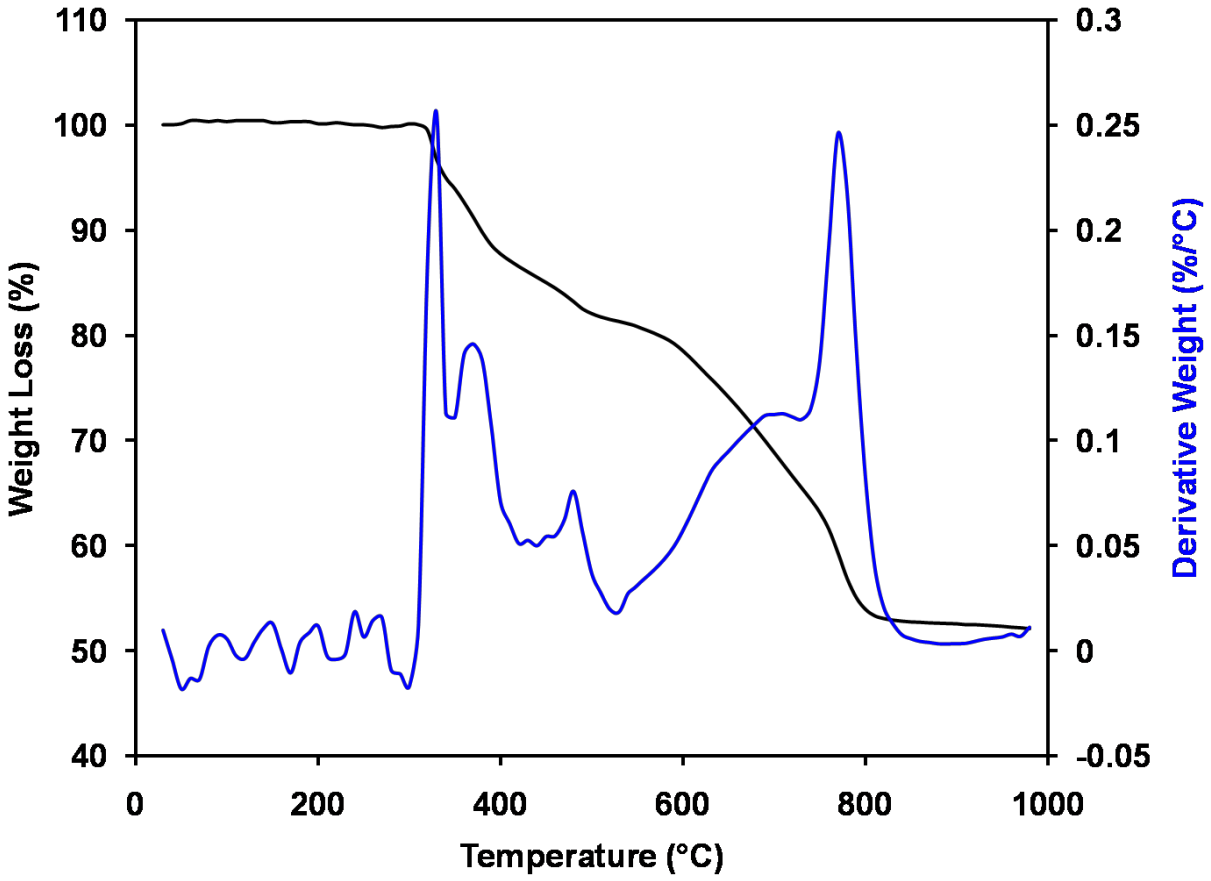

Figure B2. TGA of 1.

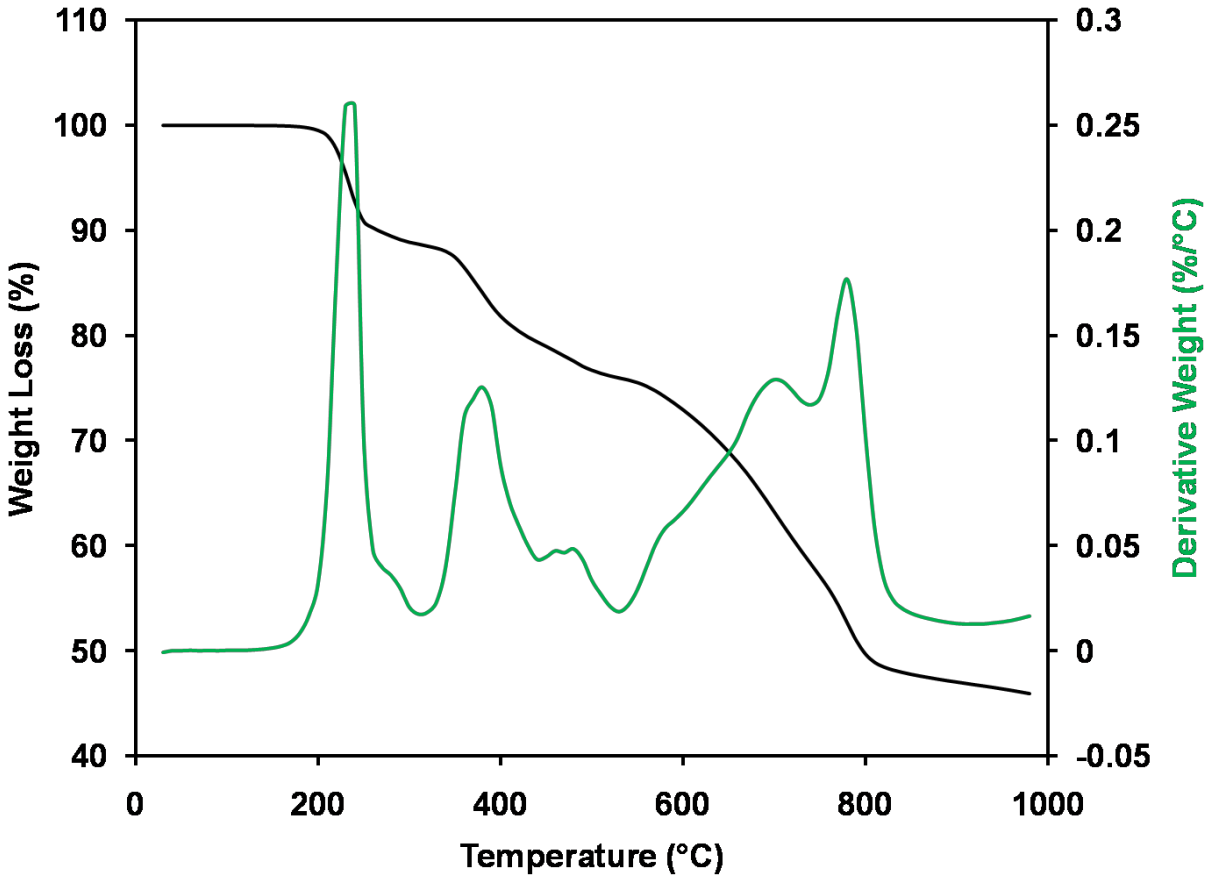

Figure B3. TGA of 2.

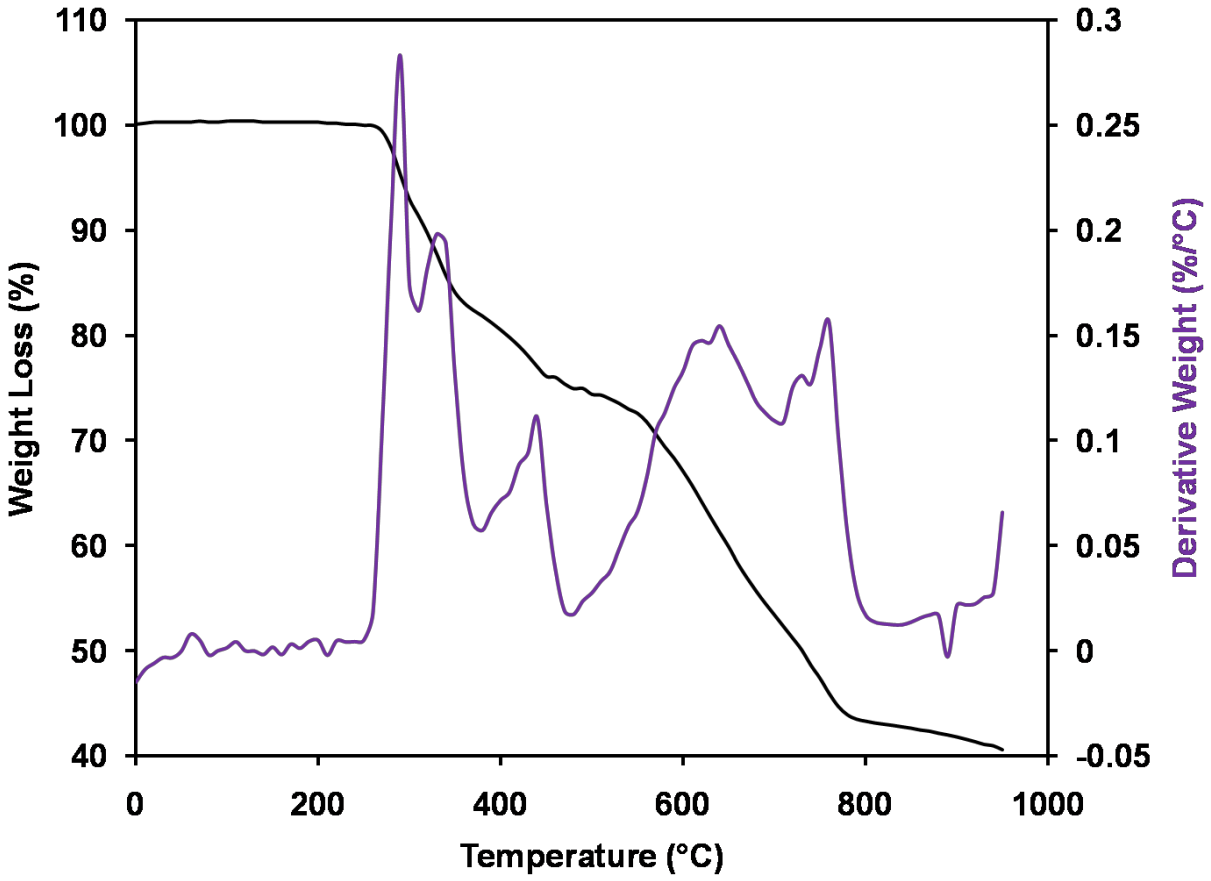

Figure B4. TGA of 3.

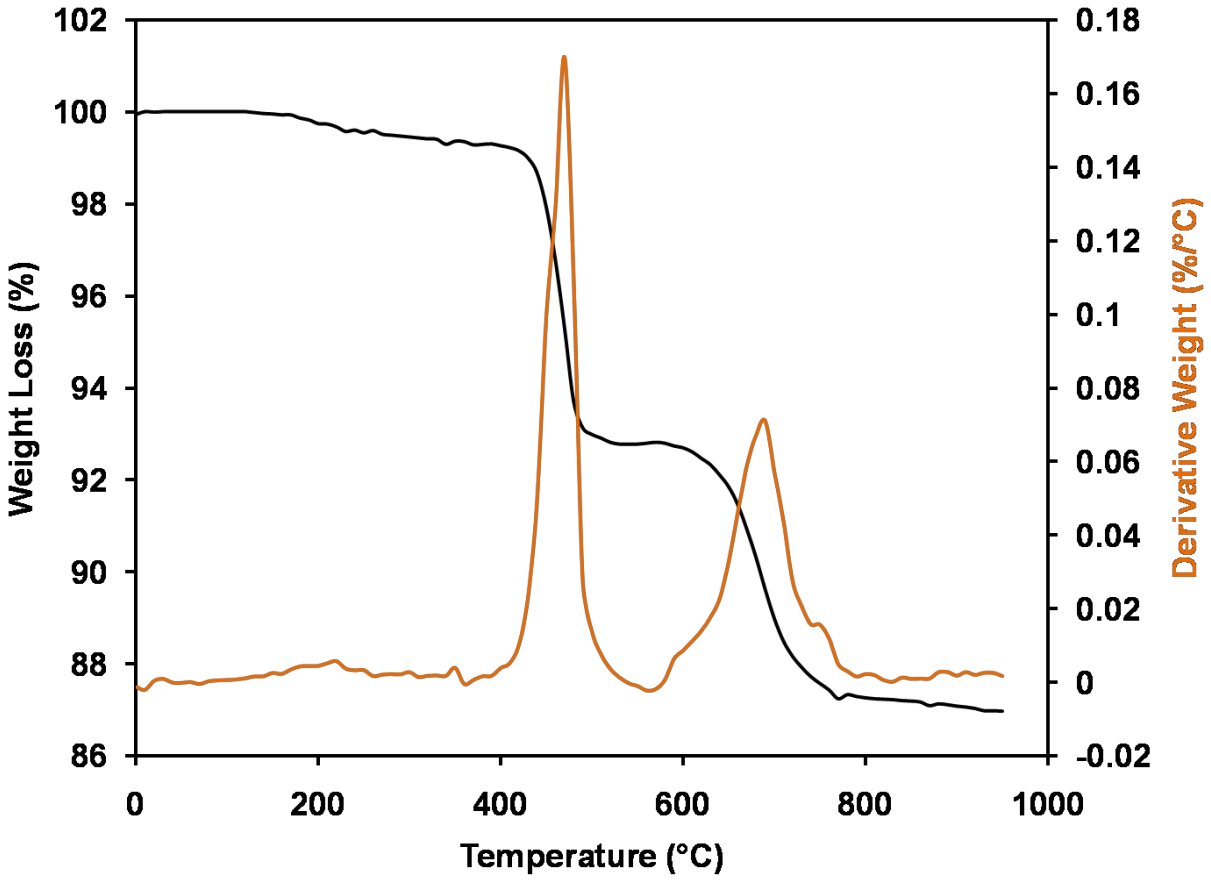

Figure B5. TGA of 4.

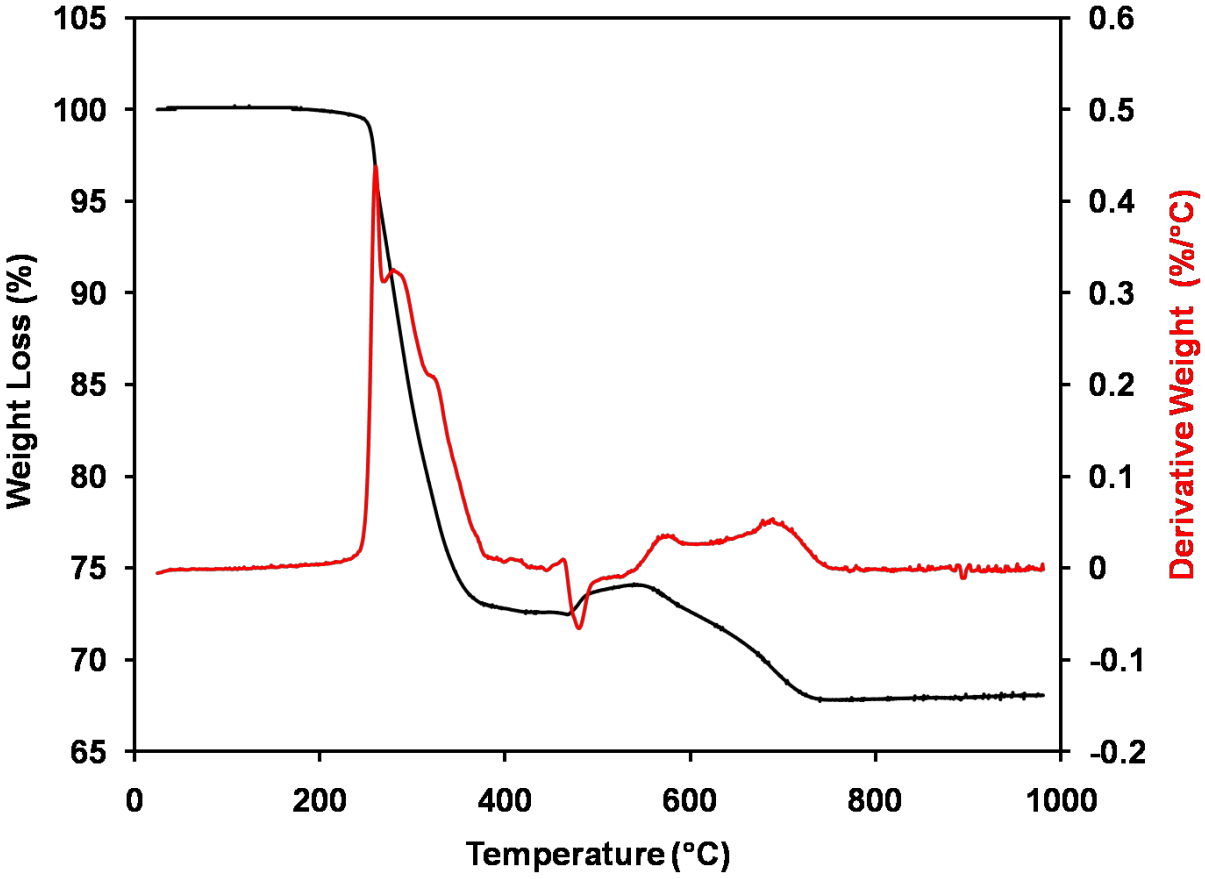

Figure B6. TGA of 5.

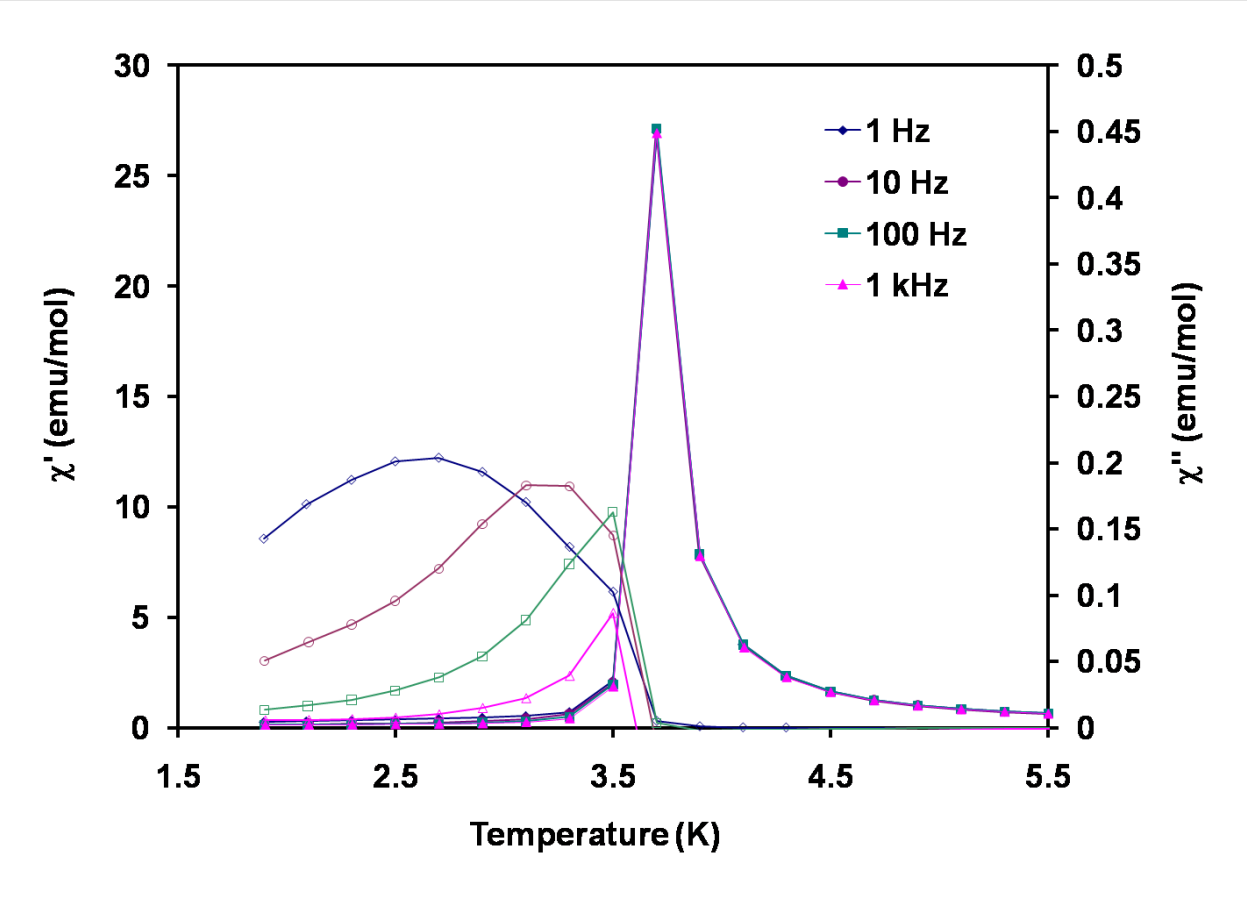

Figure B7. Temperature dependences of the real χ' (full symbols) and imaginary χ'' (open symbols) components of the AC magnetic susceptibility for 1 measured in an oscillating field of 5 Oe at different frequencies.

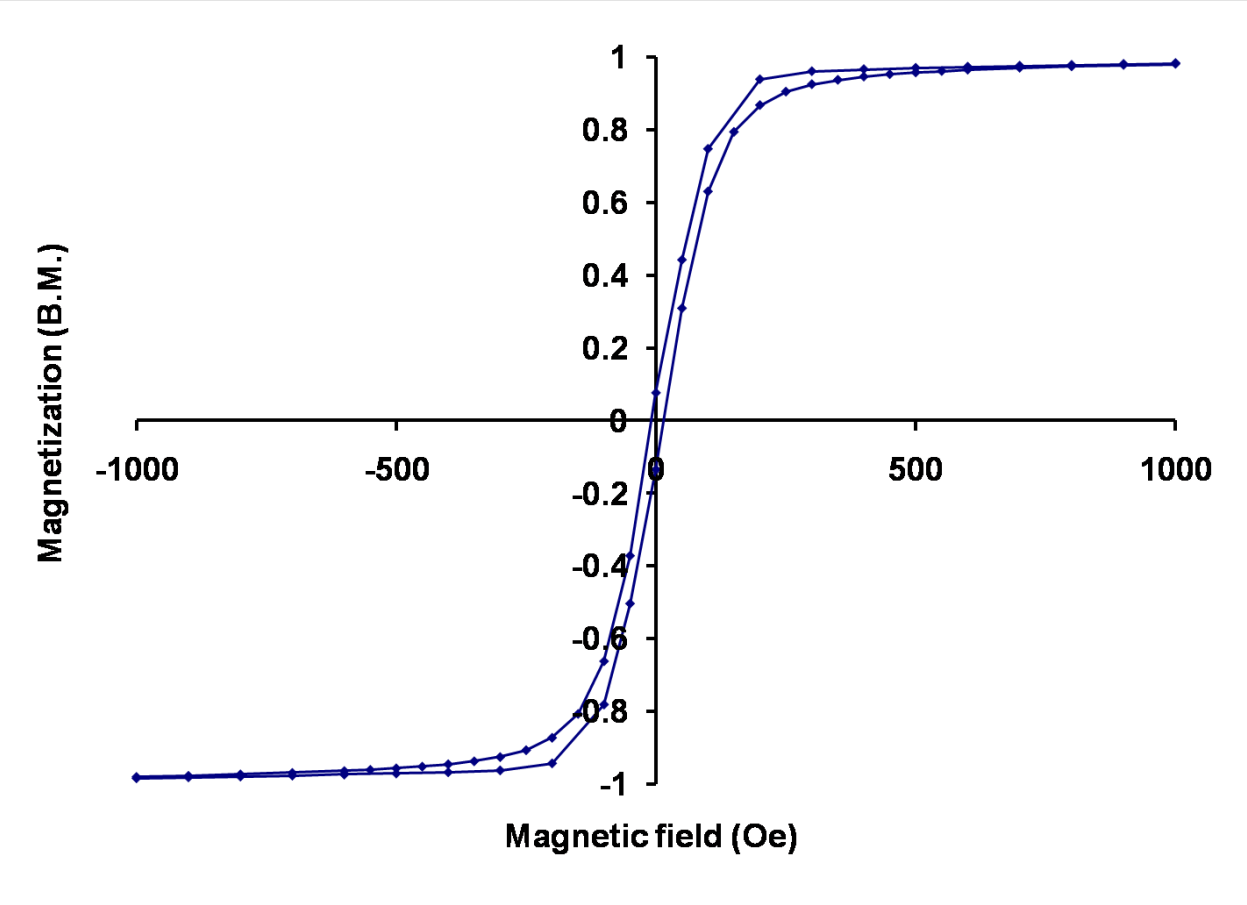

Figure B8. Hysteresis loop for 1 at 1.8 K.

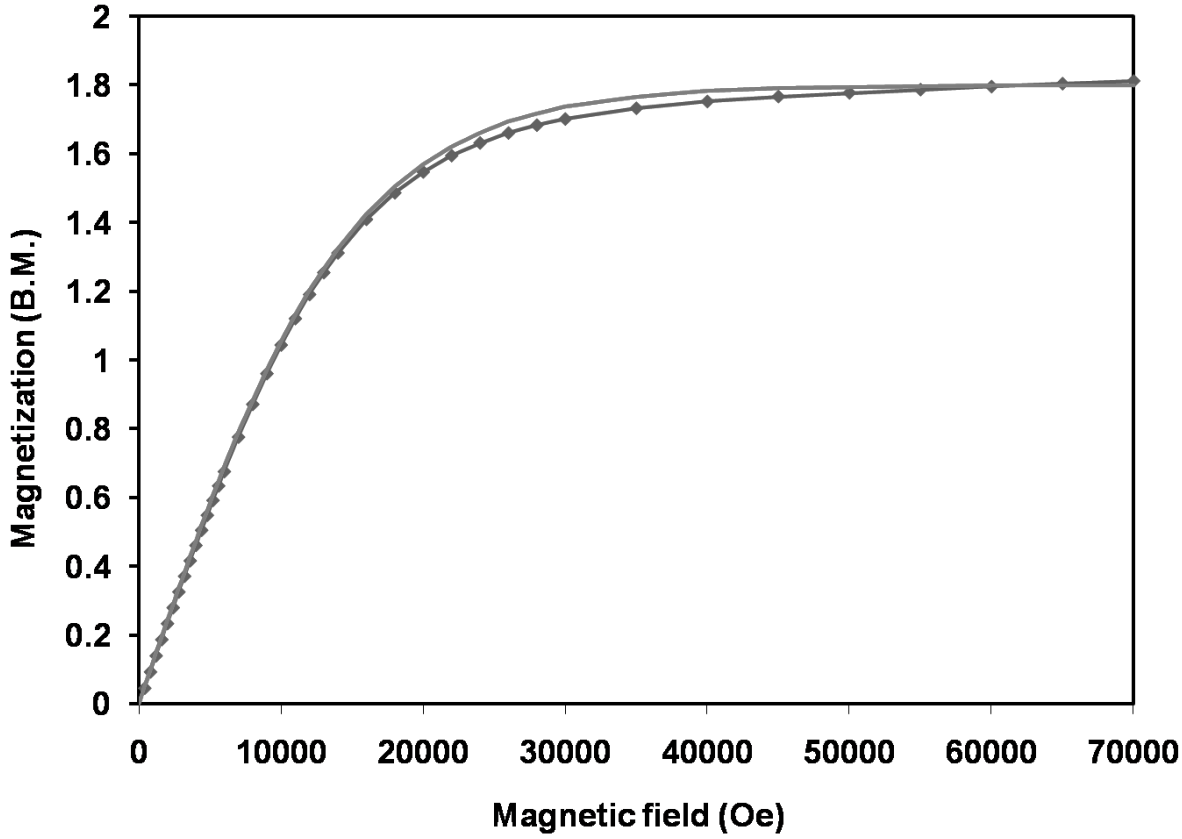

Figure B9. The field dependence of magnetization for 2. The solid line corresponds to the best fit to the Brillouin function.

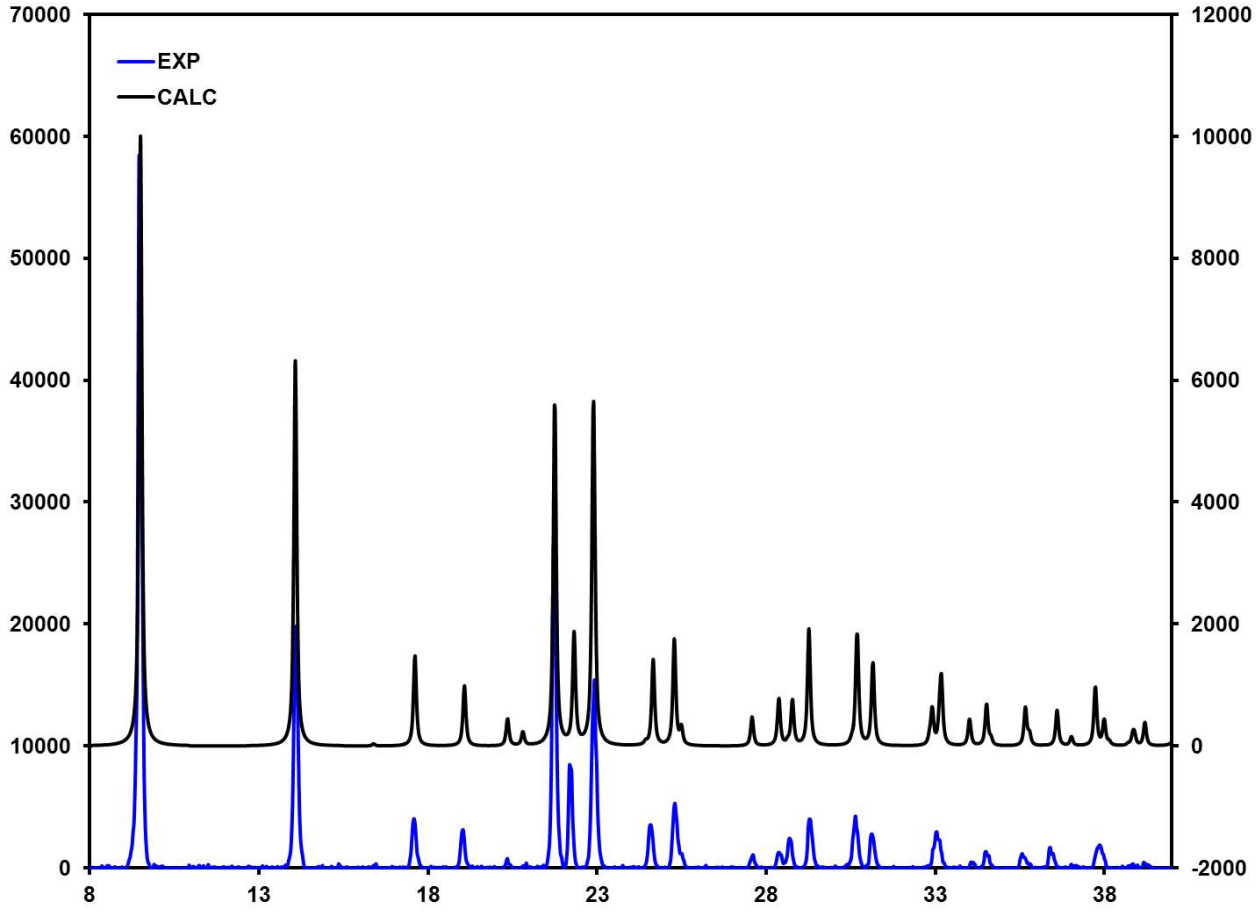

Figure B10. PXRD of 1.

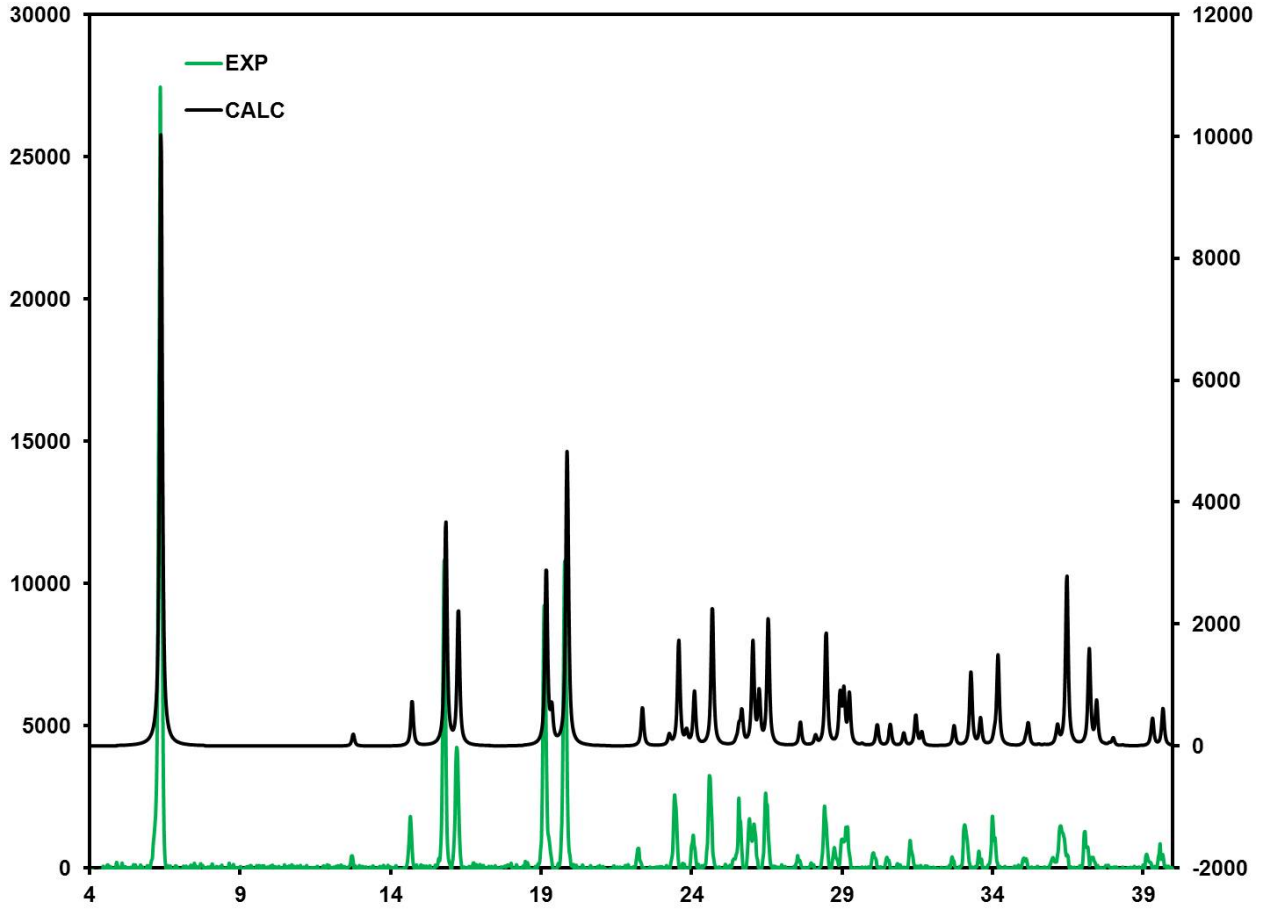

Figure B11. PXRD of 2.

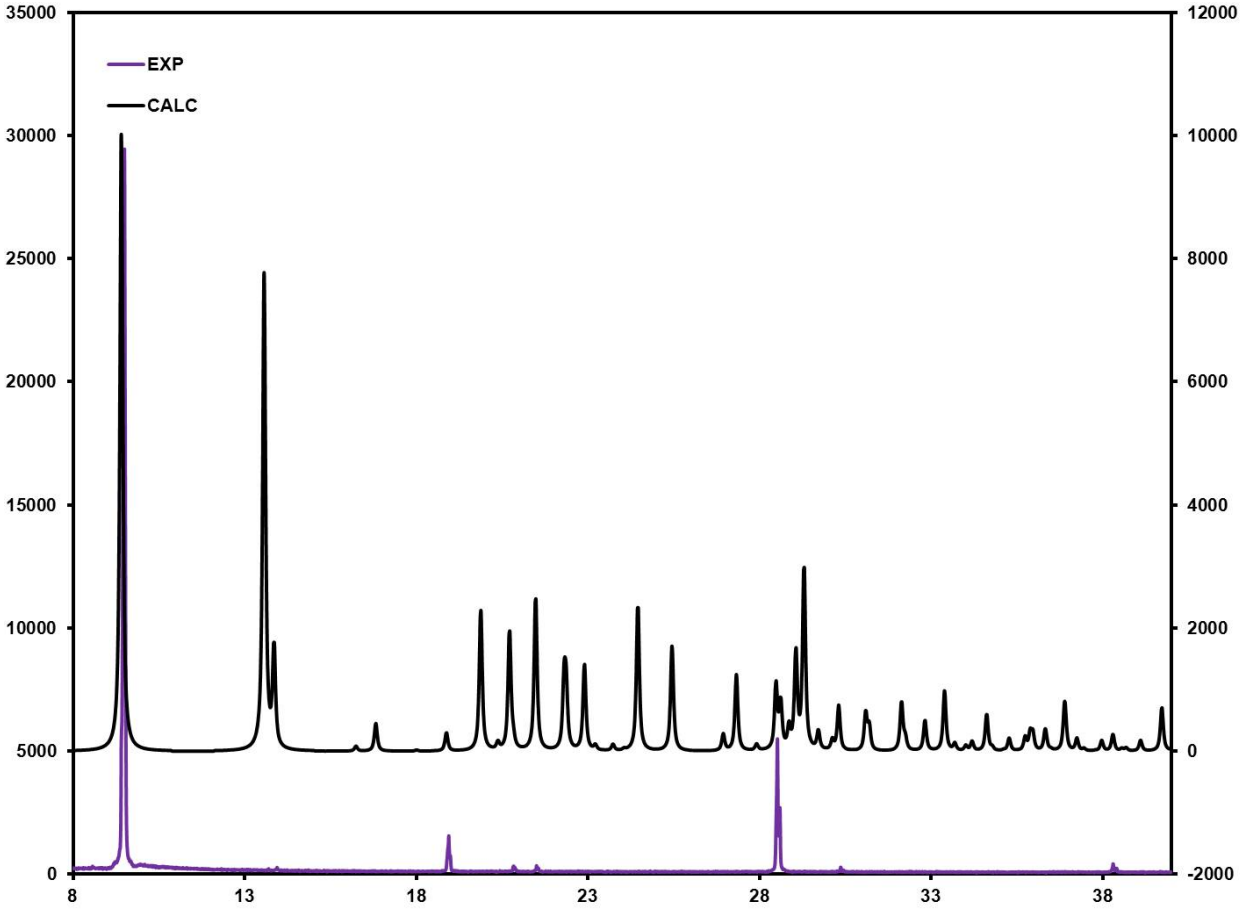
EXP
CALC
35000
30000
25000
20000
15000
10000
5000
0
12000
10000
8000
6000
4000
2000
0
-2000
8
13
18
23
28
33
38

Figure B12. PXRD of 3. Due to the small sample size and nature of this material, it suffers from severe preferential orientation.

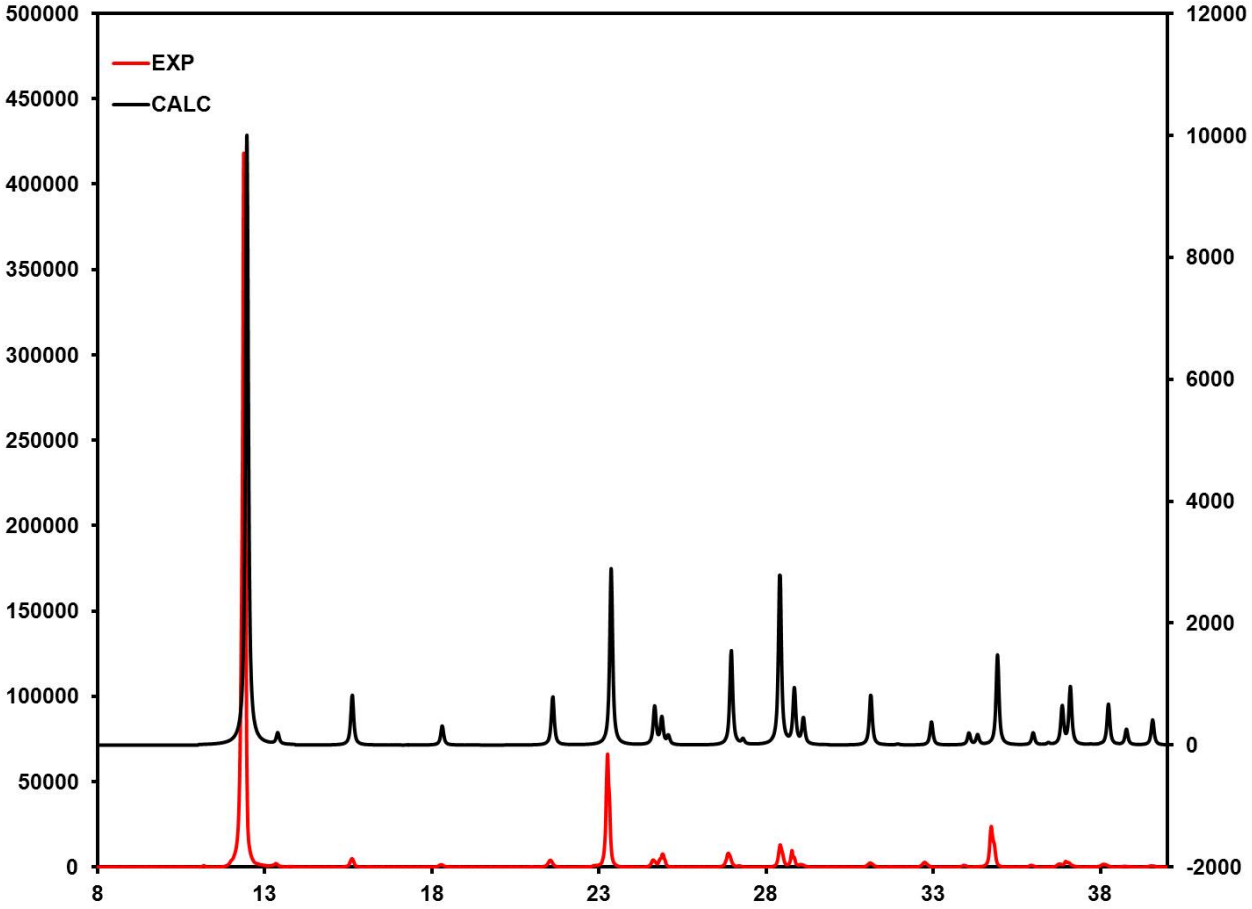

Figure B13. PXRD of 5. Due to the small sample size and nature of this material, it suffers from severe preferential orientation.

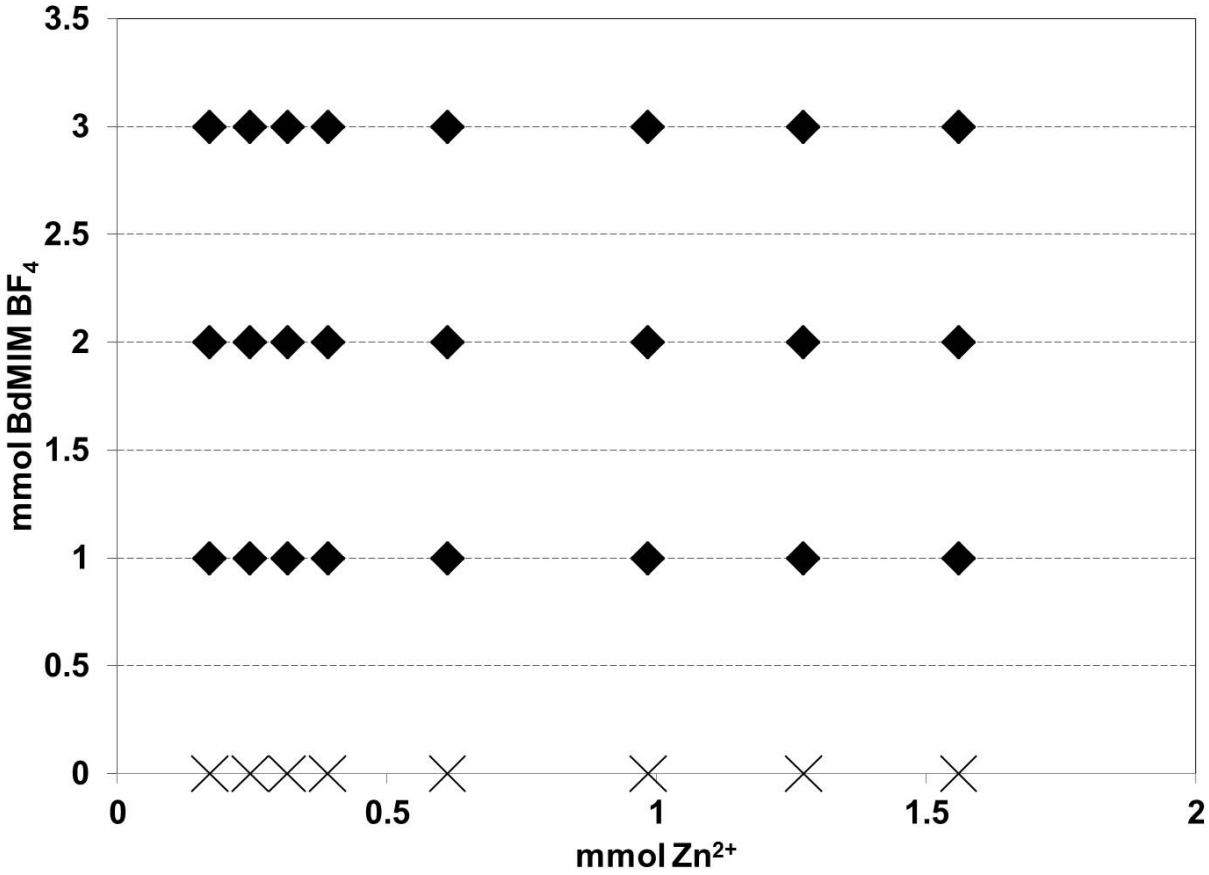

Figure B14. Synthesis field of reaction of $ZnCl_2$ with IBMPA. × = no reaction; ♦ = compound 4.